

Dissertation
submitted to the
Combined Faculties for the Natural Sciences and for Mathematics
of the Ruperto-Carola University of Heidelberg, Germany
for the degree of
Doctor of Natural Sciences

Put forward by
Diplom-Physiker M. Sc. Andreas Ernst
Born in: Marburg, Germany
Oral examination: April 15, 2009

Dissolution of Star Clusters in the Galaxy and its Center

Referees:

PD Dr. Andreas Just

Prof. Dr. Rainer Spurzem

Zusammenfassung

Diese Arbeit widmet sich Untersuchungen zur Auflösung von Sternhaufen im Gezeitenfeld der Milchstraße und insbesondere ihres Zentrums. Es wird zunächst der Fluchtprozess von Sternen aus Sternhaufen im Rahmen chaostheoretischer Überlegungen betrachtet. Schon in der linearen Gezeitenapproximation ist es möglich, “Flucht-Basins” und den chaotischen Sattel für das System zu berechnen. Nachdem Sterne den Sternhaufen verlassen haben, bilden sie aufgrund der differentiellen Rotation der Galaxie Gezeitenarme. Für Sternhaufen auf Kreisbahnen wird der theoretische Rahmen zur Untersuchung der Eigenschaften der Gezeitenarme diskutiert. Die Theorie wird auf einen Modell-Sternhaufen im Zentrum der Milchstraße angewandt. Zu diesem Zweck wurde ein neues N -Körper-Programm namens NBODY6GC entwickelt. Der Algorithmus wird im Detail beschrieben und die Resultate der durchgeführten N -Körper-Simulationen diskutiert. An bestimmten Stellen in den Gezeitenarmen bilden sich aufgrund der Epizykelbewegung der Sterne wohldefinierte Klumpen. Die Positionen der Klumpen werden mit der analytischen Theorie berechnet. Darüber hinaus wird eine Klassifikation der Haufensterne nach Radius und spezifischer Jacobi-Energie vorgestellt, um die Auflösungszeiten zu erklären, und es werden einige Resultate hinsichtlich des “Paradoxes der Jugend” formuliert.

Abstract

This thesis is concerned with investigations on the dissolution of star clusters in the tidal field of the Galaxy and in particular its center. At first the escape process of stars from star clusters is studied in the framework of chaos-theoretical considerations. Already in the linear tidal approximation it is possible to compute the basins of escape and the chaotic saddle for the system. After the stars have left the star cluster they form tidal arms (or tails) due to the differential rotation of the Galaxy. For star clusters on circular orbits the theoretical framework for the investigation of the properties of tidal arms is discussed. The theory is applied for a star cluster model in the Galactic center. For this purpose a new N -body program called NBODY6GC has been developed. The algorithm is described in detail and the results of N -body simulations are discussed. At certain positions, well-defined clumps develop in the tidal arms due to the epicyclic motion of the stars. The positions of the clumps are calculated with the analytical theory. Furthermore, a classification of the cluster stars according to radius and specific Jacobi energy is introduced in order to explain the dissolution times and a few results on the “paradox of youth” are formulated.

Seh' ich die Werke der Meister an,
So seh ich das, was sie getan;
Betracht ich meine Siebensachen,
Seh' ich, was ich hätt' sollen machen.

J. W. v. Goethe

Meiner Familie gewidmet

Contents

1	Preface	1
2	Stellar systems theory	4
2.1	Spherically symmetric models	4
2.2	Scale free models	6
2.3	Plummer model	6
2.4	King model	8
3	Escape and chaos theory	12
3.1	Introduction	12
3.2	Tidal approximation	15
3.3	A simple model	16
3.4	Poincaré surfaces of section	17
3.5	The basins of escape	18
3.6	The chaotic saddle	19
4	Theory of tidal arms	26
4.1	Taylor expansions	26
4.1.1	R -expansions	26
4.1.2	η -expansions	28
4.1.3	L -expansions	29
4.1.4	ω -expansions	32
4.1.5	Other expansions	33
4.2	Dynamics in tidal arms	33
5	The Galactic center	36
5.1	The paradox of youth	37
5.2	He I emission line stars	39
5.3	Comoving groups	40
5.3.1	IRS 13E	40
5.3.2	IRS 16SW	41
5.3.3	IRS 13N	41
5.4	CWS and CCWS	41
5.5	Young stars	42
5.5.1	WR stars, Ofpe/WN9 stars and LBVs	42
5.5.2	OB stars	42
5.5.3	S stars	42
5.6	Masers	43
5.6.1	OH masers	43
5.6.2	H ₂ O masers	44
5.6.3	Methanol masers	45

5.7	Young star clusters	45
5.7.1	Quintuplet	45
5.7.2	Arches	46
5.8	Numerical works	47
6	Strong tidal field	50
6.1	Effective potential	50
6.2	Poincaré surfaces of section	52
7	Gravitational N-body models	56
7.1	The gravitational N -body problem	56
7.2	The scaling problem	57
7.3	N -body units	57
7.4	Regularization	58
8	Numerical methods	60
8.1	The computer program NBODY6GC	60
8.1.1	Cluster orbit	60
8.1.2	Stellar orbits	61
8.2	Integrators	63
8.2.1	Hermite scheme	63
8.2.2	Composition scheme	64
8.2.3	Implicit midpoint method	66
8.3	Energy balance	68
8.3.1	Friction and mass loss	68
8.3.2	Energy checking	68
8.4	Density center correction	69
8.5	The computer program INTGC	70
8.6	Tidal arm coordinate system	71
9	Simulations	72
9.1	A test case	72
9.2	Properties of tidal arms	81
9.3	Lifetime scaling and RE classification	97
9.4	Eccentric star cluster orbit scenario	103
10	Conclusions	106
A	Useful expressions	108
A.1	Constants and units	108
A.2	Formulas	108
B	Basins of attraction	109
C	GRID computing	111
D	Dynamical friction	114
D.1	Variable Coulomb logarithm	116
D.2	Realistic χ function	116
E	New Subroutines	119
F	Input file: galcen.dat	120

G Documentation file: model-par.txt	121
H Setting up a run	122
I Abbreviations	123
Bibliography	123
Danksagung	133

Chapter 1

Preface

The dissolution of star clusters is a problem with a long history in stellar dynamics. The pioneering works are by Ambartsumian (1938) [1] and Spitzer (1940) [2]. Many other stellar dynamicists worked on the dissolution of star clusters since that time, as Chandrasekhar, King, Hénon, Wielen, Fukushige, Heggie and Baumgardt. A brief historical overview of their investigations will be given in the introduction to Chapter 3 of this thesis. While the author worked on his diploma thesis on the dynamical evolution of rotating star clusters [3, 4] in the years 2004/05 at the Astronomisches Rechen-Institut (ARI) in Heidelberg, he became more and more interested in the fascinating problem of escape of stars from a star cluster. Can the process of escape lead to the complete dissolution of a star cluster until a single binary star remains as a remnant?

The analysis of the escape process presented in Chapter 3 of this thesis shows that it can be studied in the framework of chaos theory. For certain values of the Jacobi energy, a star cluster in the tidal field of a galaxy is a dynamical system with a divided phase space: Both regular and chaotic orbits can be found. The Poincaré surfaces of section show the effect of a Coriolis asymmetry between regular and chaotic orbits. Most of the retrograde orbits with respect to the motion of the star cluster around the galaxy are regular (Fukushige & Heggie 2000 [5]). The regular orbits are bound to the region of the star cluster by a non-classical integral of motion. On the other hand, the chaotic orbits escape if their Jacobi energy exceeds a certain threshold. Since the stars can leave the star cluster in two different directions while they pass one of the two Lagrange points L_1 or L_2 it is possible to obtain basins of escape similar to basins of attraction in dissipative systems or the well-known Newton-Raphson fractals (see Appendix B for two examples). The chaos in the escape process from star clusters is related to a fractal structure in the phase space which has the form of a Cantor set (Cantor 1884 [6]) and is called the chaotic saddle. It contains hyperbolic points which belong to unstable periodic orbits. As is well-known, the unstable periodic orbits introduce chaos into a dynamical system (e.g. Contopoulos 2002 [7]).

The escaping stars form tidal arms (or tails) which extend along the potential wall of the effective galactic potential. A famous observation of tidal tails has been published in the works by Odenkirchen et al. (2001 [10], 2003 [8]) on the tidal tails of the star cluster Palomar 5. The tidal tails of Palomar 5 are shown in Figure 1.1. One can see that they are not homogeneous but show well-defined clumps at positions where the density has local maxima. Such clumps have been noticed in computer simulations (Capuzzo-Dolcetta, di Matteo & Miocchi 2005 [11], di Matteo, Capuzzo-Dolcetta & Miocchi 2005 [9]; see also Figure 1.2). The existence of clumps in the tidal tails of star clusters is related to the shape of the orbits of the escaping stars (e.g. Küpper et al. 2008 [12]). The position of the clumps can be calculated from the angular momenta of the stars in the tidal tails (Just et al. 2009 [13]). The detailed analytical theory based on Taylor expansions is presented in Chapter 4 of this thesis. We use the theory in order to calculate the positions of the clumps for the special case of a dissolving star cluster close to the Galactic center. The simulations are carried out with a new N -body program called NBODY6GC. The algorithm

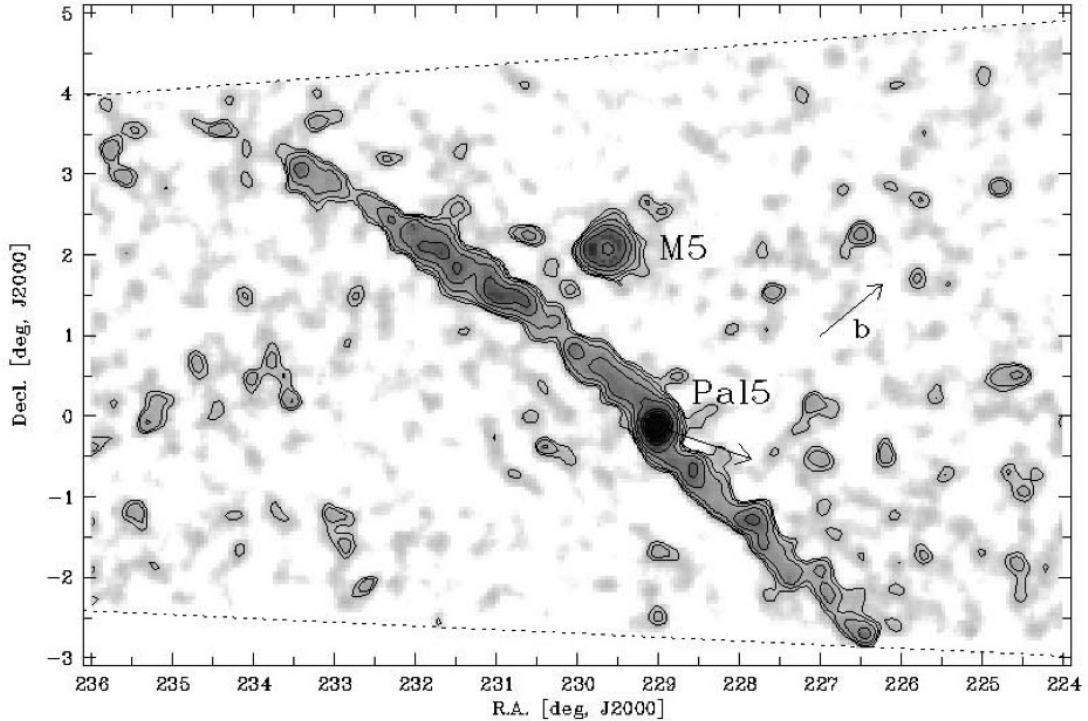


Figure 1.1: Tidal tails of the star cluster Palomar 5. From Odenkirchen et al. (2003) [8].

is in detail described in Chapter 8. The results of several N -body simulations with the program NBODY6GC are presented in Chapter 9 of this thesis.

The Galactic center is currently a field of very intensive research. The Galactic center region spans roughly *nine* orders of magnitude in galactocentric radii ranging from a rough outer radius of the central molecular zone ($R_{\text{CMZ}} \approx 200$ pc, Morris & Serabyn 1996 [14]) down to the Schwarzschild radius of the Galactic super-massive black hole ($R_{\bullet} \approx 4 \times 10^{-7}$ pc) which resides at the position of the strong radio source named Sgr A*. This large range in radial scales already suggests that the physics in the Galactic center region is extremely rich in content. Two young star-burst clusters named Quintuplet (Nagata et al. 1990 [15], Okuda et al. 1990 [16]) and Arches (Nagata et al. 1995 [17]) have been discovered at projected distances less than 35 pc away from the Galactic center. They have quite extraordinary properties and stellar contents. Their formation still requires clarification. However, both clusters are located (at least, in projection) near the Galactic center “Radio Arc” (Yusef-Zadeh, Morris & Chance 1984 [18], Timmermann et al. 1996 [19]), which is a region rich in molecular clouds and gaseous filaments (Morris & Serabyn 1996 [14], Lang et al. 2005 [20]).

Young stars have been discovered in the central parsec around the Galactic center. Their presence in the close vicinity of the Galactic supermassive black hole ($M_{\bullet} \approx (3 - 4) \times 10^6 M_{\odot}$) is currently a heavily disputed topic within the astrophysical community. For example, the comoving groups IRS 13E (Coker & Pittard 2002 [21], Maillard et al. 2004 [22]), IRS 16SW (Tamblyn & Rieke 1993 [23], Krabbe et al. 1995 [24], Lu et al. 2005 [25]) and IRS 13N (Mužić et al. (2008) [26]), which consist of young, massive stars, orbit Sgr A* at a distance smaller than one parsec. In addition, Wolf-Rayet stars, Ofpe/WN9 stars, luminous blue variables and, recently, many OB stars (Paumard et al. 2006) have been identified within a radius of one parsec around Sgr A*. Also, the cluster of S stars roughly resides within the central arcsecond around Sgr A* (Ghez et al.

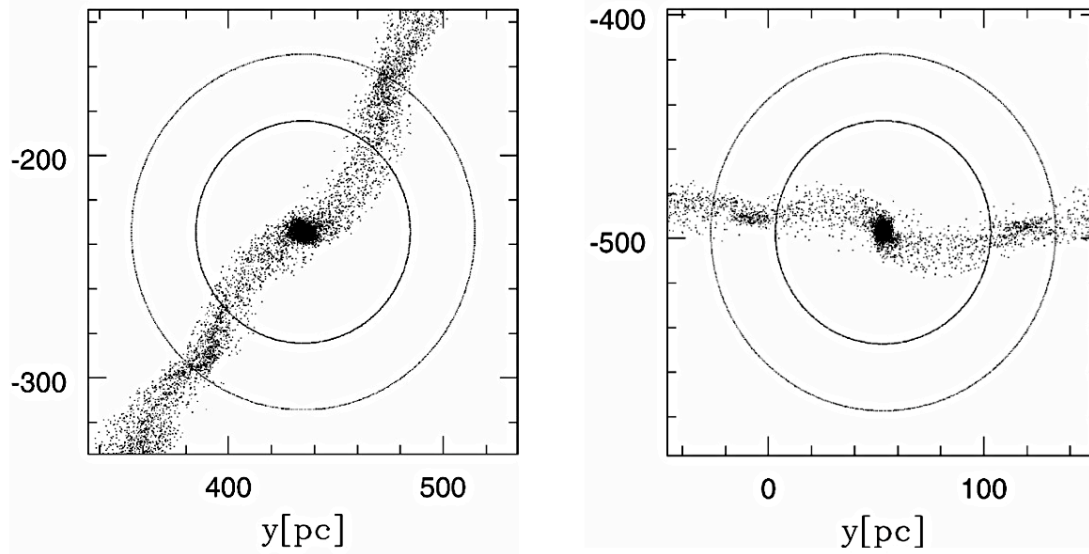


Figure 1.2: Clumpy substructures in globular cluster tidal tails. From di Matteo, Capuzzo-Dolcetta & Miocchi 2005 [9].

2005 [27], Eisenhauer et al. 2005 [28]). Star formation within the central parsec of our Galaxy is problematic because of the presence of the super-massive black hole, since its tidal field dissolves gas clouds from which stars could form by gravitational collapse. The required high mean number densities can only be achieved by a strong compression of the gas and are not present within the central parsec. Rather, the cavity within the circum-nuclear ring contains only atomic and ionized hydrogen. The raw material for star formation is currently lacking (Morris 1993 [29]). For these reasons one may wonder why we observe young stars in the central parsec: Their presence in the central parsec constitutes the “paradox of youth” (Ghez et al. 2003 [30]).

Gerhard (2001) [31] proposed that young stars formed in a massive $10^6 M_{\odot}$ star cluster in a sufficiently large distance from Sgr A* which spiralled into the Galactic center by dynamical friction within the lifetime of its most massive stars and dissolved there. The young stars in the central parsec could be remnants of such a dissolved star cluster. It may be that comoving groups like IRS 13E, IRS 16SW or IRS 13N are remaining cores of such star clusters, as some authors proposed. To test the star cluster inspiral scenario was the initial motivation for this thesis.

With two examples of very massive ($M_{cl} = 10^6 M_{\odot}$) star clusters at initial galactocentric radii of $R_g(0) = 20$ pc - one on a mildly eccentric and one on a circular orbit -, numerical evidence will be given for the fact that realistic values of the Coulomb logarithm of dynamical friction lead to ratios of inspiral to dissolution time scales which are far too large to make the star cluster inspiral scenario probable. Instead, a different scenario is considered. The author demonstrates numerically that a star cluster with a small mass on a very eccentric orbit can indeed transport stars into the central parsec within the lifetime of its most massive stars. In the “eccentric star cluster orbit scenario”, the eccentricity of the star cluster orbit is crucial for the transport of young stars into the central parsec and not its orbital decay due to dynamical friction.

Chapter 2

Stellar systems theory

2.1 Spherically symmetric models

If a stellar system is spherically symmetric, spherical coordinates (r, θ, ϕ) are the appropriate coordinates. Gravitational potential $\Phi(r)$, cumulative mass $M(r)$, and density $\rho(r)$ do not depend on θ and ϕ , and they are related in a particularly simple way. In the following discussion, we use the Poisson equation for a spherically symmetric system,

$$\nabla^2 \Phi(r) = \frac{1}{r^2} \frac{\partial}{\partial r} \left(r^2 \frac{\partial \Phi(r)}{\partial r} \right) = 4\pi G \rho(r) \quad (2.1)$$

where ∇^2 is the Laplacian operator and G is the gravitational constant. Since the vector field of specific gravitational force $\mathbf{f}(r)$ (or force on a unit mass) is conservative,¹ it can be written as the gradient of the scalar gravitational potential $\Phi(r)$,

$$\mathbf{f}(r) = -\nabla \Phi(r) = -\frac{\partial \Phi(r)}{\partial r} \frac{\mathbf{r}}{r} = f(r) \frac{\mathbf{r}}{r} \quad (2.2)$$

where ∇ is the gradient operator, and Equation (2.1) can be written as

$$\nabla \cdot \mathbf{f}(r) = -\frac{1}{r^2} \frac{\partial}{\partial r} \left(r^2 f(r) \right) = -4\pi G \rho(r) \quad (2.3)$$

where $\nabla \cdot$ is the divergence operator.

Starting from a known potential, we have

$$\frac{\partial \Phi(r)}{\partial r} = \frac{GM(r)}{r^2} = -f(r) \quad (2.4)$$

$$\rho(r) = \frac{1}{4\pi r^2} \frac{\partial M(r)}{\partial r} \quad (2.5)$$

we have used Newton's second theorem (see Binney & Tremaine 1987 [32], p. 34f.) together with Newton's law of gravitation in the first step.

Starting from a known density distribution, we have

¹A force is conservative (i.e. it has a potential) if and only if its curl vanishes. Central forces are conservative if and only if they are spherically symmetric:

$$\nabla \times \left[f(\mathbf{r}) \cdot \frac{\mathbf{r}}{r} \right] = \frac{f(\mathbf{r})}{r} \nabla \times \mathbf{r} + \left[\nabla \frac{f(\mathbf{r})}{r} \right] \times \mathbf{r}$$

We have $\nabla \times \mathbf{r} = \mathbf{0}$. The second term vanishes only for spherically symmetric equipotential surfaces.

$$M(r) = \int_0^r dM(r') = 4\pi \int_0^r \rho(r') r'^2 dr' \quad (2.6)$$

$$\Phi(r) = -G \int_r^\infty \frac{M(r')}{r'^2} dr' \quad (2.7)$$

where we assume in the last step $\lim_{r \rightarrow \infty} \Phi(r) = 0$.

Other useful quantities are circular velocity $v_c(r)$ and escape velocity $v_e(r)$

$$v_c^2(r) = \frac{\partial \Phi(r)}{\partial \ln(r)} = r \frac{\partial \Phi(r)}{\partial r} = \frac{GM(r)}{r} \quad (2.8)$$

$$v_e^2(r) = 2|\Phi(r)| \quad (2.9)$$

The total potential energy W is given by the equivalent integrals

$$W = \frac{4\pi}{2} \int_0^\infty \rho(r) \Phi(r) r^2 dr \quad (2.10)$$

$$= -\frac{1}{2G} \int_0^\infty |f(r)|^2 r^2 dr = -\frac{G}{2} \int_0^\infty \frac{M^2(r)}{r^2} dr \quad (2.11)$$

$$= -4\pi G \int_0^\infty \rho(r) M(r) r dr = -G \int_0^\infty \frac{M(r)}{r} dM(r). \quad (2.12)$$

For details of the derivation of the above integrals, please see chapter 2 of Binney & Tremaine 1987 [32]. If the system is in virial equilibrium, the value of W determines the values of total kinetic energy $K = -W/2$ and the total energy $E = -K = W/2$.

From (2.12) follows the root mean squared escape speed,

$$\langle v_e^2 \rangle = 2 \langle |\Phi| \rangle = -\frac{4W}{M}, \quad (2.13)$$

provided that the total mass M is finite.

If the velocity dispersion tensor is isotropic, we can recover the velocity dispersion by integrating the equation of hydrostatic equilibrium (i.e., the Jeans equation involving the second moment of the velocity distribution),

$$\frac{d(\rho(r)\sigma^2(r))}{dr} = -\rho(r) \frac{d\Phi(r)}{dr}. \quad (2.14)$$

Therefore the velocity dispersion is in this case given by the integral

$$\sigma^2(r) = \frac{G}{\rho(r)} \int_r^\infty \frac{\rho(r') M(r')}{r'^2} dr'. \quad (2.15)$$

The total kinetic energy due to random motion is given by the integral

$$\Pi = \frac{3}{2} \cdot 4\pi \int_0^\infty \rho(r) \sigma^2(r) r^2 dr = \underbrace{2\pi r^3 \rho(r) \sigma^2(r)}_C \Big|_0^\infty - 2\pi \int_0^\infty \frac{d}{dr} [\rho(r) \sigma^2(r)] r^3 dr = C - \frac{W}{2}, \quad (2.16)$$

where we² have carried out an integration by parts in the first step and plugged in the condition (2.14) of hydrostatic equilibrium in the second step. It turns out that if

$$\Pi \text{ finite} \Leftrightarrow C = 0 \quad (2.17)$$

and the virial theorem is fulfilled.

²We means Dr. Patrick Glaschke and I.

2.2 Scale free models

Spherically symmetric scale free models (i.e. models which are self-similar under scaling of lengths) can be represented by potential/mass/density distributions, which are power laws in radius R ,

$$\Phi(u) = \begin{cases} \Phi_0 u^{\alpha-1} & \alpha \neq 1, \\ \Phi_0' \ln u & \alpha = 1 \end{cases} \quad (2.18)$$

$$M(u) = M_0 u^\alpha \quad (2.19)$$

$$\rho(u) = \rho_0 u^{\alpha-3} \quad (2.20)$$

where

$$u = \frac{R}{R_0}, \quad \rho_0 = \frac{\alpha M_0}{4\pi R_0^3}, \quad \Phi_0 = \frac{1}{\alpha-1} \frac{GM_0}{R_0} = \frac{4\pi G}{\alpha(\alpha-1)} \rho_0 R_0^2 \quad (\alpha \neq 1), \quad (2.21)$$

α is the power law exponent of the cumulative mass profile, G is the gravitational constant and R_0 is a length unit (which is not inherent in nature but simply a human convention). The circular frequency ω is given by

$$\omega(u) = \omega_0 u^{(\alpha-3)/2}, \quad \omega_0 = \sqrt{\frac{4\pi G \rho_0}{\alpha}} \quad (2.22)$$

The ratio of the epicyclic frequency κ to the circular frequency ω is given by

$$\beta_S = \frac{\kappa}{\omega} = \sqrt{2 \left[\frac{d \ln \omega}{d \ln u} + 2 \right]} = \sqrt{\alpha + 1} \quad (2.23)$$

The angular momentum of the circular orbit is given by

$$L_z(u) = L_0 u^{(\alpha+1)/2}, \quad L_0 = \omega_0 R_0^2. \quad (2.24)$$

Probably the most well-known example of a scale free model in stellar dynamics is the singular isothermal sphere with $\alpha = 1$. Except for the case $\alpha = 0$, which corresponds to the ideal case of a point mass at $u = 0$, scale free models always have an infinite total mass. In general, a model with a finite mass cannot be scale free but must show a “scale violation”³: It must contain a physically significant intrinsic length scale, at which a transition from $\alpha > 0$ to $\alpha = 0$ occurs. The magnitude of this length scale influences the value of the total mass of the system, which is obtained by integrating the density over all space.

2.3 Plummer model

The most well-known potential-density pair for a star cluster model with a finite mass is the Plummer model. It is an analytic solution of the Lane-Emden equation and corresponds to a stellar polytrope of index $n = 5$. Its distribution function is given by (e.g. Spitzer & Shull (1975) [33])

$$f_{\text{Pl}}(\mathcal{E}) = \begin{cases} F \mathcal{E}^{7/2}, & \mathcal{E} > 0; \\ 0, & \mathcal{E} \leq 0, \end{cases} \quad (2.25)$$

which depends on the phase space coordinates only through the relative energy $\mathcal{E} = -v^2/2 - \Phi(r) > 0$ (see Binney & Tremaine 1987 [32], p. 222f.) and therefore is a steady state solution of the

³This term is borrowed from particle physics.

collisionless Boltzmann equation. Since it satisfies both the Poisson equation and the collisionless Boltzmann equation, the Plummer model is a self-consistent model of a stellar system. The gravitational potential, cumulative mass and density are given by

$$\Phi(y) = -\Phi_0 \frac{1}{\sqrt{1+y^2}} = -\Phi_0 \cos \phi \quad (2.26)$$

$$M(y) = M \frac{y^3}{(1+y^2)^{3/2}} = M \sin^3 \phi \quad (2.27)$$

$$\rho(y) = \rho_0 \frac{1}{(1+y^2)^{5/2}} = \rho_0 \cos^5 \phi \quad (2.28)$$

with $y = r/r_{\text{Pl}} \geq 0$, $\phi = \arctan(y)$ and the Plummer radius

$$r_{\text{Pl}} = \frac{GM}{\Phi_0} = \left(\frac{3M}{4\pi\rho_0} \right)^{1/3} \quad (2.29)$$

where M is the total mass, $-\Phi_0$ is the central potential and ρ_0 the central density, all of them being finite. The length scale r_{Pl} occurs in (2.26), (2.27) and (2.28).⁴ For the Plummer model, we have $\lim_{r \rightarrow 0} \alpha = 3$ and $\lim_{r \rightarrow \infty} \alpha = 0$, where α is the power law index of the mass profile. Such a model fits the observed density profiles of some globular clusters fairly well. From (2.27) we find the half mass radius

$$y_h = \left(2^{2/3} - 1 \right)^{-1/2} = \tan \left(\arcsin \sqrt[3]{1/2} \right) \approx 1.30476603 \quad (2.30)$$

The circular speed is given by

$$v_c^2(y) = \Phi_0 \frac{y^2}{(1+y^2)^{3/2}} = \Phi_0 \sin^2 \phi \cos \phi \quad (2.31)$$

The total potential energy is given by the integral (2.12),

$$W = -4\pi G r_{\text{Pl}}^2 \rho_0 M \underbrace{\int_0^\infty \frac{y^4 dy}{(1+y^2)^4}}_{\pi/32} = -\frac{3\pi}{32} \frac{GM^2}{r_{\text{Pl}}}, \quad (2.32)$$

In the isotropic case, the velocity dispersion can be obtained by integrating the equation of hydrostatic equilibrium. It is then given by the integral (2.15),

$$\sigma^2(y) = \frac{\Phi_0}{6} \frac{1}{\sqrt{1+y^2}} = \frac{\Phi_0}{6} \cos \phi \quad (2.33)$$

Therefore the relation

$$v_e^2(y) = 12\sigma^2(y), \quad (2.34)$$

where v_e is the escape velocity, strictly holds at any radius. The total kinetic energy due to random motion can now be evaluated according to the integral (2.16),

$$\Pi = \frac{3}{2} 4\pi\rho_0 \frac{\Phi_0}{6} r_{\text{Pl}}^3 \underbrace{\int_0^\infty \frac{y^2 dy}{(1+y^2)^3}}_{\pi/16} = \frac{3\pi}{64} \frac{GM^2}{r_{\text{Pl}}} = -\frac{W}{2}. \quad (2.35)$$

⁴Note that the identities (A.1) and (A.2) given in the appendix have been used in the trigonometric parametrization of the Plummer model.

The result shows that a Plummer model is in virial equilibrium.

The distribution function (2.25) implies the isotropic velocity distribution

$$f_{\text{Pl}}(x) = \frac{512}{7\pi} x^2 (1 - x^2)^{7/2}, \quad (2.36)$$

where $x = v/v_e$ is the velocity in units of the escape velocity. Its first few moments are

$$N = \int_0^1 f_{\text{Pl}}(x) dx = 1 \quad (2.37)$$

$$\langle x \rangle = \int_0^1 x f_{\text{Pl}}(x) dx = \frac{1024}{693\pi} \approx 0.470345344 \quad (2.38)$$

$$\langle x^2 \rangle = \int_0^1 x^2 f_{\text{Pl}}(x) dx = \frac{1}{4} \quad (2.39)$$

The maximum probability is at

$$x_{\text{max}} = \frac{\sqrt{2}}{3} \approx 0.471404521, \quad (2.40)$$

which is very close, but not identical to the mean.

The χ function for dynamical friction (cf. Appendix D.2) is given analytically as well by

$$\begin{aligned} \chi(x) &= \int_0^x f_{\text{Pl}}(x') dx' \\ &= \frac{2}{105\pi} \left[x\sqrt{1-x^2} (-105 + 1210x^2 - 2104x^4 + 1488x^6 - 384x^8) \right. \\ &\quad \left. + 105 \arcsin(x) \right] \end{aligned} \quad (2.41)$$

In N -body units ($G = 1, M_{cl} = 1, E = -1/4$), we have

$$r_{\text{Pl}} = \frac{3\pi}{16} \approx 0.589048623 \quad (2.42)$$

$$r_h = \frac{3\pi}{16} \left(2^{2/3} - 1 \right)^{-1/2} \approx 0.768570631 \quad (2.43)$$

$$v_e(0) = 2\sqrt{\frac{8}{3\pi}} \approx 1.84263546 \quad (2.44)$$

for the Plummer radius, the half-mass radius and the maximum escape speed, respectively. The Plummer model has been first used in 1911 by Plummer (1911) [34]. Generalizations of Plummer models with axial symmetry and anisotropy have been introduced by Miyamoto & Nagai (1975) [35] and Dejonghe (1987) [36], respectively.

2.4 King model

Another example for a self-consistent model with finite mass is the King model discussed by King (1966)[37]. The distribution function of a King model is given by

$$f_{\text{K}}(\mathcal{E}) = \begin{cases} F [\exp(\mathcal{E}/\sigma_K^2) - 1], & \mathcal{E} > 0; \\ 0, & \mathcal{E} \leq 0, \end{cases} \quad (2.45)$$

where $\mathcal{E} = \Psi(r) - v^2/2$ is the relative energy, and we chose a constant Φ_t such that the relative potential $\Psi(r) = \Phi_t - \Phi(r)$ vanishes at the outer boundary of the King model (see Binney &

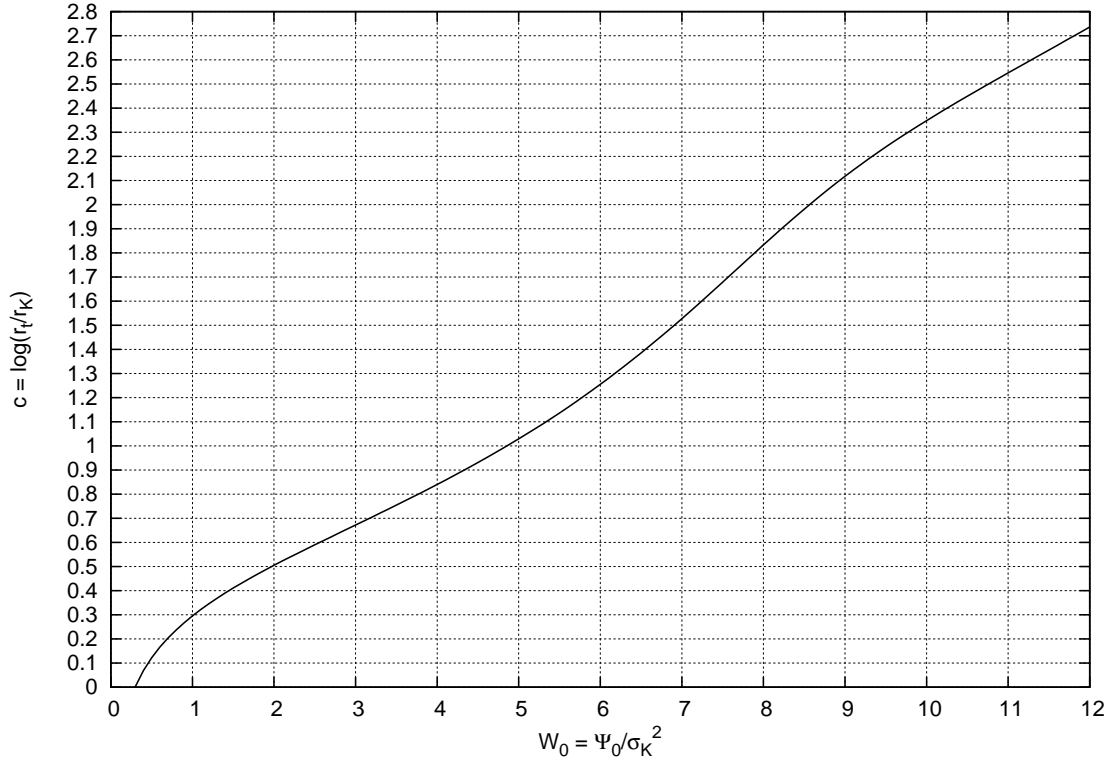


Figure 2.1: Relation between concentration and King parameter

Tremaine 1987 [32], p. 222). Zero relative energy corresponds then to an ability barely to reach the outer boundary of the King model, where its density drops to zero. The distribution function (2.45) is sometimes called a “lowered Maxwellian” because of the cutoff of the Boltzmann factor at small relative energies, i.e. at large radii leading to a finite total mass of the King model. Since the distribution function (2.45) depends on the phase space coordinates only through the relative energy, the King model is, as the Plummer model, also a steady-state solution of the collisionless Boltzmann equation.

A King model is characterized by the dimensionless King parameter

$$W_0 = \frac{\Psi_0}{\sigma_K^2} \quad (2.46)$$

where Ψ_0 is the central potential and σ_K is the King velocity dispersion. The concentration of a King model is given by

$$c = \log_{10}(r_t/r_K), \quad (2.47)$$

where r_t is the tidal radius of the King model, i.e. the radius where its density approaches zero. The relation between W_0 and c is shown in Figure 2.1.

The King radius is given by

$$r_K = \sqrt{\frac{9 \sigma_K^2}{4\pi G \rho_0}}, \quad (2.48)$$

where ρ_0 is the finite central density and G is the gravitational constant.

W_0	c	r_K [Nbu]	r_h [Nbu]	r_t [Nbu]
1	0.2954	0.6703	0.8575	2.565
2	0.5049	0.6115	0.8491	2.797
3	0.6720	0.5426	0.8390	3.131
4	0.8400	0.4653	0.8267	3.621
5	1.029	0.3815	0.8140	4.357
6	1.254	0.2931	0.8040	5.464
7	1.527	0.2031	0.8115	6.975
8	1.832	0.1210	0.8717	8.326
9	2.117	0.06329	0.9801	8.354
10	2.348	0.03304	1.029	7.409
11	2.545	0.01868	1.011	6.606
12	2.736	0.01132	0.9788	6.208

Table 2.1: Parameters of King models. The King parameter W_0 and the concentration c are dimensionless. The King radius r_K , the half-mass radius r_h and the tidal radius r_t are given in N -body units ($G = M_{cl} = -4E = 1$). Columns 3-5 from M. Freitag (priv. comm.).

King models fit the observed density profiles of globular clusters even better than Plummer models. The density as a function of the relative potential is given by (cf. Binney & Tremaine 1987 [32], p. 232)

$$\begin{aligned}
\rho_K(\Psi) &= \frac{4\pi\rho_1}{(2\pi\sigma_K^2)^{3/2}} \int_0^{\sqrt{2\Psi}} \left[\exp\left(\frac{\Psi - \frac{1}{2}v^2}{\sigma_K^2}\right) - 1 \right] v^2 dv \\
&= \rho_1 \left[\exp\left(\frac{\Psi}{\sigma_K^2}\right) \operatorname{erf}\left(\frac{\sqrt{\Psi}}{\sigma_K}\right) - \sqrt{\frac{4\Psi}{\pi\sigma_K^2}} \left(1 + \frac{2\Psi}{3\sigma_K^2}\right) \right]. \quad (2.49)
\end{aligned}$$

We can plug the density (2.49) into the Poisson equation and integrate it numerically, starting in the center with the King parameter W_0 and a flat core as initial conditions to obtain the potential as a function of radius. Then, we obtain the density as a function of radius by plugging the potential into the expression (2.49). One also obtains the cumulative mass as a result of the decomposition of the second-order Poisson equation into a system of two first-order differential equations. The profiles of density, cumulative mass and potential of King models are shown in Figure 2.2. In Table 2.1, some parameters of King models are given, which will be used later.

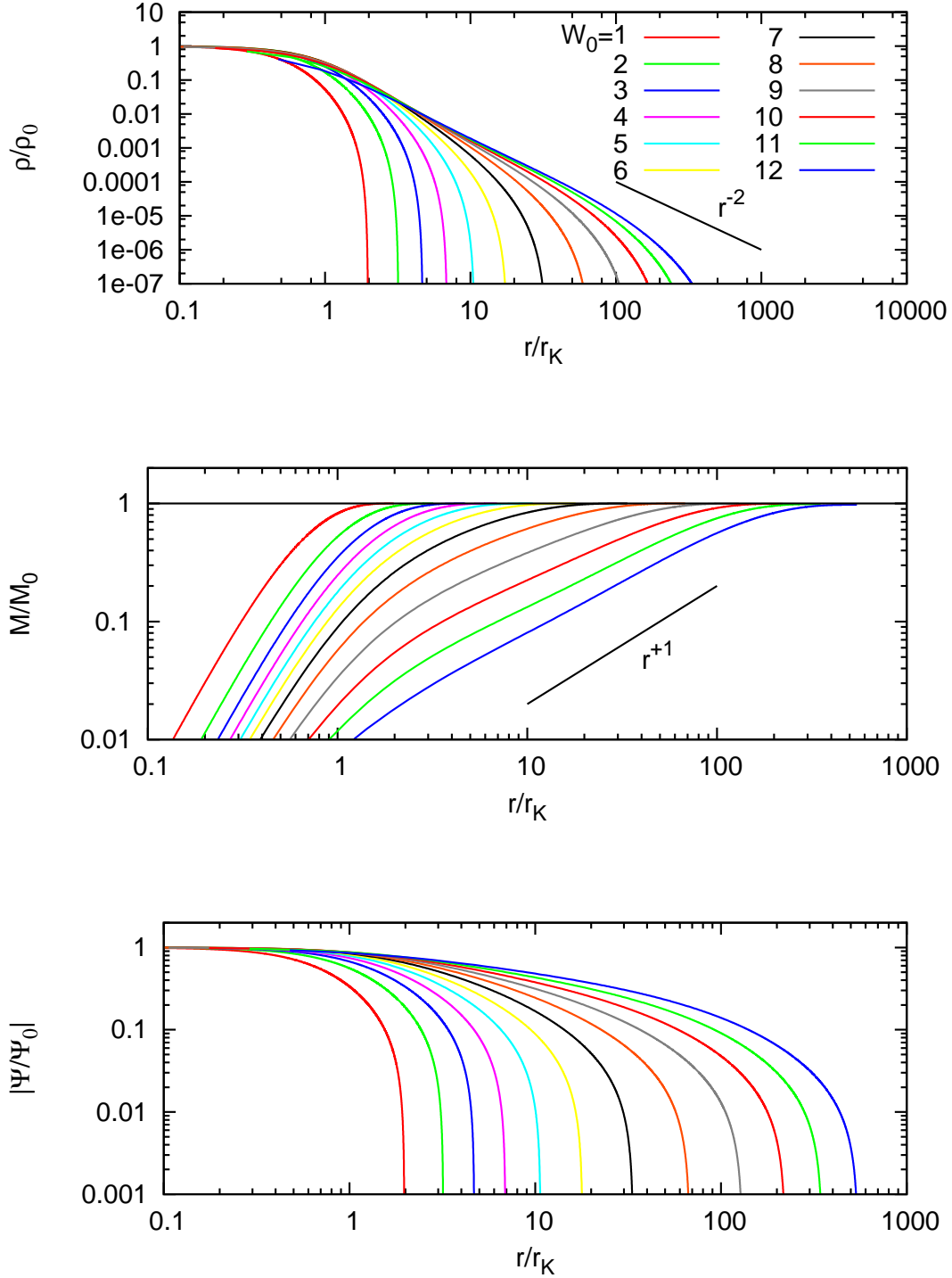


Figure 2.2: Density (top), cumulative mass (middle), potential (bottom) profiles of King models. Radius, density, cumulative mass and potential are given in units of the King radius, the central density, the total mass and the central potential, respectively. The slopes for the singular isothermal sphere are also shown.

Chapter 3

Escape and chaos theory

This chapter is based on the paper by A. Ernst, A. Just, R. Spurzem, O. Porth, *Escape from the vicinity of fractal basin boundaries of a star cluster*, MNRAS 383, 897 (2008) [38].

3.1 Introduction

The dissolution process of star clusters is an old problem in stellar dynamics. Once a star cluster has formed somewhere in a galaxy, it tends to lose mass due to dynamical interactions until it has completely dissolved. If a star cluster of finite mass were isolated, in virial equilibrium (i.e. $\langle v_e^2 \rangle = 12\sigma_{1D}^2$) and the velocity distribution given by a Maxwellian

$$f_M(X) = \frac{4}{\sqrt{\pi}} X^2 \exp(-X^2), \quad (3.1)$$

where $X = v/(\sqrt{2}\sigma_{1D})$ and v, v_e and σ_{1D} are the velocity, the escape velocity and the velocity dispersion, respectively, the fraction of stars which are faster than the rms escape speed were given by

$$\chi_e = \int_{\sqrt{6}}^{\infty} f_M(X) dX = 2\sqrt{\frac{6}{\pi}} \exp(-6) + \operatorname{erfc}\sqrt{6} \approx 0.00738316. \quad (3.2)$$

where $\operatorname{erfc}(x)$ is the complementary error function. This simple analytical result was published by Ambartsumian (1938) [1] and two years later, independantly by Spitzer (1940) [2] who named this effect “evaporation”. A process which can bring stars above the escape speed and let them evaporate, is two-body relaxation. The time scale of relaxation, which determines the rate of dynamical evolution of a star cluster, yields thus an upper limit to the lifetime of any star cluster. However, since χ_e is so small (and relaxation time relatively long), the evaporation time is much longer than a Hubble time for typical globular clusters. Following a suggestion of Chandrasekhar (1942) [39], King (1959) [40] studied the effect of “potential escapers”. These are stars which have been scattered above the escape energy but which have not yet left the cluster. These may be scattered back to negative energies within a crossing time and remain bound. Hénon (1960 [41], 1969 [42]) stressed the importance of few close encounters between stars for the rate of mass loss of star clusters. The Fokker-Planck approximation, which is widely used to study the dynamical evolution of star clusters, neglects strong encounters by construction. Nevertheless, close encounters could still be interpreted statistically as a certain discontinuous Markov process (Tscharnuter 1971 [43]). However, direct N -body models seem to be ideally suited to study this phenomenon in more detail. Spitzer & Shapiro (1972) [44] estimate that “close encounters may produce effects perhaps as great as 10 percent of the “dominant” distant encounters” and ignore

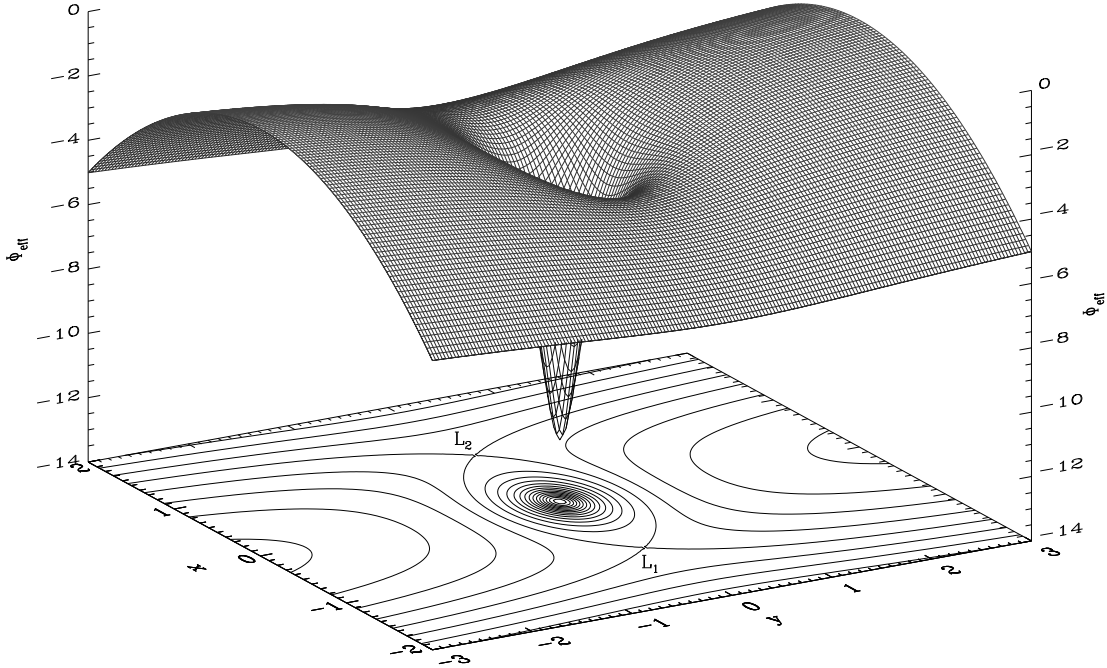


Figure 3.1: Effective potential in the tidal approximation ($z = 0$ plane). The Lagrangian points at $L_1 = (-1, 0)$ and $L_2 = (1, 0)$ can be seen. The escapers pass these saddle points while they leak out. The equipotential lines connecting them mark the tidal boundary of the star cluster. The details of the model are given in Section 3.3.

them. An additional process which can raise the energy of stars in a star cluster is the mass loss of the star cluster itself since it changes the gravitational potential.

Nature provides an environment for star clusters in which the escape rate is typically strongly enhanced as compared with the slow evaporation rate of isolated star clusters: The tidal field of a galaxy induces saddle-like troughs in the walls of the potential well of a star cluster (cf. Figure 1). It therefore lowers the energy threshold in star clusters above which stars can escape from zero to a negative value (Wielen 1972 [45], 1974 [46]). Moreover, if we consider a star cluster in the tidal field of a galaxy as a dynamical system, the tidal field can change the system's dynamics in a dramatical way as compared with an isolated system.

In general, the escape process from star clusters in a tidal field proceeds in two stages: (1) Scattering of stars into the “escaping phase space” by two-body encounters or a drift into the “escaping phase space” due to a changing cluster potential and (2) leakage through openings in the equipotential surfaces around saddle points of the potential. The “escaping phase space” is defined as the subset of phase space, from which escape is possible. It seemed well understood that the time scale for a star to complete stage (1) scales with relaxation time. However, the energy change due to a changing cluster potential may also change the energy of stars on a different time scale. The importance of this second process has not yet been investigated in detail. On the other hand, the time scale for a star to complete stage (2) depends mainly on its energy (but also on its location in phase space as we will see). When we neglect the effect of two-body relaxation or a time-dependent cluster potential for the consideration of stage (2), the motion of a single star in

the star cluster is determined between times t_1 and t_2 only by the smooth gravitational potential in which the star moves. The potential itself is generated by the other stars in the star cluster disregarding their “grainyness” and by the superposed galactic gravitational field, which is due to the matter distribution of the galaxy. Within this framework, we will study stage (2) of the escape process in this chapter. In this connection, the work of Fukushige & Heggie (2000) [5] is of major interest. Their main result is an expression for the time scale of escape for a star in stage (2) which has just completed stage (1). The dependance of the escape process on two (or more) time scales which scale differently with the particle number N imposes a severe scaling problem for N -body simulations (see Section 7.2). The scaling problem is of relevance since the it is on today’s general-purpose hardware architectures not yet simply feasible to simulate the evolution of globular clusters with realistic particle numbers of a few hundred thousands or even millions of stars by means of direct N -body simulations. The result of Fukushige & Heggie has been applied in Baumgardt (2001) [47] to solve the important scaling problem for the dissolution time of star clusters in the special case of circular cluster orbits. The obtained scaling law $t_{dis} \propto t_{rh}^{3/4}$, where t_{dis} and t_{rh} are the dissolution and half-mass relaxation times, respectively has been verified, e.g. in Spurzem et al. (2005) [48].

The problem of escape has also a long history in the context of the theories of dynamical systems and chaos. It is well-known for a long time, that certain Hamiltonian systems allow for escape of particles towards infinity. Such “open” Hamiltonian systems have been studied by Rod (1973) [49], Churchill et al. (1975) [50], Contopoulos (1990) [51], Contopoulos & Kaufmann (1992) [52], Siopis et al. (1997) [53], Navarro & Henrard (2001) [54] and Schneider, Tél & Neufeld (2002) [55]. The related chaotic scattering process, in which a particle approaches a dynamical system from infinity, interacts with the system and leaves it, escaping to infinity, was investigated by many authors, as Eckhardt & Jung (1986) [56], Jung (1987) [57], Jung & Scholz (1987) [58], Eckhardt (1987) [59], Jung & Pott (1989) [60], Bleher, Ott & Grebogi (1989) [61] and Jung & Ziemniak (1992) [62]. Typically, the infinity acts as an attractor for an escaping particle, which may escape through different exits in the equipotential surfaces. Thus it is possible to obtain basins of escape (or “exit” basins), similar to basins of attraction in dissipative systems or the well-known Newton-Raphson fractals (see Appendix B for two examples). Special types of basins of attraction (i.e. “riddled” or “intermingled” basins) have been explored by Ott et al. (1993) [63] and Sommerer & Ott (1993 [64], 1996 [65]). Basins of escape have been studied by Bleher et al. (1988) [66], and they are discussed in Contopoulos (2002) [7]. Research on escape from the paradigmatic Hénon-Heiles system has been done by de Moura & Letelier (1999) [67], Aguirre, Vallejo & Sanjuán (2001) [68], Aguirre & Sanjuán (2003) [69], Aguirre, Vallejo & Sanjuán (2003) [70], Aguirre (2004) [71] and Seoane Sepúlveda (2007) [72]. These papers served as the basis of this chapter. Relatively early, it was recognized, that the key to the understanding of the the chaotic scattering process is a fractal structure in phase space which has the form of a Cantor set (Cantor 1884) [6] and is called the chaotic saddle. Its skeleton consists of unstable periodic orbits (of any period) which are dense on the chaotic saddle (e.g. Lai 1997 [73]) and introduce chaos into the system (e.g. Contopoulos 2002) [7]. The properties of chaotic saddles have been investigated by different authors, as Hunt (1996) [74], Lai et al. (1993) [75], Lai (1997) [73] or Motter & Lai (2001) [76]. Both hyperbolic and non-hyperbolic chaotic saddles occur in dynamical systems. In the first case, there are no Kolmogorov-Arnold-Moser (KAM) tori, which means that all periodic orbits are unstable. In the second case, there are both KAM tori and chaotic sets in the phase space (J. C. Vallejo, priv. comm. and e.g. Lai et al. 1993 [75]). We note that all of the above references on the chaotic dynamics are exemplary rather than exhaustive since there exists a vast amount of literature on these topics.

3.2 Tidal approximation

The “tidal approximation” which is widely used in stellar and galactic dynamics for studies of stellar systems in a tidal field is nothing else than a simple approximation which, historically, has been applied already in the 19th century in “Hill’s problem” (e.g. Stumpff 1965 [77], Szebehely 1967 [78], Siegel & Moser 1971 [79]) in the context of the (rather intricate) lunar theory. The difference to the tidal approximation lies merely in the form of the gravitational potentials which are used. The assumption that a star cluster moves around the Galactic center on a circular orbit allows to use the epicyclic approximation to calculate steady linear tidal forces acting on the stars in the star cluster. As in the circular restricted three-body problem the appropriate coordinate system is a rotating reference frame in which both the star cluster center and the Galactic center (i.e., the primaries) are at rest. Its origin is the star cluster center, sitting in the extremum of the effective galactic potential. The x-axis points away from the Galactic center; the y-axis points in the direction of the rotation of the star cluster around the Galactic center; the z-axis lies perpendicular to the orbital plane and points towards the Galactic North pole. We define corotating coordinates (x, y, z) as

$$x = (R - R_C), \quad y \approx R_C (\phi - \omega_C t), \quad z = z' \quad (3.3)$$

where (R, ϕ, z') are galactocentric cylindrical coordinates, R_C and ω_C are the radius and the frequency of the circular orbit, respectively, the subscript “C” denotes physical quantities at R_C in the following discussions and t is time (in the context of “Hill’s problem” cf. Glaschke 2006 [80]). Since the coordinate system is rotating, centrifugal and Coriolis forces appear according to classical mechanics. In addition, tidal forces enter the equations of motion for stellar orbits near the origin of coordinates. To first order, we have in the rotating frame

$$\ddot{x} = -\frac{\partial \Phi_{cl}}{\partial x} - \left(\frac{\partial^2 \Phi_g}{\partial R^2} \right)_{(R_C, 0)} x + \omega_C^2 x + 2\omega_C \dot{y} \quad (3.4)$$

$$\ddot{y} = -\frac{\partial \Phi_{cl}}{\partial y} - 2\omega_C \dot{x} \quad (3.5)$$

$$\ddot{z} = -\frac{\partial \Phi_{cl}}{\partial z} - \left(\frac{\partial^2 \Phi_g}{\partial z^2} \right)_{(R_C, 0)} z \quad (3.6)$$

where $\Phi_{cl}(x, y, z)$ and $\Phi_g(R, z')$ are the star cluster potential and the axisymmetric galactic potential, respectively. The second-last term on the right hand side in (3.4) is the centrifugal force and the last terms in (3.4) and (3.5) are Coriolis forces. According to Binney & Tremaine (1987) [32], the epicyclic frequency κ_C and the vertical frequency ν_C are given by

$$\kappa_C^2 = \left(\frac{\partial^2 \Phi_g}{\partial R^2} \right)_{(R_C, 0)} + 3\omega_C^2, \quad \nu_C^2 = \left(\frac{\partial^2 \Phi_g}{\partial z^2} \right)_{(R_C, 0)} \quad (3.7)$$

Thus the equations of motion can be written as

$$\ddot{x} = f_x - (\kappa_C^2 - 4\omega_C^2)x + 2\omega_C \dot{y} \quad (3.8)$$

$$\ddot{y} = f_y - 2\omega_C \dot{x} \quad (3.9)$$

$$\ddot{z} = f_z - \nu_C^2 z, \quad (3.10)$$

where $(f_x, f_y, f_z) = -\nabla \Phi_{cl}$ is the (specific) force vector from the other cluster member stars which typically depends non-linearly on the coordinates. It is of interest for the following discussion that the equations of motion (3.8) - (3.10) are invariant under time reversal.¹ Note that under a time

¹The invariance under time reversal is related to the existence of a discrete group with only two elements, which acts on the space of solutions of the equations of motion (3.8) - (3.10). In our case, the effective potential (3.12) and the Coriolis forces are time-symmetric, which implies the same symmetry of the equations of motion.

reversal the frequencies also change their sign. Also, the equations of motion (3.8) - (3.10) admit an isolating integral of motion, the Jacobian

$$E_J = \frac{1}{2} (\dot{x}^2 + \dot{y}^2 + \dot{z}^2) + \Phi_{\text{eff}}(x, y, z), \quad (3.11)$$

where

$$\Phi_{\text{eff}}(x, y, z) = \Phi_{\text{cl}}(x, y, z) + \frac{1}{2}(\kappa_C^2 - 4\omega_C^2)x^2 + \frac{1}{2}\nu_C^2 z^2 \quad (3.12)$$

is the effective potential, which is plotted in Figure 1 for the 2D case. Other isolating integrals are not given in the form of a simple analytical expression. However, some solutions of (3.8) - (3.10) are subject to a non-classical integral (Hénon & Heiles 1964) [81], as has been demonstrated numerically by Fukushige & Heggie (2000) [5], who calculated a Poincaré surface of section. In principle, one may obtain power series expansions of such non-classical integrals², see the original works by Gustavson (1966) [82] and Finkler, Jones & Sowell (1990) [83] and the review in Moser (1968) [84]. Also, third integrals can be related to the existence of Killing tensor fields which are well-known in General Relativity (Clementi & Pettini 2002 [85]). At last, the tidal radius (King 1962) [86]

$$r_t = \left(\frac{GM_{cl}}{4\omega_C^2 - \kappa_C^2} \right)^{1/3} \quad (3.13)$$

where M_{cl} is the star cluster mass, provides a fundamental length scale of the problem. It is the distance from the origin of coordinates to the Lagrangian points L_1 and L_2 (which lie on the x axis, see Figure 3.1).

3.3 A simple model

The characteristic frequencies ω_C, κ_C and ν_C arise as properties of the galactic gravitational potential. Throughout the paper, we use the values of the characteristic frequencies in the solar neighborhood. All of them can be expressed in terms of Oort's constants A and B (see, e.g., Binney & Tremaine 1987 [32]): $\omega_C^2 = (A - B)^2$, $\kappa_C^2 = -4B(A - B)$, $\kappa_C^2 - 4\omega_C^2 = -4A(A - B)$, $\nu_C^2 = 4\pi G\rho_g + 2(A^2 - B^2)$. The vertical frequency ν_C can be derived from the Poisson equation for an axisymmetric system (see Oort 1965 [87]) and ρ_g is the local Galactic density, which contributes to the dominant first term. We obtain both dimensionless parameters $\kappa_C^2/\omega_C^2 \approx 1.8$ and $\nu_C^2/\omega_C^2 \approx 7.6$ using the values of Oort's constants given in Feast & Whitelock (1997) [88] and the value for local Galactic density given in Holmberg & Flynn (2000) [89]. It is then convenient to choose the following system of units:

$$G = 1, \quad \omega_C = 1, \quad M_{cl} = 2.2 \quad (3.14)$$

The resulting length unit is the tidal radius r_t and the formulation of the dynamical problem with its equations of motion is completely dimensionless. For the star cluster, we use a Plummer model, the most simple analytic model for a star cluster. The density profiles of King models which have a cutoff radius, where the density drops to zero, fit the measured density profiles of globular clusters better than Plummer models (King 1966 [37]). Since they are tidally limited by construction, they are at first glance ideally suited for our purpose. However, the gravitational force field can only be tabulated from a numerical integration of a non-linear differential equation. We have made a compromise which is not relevant for the interesting physics: We choose the Plummer radius in such a way, that the Plummer model (see Section 2.3) is the best fit to a King model with $W_0 = 4$ (i.e. with concentration $c = \log_{10}(r_t/r_K) \approx 0.840$), which completely fills the Roche lobe in the

²e.g. adelpic or third integrals

tidal field, i.e. the density of the King model approaches zero at the tidal radius (3.13). The fit of the density profiles is quite acceptable for density contrasts of $\log_{10}(\rho_c/\rho(r)) \lesssim 3$, where ρ_c and $\rho(r)$ are the central density and the density as a function of radius, respectively. For the deviation between the King density profile and the Plummer fit we obtain $(\rho_{Pl}(r) - \rho_K(r))/\rho_c < 1.2\%$. The ratio of the Plummer radius to the King radius and the “concentration” of the Plummer model (which can only be defined because of the existence of a tidal radius) are then $r_{Pl}/r_K \approx 1.257$ and $c_{Pl} = \log_{10}(r_t/r_{Pl}) \approx 0.741$, respectively. In our units, the Plummer radius is therefore $r_{Pl} \approx 0.182$.

As a more technical remark, the author notes that he used an 8th-order Runge-Kutta scheme for the orbit integrations. The relative error in the Jacobian E_J was always limited to $\Delta E_J/E_J < 10^{-10}$ for all orbit integrations.³

3.4 Poincaré surfaces of section

A critical Jacobi constant

$$E_{J,L} = \Phi_{\text{eff}}(r_t, 0, 0) = \Phi_{\text{eff}}(-r_t, 0, 0) \quad (3.15)$$

is given by the value of the effective potential (3.12) at the Lagrangian points L_1 and L_2 . For our model we have $E_{J,L} = -3.264444506$. For a Jacobian $E_J > E_{J,L}$ the equipotential surfaces are open and particles can escape. Furthermore, we define the dimensionless deviation from $E_{J,L}$ by

$$\widehat{E}_J = (E_{J,L} - E_J)/E_{J,L}, \quad (3.16)$$

where E_J is some other value of the Jacobian. The dimensionless deviation \widehat{E}_J is positive for $E_J > E_{J,L}$ if E_J and $E_{J,L}$ are both negative, which is always the case in this paper. A first insight can be gained by calculating Poincaré surfaces of section which are shown in Figure 3.2 for two different Jacobi constants: The upper left surface of section is at the critical Jacobian $E_{J,L}$ at which all orbits still remain within a bounded area in phase space and we have no escapers. We can see that this is a system with divided phase space, i.e. we have both chaotic and regular orbits. It is striking that the left half of the surface of section is almost completely occupied by regular, quasiperiodic orbits. These orbits are retrograde with respect to the orbit of the star cluster around the galactic center (Fukushige & Heggie 2000 [5]), as can be seen by looking at the sketch in Figure 3.4, and they are subject to a non-classical integral of motion. On the other hand, most of the prograde orbits are chaotic apart from a few smaller regular islands. Since the effective potential is mirror-symmetrical with respect to both the x - and y -axes (see Figure 3.1), the asymmetry seen in the surfaces of section must be due to the Coriolis forces. Thus such a behavior might be termed a “Coriolis asymmetry” (cf. Innanen 1980 [90]). The Coriolis forces are special in the sense that their direction is not perpendicular to the tangent plane to the equipotential surfaces but to the velocity of a particle. The upper right surface of section is at a higher Jacobi constant. The particles can leak out through the openings in the equipotential surfaces and escape towards infinity (positive x -direction) or the galactic center (negative x -direction). It is remarkable, that only the chaotic orbits escape, while the regular, quasiperiodic orbits remain within the tidal boundary of the star cluster, since the non-classical integral restricts their accessible phase space and hinders their escape. In star clusters, two-body relaxation may scatter stellar orbits beyond the critical Jacobi constant. However, if the orbits are retrograde, the stars will remain bound to the star cluster with high probability until two-body relaxation further scatters them into the escaping phase space. The two lower surfaces of section in Figure 3.2 indicate the orbital structure in position space at $E_J = E_{J,L}$, where all orbits are restricted to the region within the almond-shaped tidal boundary of the star cluster (cf. Figure 3.1). One notes that certain parts of the

³Erratum: Due to a sign neglect in the evaluation of the relative error in the Jacobian it was stated wrongly in the paper.

Plot (Figure 3.5)	Black	Red	Yellow
Top left	25.4	36.6	38.0
Top right	12.5	19.3	68.2
Middle left	36.9	31.5	31.5
Middle right	21.4	36.8	41.8
Bottom left	40.9	29.5	29.6
Bottom right	27.2	36.2	36.6

Table 3.1: Fraction of orbits (in percent) belonging to the intersection of the basins of escape with Poincaré surfaces of section which are shown in Figure 3.5.

chaotic regions of the lower surfaces of section are less densely filled by stellar orbits which is a common property of dynamical systems.

Figure 3.3 shows typical examples of the two main types of orbits. The regular orbit resembles a rosette orbit in an axisymmetric potential or a loop orbit which suggests that the non-classical integral is some sort of generalization of angular momentum (Binney & Tremaine 1987 [32]). We found indeed that the angular momentum is approximately conserved for the left orbit of Figure 3.3, while it is not at all conserved for the right orbit. Other types of orbits can be found which are associated with the smaller regular islands in the surfaces of section and which may look rather interesting. At last, the author remarks that the difference between retrograde and prograde orbits appears prominently in N -body models of dissolving *rotating* star clusters within the framework of the tidal approximation: Where either the regular or the chaotic domains in phase space are more strongly occupied by stellar orbits due to the existence of a net angular momentum of the cluster in one direction (see Ernst et al. 2007 [4]).

3.5 The basins of escape

Figure 3.5 shows the basins of escape for a tidally limited star cluster within the framework of the tidal approximation. For the plots on the left-hand side, $\sim 3 \times 10^5$ orbits have been integrated; for the plots on the right-hand side, it were $\sim 6 - 8 \times 10^5$ orbits, depending on the area of the surface of section containing initial conditions. The phase space is divided into the escaping phase space (red and yellow regions) and the non-escaping phase space (black regions). The red regions denote initial conditions, where the escaping stars pass L_1 while the yellow regions represent initial conditions, where the escaping stars pass L_2 . The black regions show those initial conditions, where stars do not escape. These are first and foremost the regular regions where a non-classical integral is present. Note that the stable manifold of the chaotic saddle is not marked in black, since it is of Lebesgue measure zero (cf. next Section). Since there exist regular regions (with KAM tori), the system is non-hyperbolic, i.e. there exist stable periodic orbits with corresponding elliptic points in the surfaces of section (cf. Section 3.4 and Figure 3.2). We can see that in the escaping phase space there exist regions, where we have a very sensitive dependence of the escape process on the initial conditions, i.e. a slight change of the initial conditions makes the star escape through the opposite Lagrangian point. This is the classical indication of chaos. It is interesting to note that these regions arise from immediate vicinity of the black regions where orbits are regular. In these domains of phase space the red and yellow regions are completely intertwined with respect to each other: The boundary between these regions is fractal. The volume in phase space occupied by these regions (with sensitive dependence on the initial conditions) increases as the Jacobian E_J approaches the critical Jacobi constant $E_{J,L}$ (i.e. in the limit $\hat{E}_J \rightarrow 0$) and the exits become smaller. At $\hat{E}_J \rightarrow 0$ there is a maximal “fractalization” of phase space; when the system approaches the limit of small exits the basins become uncertain (Aguirre & Sanjuán 2003 [69]). The term “uncertain” means that we become unable to follow the real trajectory of a

particle by means of numerical integration.⁴ Moreover, the following theorem can be formulated: “For all points P in the escaping phase space of an open Hamiltonian system, and for all $\delta > 0$ (precision of the experiment), there exists a critical size of the exits $w_c > 0$ such that for all $w \leq w_c$ we can find a point P' in a ball centered in P and radius δ that belongs to a different basin than P ” (Aguirre & Sanjuán 2003 [69]).

Table 3.1 shows the fraction of orbits (in percent) belonging to the intersection of the basins of escape with Poincaré surfaces of section which are shown in Figure 3.5. It can be seen that in the limit $\widehat{E}_J \rightarrow 0$ the fractions of particles passing L_1 and L_2 tend to be equal while this must not be the case if there are large areas without sensitive dependence of the escape process on the initial conditions.

Figure 3.6 shows how the escape times are distributed on surfaces of section. The longest escape times correspond to initial conditions near the boundaries between the basins of escape of Figure 3.5. The shortest escape times have been measured for the ordered regions without sensitive dependence on the initial conditions, i.e. those far away from the fractal basin boundaries.

Figure 3.7 shows the fraction of remaining (non-escaped) orbits $N_e(t_e > t)/N_{e,0}$ after time t corresponding to the basins of escape shown in Figure 3.5. Only the escaping orbits have been used for the statistics. The orbits corresponding to the regions without sensitive dependence on the initial conditions shown in Figure 3.5 have short escape times as can be seen in Figure 3.6. For these orbits, the decay law is a power law as shown in the inlays for the solid curve ($\widehat{E}_J = 0.1$). On the other hand, the decay law is exponential for the chaotic orbits near the fractal basin boundaries (i.e. the orbits with long escape times which correspond to the regions with sensitive dependence on the initial conditions). The slopes of the exponentials (i.e. the decay constants) depend on the value of \widehat{E}_J but are identical for both surfaces of section. The exponential decay law indicates that the underlying process is of a statistical nature similar to the radioactive decay of unstable nuclides or that of bubbles in beer foam.

3.6 The chaotic saddle

The stable manifold of the chaotic saddle is shown in the top row of Figure 3.8 for two Poincaré surfaces of section. The stable manifold coincides with the fractal basin boundaries of Figure 3.5 and therefore acts as a separatrix between the exit basins. With data points of finite size, the top row shows orbits which do not escape for time $t \rightarrow \infty$, although, strictly speaking, their Lebesgue measure is zero. The unstable manifold of the chaotic saddle is shown in the middle row of Figure 3.8. These are orbits which do not escape for time $t \rightarrow -\infty$. Note that the stable and unstable manifolds are symmetric with respect to each other, since the equations of motion (3.8) - (3.10) are time-symmetric. For the plots in the middle row of Figure 3.8, the sign of the time step in the Runge-Kutta integrator has been reversed. The bottom row of Figure 3.8 shows the intersection of the chaotic saddle (i.e. a non-hyperbolic chaotic invariant set) with the two Poincaré surfaces of section. It is the invariant set of non-escaping orbits for time $t \rightarrow \infty$ and $t \rightarrow -\infty$. The chaotic saddle has the form of a Cantor set (Cantor 1884 [6]) which is formed by the intersection of its stable and unstable manifolds. The fact that the system is non-hyperbolic implies that there are tangencies between the stable and unstable manifolds, i.e. that their angle is not always bounded away from zero (Lai et al. 1993 [75]). The unstable (hyperbolic) points in the intersection of the Poincaré surface of section with the chaotic saddle correspond to unstable periodic orbits. As is well-known (e.g. Contopoulos 2002) [7], these introduce chaos into the system since they repel the orbits in their neighborhood in the direction of their unstable eigenvectors. The remarkable similarity of our system with the Hénon-Heiles system (see Aguirre, Vallejo & Sanjuán 2001 [68]) is that the fractal dimension of the chaotic saddle tends to three in the limit $\widehat{E}_J \rightarrow 0$ (i.e. the black areas in Figure 3.8 grow until we have a maximal fractalization of the phase space, cf. Aguirre & Sanjuan 2003 [69]), which is the dimension of the hypersurface of phase space with constant

⁴In other words, the computer fails here to be a Laplacian demon (Laplace 1814 [91]).

Jacobian. At $\widehat{E}_J = 0$ there is a sudden transition where the non-hyperbolic invariant set abruptly fills the whole non-regular subset of phase space within the last closed equipotential surface and no escape is possible any more. This situation can be seen in the Poincaré surfaces of section in Figure 3.2 in Section 3.4 which shows the chaotic domains of phase space as a dotted area.

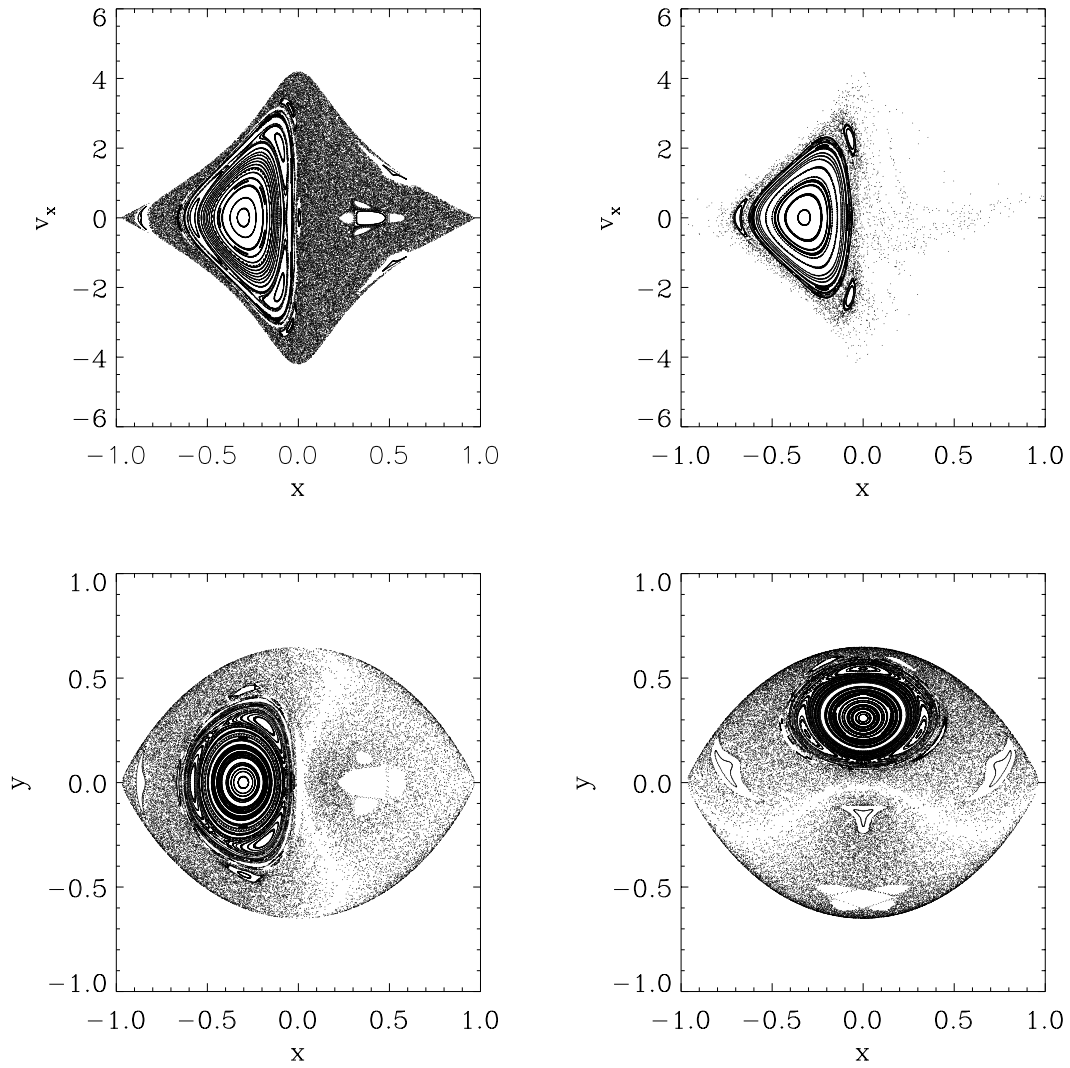


Figure 3.2: Poincaré surfaces of section. Top left: At $\widehat{E}_J = 0$ for orbits crossing $y = 0$ with $\dot{y} > 0$, Top right: Same as top left, but at $\widehat{E}_J = 0.1$, Bottom left: At $\widehat{E}_J = 0$ for orbits crossing $\dot{x} = 0$ with $\dot{y} > 0$, Bottom right: At $\widehat{E}_J = 0$ for orbits crossing $\dot{y} = 0$ with $\dot{x} > 0$. The variable \widehat{E}_J is defined in Equation (3.16).

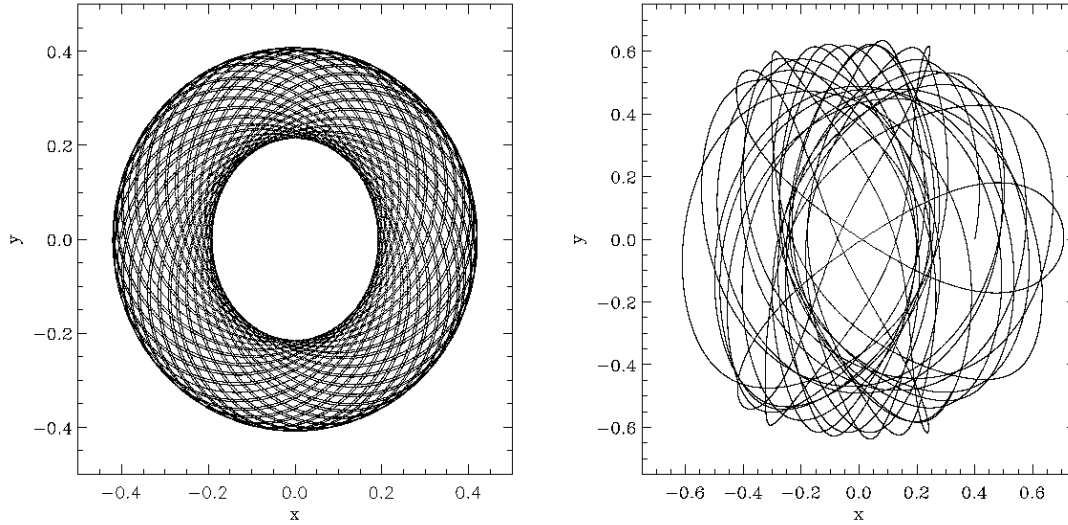


Figure 3.3: The two main types of orbits at $\widehat{E}_J = 0$. Left: Regular retrograde orbit, Right: Chaotic prograde orbit. The variable \widehat{E}_J is defined in Equation (3.16).

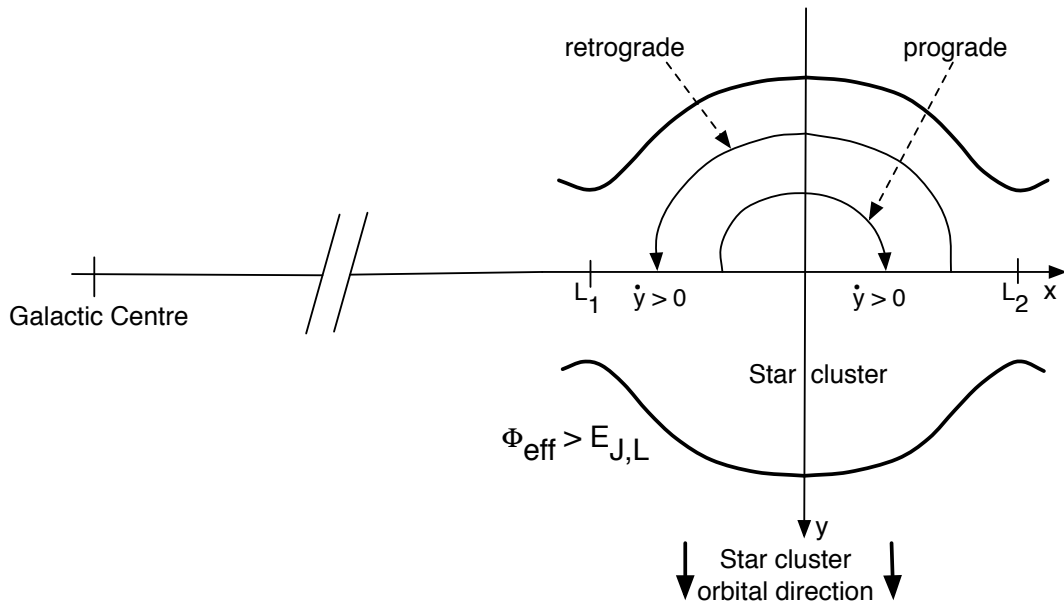


Figure 3.4: Sketch of the coordinate system. The escapers leak out through the openings in the equipotential surfaces passing either L_1 or L_2 . Only schematically, two orbits are shown which cross the x axis with $\dot{y} > 0$.

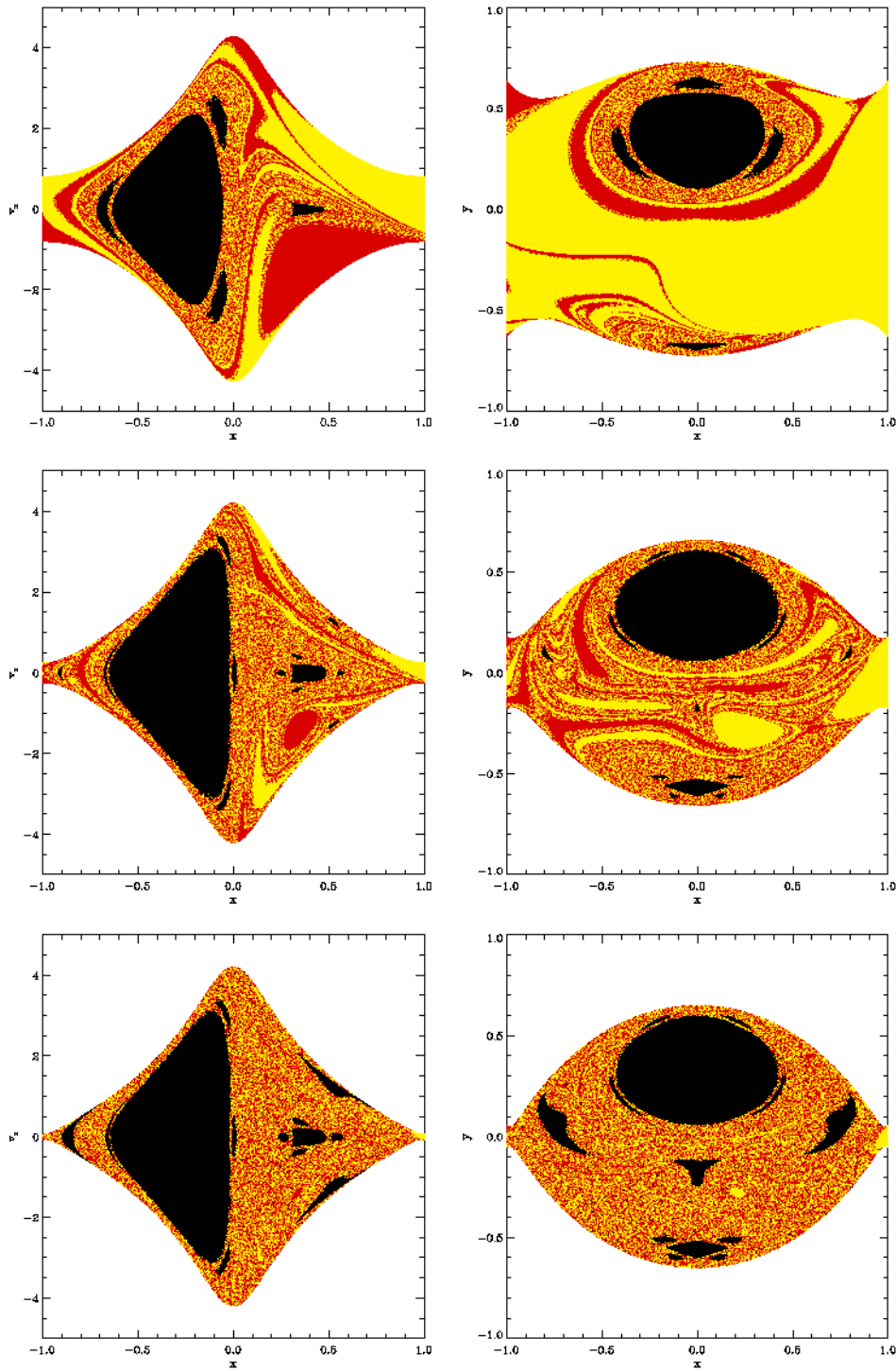


Figure 3.5: The basins of escape. Top left: At $\widehat{E}_J = 0.1$ for orbits crossing $y = 0$ with $\dot{y} > 0$, Top right: At $\widehat{E}_J = 0.1$ for orbits crossing $\dot{y} = 0$ with $\dot{x} > 0$, Middle row: As the upper row, but at $\widehat{E}_J = 0.01$, Bottom row: As the middle row, but at $\widehat{E}_J = 0.001$. The red regions denote initial conditions, where the escaping stars pass L_1 while the yellow regions represent initial conditions, where the escaping stars pass L_2 . The black regions show those initial conditions, where stars do not escape. The variable \widehat{E}_J is defined in Equation (3.16).

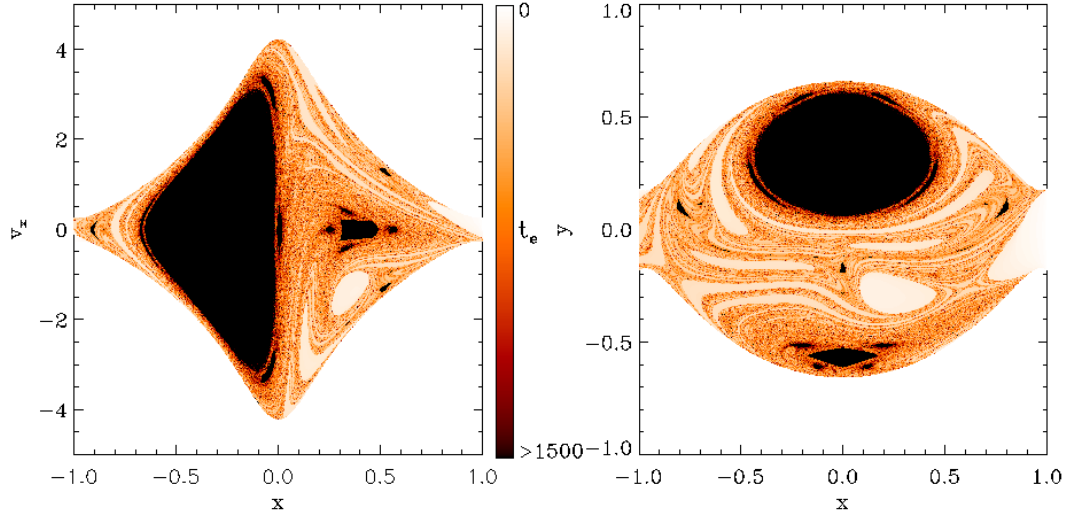


Figure 3.6: Distribution of escape times t_e on surfaces of section for $\widehat{E}_J = 0.01$. Top: For the $x - v_x$ surface of section of Figure 3.5, Bottom: For the $x - y$ surface of section of Figure 3.5. The darker the color, the longer the escape time.

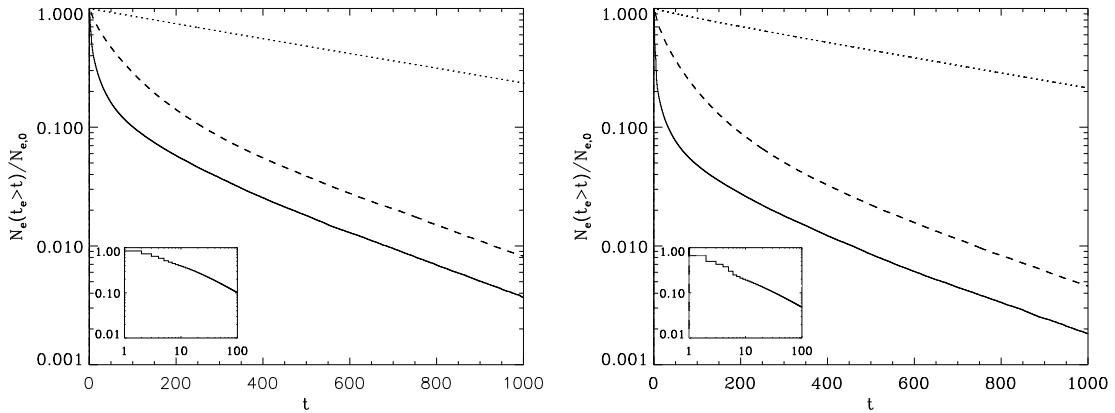


Figure 3.7: Histogram of the fraction of remaining (non-escaped) orbits $N_e(t_e > t)/N_{e,0}$ after time t . Top: For the $x - v_x$ surfaces of section of Figure 3.6, Bottom: For the $x - y$ surfaces of section of Figure 3.6, Solid: $\widehat{E}_J = 0.1$, Dashed: $\widehat{E}_J = 0.01$, Dotted: $\widehat{E}_J = 0.001$. The inlays with two logarithmic axes show the early phase for the solid line (i.e. for $\widehat{E}_J = 0.1$). The variable \widehat{E}_J is defined in Equation (3.16).

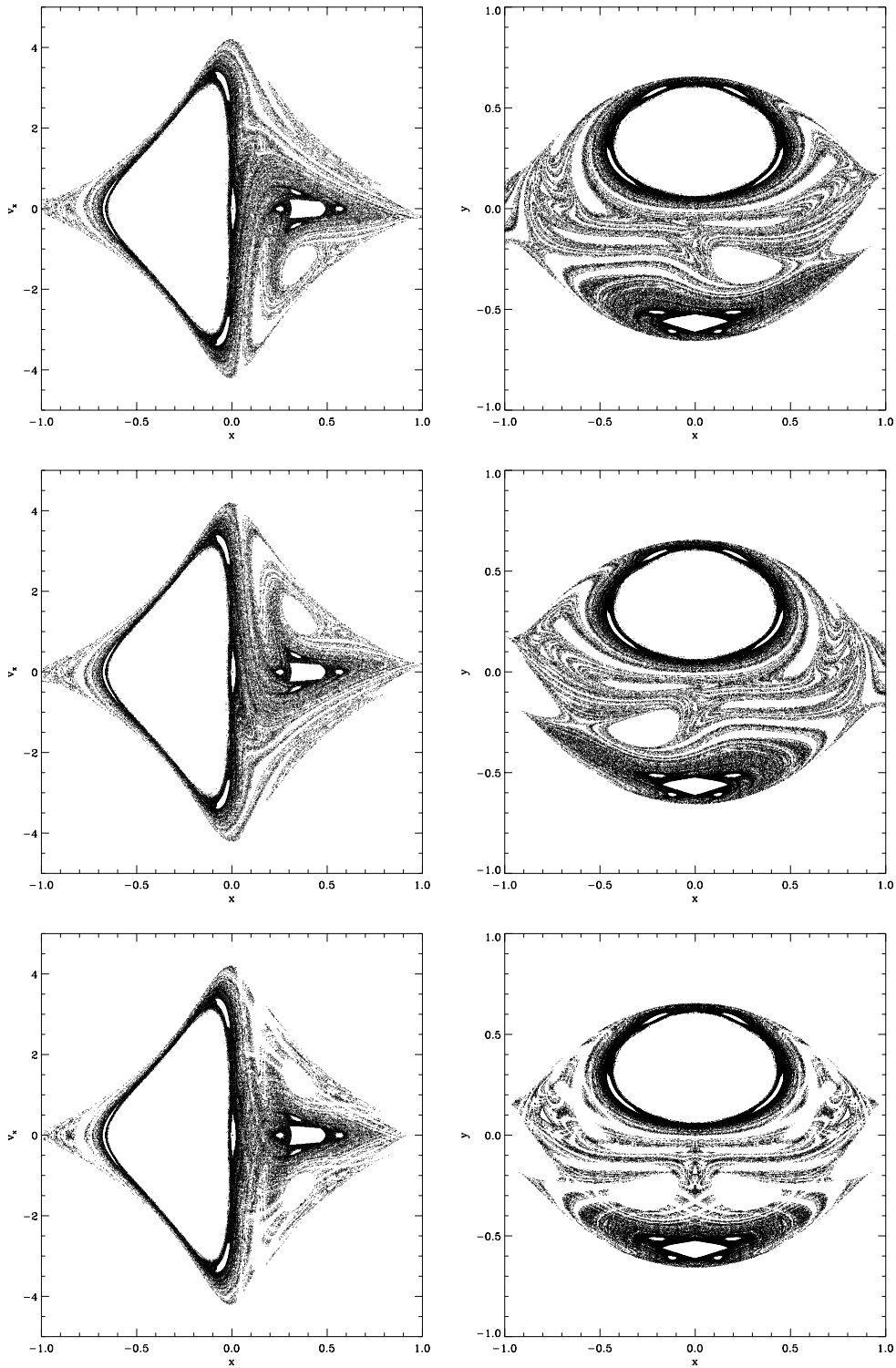


Figure 3.8: The non-hyperbolic invariant set and its stable and unstable invariant manifolds at $\hat{E}_J = 0.01$. Top row: Stable manifold, Middle row: Unstable manifold, Bottom row: Invariant set. The variable \hat{E}_J is defined in Equation (3.16).

Chapter 4

Theory of tidal arms

This chapter is based on the paper by A. Just, P. Berczik, M. Petrov, A. Ernst, *Quantitative analysis of clumps in the tidal tails of star clusters*, MNRAS 392, 969 (2009) [13]. The theoretical ideas which are presented here in greater detail stem from A. Just.

4.1 Taylor expansions

We calculate Taylor expansions of the potential and other physical quantities. The subscript “C” denotes physical quantities at the radius of the circular orbit in the following discussion.

4.1.1 R -expansions

We define

$$\beta = \frac{\kappa}{\omega}, \quad \beta' = \frac{d\beta}{d \ln R} \quad (4.1)$$

where κ and ω are the epicyclic and the circular frequencies, respectively. We have

$$\beta^2 = 2 \left(2 + \frac{d \ln \omega}{d \ln R} \right), \quad \frac{d\omega}{dR} = \frac{\beta^2 - 4}{2} \frac{\omega}{R}. \quad (4.2)$$

The derivatives of the galactic potential are given by

$$\frac{d\Phi_g}{dR} = R\omega^2 \quad (4.3)$$

$$\frac{d^2\Phi_g}{dR^2} = (\beta^2 - 3)\omega^2 \quad (4.4)$$

$$\frac{d^3\Phi_g}{dR^3} = [(\beta^2 - 3)(\beta^2 - 4) + 2\beta\beta'] \frac{\omega^2}{R} \quad (4.5)$$

We define $x = \Delta R = R - R_C$, where R_C is the radius of the circular orbit. Then the Taylor expansion of the galactic potential is given up to third order by

$$\Phi_g(R) \approx \Phi_g(R_C) + \omega_C^2 R_C x + \frac{1}{2}(\beta_C^2 - 3)\omega_C^2 x^2 + \frac{1}{6} [(\beta_C^2 - 3)(\beta_C^2 - 4) + 2\beta_C\beta_C'] \frac{\omega_C^2}{R_C} x^3 \quad (4.6)$$

The centrifugal potential is given by

$$\Phi_c = -\frac{1}{2}\omega_C^2 R^2 \quad (4.7)$$

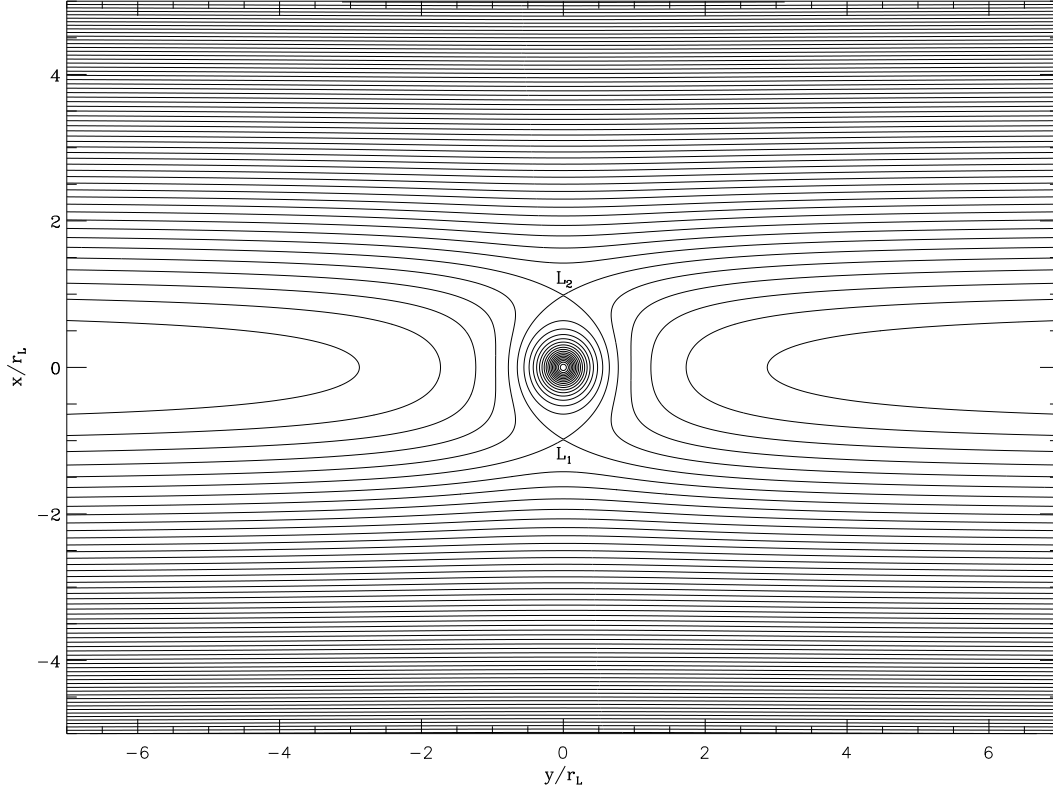


Figure 4.1: Equipotential lines of the effective potential in the tidal approximation ($z = 0$ plane). Shown is a larger area than in Figure 3.1. The parabolic potential wall of the effective potential can be seen in more detail. The star cluster lies in the middle of it.

It is second-order and the direction of the corresponding force is opposite to the gravitational force. Its derivatives are given by

$$\frac{d\Phi_c}{dR} = -\omega_C^2 R \quad (4.8)$$

$$\frac{d^2\Phi_c}{dR^2} = -\omega_C^2 \quad (4.9)$$

Thus the Taylor expansion of the effective potential is given by

$$\Phi_{\text{eff}}(R) = \Phi_g(R) + \Phi_c(R) \quad (4.10)$$

$$\approx \Phi_{\text{eff}}(R_C) + \frac{1}{2}(\beta_C^2 - 4)\omega_C^2 x^2 + \frac{1}{6}[(\beta_C^2 - 3)(\beta_C^2 - 4) + 2\beta_C\beta'_C] \frac{\omega_C^2}{R_C} x^3 \quad (4.11)$$

up to third order. The first-order term vanishes.

We can also Taylor expand the angular momentum. We have

$$\frac{dL}{dR} = \frac{\beta^2}{2}\omega R \quad (4.12)$$

$$\frac{d^2L}{dR^2} = \left[\frac{1}{4}\beta^2(\beta^2 - 2) + \beta\beta' \right] \omega \quad (4.13)$$

Thus the angular momentum difference is given by

$$\frac{\Delta L}{L_C} \approx \frac{\beta_C^2}{2} \frac{\Delta R}{R_C} + \frac{1}{2} \left[\frac{1}{4} \beta_C^2 (\beta_C^2 - 2) + \beta_C \beta'_C \right] \frac{\Delta R^2}{R_C^2} \quad (4.14)$$

to second order, where $\Delta L = L - L_C$.

Similarly, we can Taylor expand the angular speed. We have

$$\frac{d\omega}{dR} = \frac{\beta^2 - 4}{2} \frac{\omega}{R} \quad (4.15)$$

$$\frac{d^2\omega}{dR^2} = \left[\frac{1}{4} (\beta^2 - 4)(\beta^2 - 6) + \beta\beta' \right] \quad (4.16)$$

Thus the angular speed difference is given by

$$\frac{\Delta\omega}{\omega_C} \approx \frac{\beta_C^2 - 4}{2} \frac{\Delta R}{R_C} + \frac{1}{2} \left[\frac{1}{4} (\beta_C^2 - 4)(\beta_C^2 - 6) + \beta_C \beta'_C \right] \frac{\Delta R^2}{R_C^2} \quad (4.17)$$

to second order, where $\Delta\omega = \omega - \omega_C$.

The Taylor expansion of the kinetic energy of the circular orbit is necessary in order to expand the energy. The derivatives are given by

$$\frac{d}{dR} \left(\frac{\omega^2 R^2}{2} \right) = \frac{\beta^2 - 2}{2} \omega^2 R \quad (4.18)$$

$$\frac{d^2}{dR^2} \left(\frac{\omega^2 R^2}{2} \right) = \left[\frac{1}{2} (\beta^2 - 2)(\beta^2 - 3) + \beta\beta' \right] \omega^2 \quad (4.19)$$

Thus the R -expansion of the kinetic energy is given by

$$\frac{\omega^2 R^2}{2} \approx \frac{\omega_C^2 R_C^2}{2} + \frac{\beta_C^2 - 2}{2} \omega_C^2 R_C \Delta R + \frac{1}{2} \left[\frac{1}{2} (\beta_C^2 - 2)(\beta_C^2 - 3) + \beta_C \beta'_C \right] \omega_C^2 \Delta R^2 \quad (4.20)$$

From (4.6) and (4.20) follows

$$E = \Phi_g(R) + \frac{\omega^2 R^2}{2} \quad (4.21)$$

$$\approx \Phi_g(R_C) + \frac{\omega_C^2 R_C^2}{2} + \frac{\beta_C^2}{2} \omega_C^2 R_C \Delta R + \frac{1}{2} \left[\frac{1}{2} \beta_C^2 (\beta_C^2 - 3) + \beta_C \beta'_C \right] \omega_C^2 \Delta R^2 \quad (4.22)$$

For the Jacobi energy we obtain

$$E_J = E - \omega_C L \approx \Phi_g(R_C) - \frac{\omega_C^2 R_C^2}{2} + \frac{1}{8} \beta_C^2 (\beta_C^2 - 4) \omega_C^2 \Delta R^2 \quad (4.23)$$

The first-order term and the term involving β'_C vanish.

4.1.2 η -expansions

We define $\eta = 1/R$, $\eta_C = 1/R_C$ and

$$\dot{\beta} = \frac{d\beta}{d \ln \eta} = -\beta' \quad (4.24)$$

We have

$$\beta^2 = -2 \frac{d \ln L}{d \ln \eta}, \quad \frac{dL}{d\eta} = -\frac{\beta^2 L}{2 \eta}. \quad (4.25)$$

The derivatives of the galactic potential are given by

$$\frac{d\Phi_g}{d\eta} = -\eta L^2 \quad (4.26)$$

$$\frac{d^2\Phi_g}{d\eta^2} = L^2(\beta^2 - 1) \quad (4.27)$$

$$\frac{d^3\Phi_g}{d\eta^3} = -2 \frac{L^2}{\eta} [\beta^2(\beta^2 - 1) - 2\beta\dot{\beta}] \quad (4.28)$$

We define $\Delta\eta = \eta - \eta_C = 1/R - 1/R_C$. Then the Keplerian approximation (Dekker 1976 [92]) of the galactic potential is given up to third order by

$$\Phi_g(\eta) \approx \Phi_g(\eta_C) - \eta_C L_C^2 \Delta\eta + \frac{1}{2} L_C^2 (\beta_C^2 - 1) \Delta\eta^2 - \frac{1}{6} \frac{L_C^2}{\eta_C} [\beta_C^2 (\beta_C^2 - 1) - 2\beta_C \dot{\beta}_C] \Delta\eta^3 \quad (4.29)$$

In the Keplerian approximation, the centrifugal potential is given by

$$\Phi_c(\eta) = -\frac{1}{2} \eta_C^4 L_C^2 \frac{1}{\eta^2} \quad (4.30)$$

Its derivatives are given by

$$\frac{d\Phi_c}{d\eta} = \eta_C^4 L_C^2 \frac{1}{\eta^3} \quad (4.31)$$

$$\frac{d^2\Phi_c}{dR^2} = -3\eta_C^4 L_C^2 \frac{1}{\eta^4} \quad (4.32)$$

$$\frac{d^3\Phi_c}{dR^3} = 12\eta_C^4 L_C^2 \frac{1}{\eta^5} \quad (4.33)$$

Thus the effective potential in the Keplerian approximation is given by

$$\Phi_{\text{eff}}(\eta) = \Phi_g(\eta) + \Phi_c(\eta) \quad (4.34)$$

$$\approx \Phi_{\text{eff}}(\eta_C) + \frac{1}{2} L_C^2 (\beta_C^2 - 4) \Delta\eta^2 - \frac{1}{6} \frac{L_C^2}{\eta_C} [(\beta_C^2 - 4)(\beta_C^2 + 3) - 2\beta_C \dot{\beta}_C] \Delta\eta^3 \quad (4.35)$$

up to third order. The first-order term vanishes. Note that the centrifugal potential propagates to higher orders.

4.1.3 L -expansions

The Taylor expansions with respect to $\Delta L = L - L_C$ are useful, because ΔL is easy to measure in simulations. We use the following relations,

$$L = \omega R^2, \quad \frac{dL}{dR} = \frac{\beta^2}{2} \omega R = \frac{\beta^2}{2} \sqrt{\omega L}, \quad \frac{d\omega}{dL} = \frac{\beta^2 - 4}{\beta^2} \frac{\omega}{L}, \quad \frac{d\beta}{dL} = \frac{2\beta'}{\beta^2} \frac{1}{L}. \quad (4.36)$$

The derivatives of the galactic potential are given by

$$\frac{d\Phi_g}{dL} = \frac{2}{\beta^2}\omega \quad (4.37)$$

$$\frac{d^2\Phi_g}{dL^2} = \frac{2}{\beta^4}\left(\beta^2 - 4 - 4\frac{\beta'}{\beta}\right)\frac{\omega}{L} \quad (4.38)$$

Thus the Taylor expansion is given by

$$\Phi_g(L) \approx \Phi_g(L_C) + \frac{2}{\beta_C^2}\omega_C\Delta L + \frac{1}{\beta_C^4}\left(\beta_C^2 - 4 - 4\frac{\beta'_C}{\beta_C}\right)\frac{\omega_C}{L_C}\Delta L^2 \quad (4.39)$$

up to second order. We can also expand the kinetic energy of the circular orbit in powers of ΔL . We have

$$\frac{d}{dL}\left(\frac{\omega L}{2}\right) = \left(1 - \frac{2}{\beta^2}\right)\omega \quad (4.40)$$

$$\frac{d^2}{dL^2}\left(\frac{\omega L}{2}\right) = \frac{1}{\beta^4}\left[(\beta^2 - 2)(\beta^2 - 4) + 8\frac{\beta'}{\beta}\right]\frac{\omega}{L} \quad (4.41)$$

Thus the Taylor expansion is given by

$$\frac{\omega L}{2} \approx \frac{\omega_C L_C}{2} + \left(1 - \frac{2}{\beta_C^2}\right)\omega_C\Delta L + \frac{1}{\beta_C^4}\left[\frac{1}{2}(\beta_C^2 - 2)(\beta_C^2 - 4) + 4\frac{\beta'_C}{\beta_C}\right]\frac{\omega_C}{L_C}\Delta L^2 \quad (4.42)$$

up to second order.

The energy follows from Equations (4.39) and (4.42),

$$E \approx \Phi_g(R_C) + \frac{\omega_C L_C}{2} + \omega_C\Delta L \left[1 + \frac{\beta^2 - 4}{2\beta^2}\frac{\Delta L}{L_C}\right] \quad (4.43)$$

It is interesting to note that the term involving β' vanishes.

For the radius we obtain

$$\frac{dR}{dL} = \frac{2}{\beta^2}\frac{R}{L} \quad (4.44)$$

$$\frac{d^2R}{dL^2} = -\frac{2}{\beta^4}\left(\beta^2 - 2 + 4\frac{\beta'}{\beta}\right)\frac{R}{L^2}. \quad (4.45)$$

This yields

$$\frac{\Delta R}{R_C} \approx \frac{2}{\beta_C^2}\frac{\Delta L}{L_C} - \frac{1}{\beta_C^4}\left(\beta_C^2 - 2 + 4\frac{\beta'_C}{\beta_C}\right)\frac{\Delta L^2}{L_C^2}. \quad (4.46)$$

Assuming that $\beta' = 0$ we obtain

$$\frac{\Delta R}{R_C} \approx \frac{2}{\beta_C^2}\frac{\Delta L}{L_C} - \frac{1}{\beta_C^4}(\beta_C^2 - 2)\frac{\Delta L^2}{L_C^2} + \frac{2}{3\beta_C^6}(\beta_C^2 - 1)(\beta_C^2 - 2)\frac{\Delta L^3}{L_C^3}. \quad (4.47)$$

to third order.

The angular speed difference is obtained by

$$\frac{d\omega}{dL} = \frac{\beta^2 - 4}{\beta^2} \frac{\omega}{L} \quad (4.48)$$

$$\frac{d^2\omega}{dL^2} = -\frac{4}{\beta^4} \left[\beta^2 - 4 - 4\frac{\beta'}{\beta} \right] \frac{\omega}{L^2} \quad (4.49)$$

These expressions yield

$$\frac{\Delta\omega}{\omega_C} \approx \frac{\beta_C^2 - 4}{\beta_C^2} \frac{\Delta L}{L} - \frac{2}{\beta_C^4} \left[\beta_C^2 - 4 - 4\frac{\beta'_C}{\beta_C} \right] \frac{\Delta L^2}{L_C^2} \quad (4.50)$$

to second order.

If we assume that $\beta' = 0$ we obtain

$$\frac{\Delta\omega}{\omega_C} \approx \frac{\beta_C^2 - 4}{\beta_C^2} \frac{\Delta L}{L} - \frac{2}{\beta_C^4} (\beta_C^2 - 4) \frac{\Delta L^2}{L_C^2} + \frac{2}{3\beta_C^6} (\beta_C^2 - 4)(\beta_C^2 + 4) \frac{\Delta L^3}{L_C^3} \quad (4.51)$$

to third order.

The expansion of $1/\omega$ is also useful. We have

$$\frac{d}{dL} \left(\frac{1}{\omega} \right) = -\frac{\beta^2 - 4}{\beta^2} \frac{1}{\omega L} \quad (4.52)$$

$$\frac{d^2}{dL^2} \left(\frac{1}{\omega} \right) = \frac{2}{\beta^4} \left[(\beta - 2)(\beta - 4) - 8\frac{\beta'}{\beta} \right] \frac{1}{\omega L^2} \quad (4.53)$$

and obtain

$$\frac{1}{\omega} \approx \frac{1}{\omega_C} \left\{ 1 - \frac{\beta_C^2 - 4}{\beta_C^2} \frac{\Delta L}{L_C} + \frac{1}{\beta_C^4} \left[(\beta_C^2 - 2)(\beta_C^2 - 4) - 8\frac{\beta'_C}{\beta_C} \right] \frac{\Delta L^2}{L_C^2} \right\}. \quad (4.54)$$

Under the assumption that $\beta' = 0$ we obtain

$$\frac{1}{\omega} \approx \frac{1}{\omega_C} \left\{ 1 - \frac{\beta_C^2 - 4}{\beta_C^2} \frac{\Delta L}{L_C} + \frac{1}{\beta_C^4} (\beta_C^2 - 2)(\beta_C^2 - 4) \frac{\Delta L^2}{L_C^2} - \frac{1}{3\beta_C^6} (\beta_C^2 - 2)(\beta_C^2 - 4)(3\beta_C^2 - 4) \frac{\Delta L^3}{L_C^3} \right\}. \quad (4.55)$$

to third order.

We can also expand the circular speed V in order to calculate the shear flow in the vicinity of the circular orbit. We have $V = L/R$, $V_C = L_C/R_C$ and

$$\frac{d}{dL} \left(\frac{L}{R} \right) = \frac{\beta^2 - 2}{\beta^2} \frac{1}{R} \quad (4.56)$$

$$\frac{d^2}{dL^2} \left(\frac{L}{R} \right) = -\frac{2}{\beta^4} \left[\beta^2 - 2 - 4\frac{\beta'}{\beta} \right] \frac{1}{RL}. \quad (4.57)$$

This yields

$$V \approx V_C \left\{ 1 + \frac{\beta_C^2 - 2}{\beta_C^2} \frac{\Delta L}{L_C} - \frac{1}{\beta_C^4} \left[\beta_C^2 - 2 - 4\frac{\beta'_C}{\beta_C} \right] \frac{\Delta L^2}{L_C^2} \right\} \quad (4.58)$$

If we assume that $\beta' = 0$ we obtain

$$V \approx V_C \left\{ 1 + \frac{\beta_C^2 - 2}{\beta_C^2} \frac{\Delta L}{L_C} - \frac{1}{\beta_C^4} (\beta_C^2 - 2) \frac{\Delta L^2}{L_C^2} + \frac{1}{3\beta_C^6} (\beta_C^2 - 2)(\beta_C^2 + 2) \frac{\Delta L^3}{L_C^3} \right\} \quad (4.59)$$

to third order.

In the corotating reference frame we therefore have

$$V - \omega_C R = \Delta\omega R \approx V_C \left\{ \frac{\beta_C^2 - 4}{\beta_C^2} \frac{\Delta L}{L_C} + 8 \frac{\beta'_C}{\beta_C^5} \frac{\Delta L^2}{L_C^2} \right\} \quad (4.60)$$

to second order.

Under the assumption that $\beta' = 0$ we obtain

$$V - \omega_C R = \Delta\omega R \approx V_C \left\{ \frac{\beta_C^2 - 4}{\beta_C^2} \frac{\Delta L}{L_C} - \frac{1}{3\beta_C^6} (\beta_C^2 - 2)(\beta_C^2 - 4) \frac{\Delta L^3}{L_C^3} \right\} \quad (4.61)$$

to third order. The second-order term vanishes. If we multiply the expressions (4.60) and (4.61) with a time scale, we obtain arc lengths for the shear flow in the vicinity of the circular orbit.

4.1.4 ω -expansions

For completeness the author also gives two Taylor expansions with respect to $\Delta\omega = \omega - \omega_C$, where ω_C is the frequency of the circular orbit. We use

$$\frac{d\beta}{d\omega} = \frac{2\beta'}{\beta^2 - 4} \frac{1}{\omega} \quad (4.62)$$

The derivatives of the galactic potential are given by

$$\frac{d\Phi_g}{d\omega} = \frac{2L}{\beta^2 - 4} \quad (4.63)$$

$$\frac{d^2\Phi_g}{d\omega^2} = \frac{2}{(\beta^2 - 4)^2} \left[\beta^2 - \frac{4\beta\beta'}{\beta^2 - 4} \right] \frac{L}{\omega} \quad (4.64)$$

Thus the Taylor expansion is given by

$$\Phi_g(\omega) \approx \Phi_g(\omega_C) + \frac{2L_C}{\beta_C^2 - 4} \Delta\omega + \frac{1}{(\beta_C^2 - 4)^2} \left[\beta_C^2 - \frac{4\beta_C\beta'_C}{\beta_C^2 - 4} \right] \frac{L_C}{\omega_C} \Delta\omega^2 \quad (4.65)$$

up to second order.

The angular momentum difference is obtained from

$$\frac{dL}{d\omega} = \frac{\beta^2}{\beta^2 - 4} \frac{L}{\omega} \quad (4.66)$$

$$\frac{d^2L}{d\omega^2} = -\frac{4}{(\beta^2 - 4)^2} \left[\beta^2 + \frac{4\beta\beta'}{\beta^2 - 4} \right] \frac{L}{\omega^2}. \quad (4.67)$$

This yields

$$\frac{\Delta L}{L_C} \approx \frac{\beta_C^2}{\beta_C^2 - 4} \frac{\Delta\omega}{\omega_C} - \frac{2}{(\beta_C^2 - 4)^2} \left[\beta_C^2 + \frac{4\beta_C\beta'_C}{\beta_C^2 - 4} \right] \frac{\Delta\omega^2}{\omega_C^2} \quad (4.68)$$

to second order.

4.1.5 Other expansions

The energy for the apo- and pericenter x_m of an oscillation around a circular reference orbit is given by

$$E = \Phi_g(R_C + x_m) + \frac{L_C^2}{2(R_C + x_m)^2} \quad (4.69)$$

$$\approx \Phi_g(R_C + x_m) + \frac{L_C^2}{2R_C^2} \left(1 - 2\frac{x_m}{R_C} + 3\frac{x_m^2}{R_C^2} - 4\frac{x_m^3}{R_C^3} + \dots \right) \quad (4.70)$$

With Equation (4.6) and $E_C = \Phi_g(R_C) + L_C^2/(2R_C^2)$ we find the energy difference with respect to the reference energy E_C ,

$$\Delta E = E - E_C \approx \frac{\beta_C^2}{2} \frac{L_C^2}{R_C^4} x_m^2 + \frac{1}{6} [(\beta_C^2 - 3)(\beta_C^2 - 4) + 2\beta_C\beta'_C - 12] \frac{L_C^2}{R_C^5} x_m^3 \quad (4.71)$$

to third order. Similarly, we obtain

$$\Delta E \approx \frac{\beta_C^2}{2} L_C^2 \Delta\eta_m^2 - \frac{1}{6} [\beta_C^2(\beta_C^2 - 1) - 2\beta_C\dot{\beta}_C] \frac{L_C^2}{\eta_C} \Delta\eta_m^3 \quad (4.72)$$

in the η_m -expansion, where $\eta_m = 1/x_m$.

4.2 Dynamics in tidal arms

A comparison of the first-order terms in the Taylor expansions yields the relations between the logarithmic differentials,

$$\frac{\Delta R}{R_C} \approx -\frac{\Delta\eta}{\eta_C} \approx \frac{2}{\beta_C^2} \frac{\Delta L}{L_C} \approx \frac{2}{\beta_C^2 - 4} \frac{\Delta\omega}{\omega_C} \approx \frac{2}{\beta_C^2 - 2} \frac{\Delta V}{V_C}. \quad (4.73)$$

to first order.

For the tidal approximation, Figure 4.2 shows that the stars in the tidal arms move on cycloids. These are the analytical solutions of the linear system of equations of motion (3.8) - (3.10) for a vanishing cluster force (e.g. Küpper et al. 2008 [12]). In the following discussion, we denote physical quantities at the epicenter of the cycloid with subscript ‘‘E’’. For star clusters far away from the Galactic center (where the tidal approximation holds), the tangential distance of the pericenters of the cycloid orbits with period $T_\kappa = 2\pi/\kappa$ is given by

$$y(T_\kappa) = R_C \Delta\omega T_\kappa \approx \frac{2\pi}{\beta_C} R_C \frac{\Delta\omega}{\omega_C} \quad (4.74)$$

$$\approx \frac{2\pi}{\beta_C} \frac{\beta_C^2 - 4}{2} \Delta R \approx \frac{2\pi}{\beta_C} \frac{\beta_C^2 - 4}{\beta_C^2} R_C \frac{\Delta L}{L_C} \quad (4.75)$$

to first order.

As a further example, we consider the Galactic center case. We need to be more precise here, since the epicyclic frequencies κ_C and κ_E differ considerably. However, for a scale free model (see Section 2.2) of the Galactic center region we have $\beta' = 0$ and the ratio $\beta_S = \beta_C = \beta$ is constant, where the subscript ‘‘S’’ denotes the scale free model. It is more appropriate to calculate instead of the tangential distance $y(T_\kappa)$ the angle φ between the clumps as seen from the Galactic center. It is given by

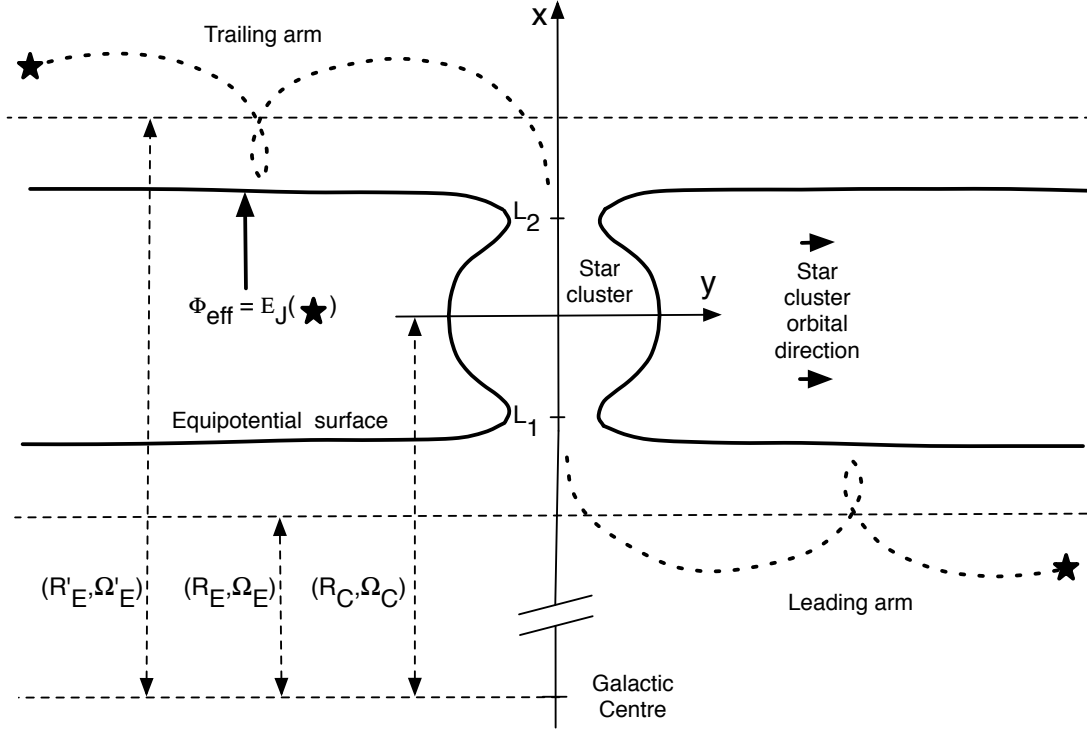


Figure 4.2: Sketch of the escape process into the tidal arms. The particles in the tidal arms move on cycloids (e.g. Küpper et al. 2008 [12], Just et al. 2009 [13]).

$$\varphi = \Delta\omega T_\kappa = \frac{2\pi}{\beta} \left[1 - \frac{\omega_C}{\omega} \right] \quad (4.76)$$

$$\approx \frac{2\pi}{\beta_S} \left[\frac{\beta_S^2 - 4}{\beta_S^2} \frac{\Delta L}{L_C} - \frac{\beta_S^2 - 2}{\beta_S^2} \frac{\beta_S^2 - 4}{\beta_S^2} \frac{\Delta L^2}{L_C^2} + \frac{1}{3} \frac{\beta_S^2 - 2}{\beta_S^2} \frac{\beta_S^2 - 4}{\beta_S^2} \frac{3\beta_S^2 - 4}{\beta_S^2} \frac{\Delta L^3}{L_C^3} \right] \quad (4.77)$$

to third order, where β_S is given in Equation (2.23) and we have used the expansion (4.55).

If we measure the Jacobi energy of the particles in addition, we can calculate the epicyclic amplitude x_m . The Jacobi energy E_J of a star is given by

$$E_J = E - \omega_C L \quad (4.78)$$

The Jacobi energy difference with respect to the effective potential at the cluster center is given by

$$\Delta E_J = E_J - \Phi_{\text{eff}}(R_C) = E - E_C - \omega_C(L - L_C) = E - E_C - \omega_C \Delta L \quad (4.79)$$

The energy difference ΔE with respect to the epicenter energy E_E determines the amplitude of the epicycle. We obtain

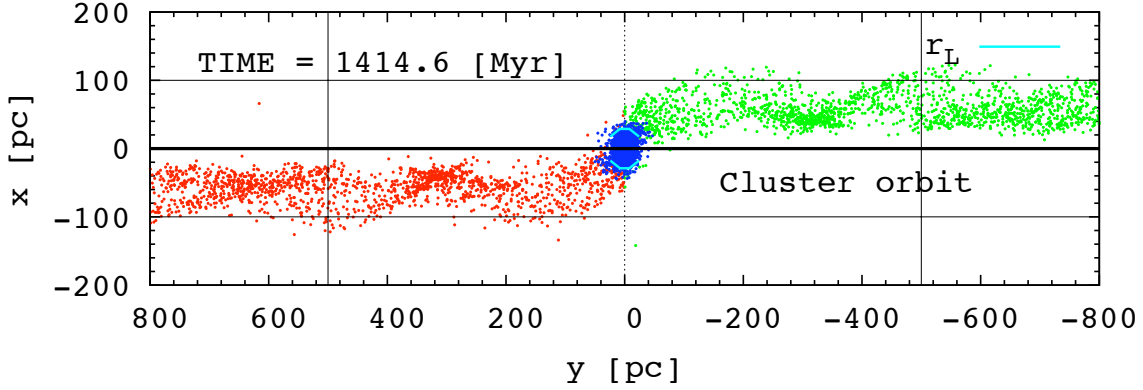


Figure 4.3: Clumps in the tidal tails of a dissolving star cluster. The simulation and the figure are by Peter Berczik [13].

$$\Delta E = E - E_E = E - E_C - \Delta E_E = \Delta E_J + \omega_C \Delta L - \Delta E_E \quad (4.80)$$

$$\approx \Delta E_J - \omega_C L_C \frac{\beta^2 - 4}{2\beta^2} \frac{\Delta L^2}{L_C^2} \quad (4.81)$$

$$\approx \Delta E_J - \omega_C^2 R_C^2 \frac{\beta_C^2}{2} \frac{\beta_C^2 - 4}{4} \frac{\Delta R^2}{R_C^2} \quad (4.82)$$

where $\Delta E_E = E_E - E_C$ and the second line follows from Equation (4.43) and the third line from Equations (4.22) and (4.17). According to Equation (4.71) the amplitude of the epicycle is given approximately by

$$x_m^2 \approx \frac{2\Delta E}{\beta_C^2 \omega_C^2} \approx \frac{2\Delta E_J}{\beta_C^2 \omega_C^2} - \frac{\beta_C^2 - 4}{\beta_C^4} R_C^2 \frac{\Delta L^2}{L_C^2} \quad (4.83)$$

$$= \frac{2\Delta E_J}{\beta_C^2 \omega_C^2} - \frac{\beta_C^2 - 4}{4} \Delta R^2. \quad (4.84)$$

For the Galactic center case we have to use the expression

$$x_m^2 \approx \frac{2\Delta E}{\beta_E^2 \omega_E^2} \quad (4.85)$$

instead, where β_E and ω_E are evaluated at the epicyclic radius R_E .

Figure 4.3 shows an application of the theory considered in this chapter. The tidal tails in the simulation by Peter Berczik show well-defined clumps at the positions of the loops or turning points of the cycloid orbits. The theory applies well. However, we will use it in order to study the tidal arms of dissolving star clusters in the Galactic center.

Chapter 5

The Galactic center

The center of the Milky Way is currently a field of very intensive research. Observations have to be carried out in other wavelengths than visual due to the huge extinction ($A_V \approx 30$ mag). Directly in the Galactic center resides the strong radio source Sgr A* at the location of the Galactic supermassive black hole ($M_\bullet \approx (3 - 4) \times 10^6 M_\odot$, e.g. Genzel et al. 2000 [98], Ghez et al. 2000 [99], Schödel et al. 2002 [100], Ghez et al. 2003 [30], Eckart et al. 2005 [101], Ghez et al. 2005 [27], Beloborodov et al. 2006 [102]). Different galactocentric radial scales are shown in Figure 5.1. They range from a rough outer radius of the central molecular zone ($R_G \approx 200$ pc, Morris (1996) [14]) down to the Schwarzschild radius of the Galactic supermassive black hole ($R_G = GM_\bullet/c^2 \approx 3.4 \times 10^{-7}$ pc), where c is the speed of light. The central molecular zone (CMZ) is a region which is rich in high-density molecular gas ($n \gtrsim 10^4 \text{ cm}^{-3}$, Morris (1996) [14]) as is suggested by high-resolution observations of the CO molecule. Two young star clusters have been discovered near the Galactic center: The starburst clusters named Quintuplet (Nagata et al. 1990 [15], Okuda et al. 1990 [16]) and Arches (Nagata et al. 1995 [17]) at projected distances less than 35 pc away from Sgr A*. According to dynamical models of Portegies Zwart et al. 2002 [97], the Arches cluster may be at a distance between 50 and 90 pc from the Galactic center. Much closer to the Galactic center, between $R_g \approx 7$ down to 1.5 pc, there is the circum-nuclear ring which is an association of several clouds or filaments of warm and dense molecular gas with temperatures of several hundred Kelvin and densities up to 10^7 cm^{-3} [96]. Inside $R_g = 1.5$ pc there is a cavity where only atomic and ionized hydrogen has been detected. Several clumps and filaments of gas seem to be on in-falling trajectories towards the central parsec. Those which have reached the central parsec form a structure which resembles a distorted spiral and is called the “mini-spiral”. It contains a few tens of solar masses of gas and dust. The mini-spiral is shown in red in Figure 5.2 which is a multi-wavelength (near-infrared) picture of the central parsec around Sgr A*. The stars in the very center of our Galaxy form the nuclear stellar cluster. According to star counts, its stellar density decreases as $\rho_\star \propto r^{-1.8 \text{ to } -2}$ (e.g. Lindqvist et al. 1992 [103], Mezger, Duschl & Zylka 1996 [104], Genzel 2003 [105] or Schödel 2007 [95]). outwards from a central stellar cusp radius ($R_g = 0.22$ pc, Schödel et al. (2007) [95]). The influence radius $R_{\bullet,\text{inf}} = GM_\bullet/\sigma^2$ of the Galactic supermassive black hole, where σ is the velocity dispersion of stars which are far enough away to be unaffected by the black hole’s gravity, is $R_{\bullet,\text{inf}} \approx 2 \pm 0.8$ pc (Frank & Rees 1976 [106] and Krabbe et al. 1995 [24] for the velocity dispersion). In the central arcsecond is the cluster of S stars which orbit the supermassive black hole on elliptic Keplerian orbits. Two orbital elements of the S2 star are shown in Figure 5.1 ($R_{g,\text{peri}} \approx 0.546 \times 10^{-3}$ pc, $R_{g,\text{apo}} \approx 8.754 \times 10^{-3}$ pc, Mouawad et al. (2005) [94] and N. Mouawad, priv. comm.).

The aim of observations of stars within the Galactic center, and, in particular the central parsec of the Milky Way is twofold: 1. The classification of stars, i.e. the determination of their spectral type and luminosity class. 2. The determination of the 3-dimensional structure and dynamics of this region. Projected distances with respect to the Galactic center can be measured with high

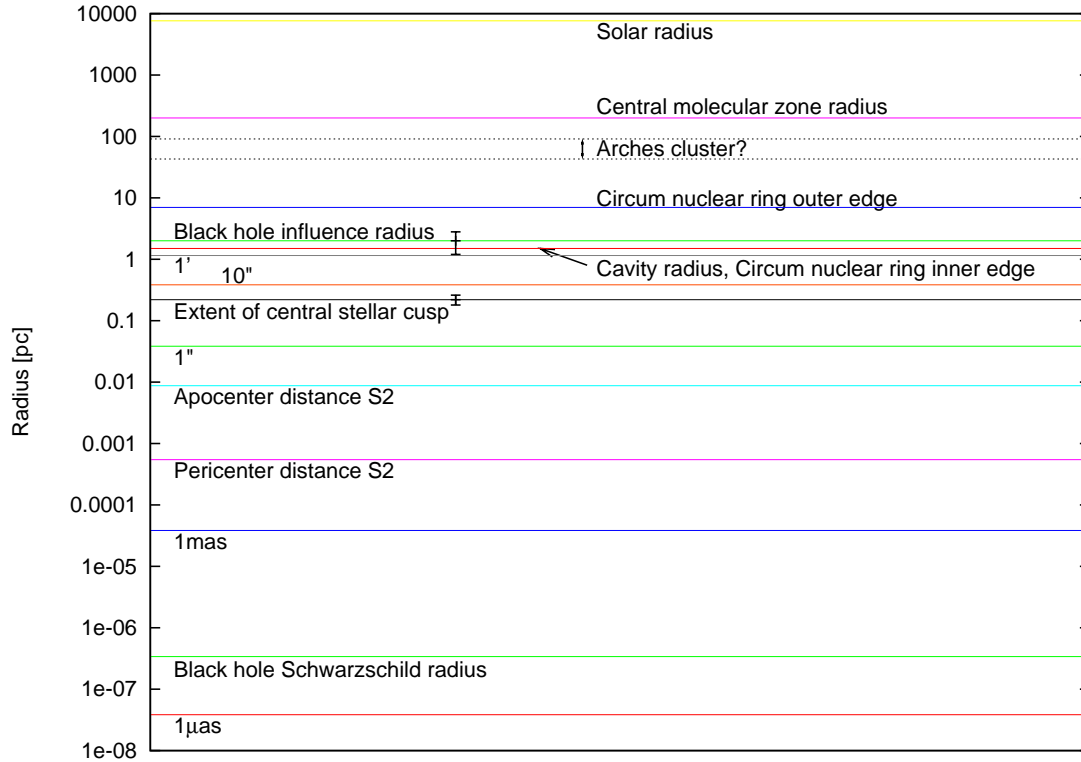


Figure 5.1: Different galactocentric radial scales. Sources: Black hole mass from Ghez et al. (2005) [27], velocity dispersion in the Galactic center from Krabbe et al. (1995) [24], distance between the Sun and the Galactic center from Eisenhauer et al. (2003) [93], orbital elements of S2 from Mouawad et al. (2005) [94] and N. Mouawad, priv. comm., extent of central stellar cusp from Schödel et al. (2007) [95], Circum Nuclear Ring radii from [96], Central Molecular Zone radius from Morris & Serabyn (1996) [14], location of Arches from Portegies Zwart et al. (2002) [97].

precision. An accurate measurement of the “Line-of-sight” coordinate is still impossible. However, it is possible to determine the full 3D velocities of stars in the Galactic center by means of radial velocity and proper motion measurements with high accuracy.

5.1 The paradox of youth

Towards the very end of the last millennium, young stars (a few Myr old) have been discovered in the central parsec around Sgr A*. Their presence in the close vicinity of the Galactic supermassive black hole is currently a heavily disputed topic within the astrophysical community. For example, the comoving groups IRS 13E (Coker & Pittard 2002 [21], Maillard et al. 2004 [22]), IRS 16SW (Tamblyn & Rieke 1993 [23], Krabbe et al. 1995 [24], Lu et al. 2005 [25]) and IRS 13N (Mužić et al. (2008) [26]), which consist of young, massive stars, orbit Sgr A* at a distance smaller than one parsec. In addition, Wolf-Rayet (WR) stars, Ofpe/WN9 stars, luminous blue variables (LBVs) and, recently, many OB stars (see Paumard et al. 2006 [107]) have been identified within a radius of one parsec around Sgr A*. In addition, there is the cluster of S stars within the central arcsecond around Sgr A* (Ghez et al. 2005 [27], Eisenhauer et al. 2005 [28]). Star formation within the central parsec of our Galaxy is, because of the presence of the Galactic supermassive black hole problematic, since the tidal field dissolves gas clouds with mean number densities of

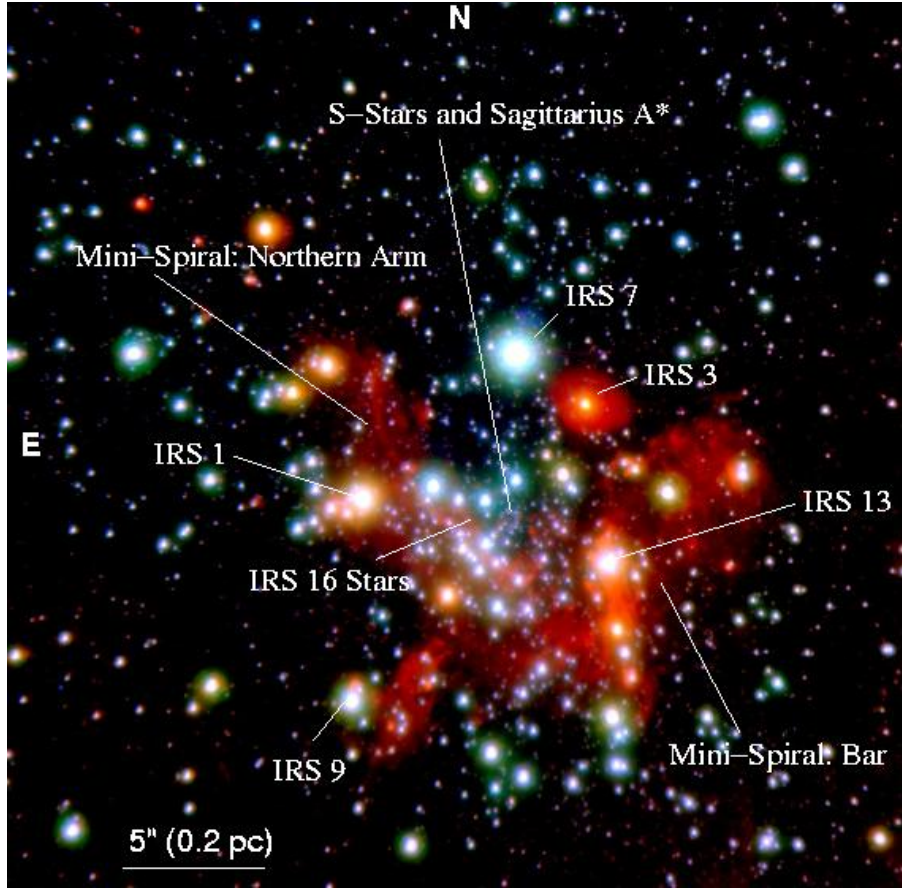


Figure 5.2: Two narrow band images (at $2.18 \mu m$ and $2.36 \mu m$) were combined with a broad band image at $3.8 \mu m$ to obtain this pseudo-colored image of the central parsec of the Milky Way. From NACO / VLT [96].

$$n < n_{\text{crit}} = 10^7 \text{ cm}^{-3} (1.6 \text{ pc}/R_G)^{1.8} \quad (5.1)$$

from which stars could form by gravitational collapse (Morris 1993 [29]). The physical reason is simply that the strength of the tidal field and the self-gravity of the cloud are of the same order at the critical mean number density n_{crit} . Such high mean number densities can only be achieved by a strong compression of the gas (e.g. through cloud collisions, strong winds or supernova shocks). Also, they are not present within the central parsec today. Rather, the cavity within the circumnuclear ring contains only atomic and ionized hydrogen. The raw material for star formation is currently lacking (Morris 1993 [29]). For these reasons one may wonder why we observe young stars in the central parsec: Their presence in the central parsec constitutes the “paradox of youth” (Ghez et al. 2003 [30]).

Gerhard (2001) [31] proposed that young stars formed in a massive $10^6 M_\odot$ star cluster in a sufficiently large distance from Sgr A* which spiralled into the Galactic center by dynamical friction within the lifetime of its most massive stars and dissolved there. The young stars in the central parsec could be remnants of such a dissolved star cluster. It may be that the comoving groups IRS 13E, IRS 16SW or IRS 13N are remaining cores of such star clusters, as some authors proposed. In this thesis, we undertake an attempt to check the viability of Gerhard’s star cluster inspiral scenario with direct N -body simulations.

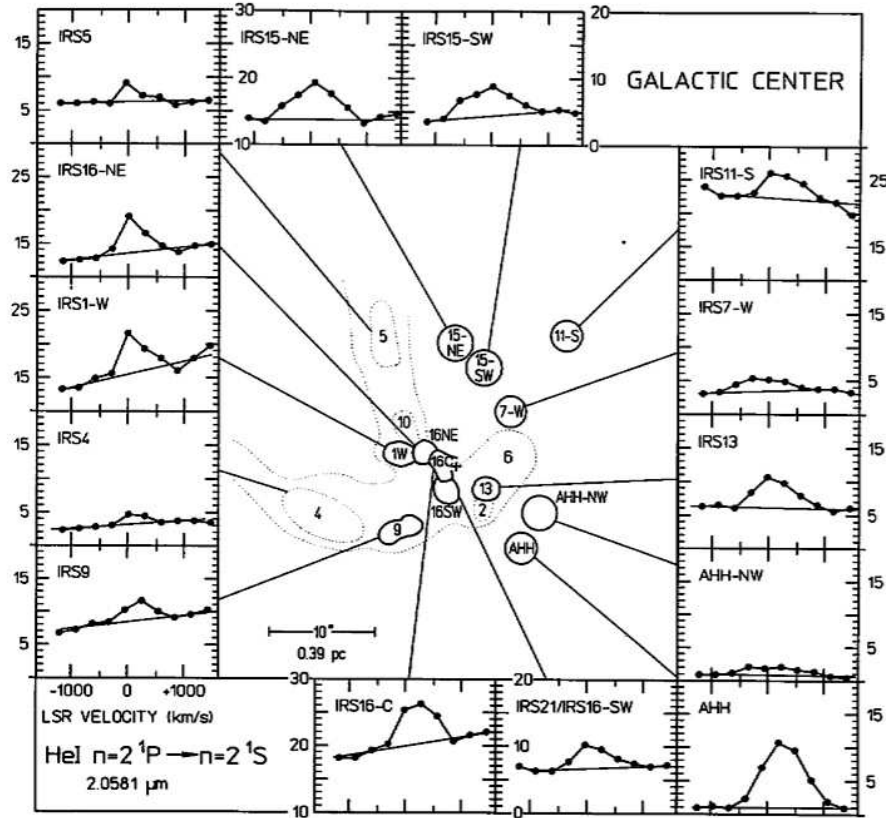


Figure 5.3: Schematic view of the sizes and locations of the He I sources within the central parsec of the Milky Way. From Krabbe et al. (1991) [115].

Aside from the star cluster inspiral scenario, another scenario has been proposed recently: The accretion disk scenario (Levin & Beloborodov 2003 [108], Goodman 2003 [109], Genzel et al. 2003 [105], Milosavljević & Loeb 2004 [110], Nayakshin et al. 2004 [111], Nayakshin & Cuadra 2005 [112], Nayakshin & Sunyaev 2005 [113], Nayakshin 2006 [114]). According to this scenario, the young stars in the central parsec formed *in situ* in one or more unstable accretion disks. In an accretion disk, the necessary densities for the gravitational collapse of a molecular cloud could be sustained despite the strong shear forces of the supermassive black hole (Milosavljević & Loeb 2004 [110]). However, the question remains, why we do not observe such an accretion disk any longer in the Galactic center. This can be explained by the presence of strong stellar winds and the tendency of such a disk, to be accreted onto the supermassive black hole through angular momentum losses due to viscous dissipation.

5.2 He I emission line stars

In 1991, Krabbe et al. [115] reported in a short paper the observation of a group of a dozen sources of He I emission (transition of neutral He I: $n = 2^1P \rightarrow n = 2^1S$ with a wavelength of $2.0581\mu\text{m}$) in the Galactic center¹. The complex named IRS 16 interpreted Krabbe et al. as a central concentration of a star cluster of He I emission line stars with a diameter of roughly one

¹Named IRS 11-S, AHH-NW, AHH, IRS 6-H II, IRS 7-W, IRS 13(H II), IRS 2-H II, IRS 15-SW, IRS 15-NE, IRS 21/16-SW, IRS 16-C, IRS 16-NE, IRS 9(H II), IRS 1-W(H II), IRS 10-H II, IRS 5-H II, IRS 4-H II.

parsec in the center of the Milky Way. The location of IRS 16 can be seen in Figure 5.2. They note that their data prove that, within the last few Myr, massive star formation has occurred in the center of the Milky Way. Two years later, Tamblyn & Rieke [23] published models of stellar populations for the complex IRS 16 which show that the age of the IRS16 stars is consistent with models with an age of 7-8 Myr. In a follow-up paper Krabbe et al. in 1995 [24] confirmed all except one² of the He I emission sources listed in their 1991 paper. They reported that the star cluster of He I stars has at least 14 but maybe as much as 20 members. Maillard et al. (2001) [116] and Paumard et al. (2001) [117] present some new results on the He I star cluster. Three new sources have been discovered and several stars previously considered as Helium stars have been discarded.

5.3 Comoving groups

5.3.1 IRS 13E

The location of the IRS 13 complex can be seen in Figure 5.2. It lies at a projected distance of roughly 0.144 pc southwest of Sgr A* and is (aside from the second brightest source IRS 13W which is notably weaker) dominated by the source IRS 13E, which is visible in IR and X-rays. People were uncertain for a long time about the nature of this source (Coker & Pittard 2000 [118], Coker et al. 2002 [21]). They speculated whether it could be an X-ray binary or a Post-LBV Wolf Rayet double star. However, in 2004 IR observations with high accuracy (using adaptive optics) revealed the true nature of the source IRS 13E: IRS 13E is a group of 7 individual sources, whose proper motions have been measured. Because of the common West direction and the amplitudes of proper motions with a mean of $\approx 280 \text{ km s}^{-1}$ (of the main components), Maillard et al. (2004) [22] argue that the individual sources 13 E1, 13 E2, 13E3A/B and 13E4 form a bound system. In addition, they determined the types of these hot, massive individual sources, whose spectral types vary from O to WR. They proposed an IMBH as the reason for the fact that the comoving group is bound. According to a simple estimate of Maillard et al. (2004), its mass should be $\geq 1300M_{\odot}$. It may be of interest to note that such a proposition had been made earlier by the theoreticians Hansen & Milosavljević (2003) [119]). With their hypothesis about the origin of the comoving group IRS 13E, Maillard et al. follow the theoretical works of Gerhard (2001) [31] and McMillan & Portegies Zwart (2003b) [120] and suggest that IRS 13E is the remaining core of a star cluster which has spiralled into the Galactic center by dynamical friction where it dissolved.

Schödel et al. (2005) [121] give a lower limit of $\approx 10^4 M_{\odot}$ for the mass of the IMBH from an estimate $M \approx \langle v^2 \rangle R/G$ over the internal velocity dispersion of IRS 13E and a method of Leonard & Merritt. However, for two reasons, Schödel et al. (2005) [121] are skeptical about the presence of a stabilizing IMBH in IRS 13E: If IRS 13E would be the remnant of a star cluster, in which an IMBH of mass $> 10^4 M_{\odot}$ has formed through runaway growth, the original star cluster had to have a mass of order $10^6 M_{\odot}$ according to the dynamical N -body models of Portegies Zwart & McMillan (2002b) [122]. This seems to be unrealistic according to Schödel et al. [121], probably because of the results of McMillan et al. (2003) [120]. In addition, they invoke the results of VLBA observations of Reid & Brunthaler (2004) [123], which gave limits on the proper motion of Sgr A* which exclude an IMBH with mass $> 10^4 M_{\odot}$ with high probability (see also Hansen 2003 [119]).

Paumard et al. (2006) [107] measured surface densities in the Galactic center. The surface density in the central cusp around Sgr A* ($r_{GC} < 0.7''$) is 32.3 ± 4.7 stars per square arcsecond. Centered around the core of IRS 13E ($r_{IRS13E} < 0.68''$), the surface density is 17.9 ± 3.5 stars per square arcsecond, i.e. a surface density which is only by a factor ≈ 1.8 lower. Paumard et al. conclude that the probability that IRS 13E is a background fluctuation is only $\approx 0.2 \%$. In addition, Paumard et al. calculate the tidal radius $r_t = (M_*/M_{\bullet})^{1/3} R$ of IRS 13E in the tidal

²IRS 11

field of Sgr A* (where M_{\bullet} is the mass of Sgr A*). They use an estimate $M_* \approx 400M_{\odot}$ for the mass of stars of IRS 13E (without IMBH) and a pericenter distance of $R = 4''$ for the orbit of IRS 13E. They find a remarkable similarity of the tidal radius and the measured core radius $r_c \approx 0.17''$ (i.e. the radius where the surface density has dropped to half of its central value) of IRS 13E. For $R \geq 4''$, IRS 13E could be a long-lived constellation. Their argument against the mass estimate from the virial theorem is that for a statistics of IRS 13E not enough (only 4!) sources are known.

5.3.2 IRS 16SW

Lu et al. (2005) [25] considered one of the two brightest members of the IRS 16 complex, IRS 16SW and the stars in the surroundings of this source. Together with IRS 13E, this is the second group of young stars with coherent proper motions. The argument of Lu et al is based on the fact that a 2D velocity dispersion map has a sharp minimum of approximately 71 km s^{-1} in the center of the sources IRS 16SW-E and IRS 16SW which is in contrast with a velocity dispersion of $100 - 250 \text{ km s}^{-1}$ of the stars which constitute the ambient medium. Such a minimum would be a clear indication of ordered motion. Following the suggestion of Maillard et al., Lu et al. note the possibility that the comoving group around IRS 16SW is also the remaining core of a star cluster which has spiralled into the Galactic center.

However, Paumard et al. (2006) [107] criticize the result of Lu et al. (2005) [25] with the following argument: For the determination of the 2-dimensional velocity dispersion at the position \mathbf{x} one has to use a smoothing kernel which has a peak at position \mathbf{x} . According to the observations of Paumard et al. (2006) [107], there is a “hole” in the counter clockwise system (CCWS, see next section) at the position of IRS 16 such that the true 2-dimensional velocity dispersion within the clockwise system was measured. However, in the surroundings of IRS 16, Lu et al. considered stars of both clockwise and counter clockwise system which would result in a higher velocity dispersion.

5.3.3 IRS 13N

IRS 13N is a small cluster of unusually red compact sources which is located approximately $0.5''$ north of IRS 13E and $3.2''$ of Sgr A*. The group consists of several Wolf-Rayet and O-type stars. Mužić et al. (2008) [26] present first proper motion measurements. They show that six of seven sources show a common proper motion indicating that IRS 13N is a new comoving group of stars in the central parsec around Sgr A*. However, they conclude that IRS 13N is probably not a bound system but currently in the process of dissolution.

5.4 CWS and CCWS

The status of more than one decade of intensive observations of the central parsec of the Galactic center is the following: The massive stars of younger type with a common age of probably $\approx 6 \pm 2$ Myr at $R_g = 0.05 - 0.5 \text{ pc}$ seem to reside in two well-defined disk structures with thickness $\langle |h|/R \rangle \approx 0.14$ which are inclined with respect to each other by an angle of $115^\circ \pm 7^\circ$ (Paumard et al. 2006 [107]). The first disk constitutes the “Clockwise System” (CWS), i.e. the stars move clockwise on the sky (Levin & Beloborodov 2003 [108]). It has been further investigated by Beloborodov et al. 2006 [102] who derived a mass estimate for the Galactic supermassive black hole. The second disk constitutes the “Counter-Clockwise System” (CCWS), i.e. the stars move counter-clockwise on the sky. The existence of the second disk is still a matter of debate and has not yet been confirmed by an independent group. The disk structures cannot be inferred from the spatial positions of the stars, since the line-of-sight coordinate cannot be measured with the necessary precision. However, the disk structures can be inferred from the 3D velocity vectors, which can be determined from accurate measurements of radial velocities and proper motions: The velocity vectors of stars which move clockwise on the sky accumulate around one plane which is only possible if the stars constitute a disk-like population (Levin & Beloborodov 2003 [108]),

Beloborodov et al. 2006 [102]). Most of the brighter stars of the complex IRS 16 are members of the CWS, while different stars of the complex IRS 13 (in particular IRS 13E) seem to belong to the CCWS (Paumard et al. 2006 [107]).

5.5 Young stars

5.5.1 WR stars, Ofpe/WN9 stars and LBVs

Wolf-Rayet (WR) stars, Ofpe/WN9 stars and luminous blue variables are highly evolved objects which are not so hard to detect because of their broad emission features. WR stars are massive, very hot (up to $\approx 5 \times 10^4 M_\odot$) and luminous (up to $10^6 L_\odot$), have strong stellar winds with high speeds and very high mass loss rates of 10^{-5} to $10^{-4} M_\odot$ per year. In fact, their surface is dominated by helium. Since the WR phase is short ($\approx 2-5$ Myr, Meynet 1995 [124]), WR stars are signposts for recent star formation. WR stars are classified into three classes, WN stars (nitrogen dominant), WC stars (carbon dominant) and WO stars ($C/O < 1$). Ofpe/WN9 stars are also very massive and eject CNO-cycle products from their surface into their circumstellar environment. In contrast to WR stars, they have slower winds. The mass loss rates range from 2 to $5 \times 10^{-5} M_\odot/\text{yr}$. Luminous blue variables (LBVs) are rare stars in a presumably short phase of evolution between the main sequence and the WR phase. Only a few are known in the Galaxy or the Magellanic clouds (Conti 1984 [125], Figer 1999 [126]). There exists already a sample of these stars in the Galactic center and, in particular, the central parsec given in Genzel et al. (1996) [127], (2000) [98], (2003) [105] and Paumard et al. (2001) [117], (2006) [107].

5.5.2 OB stars

Paumard et al. (2006) [107] published the spectroscopic identification of ≈ 40 OB super giants, giants ($m_K \approx 11-13$) and main sequence stars ($m_K \approx 13-15$) in the central parsec of the Galactic center. They report a firm detection of 29 OB supergiants (luminosity class I+II), 12 OB stars of luminosity class III+IV and 18 OB candidates whose identification they regard as tentative. All these stars are characterized by weak absorption features of He I ($\lambda = 2.058, 2.113, 2.163 \mu\text{m}$) and H I Br γ and have been detected by visual inspection of 2D continuum-subtracted line maps.

5.5.3 S stars

Figure 5.4 shows the July 20, 2007 location of the S stars. Most of them reside within the central arcsecond (or the central light-month) around the Galactic supermassive black hole. Eisenhauer et al. (2005) [28] took spectra. It turned out that nine of the 10 $K \leq 16$ stars within 0.4 arcsec exhibited prominent Br γ absorption lines characteristic of the infrared properties of early-type stars. The brighter stars also exhibited He I absorption. Over the central 0.7 arcsec in projection there were 14-15 early type stars and 9 late-type stars. It must be remarked that the measurement of the 3D velocities of the stars is essential in order to make sure that they are not foreground stars. Using the 3D velocities in addition, it turned out that within 0.7 arcsec there were 10 early-type stars and no late-type stars at all with $K \leq 16$. This increased yet further the paradox of youth. The spectral properties of the early-type S stars were identical to normal, main-sequence B0-B9 stars. The orbits of a few S stars within the central 0.5 arcsec are shown in projection in Figure 5.5. They are randomly oriented in angular momenta and apsides. Four of the six stars in the left panel have eccentricities higher than 0.85. The star S2 has the lowest orbital period of 15.24 ± 0.36 yr (Eisenhauer et al. 2005 [28]). Its orbit closed in 2007 after fifteen years of position measurements. According to Martins et al. (2008) [129] it is an early B dwarf (B0-2.5V). Recently, different physical mechanisms have been proposed to explain the origin and properties of the S stars (e.g. Löckmann, Baumgardt & Kroupa 2008 [130], Chang 2008 [131], Merritt, Gualandris & Mikkola 2008 [132]).

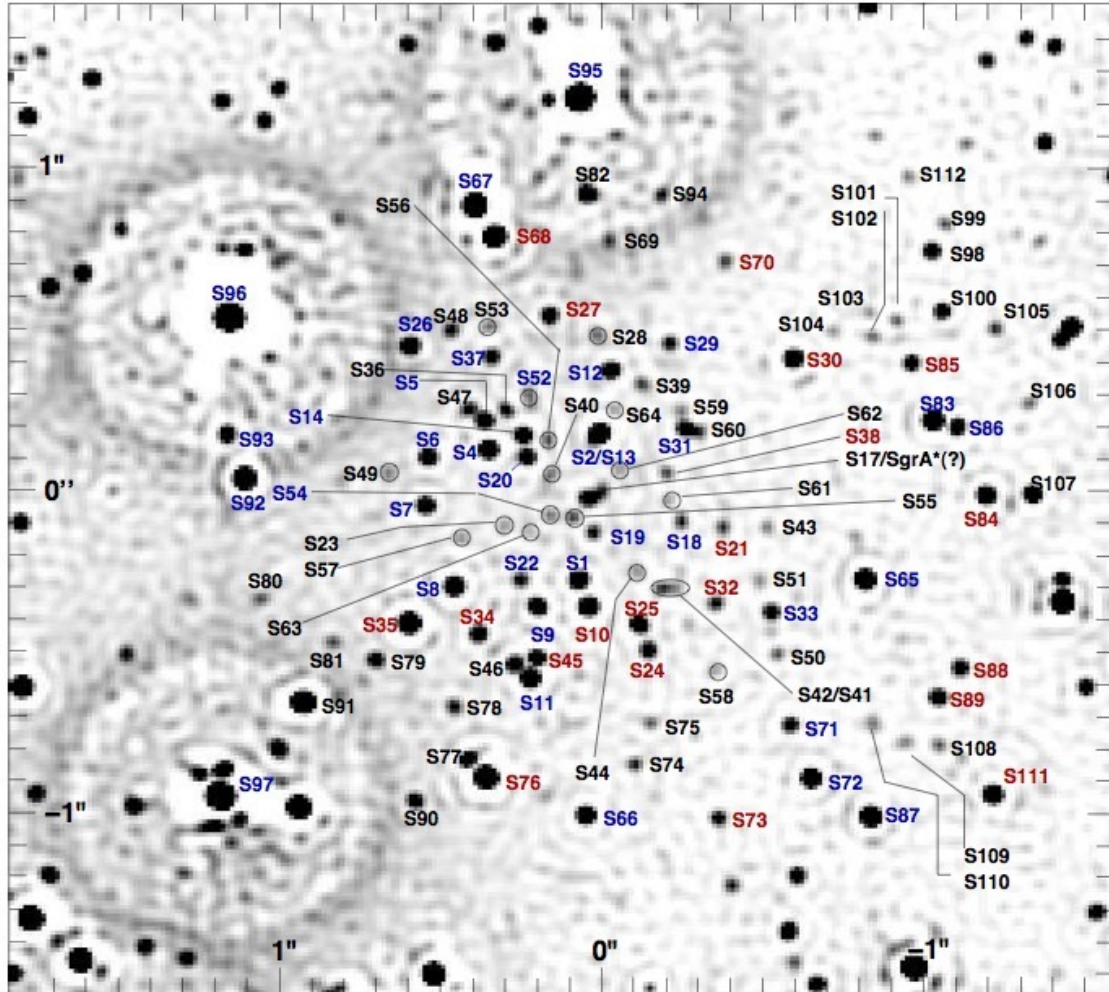


Figure 5.4: The cluster of S stars. The figure is based on a natural guide star adaptive optics image using NACO of the VLT on July 20, 2007 in the H band. From Gillessen et al. (2008) [128].

5.6 Masers

Masers are interesting objects since they can be classified without larger problems and their radial velocities and proper motions are relatively simple to measure. Therefore they are suited for accurate measurements of the trigonometric parallax using earth-bound very long baseline interferometry. Masers are ideal targets since these measurements of the trigonometric parallax require very strong and compact sources (Rygi 2008 [133]). H_2O masers have been used to determine the distance to the Galactic center, methanol masers are considered to be signposts of ongoing star formation and OH masers have been used to constrain the mass profile of the Galactic center region.

5.6.1 OH masers

The Galactic center has been extensively searched for OH/IR stars in the past two decades (Vanhollebeke et al. 2006 [134]). OH/IR stars in the Galactic center can be easily detected by the

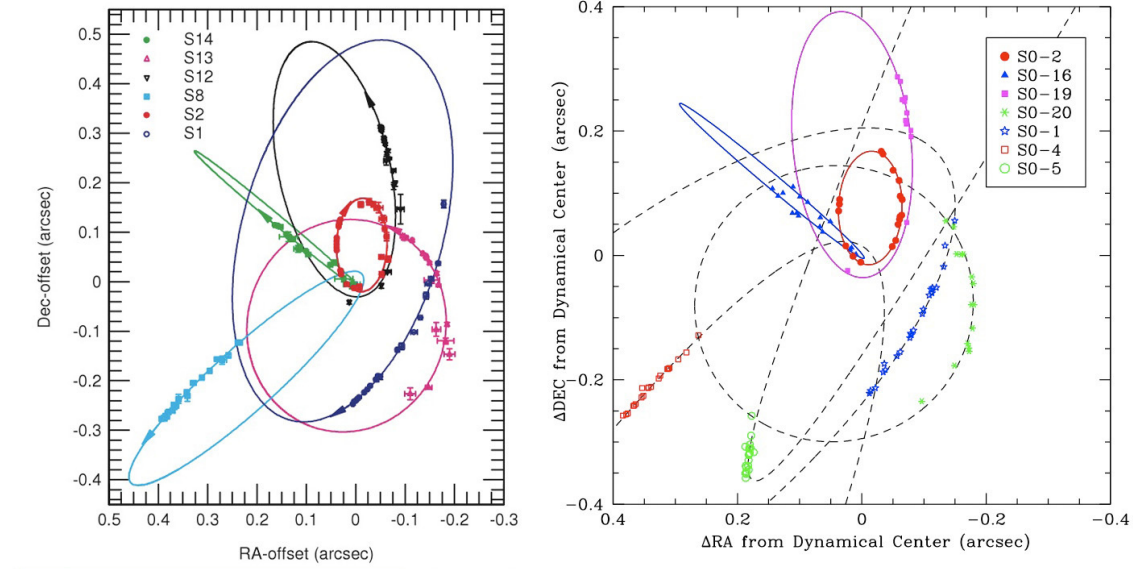


Figure 5.5: Orbits of a few S stars within 0.5 arcsec around Sgr A*. Left: From Eisenhauer et al. (2005) [28], Right: From Ghez et al. (2005) [27].

characteristic double peaked profile if they have strong OH emission lines at 1612 MHz.³ OH/IR stars are highly evolved low and intermediate mass stars ($\lesssim 9 M_{\odot}$) with very dense circumstellar envelopes, located at the tip of the asymptotic giant branch (Lindqvist et al. 1992a [135], Sjouwerman et al. 1999 [136]). Typical ages of OH/IR stars range from 100 Myr to 10 Gyr and more (L. Sjouwerman, priv. comm.). Habing et al. (1983) [137] detected already 34 OH/IR stars within 150 pc (i.e one degree) around the Galactic center. Lindqvist et al. 1992b [103] found a sample of 134 OH/IR stars within the range of ≈ 5 to 100 pc around the Galactic center. Sjouwerman et al. (1998) [138] list 155 double peak OH maser detections (from which 52 were previously unknown) within ≈ 40 projected parsecs of Sgr A*. However, no OH/IR stars have been found in the central parsec around Sgr A* and only a few in the circum-nuclear disk (in projection, L. Sjouwerman, priv. comm.). The OH/IR stars near the Galactic center cannot be used to determine the distance to the Galactic center since the angular sizes of the OH/IR stars near the Galactic center are strongly affected by scattering due to electrons in the intervening interstellar medium (Reid 1993 [139]). However, they have been used by Lindqvist et al. (1992b) [103] to constrain the mass distribution within 0.3 - 100 pc from the Galactic center. In addition to the sources mentioned above, Pihlströhm & Sjouwerman (2006) [140] report a few 1720 MHz OH masers which probably are associated with the circum-nuclear disk which is rich in warm gas and contains supernova remnants. However, they also note that 1720 MHz OH masers do not seem to belong necessarily to star-forming regions and SNR/ISM interactions. Yusef-Zadeh et al. (2007) [141] further searched for maser activity within the circum-nuclear disk. They found four Supernova remnant (SNR) OH(1720 MHz) masers, G0.0+0.0 (Sgr A East), Sgr D (G1.13-0.1), G1.4-0.1 and G359.1-0.5.

5.6.2 H₂O masers

Water masers are found in star forming regions and around late-type stars (Taylor et al. 1993 [142]). In a search in the inner 4×4 degrees of the Galaxy, 30 H₂O masers have been detected (Taylor et al. 1993 [142]). Levine et al. (1995) [143] report the detection of a late-type supergiant within 2 pc of the Galactic center and having circumstellar H₂O maser emission at 22.2 GHz. The proper

³We briefly note that the hydroxyl molecule has another spectral line at 1667 MHz.

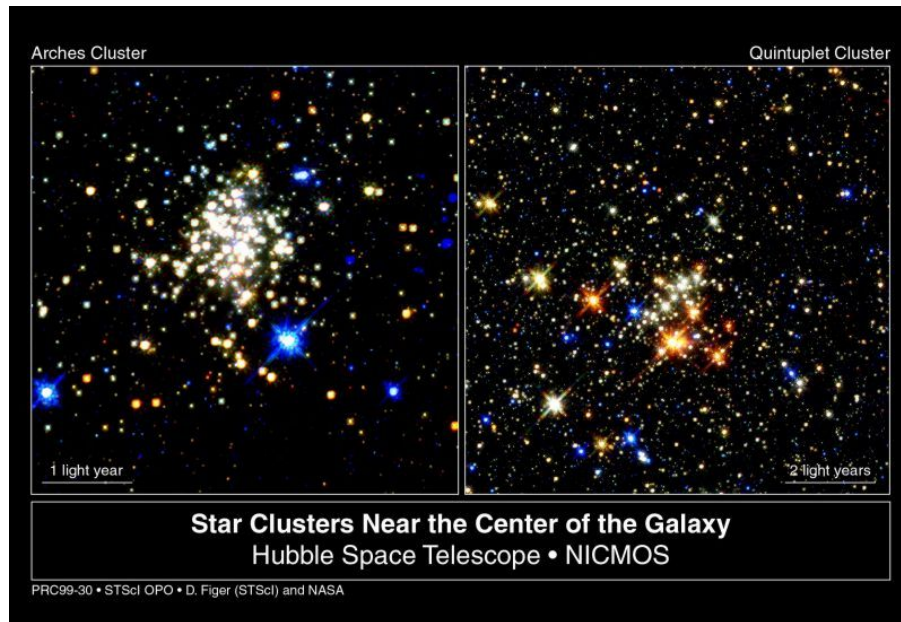


Figure 5.6: The young star clusters Arches and Quintuplet near the Galactic center.

motions of H_2O masers in the Galactic center have been used to determine the distance to the Galactic center (see Reid 1993 [139] for a review).

5.6.3 Methanol masers

It is now well established that Methanol masers are signposts of ongoing massive star formation throughout the Galaxy (Yusef-Zadeh et al. (2007) [141]). They are thought to be pumped by emission from warm dust which is heated by a young stellar object (Rygi et al. 2008 [133]). In the inner 2 degrees of the Galactic center, 23 class II methanol masers have been detected by a survey at 6.7 GHz (Caswell 1996 [144]). However, the inner 30 pc of the Galactic center show no evidence of any class II methanol masers (Yusef-Zadeh et al. (2007) [141]).

5.7 Young star clusters

The starburst clusters Arches and Quintuplet are two young star clusters at projected distances less than 35 pc from the Galactic center. They are shown in Figure 5.6 and have quite extraordinary stellar contents and properties. Their formation still requires clarification. However, Figure 5.7 shows that both clusters are located (at least, in projection) near the Galactic center “Radio Arc” (Yusef-Zadeh et al. 1984 [18]), which is a region rich in molecular clouds and gaseous filaments (Morris & Serabyn 1996 [14], Lis et al. 2001 [145], Yusef-Zadeh et al. 2002 [146], Lang et al. 2005 [20]).

5.7.1 Quintuplet

The Quintuplet cluster borrows its name from its five brightest stars in the infrared wavelengths. It has been detected in 1990 in a near-infrared survey (Nagata et al. 1990 [15], Okuda et al. 1990 [16]) and lies ≈ 30 pc in projection away from the Galactic center along the line of sight toward the crossing of the Galactic center “Radio Arc” with the Galactic plane (see also Figure 5.7). Figer et al. (1999) [126] gave convincing arguments that the Quintuplet cluster is indeed

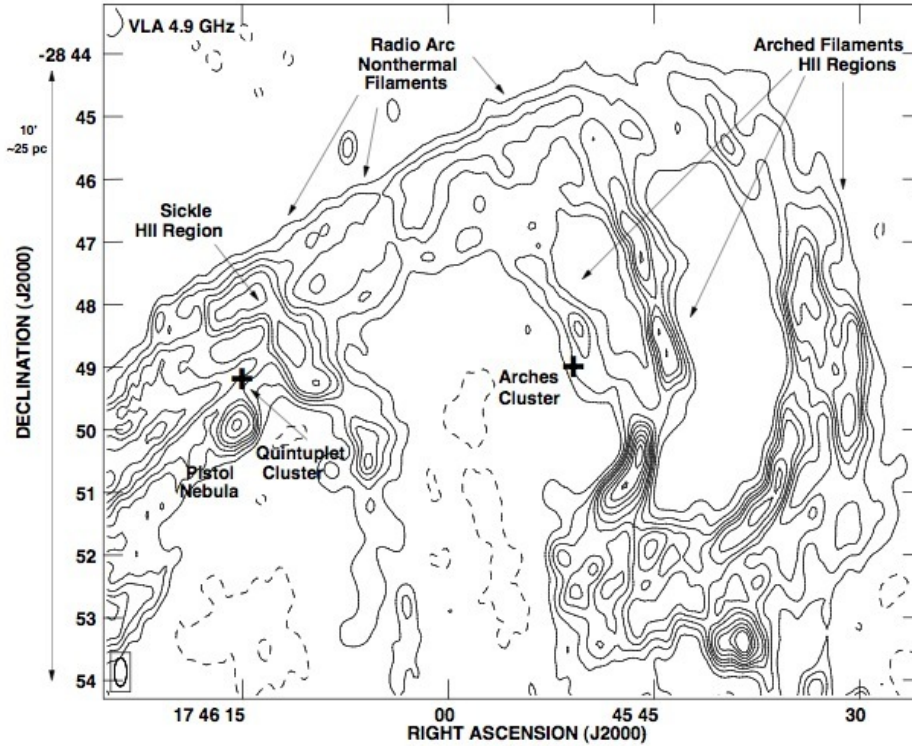


Figure 5.7: The location of Arches and Quintuplet with respect to the Galactic center “Radio Arc”. From Lang et al. (2005) [20].

close to the Galactic center and not only in projection. They also took spectra and identified young stars, e.g. OB stars, WR stars, Ofpe/WN9 stars and one LBV star. Being slightly older than the Arches cluster (see Tables 5.1 and 5.2), the Quintuplet cluster contains probably the largest accumulation of WR stars in the Galaxy (Figer et al. 1999 [126]). Most probably, it also contains the Pistol star with luminosity $\approx 10^7 L_{\odot}$ which is considered to be the most massive star in the Galaxy and has been classified as an LBV star (Figer et al. 1998 [148], Geballe et al. 2000 [149]). Table 5.1 summarizes some properties of the Quintuplet cluster according to recent observations.

5.7.2 Arches

The Arches cluster borrows its name from its proximity to the “thermal Radio Arc” or “thermal Arches” (Timmermann et al. 1996 [19]). It has been detected in 1995 in near-infrared wavelengths and was first called “Object #17” (Nagata et al. 1995 [17]). It lies ≈ 25 pc in projection away from the Galactic center at the eastern edge of the thermal “arched filaments” (see Figure 5.7). It contains very young and luminous stars. The observations by Serabyn et al. 1998 [153] showed that Arches is a rich stellar cluster with a substantial overdensity above the surrounding background stars. They estimate that it contains a total of 120 massive O stars ($\geq 20M_{\odot}$) of which a dozen may have evolved to the WR phase. Thus the Arches cluster is the most massive agglomeration of O stars in the Galaxy (Serabyn et al. 1999 [155]). The estimate for the total mass would then be $(1.5 - 6) \times 10^4 M_{\odot}$ which is comparable to that of a small globular cluster (Mandushev et al. (1991) [156]). The Arches cluster is one of the most luminous clusters in the Galaxy (Figer et al. 2002 [151]). It is also the most compact star cluster known in the Galaxy. Serabyn et al.

Quantity	Value	Lower limit	Upper limit	Remarks	Ref.
Proj. distance from GC	≈ 30 pc				[147]
Age	4 Myr	3 Myr	5 Myr		[147], [126]
Total mass	$0.6 \times 10^4 M_\odot$			$m_{\text{lower}} = 1.0$	[126]
	$1.6 \times 10^4 M_\odot$			$m_{\text{lower}} = 0.1$	[126]
	$1.3 \times 10^4 M_\odot$	$6.3 \times 10^3 M_\odot$			[147]
Luminosity	$\approx 10^{7.5} L_\odot$			total	[126]
Ionizing flux	$\approx 8 \times 10^{50}$ photons s^{-1}				[126]

Table 5.1: Properties of the Quintuplet cluster.

(1998) [153] estimate its average stellar density to be $\approx 3 \times 10^5 M_\odot \text{pc}^{-3}$. The mass function of the Arches cluster has been extensively analyzed by Stolte et al. (2002) [157], Stolte (2003) [158] and Stolte et al. (2005) [150]. Stolte et al. (2007) [154] measured the proper motion of the Arches cluster with respect to the surrounding field to be 212 ± 22 km/s. The 3-dimensional space motion turned out to be $v_{3D} = 232 \pm 30$ km/s, directed away from the Galactic center to the North-East and away from the sun. Furthermore, the authors find that the high orbital velocity is inconsistent with a circular orbit in a spherically symmetric potential of the Galactic center region and speculate that Arches is on a transitional trajectory between x1 and x2 orbits.⁴ Table 5.2 summarizes some properties of the Arches cluster according to recent observations.

5.8 Numerical works

Portegies Zwart et al. (2002) [97] studied the evolution of star clusters like Arches and Quintuplet using the STARLAB software environment. The internal dynamical evolution of their star cluster models (King models with three different concentrations) has been followed with direct N -body models. The stellar evolution of single and binary stars has been followed as well with special routines. Furthermore, the effect of a steady tidal field was considered at three different galactocentric radii. They neglected the effect of dynamical friction, since a simple estimate shows already that the time scale of dynamical friction is for a cluster like Arches more than one power of ten larger than its measured age. The main results of the work by Portegies Zwart et al. are the following: 1. The more compact the cluster is, and the closer it is located to the Galactic center, the longer is the density contrast with respect to the stellar background's density of the bulge stars high enough that the cluster may be detected by observations. The Arches cluster must therefore reside in a region within 50 – 90 pc away from the Galactic center. 2. Mass segregation and core collapse happen within 2 Myr for such clusters 3. The observed characteristics of the Arches cluster are consistent with a normal initial mass function.

McMillan & Portegies Zwart (2003) [120] present semi-analytical calculations of star clusters in order to test the star cluster inspiral scenario. They consider star clusters with (a) constant mass, (b) mass loss due to relaxation (i.e. dynamical interactions) and (c) mass loss due to stellar evolution which spiral into the Galactic center. The results of this work are as follows: 1. Only massive star clusters (i.e. with mass $\gtrsim 10^5 M_\odot$) can reach the Galactic center from an initial distance $\gtrsim 60$ pc within a few Myr. 2. A $10^6 M_\odot$ star cluster needs a few times 10 Myr to reach the Galactic center from an initial distance of $\gtrsim 30$ pc. 3. The most promising star cluster candidates would be those which have a mass of $\lesssim 10^5 M_\odot$ which have formed $\lesssim 20$ pc away from the Galactic center 4. The time for Arches and Quintuplet to reach the Galactic center would be one power of ten higher than the lifetime predicted by N -body models in [160]. We may remark here, that only circular star cluster orbits have been considered in this work and that the Coulomb logarithm in the dynamical friction formula was very high.

⁴See Contopoulos & Papayannopoulos (1980) [159] for the discussion of the families of orbits in bar potentials of different strengths.

Quantity	Value	Lower limit	Upper limit	Remark	Ref.
Proj. distance from GC	≈ 25 pc				[150]
Age	2 Myr				[150]
	2.5 Myr	2 Myr	3 Myr		[151]
		~ 2 Myr	4 Myr		[152]
	2 Myr	1 Myr	3 Myr		[147]
Total mass	$\approx (1.5 - 6) \times 10^4 M_\odot$		5 Myr	if WR stars are present	[153]
		$\approx 10^4 M_\odot$		$m_{\text{lower}} = (2 - 0.1) M_\odot$	[153]
	$1.08 \times 10^4 M_\odot$			$m_{\text{lower}} = 1.0 M_\odot$	[147]
	$1.2 \times 10^4 M_\odot$			$m_{\text{lower}} = 0.1 M_\odot$	[147]
1D velocity dispersion			$7 \times 10^4 M_\odot$	within 0.23 pc	[151]
Central density	$3 \times 10^5 M_\odot \text{ pc}^{-3}$		22 km s^{-1}		[151]
Core radius	0.2 pc			$R_{g,\odot} = 8 \text{ kpc}$	[147]
	0.23 pc			$R_{g,\odot} = 8 \text{ kpc}$	[150]
Outer cutoff radius	≈ 0.35 pc			$R_{g,\odot} = 8 \text{ kpc}$	[153]
Luminosity	$\approx 10^{7.8} L_\odot$			total	[153]
Ionizing flux	$4 \times 10^{51} \text{ photons s}^{-1}$				[151]
	$4 \times 10^{51} \text{ photons s}^{-1}$				[153]
Number of O stars	≈ 160				[147]
	≈ 120				[153]
Proper motion	212 km/s	190 km/s	234 km/s	$R_{g,\odot} = 8 \text{ kpc}$	[154]
Radial velocity	95 km/s	87 km/s	103 km/s		[151]

Table 5.2: Properties of the Arches cluster.

Portegies Zwart et al. (2003) [161] explore with direct N -body simulations with semi-analytically implemented dynamical friction the origin of the complex IRS 16. One of their results is that a cluster, whose core remained as the observed IRS 16 complex, must be a core-collapsed cluster to reach the order of the critical core density of $\rho_c \gtrsim 10^7 M_\odot \text{ pc}^{-3}$ necessary to survive in the Galactic center and which must be much larger than the local density of the stellar background. According to their results, the star cluster inspiral scenario might be viable.

Portegies Zwart et al. (2004) [162] model the Arches cluster with direct N -body simulations using the STARLAB software environment. An external galaxy potential has been implemented semi-analytically, and they consider different orbital eccentricities. Their main aim are insights about the time evolution of the mass spectrum of the model clusters and a comparison with the observed mass function of the Arches cluster (Stolte et al. 2002 [157], Stolte et al. 2003 [158]). The result is that mass segregation can explain the abundance of heavy stars within the Arches cluster.

Kim et al. (2004) [163] present N -body models of star clusters with an embedded intermediate-mass black hole (IMBH). The result is that an IMBH weakens the demand for the requirement of high central densities of inspiralling star clusters if the mass of the IMBH is of the order of 10 % of the cluster mass. However, this value is two orders of magnitude higher than the values for the collapsed core mass from which an IMBH could form (Portegies Zwart et al. 2002 [122], Guerkan et al. 2004 [164]).

Gürkan & Rasio (2005) [165] present Monte-Carlo simulations of star clusters in the Galactic center with a semi-analytically implemented inspiral rate to find the initial conditions for the star cluster inspiral scenario. Their result is that clusters which form at a galactocentric radius of $\gtrsim 10$ pc must have a mass of $10^6 M_\odot$ and must be very concentrated, i.e. with $W_0 \gtrsim 8$, to collapse.

The discussion whether the comoving group IRS 13 could contain a stabilizing IMBH (Maillard

et al. 2004 [22], Schödel et al. 2005 [121] and the discovery of a large population of transient X-ray binaries in the central parsec stimulated the paper by Portegies Zwart et al. 2006 [166]. They simulated the inner 100 pc of the Milky Way to make predictions about the formation and frequency of star cluster populations and IMBHs. Their predictions are as follows: 1. Some of the transients may contain IMBHs.⁵ 2. The cores of $\approx 10\%$ of star clusters which have formed within 100 pc around the Galactic center form IMBHs while they collapse within the lifetime of the clusters. 3. The region within < 10 pc around Sgr A* could contain ~ 50 IMBHs of mass $\sim 10^3 M_{\odot}$.

Fujii et al. (2008) [168] performed fully self-consistent N -body simulations of star clusters near the Galactic center using the Bridge code for four models. Using a variable Coulomb logarithm

$$\ln \Lambda = \ln \left(\frac{R_{\text{SC}}}{1.4\epsilon_{\text{SC}}} \right) \quad (5.2)$$

according to Hashimoto et al. (2003) [169], where R_{SC} is the distance of the star cluster from the Galactic center and ϵ_{SC} is the size of the star cluster, they find that the inspiral time scale of the star cluster is shorter than that from the “traditional” simulations and that the core collapse helps the cluster survive in the tidal field.

⁵Ultra-luminous X-ray sources (ULXs) are currently under intensive investigation since a possible connection to IMBHs may exist (e.g. Körding 2005 [167]). That ULXs with a luminosity of less than 10^{40} erg s⁻¹ contain IMBHs may be rather improbable (E. Körding, priv. comm.).

Chapter 6

Strong tidal field

In this chapter, we use the parameters given in Table 6.1. For convenience¹ we have set the length unit R_0 of the scale free model of the Galactic center region equal to the radius R_C of the circular orbit, i.e. we have $R_0 = R_C$.

6.1 Effective potential

Since we are considering a circular orbit, it is adequate to study the physics in a reference frame which is co-rotating with the frequency $\omega_C = \omega_0$ of the circular orbit. The star cluster center is taken as the origin of coordinates. Similarly to the procedure in Chapter 3, we choose a right-handed coordinate system where the x -axis points away from the Galactic center and the y -axis points in the orbital direction of the star cluster orbit around the Galactic center. In this reference frame, centrifugal and Coriolis forces naturally appear according to classical mechanics. The potential in which a particle moves is the superposition of the effective tidal potential and the star cluster potential. For short we will call this the effective potential.

The effective potential is shown in Figure 6.1. It is given by the expression

$$\begin{aligned} \Phi_{\text{eff}}(x, y, z) = & \Phi_0 \left(\frac{\sqrt{(x + R_0)^2 + y^2 + z^2}}{R_0} \right)^{\alpha-1} - \frac{1}{2} \omega_0^2 [(x + R_0)^2 + y^2 + z^2] \\ & - \frac{GM_{cl}}{\sqrt{r_{P1}^2 + x^2 + y^2 + z^2}} \end{aligned} \quad (6.1)$$

Note that Φ_0, ω_0 and R_0 are related by $\Phi_0 = \omega_0^2 R_0^2 / (\alpha - 1)$. In Equation (6.1), the first term is the gravitational potential of the Galactic center region, the second term is the centrifugal potential and the last term is the Plummer potential of a star cluster with mass M_{cl} and Plummer radius r_{P1} . The potential of the Galactic center region is not well behaved in the limit $R_0 \rightarrow 0$ if there is no black hole. However, the physics considered in this thesis happens close to the radii of the circular orbits. The Jacobi energy per unit mass $E_J = (\dot{x}^2 + \dot{y}^2 + \dot{z}^2) / 2 + \Phi_{\text{eff}}(x, y, z)$ is a conserved quantity in the co-rotating reference frame. It is of utmost interest to note that the star cluster potential breaks the axisymmetry of the effective tidal potential. This symmetry breaking implies that the angular momentum conservation is also broken locally to some extent.

The tidal terms (i.e. the first two terms on the right-hand side) of Equation (6.1) can be expanded in a Taylor series around the star cluster center $(x, y, z) = (0, 0, 0)$. Up to 5th order, the 3D Taylor expansion of the effective tidal potential for the scale free model is given by

¹of a theoretician

Parameter	Value	Parameter	Value
α	1.2	$C(L_1)$ [pc ² Myr ⁻²]	1.67546e5
R_0 [pc]	20	$C(L_2)$ [pc ² Myr ⁻²]	1.67592e5
M_0 [M_\odot]	1.67459e8	$C(L_3)$ [pc ² Myr ⁻²]	1.65965e5
ρ_0 [M_\odot pc ⁻³]	1998.90	$\Phi_{\text{eff,tid}}(R_0)$ [pc ² Myr ⁻²]	1.69502e5
Φ_0 [pc ² Myr ⁻²]	1.88335e5	$x(L_1)$ [pc]	-2.66618
ω_0 [Myr ⁻¹]	9.704	$x(L_2)$ [pc]	2.78522
M_{cl} [M_\odot]	10 ⁶		
r_{PI} [pc]	1.20213	G [pc ³ M_\odot^{-1} Myr ⁻²]	(222.3) ⁻¹

Table 6.1: Parameters used for the scale free model of the Galactic center region (Section 2.2) and the Plummer models (Section 2.3) which are used in Sections 6.1 and 6.2. $C(L_i)$ and $x(L_i)$ the value of the effective potential at the Lagrange point L_i and its location, respectively and G is the gravitational constant.

$$\begin{aligned}
\Phi_{\text{eff,tid}} \approx & \frac{1}{2} \left(\frac{3-\alpha}{\alpha-1} \right) \omega_0^2 R_0^2 + \frac{1}{2} (\alpha-3) \omega_0^2 x^2 + (\alpha-3)(\alpha-2) \frac{\omega_0^2}{6R_0} x^3 \\
& + (\alpha-3) \frac{\omega_0^2}{2R_0} x(y^2 + z^2) + (\alpha-4)(\alpha-3)(\alpha-2) \frac{\omega_0^2}{24R_0^2} x^4 \\
& + (\alpha-4)(\alpha-3) \frac{\omega_0^2}{4R_0^2} x^2(y^2 + z^2) + (\alpha-3) \frac{\omega_0^2}{4R_0^2} y^2 z^2 \\
& + (\alpha-5)(\alpha-4)(\alpha-3)(\alpha-2) \frac{\omega_0^2}{120R_0^3} x^5 + (\alpha-5)(\alpha-4)(\alpha-3) \frac{\omega_0^2}{12R_0^3} x^3(y^2 + z^2) \\
& + (\alpha-5)(\alpha-3) \frac{\omega_0^2}{8R_0^3} x(y^4 + z^4) + (\alpha-5)(\alpha-3) \frac{\omega_0^2}{4R_0^3} xy^2 z^2 \quad (6.2)
\end{aligned}$$

where R_0 and ω_0 are the radius and the frequency of the circular orbit. This solution is shown in Figure 6.4 (which may be compared with Figure 6.1). It can be seen that this Taylor expansion cannot be used to study the structure of tidal arms in the Galactic center. For extended tidal arms the exact expression of the effective potential should be used. Alternatively, one may use an expansion in cylindrical coordinates and for the radial asymmetry the exact potential.

It is easy to verify that the expansion up to the 2nd order is consistent with the tidal approximation, i.e. we have for the scale free model $(\alpha-3)\omega_0^2 = (\kappa_0^2 - 4\omega_0^2)$, where κ_0 is the epicyclic frequency.

Figure 6.2 shows a zoom into the equipotential lines around the star cluster region of Figure 6.1. Figure 6.2 also shows the location of the Lagrange points L_1 and L_2 . As usual, L_1 lies on the negative x -axis (between the cluster center and the Galactic center) while L_2 lies on the positive x -axis. L_1 and L_2 are saddle points of the effective potential. It can be seen that at the locations of L_1 and L_2 , the surface in Figure 6.1 is curved differently along the x - and y -axes.

Figure 6.3 shows the effective potential in the star cluster region along the line connecting the Galactic center with the star cluster center. The dashed line shows only the effective tidal potential $\Phi_{\text{eff,tid}}$. The corresponding 1D Taylor series of $\Phi_{\text{eff,tid}}$ along the x -axis around $x = 0$ ($y = z = 0$) is given by the power series

$$\Phi_{\text{eff,tid}} \approx \frac{1}{2} \left(\frac{3-\alpha}{\alpha-1} \right) \omega_0^2 R_0^2 + \frac{1}{2} (\alpha-3) \omega_0^2 x^2 + \sum_{k=3}^{\infty} \left\{ \left[\prod_{l=2}^k (\alpha-l) \right] \frac{\omega_0^2}{R_0^{k-2}} \frac{x^k}{k!} \right\} \quad (6.3)$$

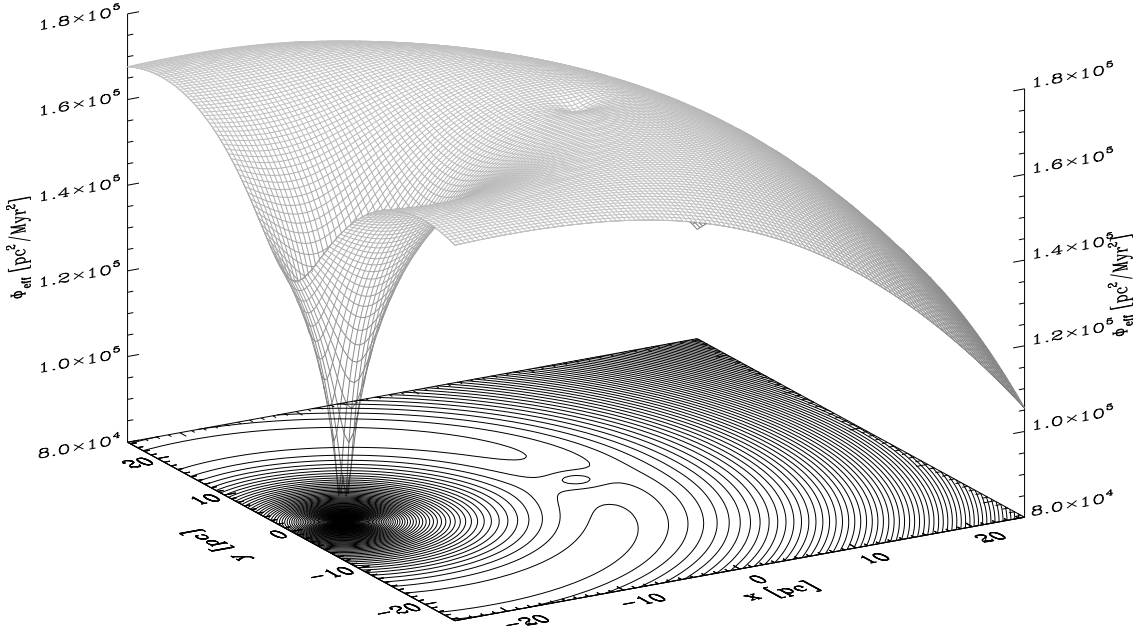


Figure 6.1: Effective potential for a star cluster in the Galactic center ($z = 0$ plane). The large potential well is due to the Galactic center and the small one is due to the star cluster.

Higher-order terms lead to an asymmetry with respect to $x = 0$ which becomes important in the vicinity of the Galactic center. A non-linearity in the tidal forces is related to this asymmetry. Such non-linear effects can be seen in Poincaré surfaces of section. The solid line in Figure 6.3 shows the full effective potential. It is the superposition of the effective tidal potential and the star cluster potential. The Lagrange points L_1 and L_2 lie at slightly different energies and at slightly different distances from the star cluster center whose position the author denoted as L_3 . The energies and locations of the Lagrange points are given in Table 6.1.

We stress that this picture is only valid for a star cluster orbit which is exactly circular. The region above the tidal effective potential (dashed line in Figure 6.3) is energetically forbidden for the cluster orbit. As soon as it becomes eccentric, the cluster center no longer remains at the position of the extremum of the effective tidal potential but oscillates around $x = 0$ and is reflected either at the centrifugal or the gravitational barrier. This oscillation leads to oscillations of the Jacobi energies of the Lagrangian points L_1 and L_2 on the orbital time scale of the star cluster orbit and can change the dynamics dramatically.

6.2 Poincaré surfaces of section

Figure 6.5 shows a few Poincaré surfaces of section for the circular star cluster orbit with Parameters given in Table 6.1. The upper row contains surfaces of section in the space of a phase portrait while the lower row shows the orbital structure in the configuration space, similar to Figure 3.2.

The left column of Figure 6.5 shows two Poincaré surfaces of section at a Jacobi energy deep in the potential well of the star cluster. The equipotential line corresponding to this Jacobi energy (which corresponds to the envelope of the lower surface of section in the left column of Figure 6.5) almost has a circular shape. The Poincaré surfaces of section at this Jacobi energy show that all orbits are regular and confined to invariant curves by a non-classical integral. Such a non-classical integral can usually be represented by a power series expansion where the lowest order is the angular momentum which would be exactly conserved if the system were spherical.

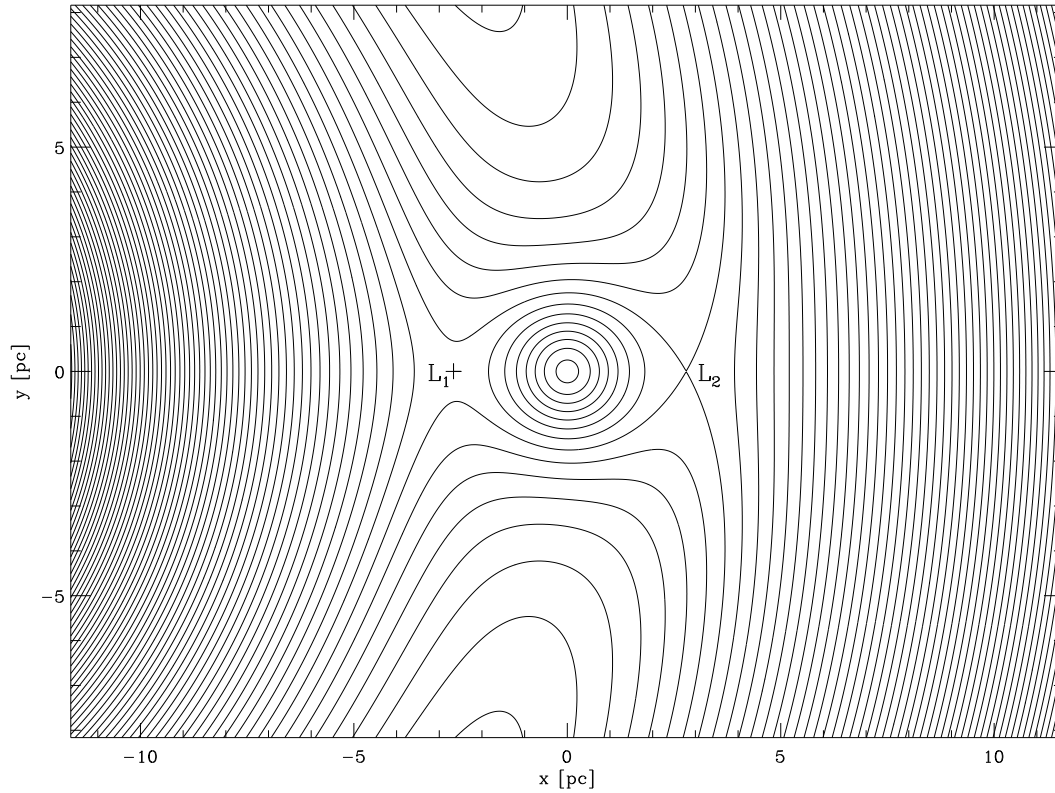


Figure 6.2: Zoom into the equipotential lines around the star cluster region of Figure 6.1. The star cluster center lies in the origin of coordinates and the Galactic center at $(x, y) = (-20 \text{ pc}, 0)$.

Since the system is in fact not exactly spherical, the angular momentum slightly oscillates around some value.

The middle column of Figure 6.5 shows two Poincaré surfaces of section at the Jacobi energy $E_J = E_J(L_2)$ which corresponds to the Lagrange point L_2 . The equipotential lines are open around L_1 and particles can escape towards the Galactic center. The phase space is divided between regular and chaotic regions.

The right column of Figure 6.5 shows two Poincaré surfaces of section at a Jacobi energy which is higher than the value of the effective potential at both Lagrange points L_1 and L_2 . The equipotential lines are wide open around L_1 and L_2 and particles can escape in both directions either into the leading or the trailing tidal arm. All orbits are chaotic.

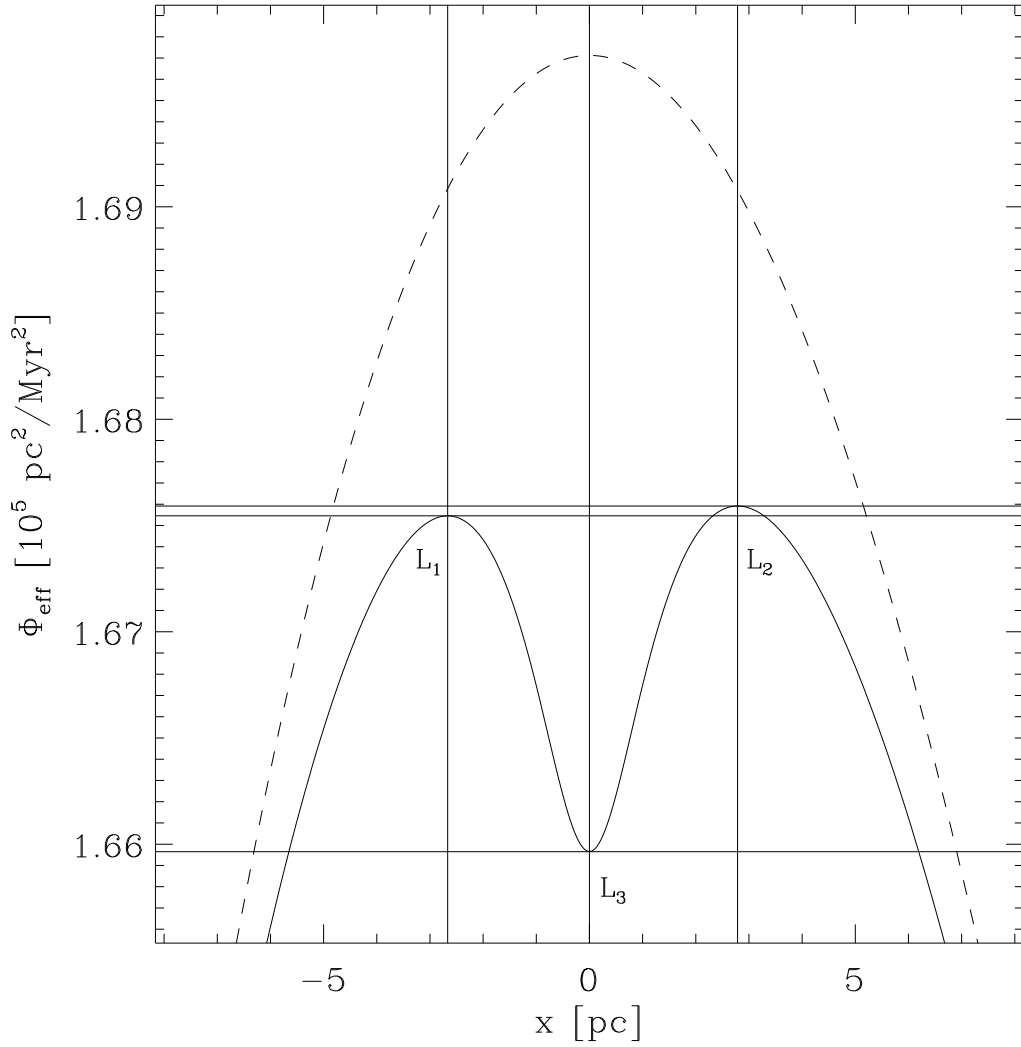


Figure 6.3: Zoom into the star cluster region of Figure 6.1 along the x axis with $y = 0$. The Galactic center lies at $x = -20$ pc. It can be seen that the Lagrangian points L_1 and L_2 lie at different energies and at different distances from the cluster center due to the asymmetry of the effective potential with respect to $x = 0$. The dashed line marks the effective tidal potential. The solid line is the full potential with the added contribution of the star cluster potential.

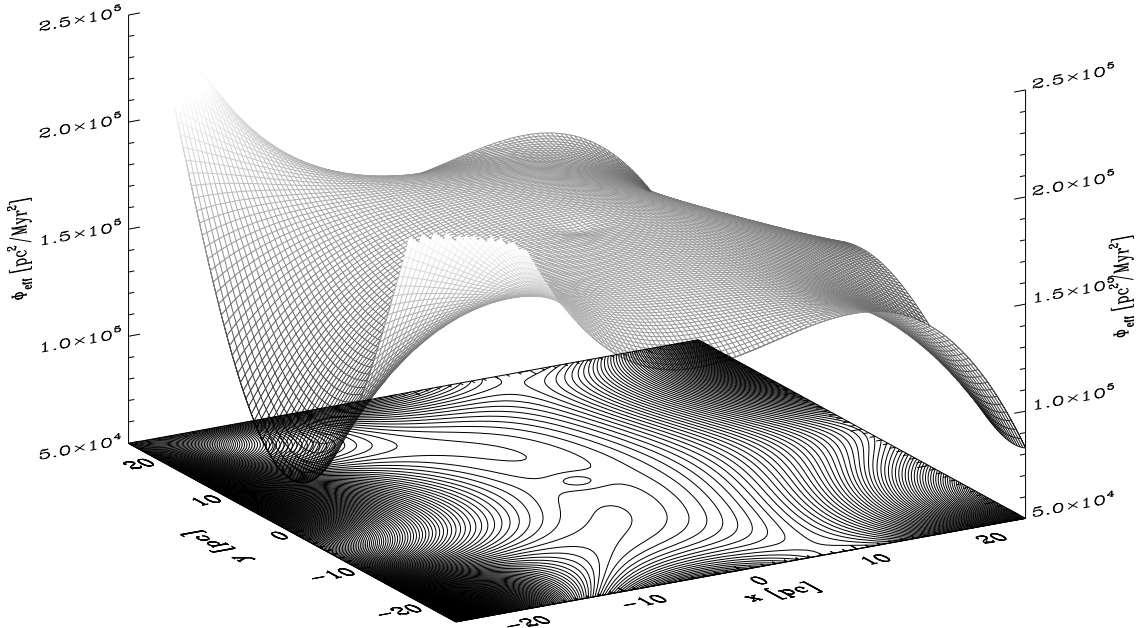


Figure 6.4: Taylor expansion (6.2) of the effective tidal potential for the scale free model up to the 5th order. The superposed star cluster potential has not been expanded in a Taylor series.

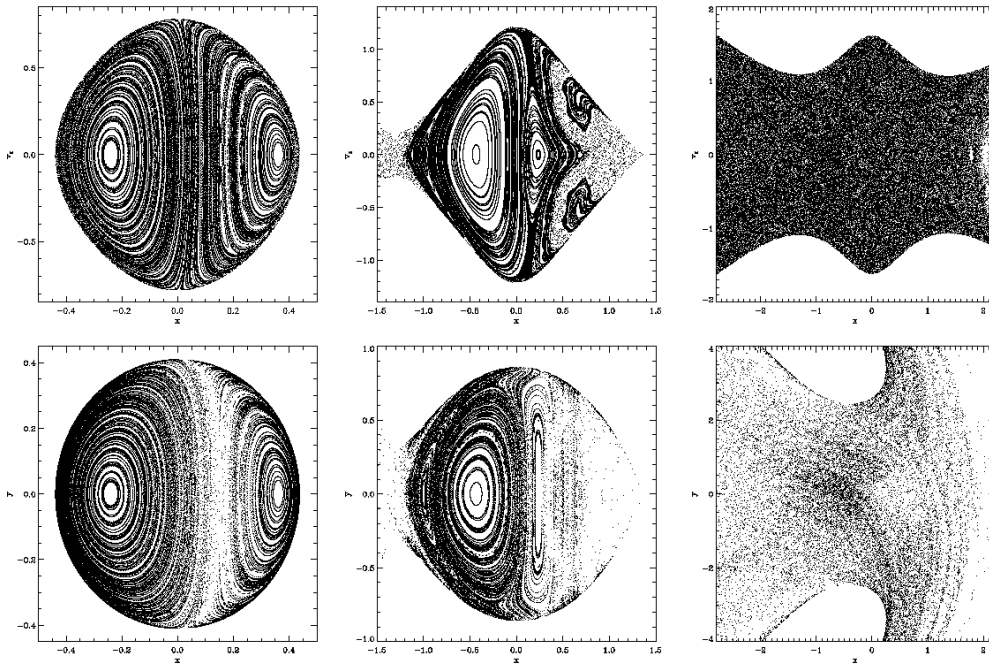


Figure 6.5: Poincaré surfaces of section. Left column: Deep in the potential well of the star cluster at $E_J = 1.66638e5 \text{ pc}^2/\text{Myr}^2$. Middle column: At $E_J = E_J(L_2)$. Right column: Above the Jacobi energies of L_1 and L_2 at $E_J = 1.68845e5 \text{ pc}^2/\text{Myr}^2$.

Chapter 7

Gravitational N -body models

7.1 The gravitational N -body problem

The gravitational N -body problem is a classical dynamical problem. That is, to find the solution of the system of $3N$ Newtonian equations of motion

$$\ddot{\mathbf{r}}_i = G \sum_{\substack{j=1 \\ j \neq i}}^N m_j \frac{\mathbf{r}_{ji}}{|\mathbf{r}_{ji}|^3}, \quad (7.1)$$

where N , G , $\mathbf{r}_{ji} = \mathbf{r}_j - \mathbf{r}_i$, m_j are the particle number, the gravitational constant, the relative position vector between the i th and j th particles and the mass of the j th particle, respectively.

As is known for a long time now, the system of ordinary differential equations (7.1) can, in general, only be solved numerically for $N > 2$. The pioneering works of Sebastian von Hoerner (1960 [170], 1963 [171]) at the Astronomisches Rechen-Institut (ARI) in Heidelberg opened up a whole field of computational N -body simulations of stellar systems. It was of much historical interest to the author that von Hoerner (1919-2003) was a doctoral student of Carl Friedrich von Weizsäcker (1912-2007) at the University of Göttingen and completed his PhD in 1951 [172]. He came to the ARI in 1957, where he completed his ‘Habilitation’ in 1959 on the rate of star formation [173]. At the same time, he began to solve the N -body problem on a Siemens 2002 during a visit at the University of Tübingen. As von Hoerner reports, the ARI had already ordered a Siemens 2002 but the waiting time was long. A historical review on the solution of the N -body problem with the first generation of computers and ‘How it all started’ can be found in von Hoerner (2001) [174]. In addition, a short historical treatise on the N -body problem with a special focus on the development of regularization techniques is given in Chapter 1 of Sverre Aarseth’s book [175]. Sverre Aarseth was a student of Fred Hoyle and continued von Hoerner’s work at the Institute of Astronomy in Cambridge (see Aarseth 1963 [176]) and dedicated his entire scientific life to the development of a series of highly efficient N -body programs (Aarseth 1999 [177], 2003 [175]). The latest computer program of Aarseth’s series, NBODY6, uses adaptive and individual time steps, which are organized in hierarchical block time steps, the Ahmad-Cohen neighbor scheme (Ahmad & Cohen 1973 [178]), Kustaanheimo-Stiefel regularization of close encounters (Kustaanheimo & Stiefel 1965 [179]) and Chain regularization (Mikkola & Aarseth 1990 [180], 1993 [181], 1996 [182], 1998 [183]). To describe the wealth of physical ideas which went into NBODY6 is beyond the scope of this thesis. NBODY6 has been adapted to massively parallel computer architectures by Rainer Spurzem (Spurzem 1999 [184]) using MPI routines. The parallel variant of NBODY6 has been called NBODY6++, and it is the basis of the code variant NBODY6GC which is used in this thesis.

N	t_{rh}/t_V	N	t_{rh}/t_V
1k	41	70k	1504
5k	152	100k	2067
10k	275	150k	2971
20k	500	200k	3847
30k	712	500k	8810
50k	1117	1M	16569

Table 7.1: Half-mass relaxation time t_{rh} in N -body time units t_V according to Equation (7.8) for $\gamma = 0.11$ in the Coulomb logarithm.

7.2 The scaling problem

On general purpose computer architectures which are available today it is not yet simply feasible to simulate the evolution of globular clusters with realistic particle numbers N , which may contain a few hundred thousands or even millions of stars. Thus, it is highly desirable to have a procedure to scale the results of low- N simulations up to higher particle numbers. In principle, theory provides means to solve this scaling problem. It is necessary to identify the underlying physical process and its dependence on the particle number N . For example, if the process proceeds on the dynamical (crossing) time scale t_{cr} , the related simulation results are independent of N . On the other hand, if the process proceeds on the relaxation time scale t_{rx} , the related simulation results need to be scaled, since

$$t_{rx} \propto \frac{N}{\ln(\gamma N)} t_{cr}. \quad (7.2)$$

The scaling problem becomes intricate, if a physical process depends on different time scales which scale differently with N . A few examples in stellar dynamics are

- The relaxation-driven escape process from star clusters. It proceeds in two stages: (1) A star is scattered into the escaping phase space on the relaxation time scale t_{rx} . (2) The star physically leaves the star cluster across the tidal radius on the dynamical (crossing) time scale t_{cr} . This process has been studied in the work by Baumgardt (2001) [47]. It turns out that the dissolution time should scale as $t_{dis} \propto t_{rh}^{3/4}$ for the special case of circular star cluster orbits in a steady tidal field.
- Accretion of stars onto supermassive black holes in galactic nuclei. There are two limiting cases: In the full loss cone (“pinhole”) regime accretion proceeds on the dynamical time scale t_{dyn} . In the empty loss cone (“diffusive”) regime the refilling of the loss cone proceeds on the relaxation time scale t_{rx} and the accretion rates are N -dependent. For a review of the theory see Porth (2007) [185]
- Dynamical effects of mass loss due to stellar evolution. Stellar evolution proceeds on the nuclear time scale $t_{nuc} \propto m_\star c^2/L$, where m_\star , c and L are the mass of the star, the speed of light and the luminosity, respectively. In the course of their evolution, the stars lose a significant fraction of their mass by a stellar wind (e.g. Prialnik 2000 [186]). This stellar mass loss has an influence on the dynamical evolution of star clusters which proceeds on the relaxation time scale t_{rx} .

7.3 N -body units

In the field of star cluster dynamics, dimensionless N -body units are frequently used. These are given by

$$G = M_{cl} = -4E = 1, \quad (7.3)$$

where G is the gravitational constant, M_{cl} is the total mass of the star cluster and E the total energy (Heggie & Mathieu 1986 [187]). The resulting length unit is the virial radius

$$r_V = -\frac{GM_{cl}^2}{4E}, \quad (7.4)$$

which is independent of the total mass of the system (because $E \propto M_{cl}^2$) and of the order of the half-mass radius of a star cluster (cf. Table 2.1 and Table 1 in Guerkan et al. 2004 [164]). The resulting time unit is then given by

$$t_V = \left(\frac{GM_{cl}}{r_V^3}\right)^{-1/2} = \frac{GM_{cl}^{5/2}}{(4|E|)^{3/2}}. \quad (7.5)$$

The half-mass relaxation time can be expressed in N -body units as follows. We have

$$t_{rh} = \frac{8\pi}{3} \frac{\left[\sqrt{2|E|/M_{cl}} r_V\right]^3 N}{15.4 G^2 M_{cl}^2 \ln(\gamma N)}. \quad (7.6)$$

with $\gamma = 0.11$ (Giersz & Heggie 1994 [188]). The above definition (7.6) is based on Equation (5) of the paper by Spitzer & Hart (1971) [189] with

$$n = \frac{3N}{8\pi r_V^3}, \quad v_m = \sqrt{\frac{2|E|}{M_{cl}}}, \quad m = \frac{M_{cl}}{N} \quad (7.7)$$

for the mean value of the particle density inside r_V , the root mean squared stellar velocity (i.e. the 3D velocity dispersion) and the mean stellar mass, respectively. In terms of t_V , (7.6) can therefore be written as

$$t_{rh} = \frac{2\sqrt{2}\pi N}{3 \cdot 15.4 \ln(\gamma N)} t_V. \quad (7.8)$$

In Table 7.1 a few values for the half-mass relaxation time t_{rh} are given in N -body time units t_V . The crossing time at the virial radius is given by $t_{cr} = 2r_V/v_m = 2\sqrt{2}t_V$.

7.4 Regularization

The idea of regularization will be briefly sketched in this section. We closely follow Aarseth 1971 [190], 1999 [177]. As two particles closely approach each other, the relative distance tends to vanish and the force goes to infinity. The adaptive time step becomes tiny and a large amount of the computing time would be required to integrate close encounters. This problem is solved by the KS regularization (Kustaanheimo & Stiefel 1965 [179]).

We introduce a time transformation

$$dt = |\mathbf{r}|d\tau \quad (7.9)$$

where $\mathbf{r} = (x, y, z, 0)$ is the relative physical separation vector between two particles with a vanishing fourth component and τ is a fictitious time. Furthermore, we introduce the Levi-Civita matrix,

$$\mathcal{L}(\mathbf{u}) = \begin{pmatrix} u_1 & -u_2 & -u_3 & u_4 \\ u_2 & u_1 & -u_4 & -u_3 \\ u_3 & u_4 & u_1 & u_2 \\ u_4 & -u_3 & u_2 & -u_1 \end{pmatrix} \quad (7.10)$$

The physical coordinates and velocities are obtained by the transformations

$$\mathbf{r} = \mathcal{L}(\mathbf{u})\mathbf{u} \quad (7.11)$$

$$\dot{\mathbf{r}} = \frac{2}{|\mathbf{r}|}\mathcal{L}(\mathbf{u})\mathbf{u}' \quad (7.12)$$

The fourth components of \mathbf{r} and $\dot{\mathbf{r}}$ are zero and the prime denotes differentiation with respect to τ . It turns out that

$$|\mathbf{r}| = u_1^2 + u_2^2 + u_3^2 + u_4^2 \quad (7.13)$$

The regularized equations of motion are given by

$$\mathbf{u}'' = \frac{h}{2}\mathbf{u} + \frac{|\mathbf{r}|}{2}\mathcal{L}^T(\mathbf{F}_i - \mathbf{F}_j), \quad (7.14)$$

where \mathbf{F}_i and \mathbf{F}_j are the perturbations from the stellar system on the two particles in physical units and h is the binding energy per unit mass,

$$h = [2\mathbf{u}' \cdot \mathbf{u}' - (m_i + m_j)]/|\mathbf{r}|, \quad (7.15)$$

where m_i and m_j are the masses of the two particles.

Chapter 8

Numerical methods

8.1 The computer program NBODY6GC

The computer program NBODY6GC which is used in this thesis is a variant of the N -body program NBODY6++ (Aarseth 1999 [177], 2003 [175], Spurzem 1999 [184]) which is suited for massively parallel computers.¹ The program NBODY6++ is a parallelized variant of the direct N -body program NBODY6 (Aarseth 1999 [177], 2003 [175]) for single-processor machines. A fourth-order Hermite scheme, applied first by Makino & Aarseth (1992) [191], is used for the direct integration of the $3N$ Newtonian equations of motion of the N -body system. It uses adaptive and individual time steps, which are organized in hierarchical block time steps, the Ahmad-Cohen neighbor scheme (Ahmad & Cohen 1973 [178]), Kustaanheimo-Stiefel (KS) regularization of close encounters (Kustaanheimo & Stiefel 1965 [179]) and Chain regularization (Mikkola & Aarseth 1990 [180], 1993 [181], 1996 [182], 1998 [183]).

8.1.1 Cluster orbit

In this thesis, the radii, velocities and accelerations related to the Galactic center will be denoted with capital letters and those related to the star cluster with small letters. Figure 8.1 shows the geometry of the problem: A star cluster is orbiting around the Galactic center. The potential in which the star cluster moves is the superposition of the Kepler potential of a super-massive black hole and a scale free potential of the central region of the Galactic bulge (cf. Section 2.2).² The two first-order equations of motion for the star cluster orbit read

$$\mathbf{V}_g(t) = \dot{\mathbf{R}}_g, \quad (8.1)$$

$$\dot{\mathbf{V}}_g(t) = -\nabla\Phi_g(|\mathbf{R}_g|) + \mathbf{A}_{df}, \quad (8.2)$$

where \mathbf{R}_g , \mathbf{V}_g , Φ_g and \mathbf{A}_{df} are the position vector, velocity vector, gravitational potential of the Galactic center region and deceleration due to dynamical friction and the dot denotes the derivative with respect to time. The equations of motion (8.1) and (8.2) for the star cluster orbit with respect to the Galactic center are solved using an 8th-order composition scheme (McLachlan 1995 [192]; for the idea see Yoshida 1990 [193]) with implicit midpoint method (e.g. Mikkola & Aarseth 2002 [194]), thereby including a realistic dynamical friction force. Although the symplectic composition schemes are by construction suited for Hamiltonian systems, they can be used for

¹The author remarks that NBODY6GC is based on a code variant called NBODY6TID which has been developed by R. Spurzem in collaboration with O. Gerhard and K.-S. Oh (unpublished). The author switched to another integrator for circular and very eccentric cluster orbits and improved the treatment of dynamical friction for studies in the Galactic center.

²The program NBODY6GC is written in a way that any analytical galactic potential can be implemented.

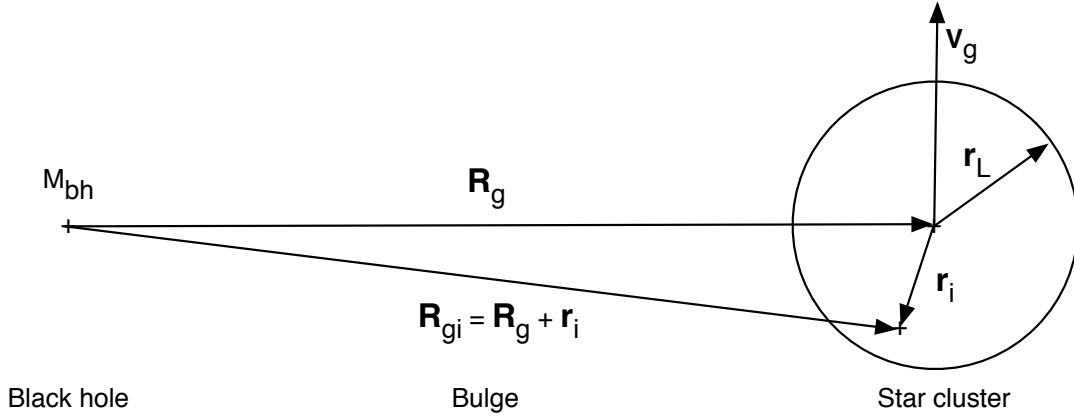


Figure 8.1: Sketch of the geometry of the problem in the galactocentric reference frame. The vector \mathbf{R}_g points from the Galactic center to the star cluster center. The vector \mathbf{r}_i points from the star cluster center to the position of the i th star. The orbital velocity of the star cluster has been denoted as \mathbf{V}_g and r_L is the tidal radius.

dissipative systems as well if the dissipative force is not too large. In our case, four iterations turned out to be sufficient to guarantee an excellent accuracy of the scheme.

We use a cluster membership criterion such that the dynamical friction force is based only on the total mass of the cluster members. We define a membership radius r_m by the condition

$$\bar{\rho}_{cl} = \frac{3M_{cl}(r_m)}{4\pi r_m^3} = \rho_g(R_g) \quad (8.3)$$

as the radius where the mean density $\bar{\rho}_{cl}$ in the star cluster is equal to the local bulge density at the cluster center which is located at radius R_g . This radius differs from the tidal radius r_L (King 1962 [86]) only by a factor of order unity. Stars within twice the membership radius as measured from the star cluster center are defined as cluster members.

8.1.2 Stellar orbits

On the other hand, the equations of motion for the orbits of stars in the star cluster are solved by the standard NBODY6/NBODY6++ routines using the 4th-order Hermite scheme (Makino & Aarseth 1992 [191]), KS or chain regularization including the full 3D tidal forces from the super-massive black hole and the Galactic bulge. The tidal force is added as a perturbation to the KS regularization. The following quantities are involved:

1. The specific force on the i th particle due to all other stars (cluster members and non-members) is given by

$$\mathbf{a}_i = G \sum_{\substack{j=1 \\ j \neq i}}^N m_j \frac{\mathbf{r}_{ji}}{|\mathbf{r}_{ji}|^3}, \quad (8.4)$$

where N , G , $\mathbf{r}_{ji} = \mathbf{r}_j - \mathbf{r}_i$, m_j are the particle number, the gravitational constant, the relative position vector between the i th and j th particles and the mass of the j th particle, respectively.

2. The specific force due to the Galactic center at the position of the cluster center is

$$\mathbf{A}_g = - \left(\frac{GC}{R_g^{2-\alpha}} + \frac{GM_{bh}}{R_g^2} \right) \frac{\mathbf{R}_g}{R_g}, \quad (8.5)$$

where C , M_{bh} and α are the normalization of the scale free bulge mass profile (see Section 2.2), the mass of the super-massive black hole and the cumulative mass profile power law index.

3. The specific force exerted on particle i due to the Galactic center is given by

$$\mathbf{A}_{gi} = - \left(\frac{GC}{R_{gi}^{2-\alpha}} + \frac{GM_{bh}}{R_{gi}^2} \right) \frac{\mathbf{R}_{gi}}{R_{gi}}, \quad (8.6)$$

4. The deceleration due to dynamical friction is given by

$$\mathbf{A}_{df} = - \frac{4\pi G^2 \rho_g M_{cl}}{V_g^2} \ln \Lambda \chi(V_g) \frac{\mathbf{V}_g}{V_g} \quad (8.7)$$

where ρ_g , M_{cl} , \mathbf{V}_g and V_g are the local bulge density at the position of the star cluster center, the star cluster mass and the velocity vector and modulus of the Galactic center, respectively. Furthermore, $\ln \Lambda$ is the Coulomb logarithm which results from the integral over impact parameters and $\chi(v_g) = \int_0^{V_g} f(v) d^3v$ is the result of the integration of the distribution function $f(v)$ of light particles over velocity space. For the Coulomb logarithm $\ln \Lambda$, the author uses according to Just & Peñarrubia (2005)

$$\ln \Lambda = \ln(b_1/b_0), \quad (8.8)$$

$$b_1^2 = b_0^2 + L^2, \quad b_0 = r_V, \quad L = \rho_g / |\nabla \rho_g| \quad (8.9)$$

where b_1 , b_0 , L are the maximum and minimum impact parameters and the local scale length of the bulge density profile, respectively, and $r_V = GM_{cl}^2 / (4|E_{cl}|) \approx r_h$ is the virial radius of the star cluster (where E_{cl} is the internal energy of the star cluster and r_h is the half-mass radius).

In the galactocentric reference frame, the total force on the i th particle would be given by

$$\mathbf{A}_{tot,i,gc} = \mathbf{a}_{i,gc} + \mathbf{A}_{gi,gc} + \mathbf{A}_{df,gc} \quad \text{members} \quad (8.10)$$

$$\mathbf{A}_{tot,i,gc} = \mathbf{a}_{i,gc} + \mathbf{A}_{gi,gc} \quad \text{non-members} \quad (8.11)$$

where the subscript “gc” denotes “galactocentric”. However, we choose the cluster rest frame as reference frame for our simulations. This is necessary, because Aarseth’s family of N -body programs is adapted to this reference frame and assumes that the cluster center is close to the origin of coordinates. This guarantees a sufficient accuracy of the Hermite scheme which is used for the orbit integration. On the other hand, this choice of the reference frame implies that the Galactic center is modelled as a pseudo-particle which orbits around the cluster center. We keep in mind that a transformation from the galactocentric frame to the cluster rest frame implies that \mathbf{r}_i , \mathbf{R}_g , \mathbf{V}_g and \mathbf{R}_{gi} in (8.4) - (8.7) change their sign. This implies that

$$\mathbf{a}_{i,cl} = -\mathbf{a}_{i,gc}, \quad \mathbf{A}_{g,cl} = -\mathbf{A}_{g,gc}, \quad (8.12)$$

$$\mathbf{A}_{gi,cl} = -\mathbf{A}_{gi,gc}, \quad \mathbf{A}_{df,cl} = -\mathbf{A}_{df,gc} \quad (8.13)$$

where the subscript “cl” denotes the cluster frame. It is then convenient for the force computations to transform to a reference frame in which the initial cluster center is force-free. Since this frame is accelerated, an apparent force

$$\mathbf{A}_{app} = -\mathbf{A}_{g,cl} - \mathbf{A}_{df,cl} \quad \text{memb.} \quad (8.14)$$

$$\mathbf{A}_{app} = -\mathbf{A}_{g,cl} \quad \text{non - memb.} \quad (8.15)$$

appears. In the accelerated cluster frame the total force on the i th particle is therefore given by

$$\mathbf{A}_{tot,i,acl} = -\mathbf{A}_{tot,i,gc} + \mathbf{A}_{app} \quad (8.16)$$

where the subscript “acl” denotes the accelerated cluster frame. Thus the second-order equations of motion for the orbits of the cluster stars read

$$\mathbf{A}_{tot,i,acl} = \mathbf{a}_{i,cl} + \mathbf{A}_{gi,cl} - \mathbf{A}_{g,cl} \quad \text{memb.} \quad (8.17)$$

$$\mathbf{A}_{tot,i,acl} = \mathbf{a}_{i,cl} + \mathbf{A}_{gi,cl} - \mathbf{A}_{g,cl} - \mathbf{A}_{df,cl} \quad \text{non - memb.} \quad (8.18)$$

It can be seen that in the accelerated cluster frame an individual star experiences only the differential tidal force between its own location and the cluster center.

A density center correction is applied in certain intervals to correct for the displacement of the density center (see Section 8.4). This was done in order to retain a consistent treatment of dynamical friction since the dynamical friction force is determined from the approximation that the star cluster mass is concentrated in the origin of coordinates.

8.2 Integrators

8.2.1 Hermite scheme

The Hermite scheme is a 4th-order predictor-corrector scheme applied first in Makino & Aarseth (1992) [191]. Positions and velocities of the i th particle are predicted according to

$$\mathbf{r}_{i,1}^p = \mathbf{r}_{i,0} + \mathbf{v}_{i,0}\Delta t + \frac{1}{2}\mathbf{a}_{i,0}\Delta t^2 + \frac{1}{6}\dot{\mathbf{a}}_{i,0}\Delta t^3, \quad (8.19)$$

$$\mathbf{v}_{i,1}^p = \mathbf{v}_{i,0} + \mathbf{a}_{i,0}\Delta t + \frac{1}{2}\dot{\mathbf{a}}_{i,0}\Delta t^2, \quad (8.20)$$

where the superscript “p” stands for “predicted” and the subscripts “0” and “1” for the current time t_0 and the following time t_1 , respectively. The acceleration $\mathbf{a}_{i,0}$ and jerk $\dot{\mathbf{a}}_{i,0}$ have been calculated from positions $\mathbf{r}_{i,0}$ and velocities $\mathbf{v}_{i,0}$ at time t_0 according to the analytical formulas

$$\mathbf{a}_i(t) = \sum_{\substack{j=1 \\ j \neq i}}^N Gm_j \frac{\mathbf{r}_{ji}}{r_{ji}^3} \quad (8.21)$$

$$\dot{\mathbf{a}}_i(t) = \sum_{\substack{j=1 \\ j \neq i}}^N Gm_j \left(\frac{\mathbf{v}_{ji}}{r_{ji}^3} - \frac{3(\mathbf{v}_{ji} \cdot \mathbf{r}_{ji})}{r_{ji}^5} \mathbf{r}_{ji} \right) \quad (8.22)$$

where $\mathbf{r}_{ji} = \mathbf{r}_j - \mathbf{r}_i$ and $\mathbf{v}_{ji} = \mathbf{v}_j - \mathbf{v}_i$ are relative positions and velocities between the i th and j th particles, respectively. Acceleration $\mathbf{a}_{i,1}^p$ and jerk $\dot{\mathbf{a}}_{i,1}^p$ at time t_1 can be calculated as well from the predicted positions (8.19) and velocities (8.20) using the analytical formulas (8.21) and (8.22).

A second way to write down $\mathbf{a}_{i,1}^p$ and $\dot{\mathbf{a}}_{i,1}^p$ approximately is by a Taylor series expansion which contains higher-order derivatives of acceleration:

$$\mathbf{a}_{i,1}^p = \mathbf{a}_{i,0} + \dot{\mathbf{a}}_{i,0}\Delta t + \frac{1}{2}\mathbf{a}_{i,0}^{(2)}\Delta t^2 + \frac{1}{6}\mathbf{a}_{i,0}^{(3)}\Delta t^3, \quad (8.23)$$

$$\dot{\mathbf{a}}_{i,1}^p = \dot{\mathbf{a}}_{i,0} + \mathbf{a}_{i,0}^{(2)}\Delta t + \frac{1}{2}\mathbf{a}_{i,0}^{(3)}\Delta t^2. \quad (8.24)$$

Since we know the quantities Δt , $\mathbf{a}_{i,0}$, $\dot{\mathbf{a}}_{i,0}$, $\mathbf{a}_{i,1}^p$ and $\dot{\mathbf{a}}_{i,1}^p$, we can solve the system of equations (8.23) – (8.24) to obtain the Hermite interpolation of the higher-order derivatives of acceleration:

$$\frac{1}{2}\mathbf{a}_{i,0}^{(2)} = -3\frac{\mathbf{a}_{i,0} - \mathbf{a}_{i,1}^p}{\Delta t^2} - \frac{2\dot{\mathbf{a}}_{i,0} + \dot{\mathbf{a}}_{i,1}^p}{\Delta t}, \quad (8.25)$$

$$\frac{1}{6}\mathbf{a}_{i,0}^{(3)} = 2\frac{\mathbf{a}_{i,0} - \mathbf{a}_{i,1}^p}{\Delta t^3} + \frac{\dot{\mathbf{a}}_{i,0} + \dot{\mathbf{a}}_{i,1}^p}{\Delta t^2}. \quad (8.26)$$

With these quantities, positions and velocities from the prediction step can be corrected to higher orders,

$$\mathbf{r}_{i,1}^c = \mathbf{r}_{i,1}^p + \frac{1}{24}\mathbf{a}_{i,0}^{(2)}\Delta t^4 + \frac{1}{120}\mathbf{a}_{i,0}^{(3)}\Delta t^5, \quad (8.27)$$

$$\mathbf{v}_{i,1}^c = \mathbf{v}_{i,1}^p + \frac{1}{6}\mathbf{a}_{i,0}^{(2)}\Delta t^3 + \frac{1}{24}\mathbf{a}_{i,0}^{(3)}\Delta t^4, \quad (8.28)$$

where the superscript "c" stands for "corrected".

8.2.2 Composition scheme

The idea of a composition scheme will be sketched in this section. We closely follow Yoshida (1990) [193]. For simplicity we assume that the phase space is only 2-dimensional and define Poisson brackets as

$$\{X, Y\} = \frac{\partial X}{\partial q} \frac{\partial Y}{\partial p} - \frac{\partial X}{\partial p} \frac{\partial Y}{\partial q}, \quad (8.29)$$

where q and p are position and momentum, respectively. We define operators with a hat as

$$\hat{Z} = \{\cdot, Z\}, \quad (8.30)$$

where \cdot denotes a placeholder. Furthermore, the dynamical vector is given by

$$\mathbf{z} = \begin{pmatrix} \mathbf{q} \\ \mathbf{p} \end{pmatrix}. \quad (8.31)$$

According to classical mechanics, its time evolution is governed by

$$\dot{\mathbf{z}} = \hat{H}\mathbf{z} \quad (8.32)$$

where H is the Hamiltonian of the system under consideration and the dot denotes differentiation with respect to time t , as usual. Note that (8.32) are the Hamiltonian equations of motion. Their solution is given formally by

$$\mathbf{z}(t) = \exp\left(t\hat{H}\right)\mathbf{z}(0) \quad (8.33)$$

where $\exp(t\hat{H})$ is called the “flow” and $\mathbf{z}(0)$ is the initial condition. We assume now that the Hamiltonian can be split in two parts,

$$H = T(p) + V(q), \quad (8.34)$$

where T and V are kinetic and potential energy, respectively, as usual. According to Yoshida (1990) [193] we can look for coefficients (c_1, c_2, \dots, c_k) and (d_1, d_2, \dots, d_k) such that the following equality holds,

$$\exp(t\hat{H}) = \exp(t(\hat{T} + \hat{V})) = \prod_{i=1}^k \exp(c_i t \hat{T}) \exp(d_i t \hat{V}) + \mathcal{O}(t^{n+1}) \quad (8.35)$$

where n is the order of the integrator. To find the coefficients (c_1, c_2, \dots, c_k) and (d_1, d_2, \dots, d_k) we use the Baker-Campbell-Hausdorff (BCH) identity: For any non-commutative operators X and Y , the product of their exponentials can be expanded as

$$\exp(X) \exp(Y) = \exp(Z) \quad (8.36)$$

where

$$\begin{aligned} Z \approx & X + Y + \frac{1}{2} [X, Y] + \frac{1}{12} ([X, X, Y] + [Y, Y, X]) + \frac{1}{24} [X, Y, Y, X] \\ & - \frac{1}{720} ([Y, Y, Y, Y, X] + [X, X, X, X, Y]) + \frac{1}{360} ([Y, X, X, X, Y] + [X, Y, Y, Y, X]) \\ & + \frac{1}{120} ([X, X, Y, Y, X] + [Y, Y, X, X, Y]) + \dots \end{aligned} \quad (8.37)$$

and where the single and multiple commutators are defined as $[X, Y] = XY - YX$ and $[X, X, Y] = [X, [X, Y]]$, respectively.

By repeated application of the BCH identity (8.36) – (8.37) one obtains

$$\exp(X) \exp(Y) \exp(X) = \exp(Z') \quad (8.38)$$

where

$$\begin{aligned} Z' \approx & 2X + Y + \frac{1}{6} ([Y, Y, X] - [X, X, Y]) + \frac{7}{360} [X, X, X, X, Y] - \frac{1}{360} [Y, Y, Y, Y, X] \\ & + \frac{1}{90} [X, Y, Y, Y, X] + \frac{1}{45} [Y, X, X, X, Y] - \frac{1}{60} [X, X, Y, Y, X] \\ & + \frac{1}{30} [Y, Y, X, X, Y] + \dots \end{aligned} \quad (8.39)$$

It is of interest to note that only odd orders in X and Y occur in (8.39). If we set $k = 2$ in the equality (8.35) and use (8.38) – (8.39) we immediately recover the 2nd-order leapfrog integrator with the coefficients $c_1 = c_2 = 1/2, d_1 = 1, d_2 = 0$, i.e. we have

$$\exp(t\hat{H}) = \exp\left(t\left(\hat{T} + \hat{V}\right)\right) = \exp\left(\frac{1}{2}t\hat{T}\right) \exp(t\hat{V}) \exp\left(\frac{1}{2}t\hat{T}\right) + \mathcal{O}(t^3) \quad (8.40)$$

We define the operator for the 2nd-order integrator as

$$S_2(t) = \exp\left(\frac{1}{2}t\hat{T}\right) \exp(t\hat{V}) \exp\left(\frac{1}{2}t\hat{T}\right) \quad (8.41)$$

$$\approx \exp(t\alpha_1 + t^3\alpha_3 + t^5\alpha_5 + \dots) \quad (8.42)$$

No.	Value	No.	Value
w_1	0.74167036435061295345	w_9	w_7
w_2	-0.40910082580003159400	w_{10}	w_6
w_3	0.19075471029623837995	w_{11}	w_5
w_4	-0.57386247111608226666	w_{12}	w_4
w_5	0.29906418130365592384	w_{13}	w_3
w_6	0.33462491824529818378	w_{14}	w_2
w_7	0.31529309239676659663	w_{15}	w_1
w_8	$1 - 2 \sum_{i=1}^7 w_i$		

Table 8.1: Coefficients by McLachlan (1995) [192] of the 8th-order composition scheme.

where the second line follows from (8.38) – (8.39) and

$$\alpha_1 = \hat{T} + \hat{V}, \quad (8.43)$$

$$\alpha_3 = \frac{1}{12} [\hat{V}, \hat{V}, \hat{T}] - \frac{1}{24} [\hat{T}, \hat{T}, \hat{V}], \quad (8.44)$$

$$\alpha_5 = \frac{7}{5760} [\hat{T}, \hat{T}, \hat{T}, \hat{T}, \hat{V}] + \dots \quad (8.45)$$

A 4th-order integrator can then be obtained by applying formulas (8.38) – (8.39) on a symmetric repetition of the expansion (8.42) of the 2nd-order integrator,

$$S_4(t) = S_2(k_1 t) S_2(k_0 t) S_2(k_1 t) \quad (8.46)$$

where we include terms up to 3rd-order. Note that the determining equations for the coefficients k_1 and k_0 become non-linear. In the same way, symplectic integrators of arbitrary even order can be obtained. Coefficients for composition schemes of different orders can be found in Yoshida (1990) [193], Suzuki 1990 [195], McLachlan (1995) [192], Kahan & Li (1997) [196] or in the review by Sutmann (2006) [197]. We use in this thesis the coefficients obtained by McLachlan (1995) [192] for an 8th-order composition scheme. The coefficients are given in Table 8.1.

8.2.3 Implicit midpoint method

Symplectic integrators are by construction suited for Hamiltonian systems. However, they may also be used for dissipative systems if the dissipative force is not too large. Following the suggestion in Mikkola & Aarseth (2002) [194] the author implemented a velocity-dependant friction force (i.e., dynamical friction) into the composition scheme. The differential equations have the form

$$\dot{\mathbf{X}} = \mathbf{V}, \quad \dot{\mathbf{V}} = -\nabla\Phi + \mathbf{f}(\mathbf{V}) \quad (8.47)$$

where \mathbf{X} , \mathbf{V} , Φ are position, velocity and potential, respectively, and $\mathbf{f}(\mathbf{V})$ is a velocity-dependent force. These can be solved by the implicit midpoint method:

$$\mathbf{V}_1 = \mathbf{V}_0 + \Delta t (-\nabla\Phi + \mathbf{f}(\mathbf{V}_a)), \quad \mathbf{V}_a = \frac{\mathbf{V}_0 + \mathbf{V}_1}{2} \quad (8.48)$$

where the subscripts “0” and “1” refer to the current time t_0 and the following time t_1 , respectively. The method is implicit in the following sense: The “kick” step in velocity uses a force which depends implicitly on the velocity at the end of the “kick” step (which is not yet known). This force can be approximately obtained by a fixed point iteration. In our application, four iterations turned out to be sufficient.

```
1 DO WHILE (TIME.GE.TCEN)
2 DO I=1,15 !Loop over composition coefficients
3 DTCEN = .5D0*W0COEFF(I) !half step
4 DO K=1,3
5 XG(K) = XG(K) + DTCEN*VG(K)
6 ENDDO
7 DO J=1,4 !Iteration (implicit midpoint method)
8 DO K=1,3
9 VA(K) = VG(K) + DTCEN*AG(K)
10 ENDDO
11 CALL GCFORCE(XMCL,XG,VA,AG,AGNEWT,AGFRIC,TMP3)
12 ENDDO
13 TCEN = TCEN + DTCEN
14 DTCEN = W0COEFF(I) !full step
15 DO K=1,3
16 VG(K) = VG(K) + DTCEN*AG(K)
17 DEFRIC = DEFRIC - DTCEN*XMCL*AGFRIC(K)*VA(K)
18 ENDDO
19 DTCEN = .5D0*W0COEFF(I) !half step
20 DO K=1,3
21 XG(K) = XG(K) + DTCEN*VG(K)
22 ENDDO
23 TCEN = TCEN + DTCEN
24 ENDDO
25 ENDDO !while
```

Listing 8.1: Code fragment containing the integrator.

8.3 Energy balance

8.3.1 Friction and mass loss

The energy of a mass losing star cluster orbiting in a spherically symmetric time-independent potential $\Phi = \Phi(|\mathbf{R}|)$ is given by

$$E = \frac{1}{2}M_{cl}(t)\mathbf{V}^2(t) + M_{cl}(t)\Phi \quad (8.49)$$

where t is time, M_{cl} is the cluster mass and \mathbf{R} and \mathbf{V} the position and velocity of the cluster center, respectively. We use the real energy, not the specific energy. Then we have

$$\dot{E} = \frac{1}{2}\dot{M}_{cl}\mathbf{V}^2 + M_{cl}\mathbf{V} \cdot \dot{\mathbf{V}} + \dot{M}_{cl}\Phi + M_{cl}(\nabla\Phi) \cdot \mathbf{V} \quad (8.50)$$

$$= \frac{\dot{M}_{cl}}{M_{cl}}E + M_{cl}\mathbf{V} \cdot \mathbf{A}_{df}, \quad (8.51)$$

where the dot denotes differentiation with respect to time t and we have inserted the equation of motion (8.2) in the last step. The energy change is therefore given by

$$dE = \dot{E}dt = E d\ln(M_{cl}) + M_{cl}\mathbf{V} \cdot \mathbf{A}_{df} dt. \quad (8.52)$$

8.3.2 Energy checking

The energy check in NBODY6GC is done in the galactocentric reference frame. The energy of the N -body system in the tidal field has different terms. We define

$$E_{\text{kin}} = \frac{1}{2} \sum_{i=1}^N m_i \mathbf{v}_i^2 \quad (8.53)$$

$$E_{\text{pot}} = \frac{1}{2} \sum_{i=1}^N m_i \Phi_{i,\text{int}} \quad \text{with} \quad \Phi_{i,\text{int}} = -G \sum_{\substack{j=1 \\ j \neq i}}^N \frac{m_j}{|\mathbf{r}_i - \mathbf{r}_j|} \quad (8.54)$$

$$E_{g,\text{kin}} = \frac{1}{2} \sum_{i=1}^N m_i \mathbf{V}_g^2 \quad (8.55)$$

$$E_{g,\text{mixed}} = \sum_{i=1}^N m_i \mathbf{v}_i \cdot \mathbf{V}_g \quad (8.56)$$

$$E_{g,\text{pot}} = \sum_{i=1}^N m_i \Phi_{i,\text{ext}} \quad (8.57)$$

$$\Delta E_{\text{fric}} = \sum_{i=1}^N \int_0^t m_i \mathbf{A}_{df} \cdot (\mathbf{V}_g + \mathbf{v}_i) dt' \quad (8.58)$$

where m_i , \mathbf{v}_i , \mathbf{V}_g , $\Phi_{i,\text{int}}$, $\Phi_{i,\text{ext}}$, t and a_{df} are the particle mass, the internal velocity, the velocity of the Galactic center pseudo particle, the internal potential of the N -body system, the external potential of the Galactic center region, the evolution time and the deceleration due to dynamical friction. We define

$$E_{\text{int}} = E_{\text{kin}} + E_{\text{pot}} \quad (8.59)$$

$$E_{\text{tide}} = E_{g,\text{kin}} + E_{g,\text{mixed}} + E_{g,\text{pot}} - E_{\text{tide},0} \quad (8.60)$$

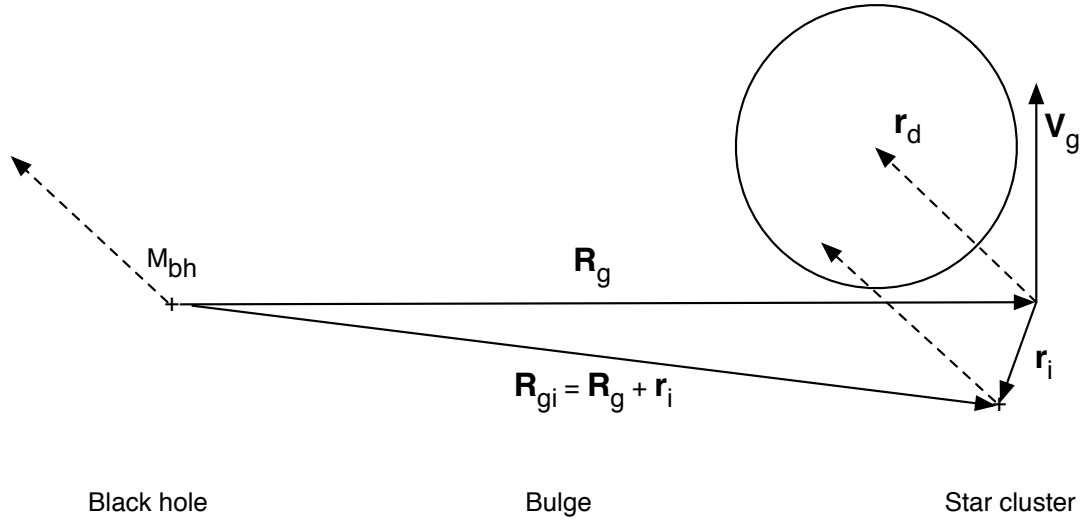


Figure 8.2: Sketch of the density center correction. The new density center of the star cluster has been denoted as \mathbf{r}_d .

where $E_{\text{tide},0}$ is a normalization such that the tidal energy E_{tide} vanishes in the beginning. The total energy is then given by

$$E_1 = E_{\text{int}} + E_{\text{tide}} \quad (8.61)$$

On the other hand, the orbital energy E_2 of the star cluster in the galactocentric reference frame is given by

$$E_2 = \frac{1}{2} M_{cl} \mathbf{V}_g^2 + M_{cl} \Phi_{ext}(|\mathbf{R}_g|) + \int_0^t M_{cl} \mathbf{A}_{df} \cdot \mathbf{V}_g dt' + \int_0^t \frac{\dot{M}_{cl}}{M_{cl}} E_2 dt' \quad (8.62)$$

where the last two terms on the right-hand side are due to dynamical friction and tidal mass loss of the star cluster, respectively (see Section 8.3.1).

Both energies E_1 and E_2 are checked at regular intervals for conservation.

8.4 Density center correction

The program NBODY6GC applies a density center correction in certain intervals. The origin of coordinates $(0, 0, 0)$ is translated back into the density center \mathbf{r}_d of the star cluster. This was done in order to retain a consistent treatment of the dynamical friction force which is determined from the approximation that the star cluster mass is concentrated in the origin of coordinates of the star cluster rest frame. Our routine is based on the routine `cmcorr` of NBODY6 (Aarseth 1999 [177], 2003 [175]). It proceeds as follows

1. Calculate the position of the density center \mathbf{r}_d (using the method by Casertano & Hut 1985 [198]).
2. Transform all positions \mathbf{r}_i , \mathbf{R}_g and \mathbf{R}_{gi} (cf. Section 8.1) to the density center frame.
3. Re-determine all former positions and velocities consistently.
4. Resolve all regularized pairs for consistency.

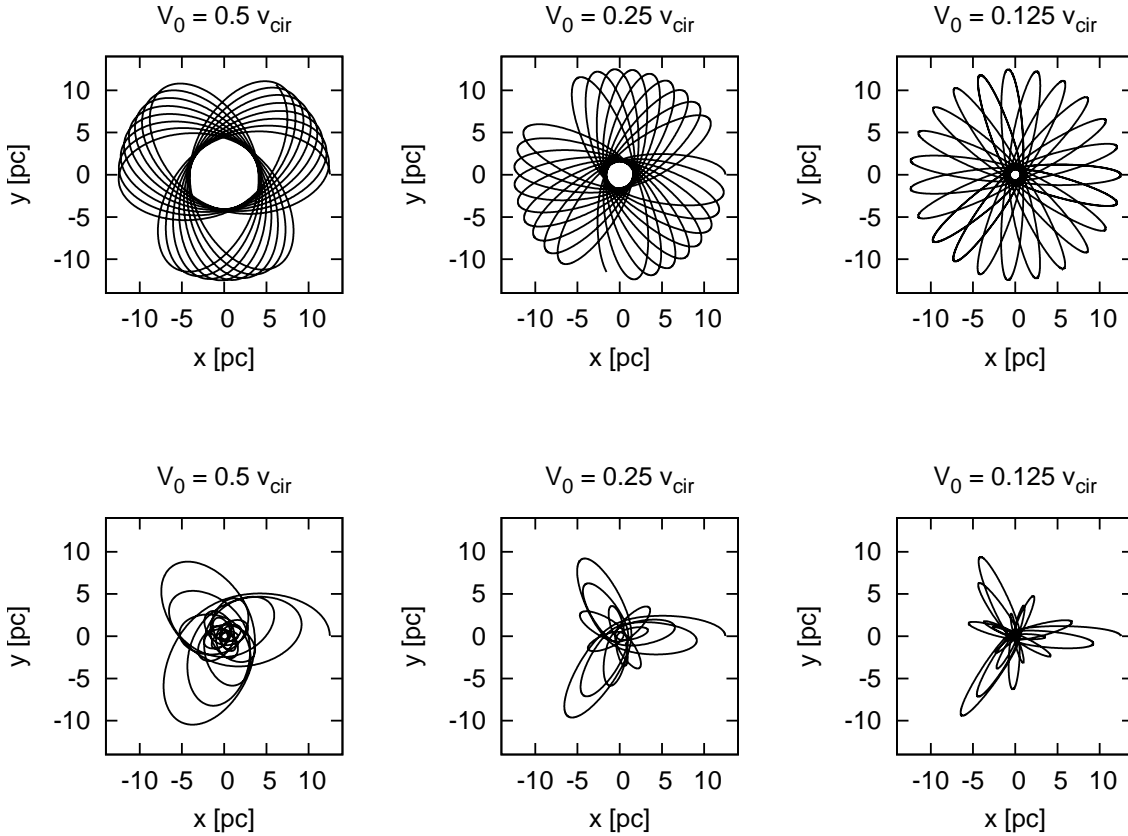


Figure 8.3: Examples of star cluster orbits of different eccentricities close to the Galactic center (integrated with INTGC). For each orbit the initial velocity is given in units of the circular velocity at the initial galactocentric radius. Top row: Without dynamical friction. Bottom row: With dynamical friction.

We remark that all galactocentric distances of the stars and the distances between the individual stars remain invariant under the density center correction. A correction with respect to the velocity of the density center turned out not to be necessary.

8.5 The computer program INTGC

The author developed the integrator INTGC whose functionality is identical to the integrator for the star cluster orbit in NBODY6GC. It uses as well the 8th-order composition scheme with implicit midpoint method (see Sections 8.2.2 and 8.2.3). However, since it does not solve the N -body problem for the star cluster but only the equations of motion (8.1) and (8.2) for the star cluster orbit around the Galactic center, it is very simple and fast. The program INTGC has been used to

1. Test the star cluster orbit integration in NBODY6GC.
2. Explore the parameter space.
3. Determine orbital and dynamical friction time scales numerically.

Figure 8.3 shows a few examples of star cluster orbits close to the Galactic center which have been integrated with INTGC. The top row shows how the orbit would look like without dynamical friction while the bottom row shows the effect of a dynamical friction force on the orbit.

8.6 Tidal arm coordinate system

Based on routines from Numerical Recipes (NR, Press et al. 2001 [199]), the author developed the eigensolver `EIGENTID` which calculates numerically a 1D coordinate system along the tidal arms and evaluates characteristic dynamical quantities along this coordinate system. We denote the coordinate along the tidal arms as w , where negative values refer to the leading arm and positive values to the trailing arm. The NR routine `tred2` uses the Householder reduction of a real symmetric $n \times n$ matrix to convert it to a tridiagonal form. The NR routine `tqli` uses the QL algorithm to determine the eigenvalues and eigenvectors of the matrix which has been brought into tridiagonal form before (see NR, Chapters 11.2 and 11.3). We use the tensor of inertia and denote the eigenvectors corresponding to the minimum eigenvalue c , the medium eigenvalue b and the maximum eigenvalue a as the minimum, medium and maximum eigenvectors, respectively. Then the algorithm proceeds as follows:

1. Read snapshot with particle masses, positions and velocities in the cluster rest frame.
2. Calculate optionally gravitational potential and density (using the method by Casertano & Hut 1985) for this snapshot.
3. Start calculation in the origin of coordinates $(0, 0, 0)$.
4. Obtain a neighbor sphere with radius R_{cut} and calculate its center of mass (x_{cm}, y_{cm}, z_{cm}) .
5. Calculate physical quantities averaged over the neighbor sphere: Mean specific angular momentum, mean specific energy, mean density, velocity dispersion, mean potential. Write all quantities to a data file.
6. Calculate the tensor of inertia of the neighbor sphere with respect to the center of mass of the neighbor sphere. It is given by

$$\Theta_{jk} = \sum_{i=1}^{N_{nb}} m_i \begin{pmatrix} \Delta y_i^2 + \Delta z_i^2 & \Delta x_i \Delta y_i & \Delta x_i \Delta z_i \\ \Delta x_i \Delta y_i & \Delta x_i^2 + \Delta z_i^2 & \Delta y_i \Delta z_i \\ \Delta x_i \Delta z_i & \Delta y_i \Delta z_i & \Delta x_i^2 + \Delta y_i^2 \end{pmatrix} \quad (8.63)$$

where $\Delta x_i = x_i - x_{cm}$, $\Delta y_i = y_i - y_{cm}$ and $\Delta z_i = z_i - z_{cm}$ are the relative positions of the i th particle in the neighbor sphere with respect to its center of mass and m_i is the mass of the i th particle.

7. Calculate the eigenvalues and eigenvectors of Θ_{jk} .
8. Go along the direction of the maximum/medium eigenvector until a critical density is reached to find the new R_{cut} .
9. Check for acute angle between previous and current minimum eigenvector. If the angle is acute, change the sign of the eigenvector.
10. Go one step along the direction of the minimum eigenvector.
11. Repeat from 4. until the particle number within the neighbor sphere drops below a certain threshold as the first tidal arm ends.
12. Start from 3. for the second tidal arm.

We remark that the inertia ellipsoids of the neighbor spheres have an oblate shape, i.e. the three eigenvalues a, b, c of Θ_{jk} satisfy $a \approx b > c$. Also, a weighting exponent can be assigned to the particle mass in the expression (8.63). In this case, the eigensolver follows the mass distribution within the tidal arms in a different way. This method has been applied for Figure 9.11.

Chapter 9

Simulations

9.1 A test case

The left panel of Figure 9.1 shows the orbit of the test case model E1 which has been integrated for $t_{\text{int}} = 12$ Myr with the integrator INTGC and then with the large N -body program NBODY6GC until the dissolution time $t_{\text{dis}} \approx 1.1$ Myr was reached (which turned out to be much shorter than t_{int}). The orbit for the model E1 is a rosette orbit with an initial galactocentric radius of $R_g(0) = 20$ pc which decays due to dynamical friction. The initial velocity has been taken to be $V_g(0) = 0.5 V_c(R_g(0))$, where V_c is the circular velocity. For the star cluster a King model with $W_0 = 6$ and a half-mass radius of $r_h = 1.64$ pc has been adopted. The particle number is $N = 5 \times 10^4$. The distribution of masses m_i is given by a Kroupa (1993) [201] initial mass function with $0.01M_\odot \leq m_i \leq 120M_\odot$. Throughout this chapter the parameters of the scale free model of the central region of the Galactic bulge are the same as in Table 6.1 in Chapter 6. The decay of the orbit due to dynamical friction with the modified Coulomb logarithm according to Equations (8.8) - (8.9) is rather slow as compared with the dissolution time scale. Assuming a constant star cluster mass, the apocenter radius reaches half of its initial value at $t_{df, \text{hapo}} = 6.21$ Myr and the orbit approaches the central parsec at $t_{df, 1\text{pc}} = 10.4$ Myr. At that time, the cluster has already dissolved in the tidal field for a long time. We note that the orbit of the real N -body simulation differs from that of Figure 9.1. In NBODY6GC, the calculation of the dynamical friction force is based on the mass of the particles which are contained in a sphere with a radius which equals twice the membership radius r_m of Equation (8.3). On the other hand, the star cluster mass stays constant in the orbit computation with INTGC.

Figure 9.2 shows the dissolution of the star cluster in the N -body simulation of model E1 as snapshots at different times. The color coding is according to the logarithm¹ of the stellar density in units of M_\odot/pc^3 . The rosette orbit is marked as a solid line. In the second row one can see a bifurcation in the trailing tidal arm. Probably it is due to the eccentricity of the orbit. The inner branch of the bifurcation may be related to the apocenter passage of the star cluster while the outer branch may be related to the pericenter passage. The leading tidal arm wraps around the Galactic center. However, it can be seen that the stars do not reach the central parsec in the snapshots which are shown in the figure. The star cluster orbit is not eccentric enough and the dynamical friction force too weak due to small values of the Coulomb logarithm.

Figure 9.3 shows the time evolution of the dynamical friction variables for the N -body simulation with NBODY6GC. The quantities R_g , V_g , ρ_g , χ and $\ln \Lambda$ are the current Galactocentric radius, the orbital velocity of the star cluster, the local Galactic density, the χ function and the Coulomb logarithm, respectively. All quantities oscillate on the orbital time scale of the eccentric cluster orbit. For the definition of the χ function and the Coulomb logarithm see Appendix D. The χ

¹to the base 10

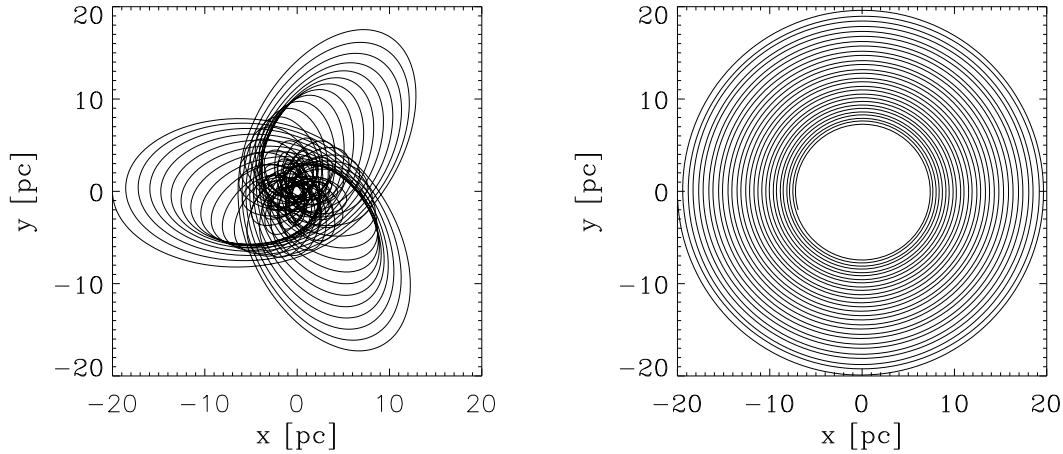


Figure 9.1: Star cluster orbits integrated with INTGC for 12 Myr. Both orbits decay due to dynamical friction with a Coulomb logarithm based on Just & Peñarrubia (2005) [200]. Left panel: For the eccentric orbit of the example model E1. Right panel: For the circular orbit of the model C9 (see next sections). The star cluster mass is $M_{cl} = 10^6 M_{\odot}$ in both cases. The rosette orbit in the left panel decays faster as compared with the circular orbit in the right panel since the dynamical friction force is stronger in the pericenter than in the apocenter.

function takes on values between 0 and 1 as in Figure D.3. The Coulomb logarithm roughly varies between 1.7 and 0.7. We have also plotted the product $\rho_g \chi \ln \Lambda$ which is the relevant quantity for dynamical friction. It oscillates with the orbital frequency between approximately two orders of magnitude.

At $t \approx 1.1$ Myr the density center of the star cluster is no longer clearly defined and the evolution of the dynamical variables in Figure 9.3, in particular R_g , becomes noisy. The density center correction breaks down which indicates that the end of the simulation has been reached.²

The top panel of Figure 9.4 shows the time evolution of the core radius, the membership radius of Equation (8.3) and a few Lagrangian radii for the model E1. The core radius is defined as

$$r_c = \sqrt{\frac{\sum_{i=1}^{\tilde{N}} |\mathbf{r}_i - \mathbf{r}_d|^2 \rho_i^2}{\sum_{i=1}^{\tilde{N}} \rho_i^2}} \quad (9.1)$$

where \mathbf{r}_i is the position of the i th particle, \mathbf{r}_d is the position of the density center and ρ_i is the stellar density at \mathbf{r}_i calculated from the distance to the fifth nearest neighbor (Casertano & Hut 1985 [198]). Note that the summation is only over \tilde{N} particles within a certain cutoff radius. The Lagrangian radii are defined as the radii of spheres which contain a fraction of the total mass of all stars in the simulation. The outer Lagrangian radii expand due to the formation of tidal arms. The core of the star cluster collapses due to heat transport from the core to the halo. As is well known, the reason for the heat transport is two-body relaxation. For the theory of the gravothermal instability, which leads to the core collapse of star clusters we refer to the original works of Antonov (1962) [202], Lynden-Bell & Wood (1968) [203] and Hachisu et al. (1978a [204]/b [205]). It is nowadays also described in many textbooks such as Binney & Tremaine 1987 [32] or Heggie &

²We can use the fact that the density center correction breaks down at some point in time as the criterion for the dissolution of the star cluster: When the evolution of certain dynamical variables (e.g. those shown in Figure 9.3) becomes noisy the dissolution time scale has been reached.

Hut (2003) [206]. The core collapse is stopped by the formation of a few binaries in the core of the star cluster by three-body processes (Giersz & Heggie 1994b [207], 1996 [208]). These produce heat at a rate slightly higher than the rate of energy loss due to two-body relaxation, thereby cooling the cluster core which has negative heat capacity. The bottom panel of Figure 9.4 shows that the number of regularized pairs in the N -body simulation increases as the core of the star cluster collapses.

Figures 9.5 and 9.6 show the time evolution of energies for the model E1. In Figure 9.5, the total energy is splitted into different terms. The definitions of the different terms of the energy balance are given in Section 8.3.2 (in Chapter 8). E'_{kin} and E'_{pot} are the internal kinetic and potential energies of the N -body system, where every regularized pair is represented by a single center of mass particle. Its mass is given by the sum of both individual masses and its position by the center of mass of the regularized pair. E_{bin} is then the binding energy of all regularized pairs based on Equation (7.15).³ The time evolution of E'_{kin} shows the effect of tidal heating, since the time evolution of E_{tide} follows that of E'_{kin} closely after the first pericenter passage. On the other hand, the time evolution of E'_{pot} shows that the potential well of the star cluster gets shallower as the cluster dissolves. E_{tide} is the tidal energy. Its different terms will be discussed below. $E_1 = E_{\text{bin}} + E_{\text{kin}} - E_{\text{pot}} + E_{\text{tide}}$ is the total energy. It is slightly deviating from the value $E_1 = -0.25$. The reason is an energy scale problem. The physical situation of a star cluster orbiting in the tidal field of a galaxy has two energy scales which are of different orders: The internal cluster energy of the N -body problem and the external energy of the star cluster orbit in the tidal field. Tidal heating can convert external potential energy into internal kinetic energy. Therefore the energy balance above contains terms of different orders of magnitude. The energy of the cluster orbit is $E_2 = 87.2584$ (cf. Section 8.3.2). If we normalize to this energy, we obtain an average energy error of $\Delta E_1/E_2 \approx 2 \times 10^{-4}$ per crossing time while $\Delta E_1/E_1 \approx 0.06$ per crossing time for all (!) particles. The large contributions to the energy error are due to the particles in the tidal arms. The energy error is lower for the particles which are deep in the potential well of the star cluster and which are not subject to strong tidal forces. Figure 9.4 shows that the numerical error of the integration does not suppress two-body relaxation within the star cluster.

In Figure 9.6, the tidal energy E_{tide} is splitted into its different terms. $E_{\text{g,kin}}$ is the orbital kinetic energy of the Galactic center particle. It oscillates with the orbital frequency within a range of approximately two orders of magnitude, since it scales as the square of the orbital velocity (which is shown in in Figure 9.3). $E_{\text{g,mixed}}$ is the mixed kinetic energy term. The increase of its modulus is only marginal in the beginning. Then the increase becomes significant, and one can see oscillations with the orbital frequency. $E_{\text{g,pot}}$ is the external potential energy term. It slightly oscillates with the orbital frequency. ΔE_{fric} is the energy loss due to dynamical friction. Its modulus increases marginally until the first pericenter has been reached. Then, the increase becomes significant but is rather slow. $E_{\text{tide}} = E_{\text{g,kin}} + E_{\text{g,mixed}} + E_{\text{g,pot}} - E_{\text{tide},0}$ is the total tidal energy.

Figure 9.7 shows the relative energy error $\Delta E_2/E_2$ of the cluster orbit integration. Its absolute value stays below 10^{-13} .

³The author neglected the splitting of the internal cluster energy in the energy of the center of mass particles and the binding energy of the regularized pairs in Section 8.3.2 for the sake of clarity. However, it is an internal feature of NBODY6 on which NBODY6CC is based.

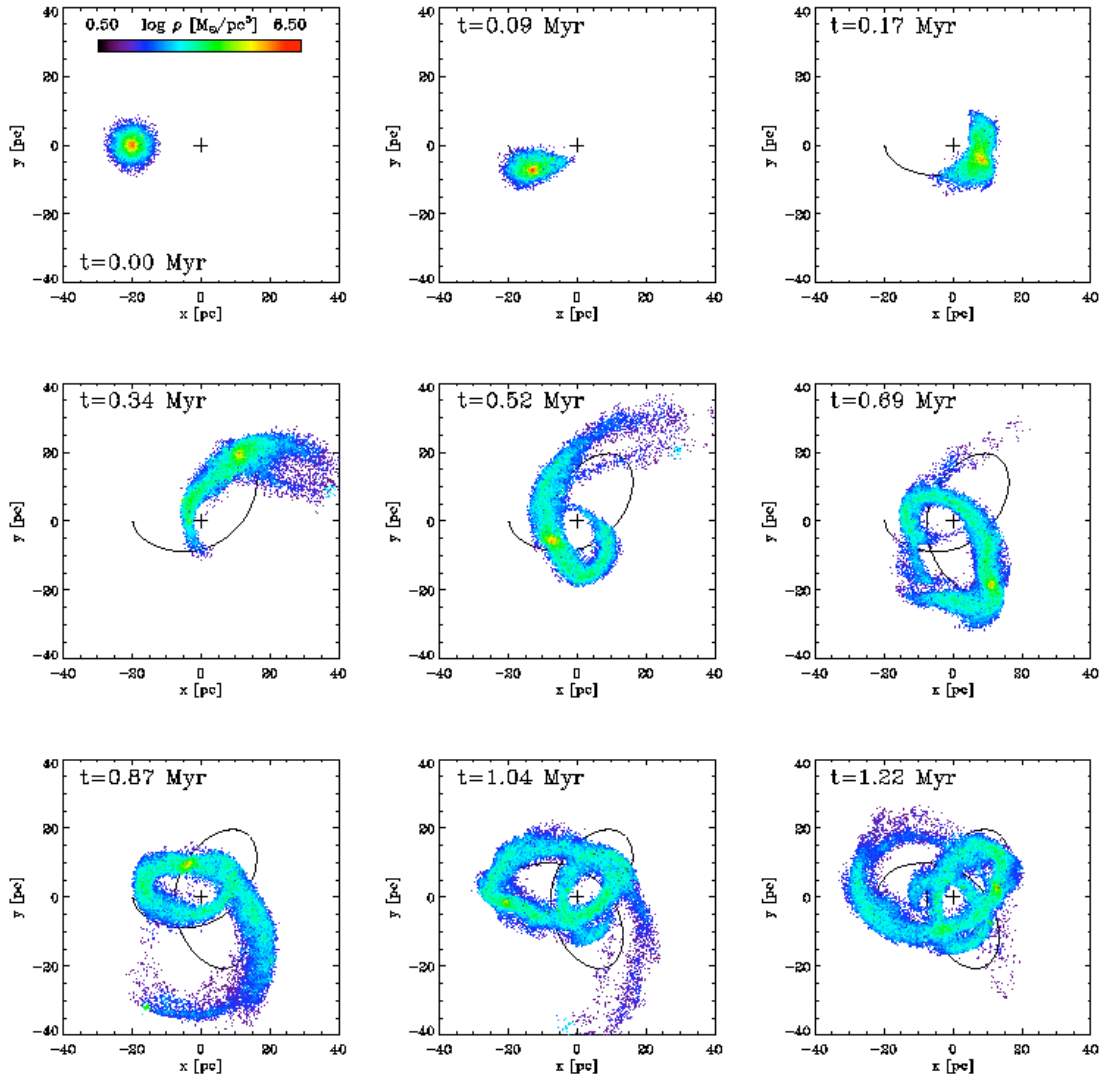


Figure 9.2: Dissolution of the star cluster in model E1.

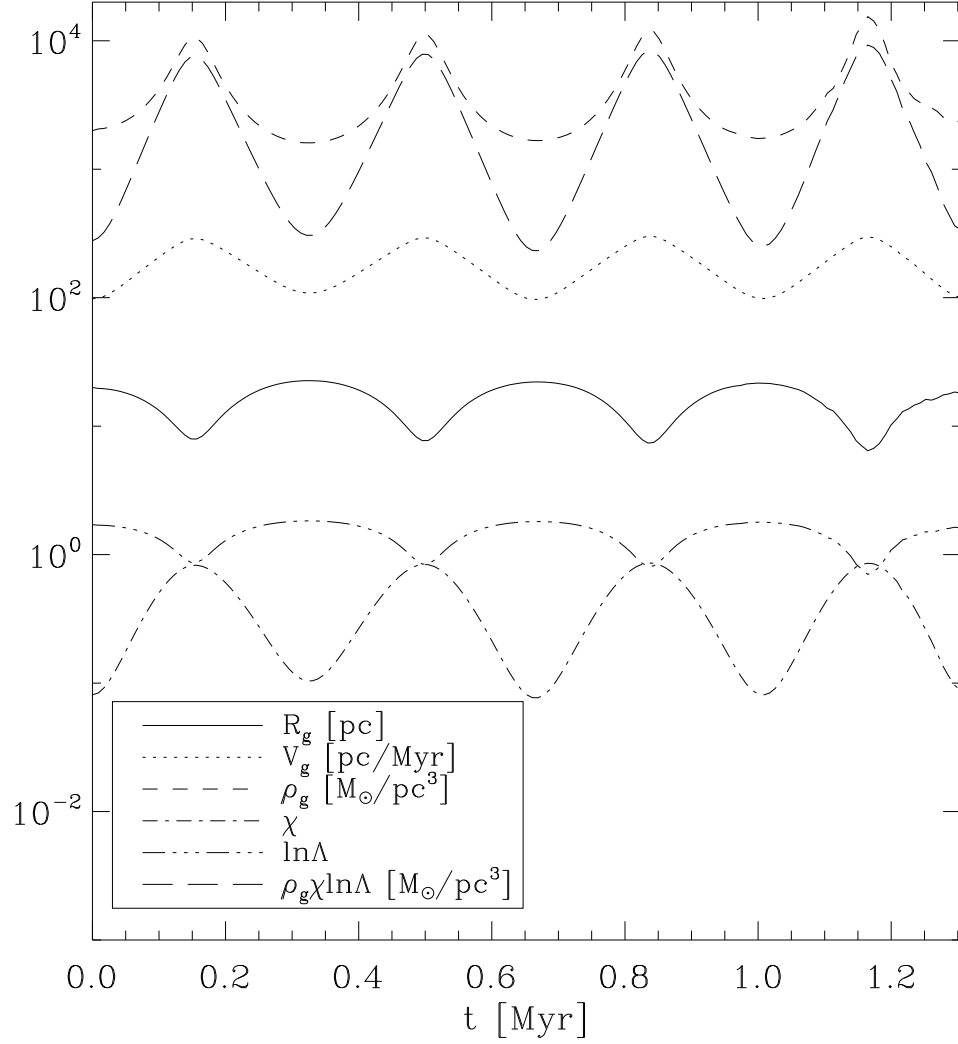


Figure 9.3: Time evolution of dynamical friction variables for model E1. R_g , V_g , ρ_g , χ and $\ln\Lambda$ are the current Galactocentric radius, the orbital velocity of the star cluster, the local Galactic density, the χ function and the Coulomb logarithm, respectively.

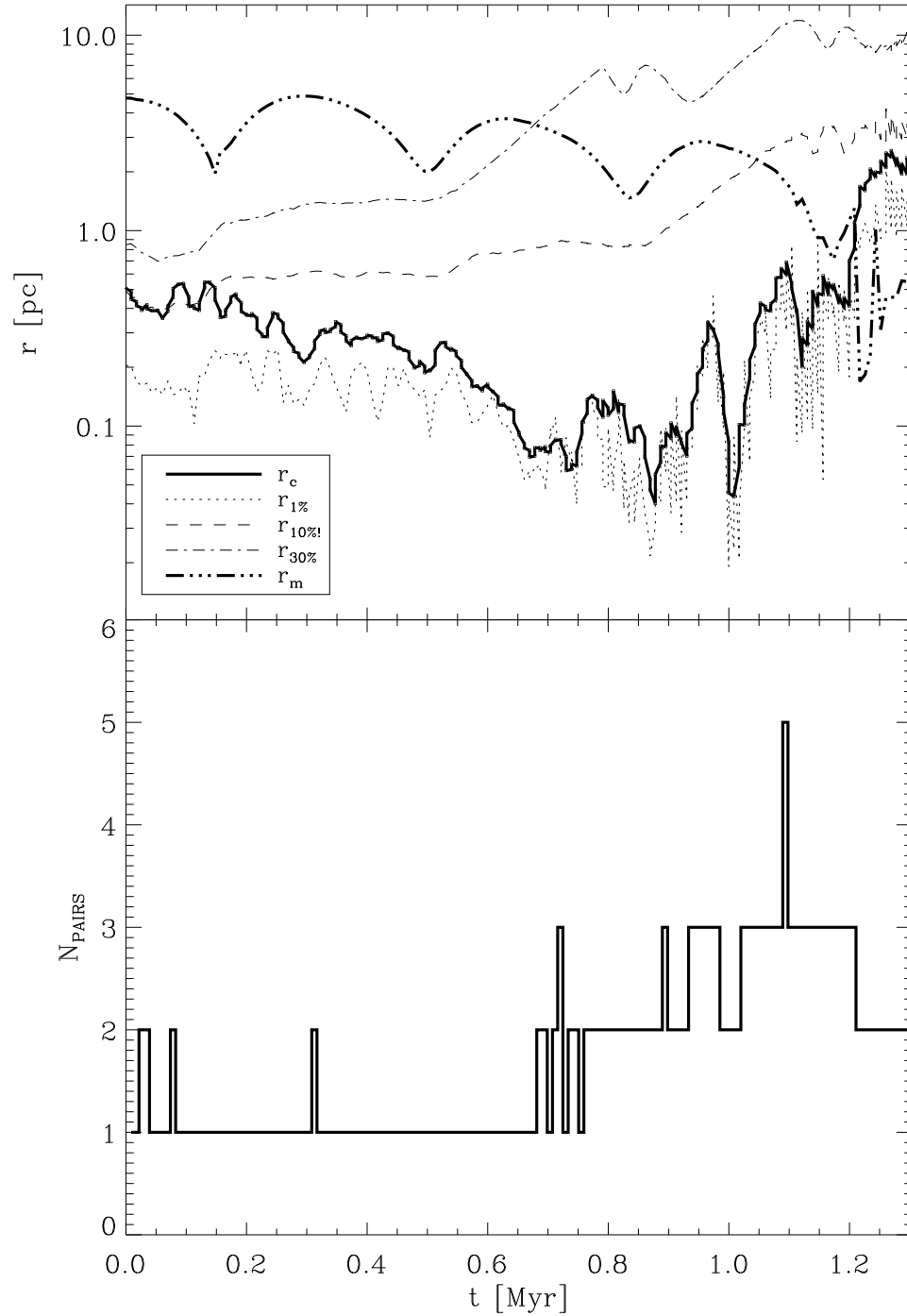


Figure 9.4: Top panel: Time evolution of the core radius r_c , the membership radius r_m and a few Lagrangian radii for the model E1. The core of the star cluster collapses. The outer Lagrangian radii expand due to the formation of tidal arms. Bottom panel: Number of regularized pairs as a function of time. Several binaries form while the core of the star cluster collapses.

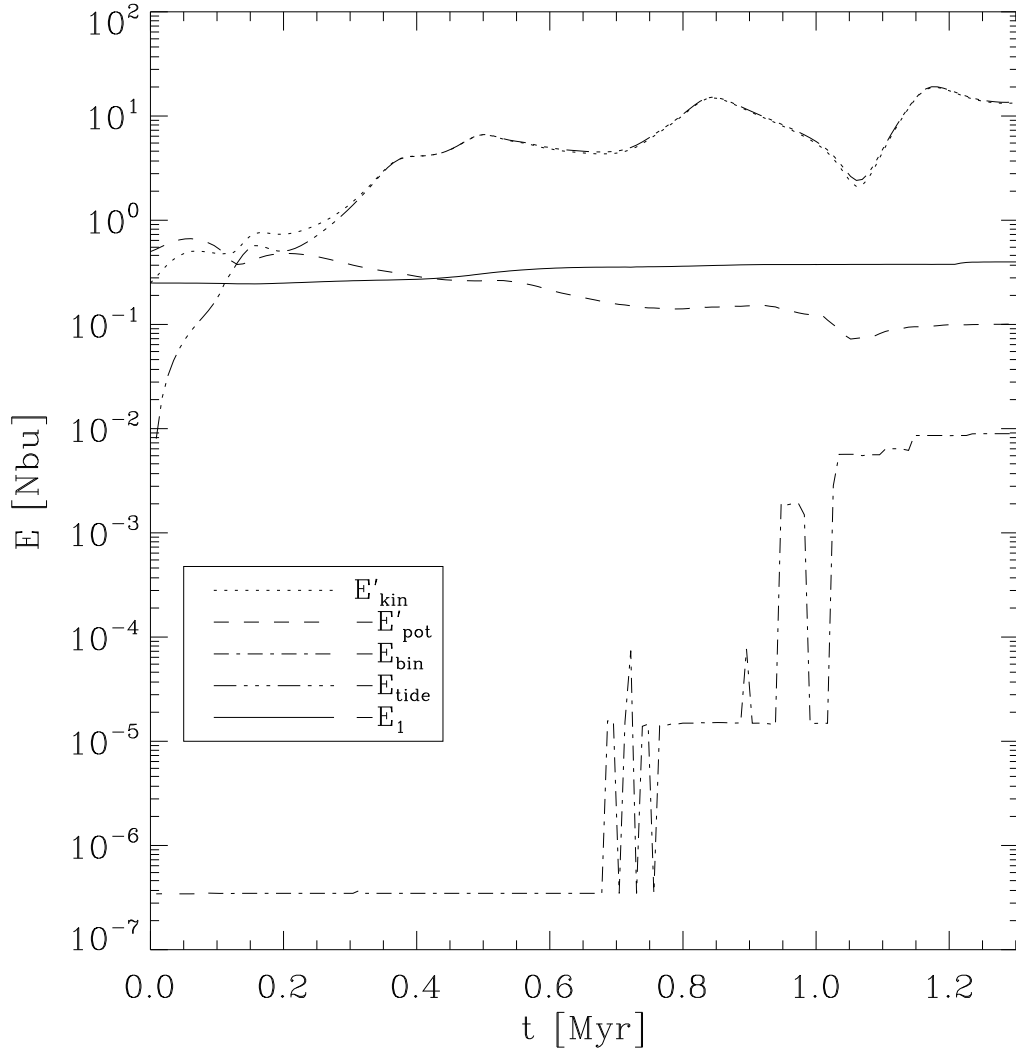


Figure 9.5: Energy balance (I) for model E1. E'_{kin} and E'_{pot} are the internal kinetic and potential energies of the N -body system, where every regularized pair is represented by a single center of mass particle. E_{bin} is the binding energy of all regularized pairs. E_{tide} is the tidal energy (cf. Figure 9.6) and $E_1 = E_{bin} + E_{kin} - E_{pot} + E_{tide}$ is the total energy. For more information see Section 8.3.2.

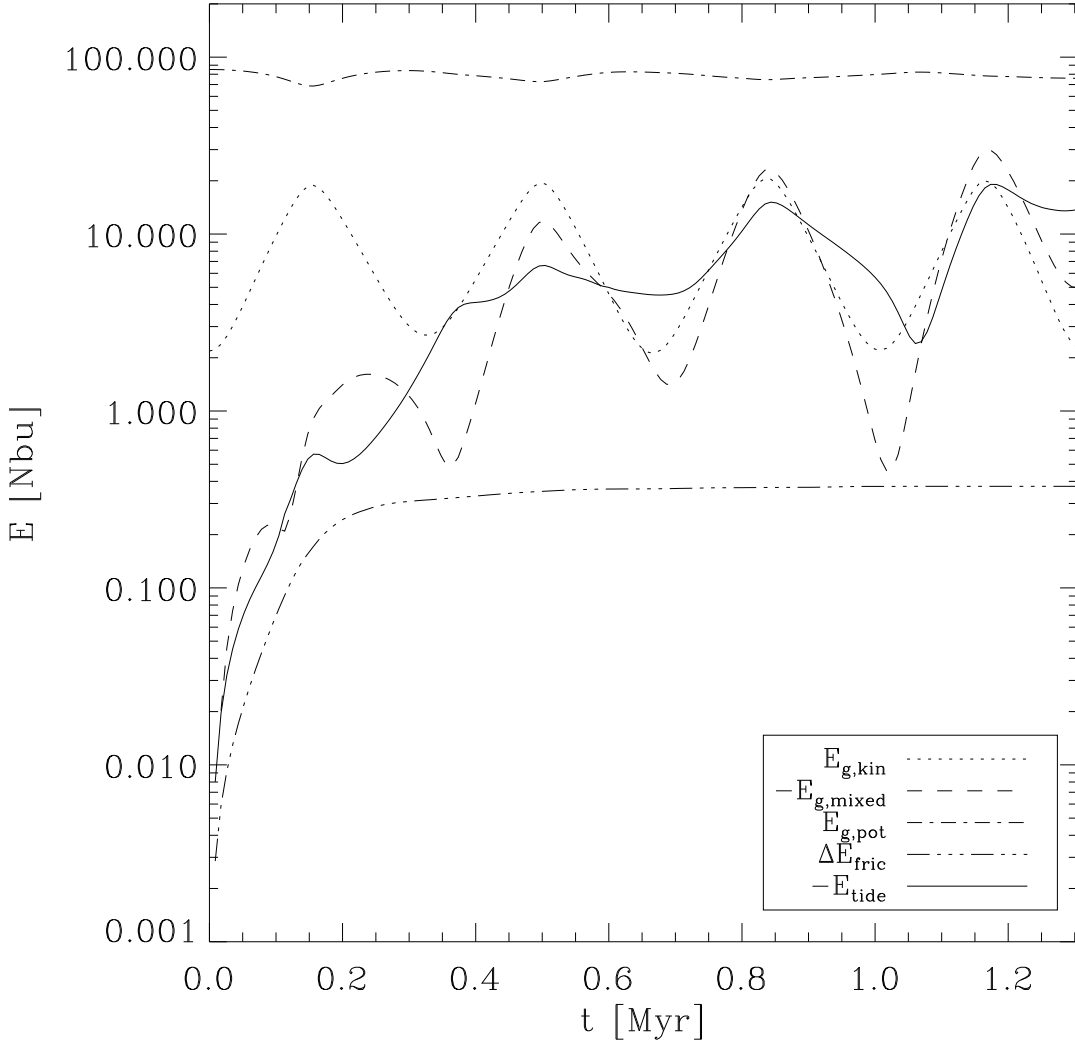


Figure 9.6: Energy balance (II) for model E1. $E_{g,kin} = \sum_i m_i \mathbf{v}_g^2$ is the orbital kinetic energy of the Galactic center particle, $E_{g,mixed} = \sum_i m_i \mathbf{v}_i \cdot \mathbf{v}_g$ is the mixed kinetic energy term, $E_{g,pot} = \sum_i m_i \Phi_{i,ext}$ is the external potential energy term, ΔE_{fric} is the energy loss due to dynamical friction, $E_{tide} = E_{g,kin} + E_{g,mixed} + E_{g,pot} + \Delta E_{fric} - E_{tide}(0)$ is the total tidal energy, where $E_{tide}(0)$ is a normalization such that $E_{tide} = 0$ in the beginning. For more information see Section 8.3.2.

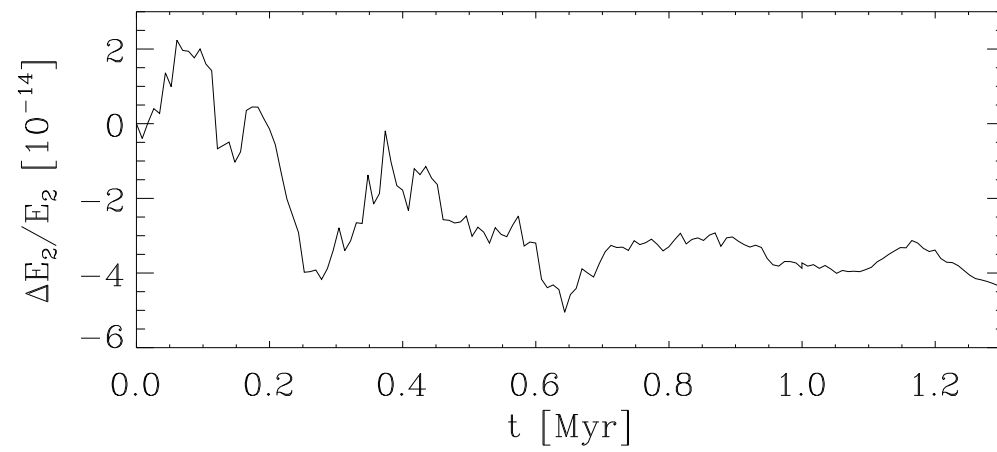


Figure 9.7: Relative energy error of the star cluster orbit integration with the 8th-order composition scheme with dissipation. The absolute value of the relative energy error stays below 10^{-13} .

9.2 Properties of tidal arms

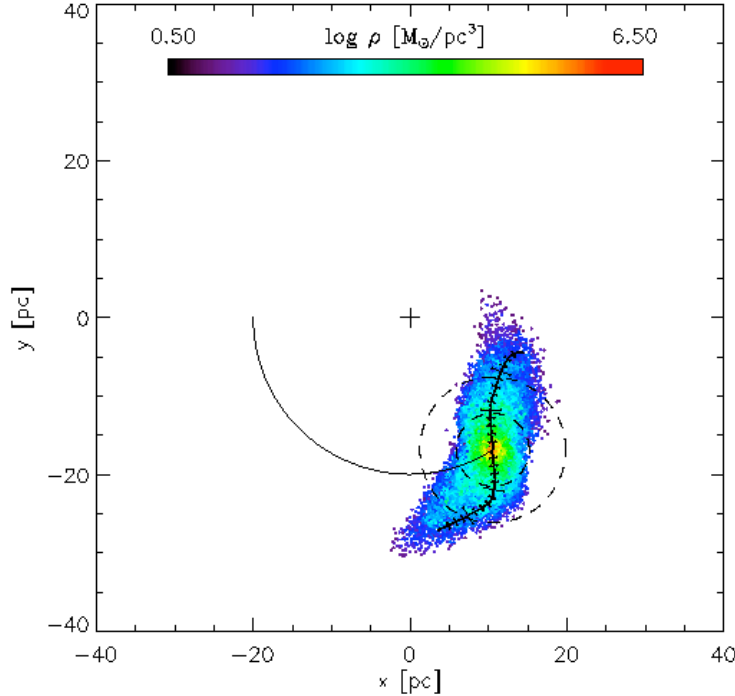


Figure 9.8: The model C9 at $t = 0.22$ Myr. The Galactic center is marked with a cross. The star cluster orbit is shown as a solid line. The dashed lines mark once and twice the membership radius. We look in the direction of the Galactic north pole. The short and long marks of the tidal arm coordinate system correspond to multiples of 1 and 5 pc, respectively.

The parameters of the N -body models of Sections 9.2 and 9.3 are given in Table 9.1. Figures 9.8 - 9.11 show the formation of the tidal arms for model C9. The initial 90% Lagrangian radius has been taken to be equal to the membership radius r_m in Equation (8.3). The star cluster dissolves in a spiral-like structure. The leading tidal arm consists of particles which pass the inner Lagrange point L_1 , while the trailing arm is formed by particles which pass the outer Lagrange point L_2 . The galactocentric radius R_C of the circular orbit is shown as a solid line. It decays very slowly due to dynamical friction with the Coulomb logarithm which was modified according to Equations (8.8) and (8.9). The initial value for the model C9 is $\ln \Lambda \approx 1.7$. Most particles of the leading arm have galactocentric radii less than R_C while most particles of the trailing arm have radii larger than R_C . The dashed lines mark once and twice the membership radius r_m .

The author has introduced a local coordinate system according to the description in Section 8.6. We denote the coordinate along the tidal arms as w , where negative values refer to the leading arm and positive values to the trailing arm. The short and long marks correspond to multiples of 1 and 5 pc, respectively.

The color coding is according to the logarithm of the stellar density. The density clearly peaks in the cluster center. However, one can observe clumps in the tidal arms where the density has local maxima. An indication for the presence of such clumps in tidal arms can already be found in the observations of Palomar 5 (Odenkirchen et al. 2001 [10], 2003 [8]). The clumps have been noticed in computer simulations by Capuzzo Dolcetta, di Matteo and Miocchi (2005) [11] and were

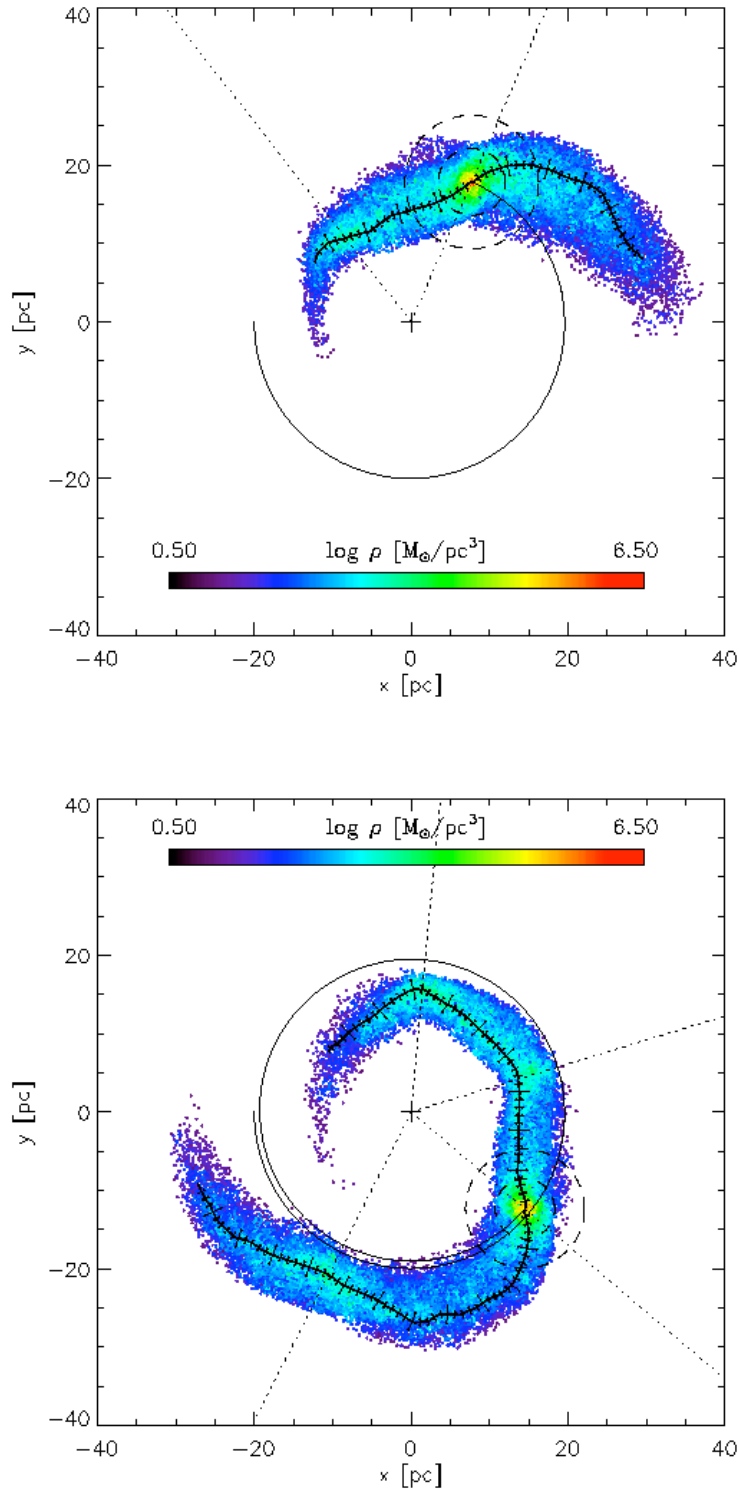


Figure 9.9: Further evolution of the model C9. Top panel: At $t = 0.43$ Myr. Bottom panel: At $t = 0.87$ Myr. The dotted lines from the Galactic center show the angles between density maxima in the leading and trailing arm, respectively, with respect to the star cluster center.

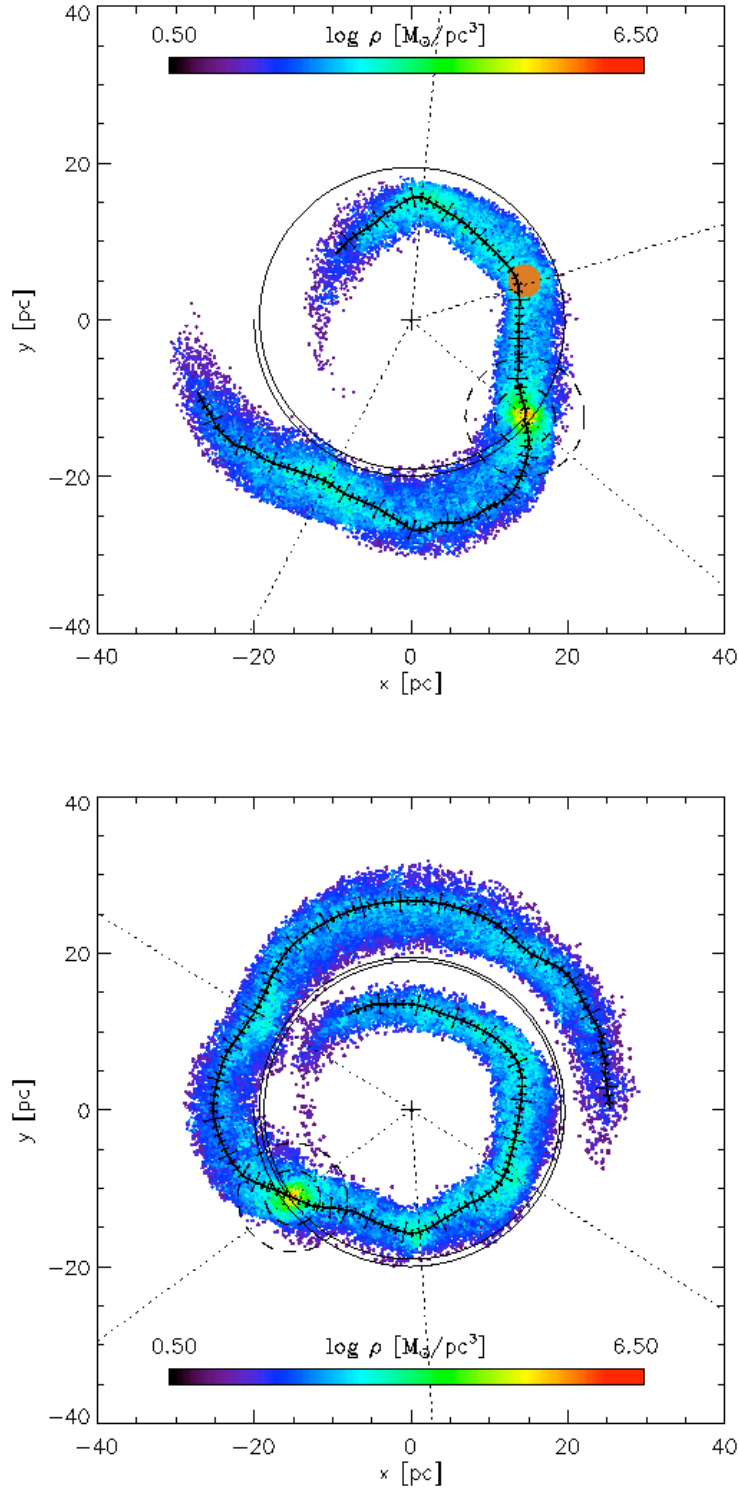


Figure 9.10: A standing density wave has developed in the model C9. Top panel: At $t = 0.87$ Myr. A spherical cloud of tracer particles has been placed into the first clump (brown colored). Bottom panel: At $t = 1.30$ Myr (without the tracer particles).

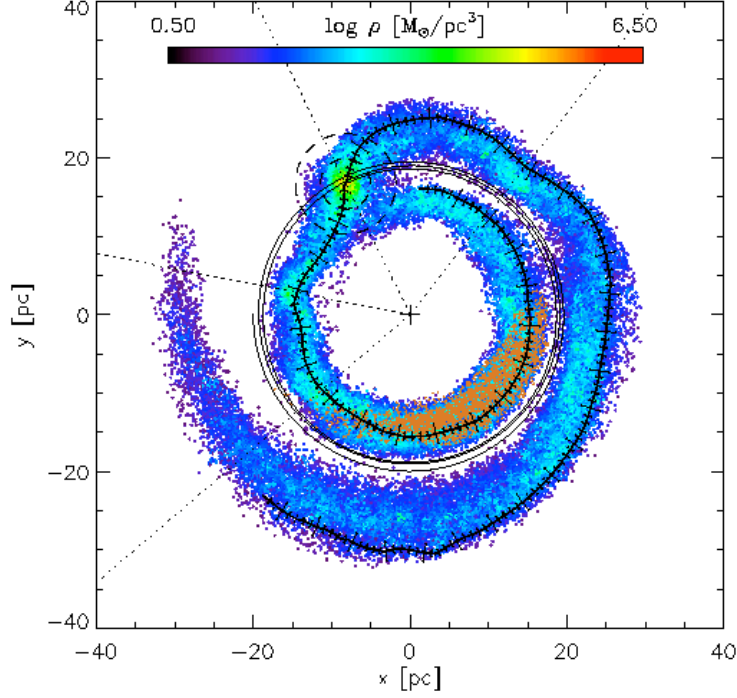


Figure 9.11: The model C9 at $t = 1.74$ Myr. The tracer particles have traveled further while the wave maximum still persists. The leading and trailing arms have wound up. They are separated by the potential wall of the effective potential. The tip of the leading arm has hit the remnant of the star cluster again. The author applied a weighting exponent to the particle mass in the expression (8.63).

King models:	
In general: $W_0 = 6$, $M_{\text{cl}} = 10^6 M_{\odot}$, $r_h = 1.64$ pc;	
C1	($N = 10^3$),
C2	($N = 2 \times 10^3$),
C3	($N = 5 \times 10^3$),
C4	($N = 10^4$),
C5	($N = 2 \times 10^4$),
C6	($N = 3 \times 10^4$),
C7	($N = 5 \times 10^4$),
C8	($N = 7 \times 10^4$),
C9	($N = 10^5$)

Table 9.1: Parameters of the N -body runs with King models on circular orbits with a dynamical friction force based on Just & Peñarrubia (2005) [200]. W_0 , M_{cl} , r_h and N are the dimensionless central potential, the total cluster mass, the half-mass radius and the particle number of the King model, respectively. The distribution of masses m_i is given by a Kroupa (1993) [201] initial mass function with masses $0.01 M_{\odot} \leq m_i \leq 120 M_{\odot}$.

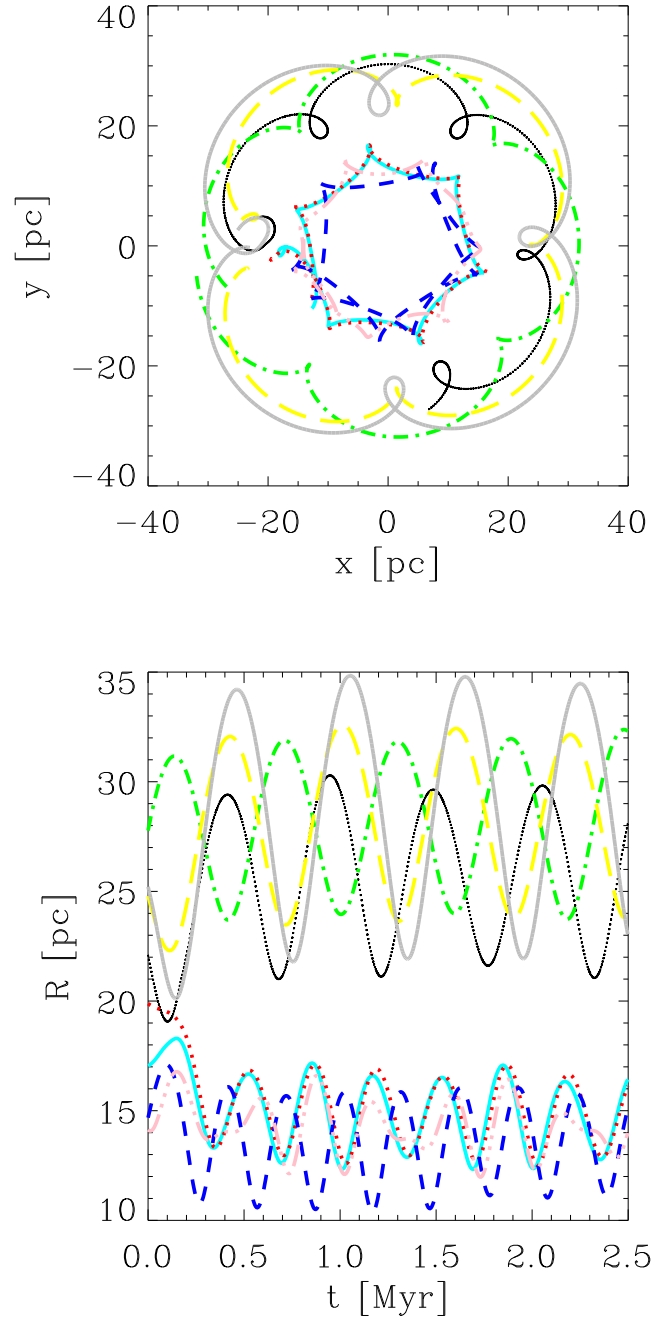


Figure 9.12: Top panel: Motion on cycloids within the tidal arms for a few particles in the model C9. The particles escape from locations near the cluster center at $(-20,0)$ either into the leading or the trailing arm. Bottom panel: Amplitude as a function of time for the same orbits. The small deviations from the harmonic motion may be apparent deviations due to the slight change of the orbital frequency by dynamical friction.

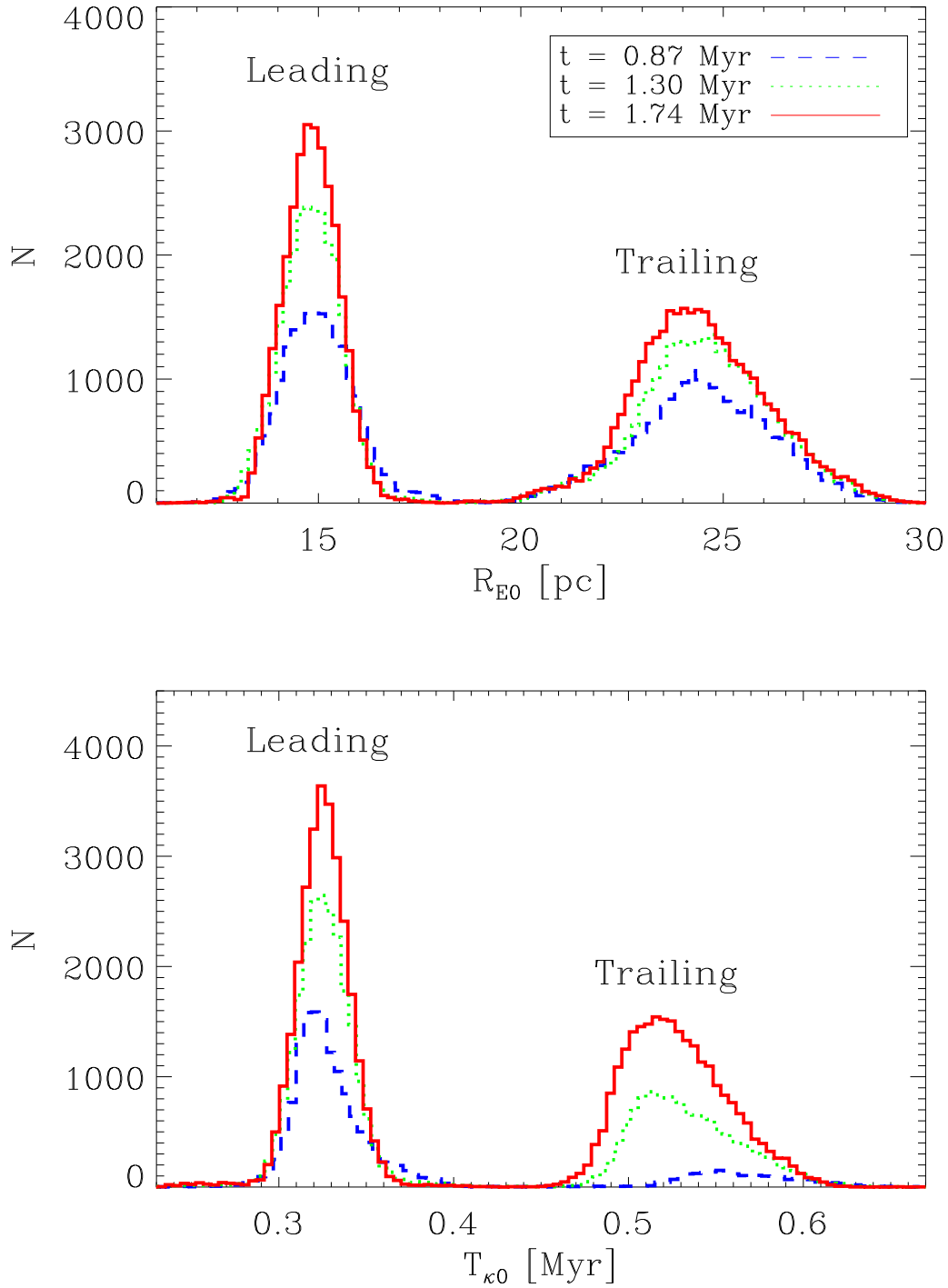


Figure 9.13: Histograms for model C9 (I). Top panel: Epicenter radius distribution. All particles within twice the initial membership radius have been excluded from the statistics. Bottom panel: Epicyclic period distribution. All particles within the initial membership radius have been excluded from the statistics. The bin frequency has been set equal to the data output frequency of NBODY6GC in order to avoid an unphysical higher harmonic in the histogram.

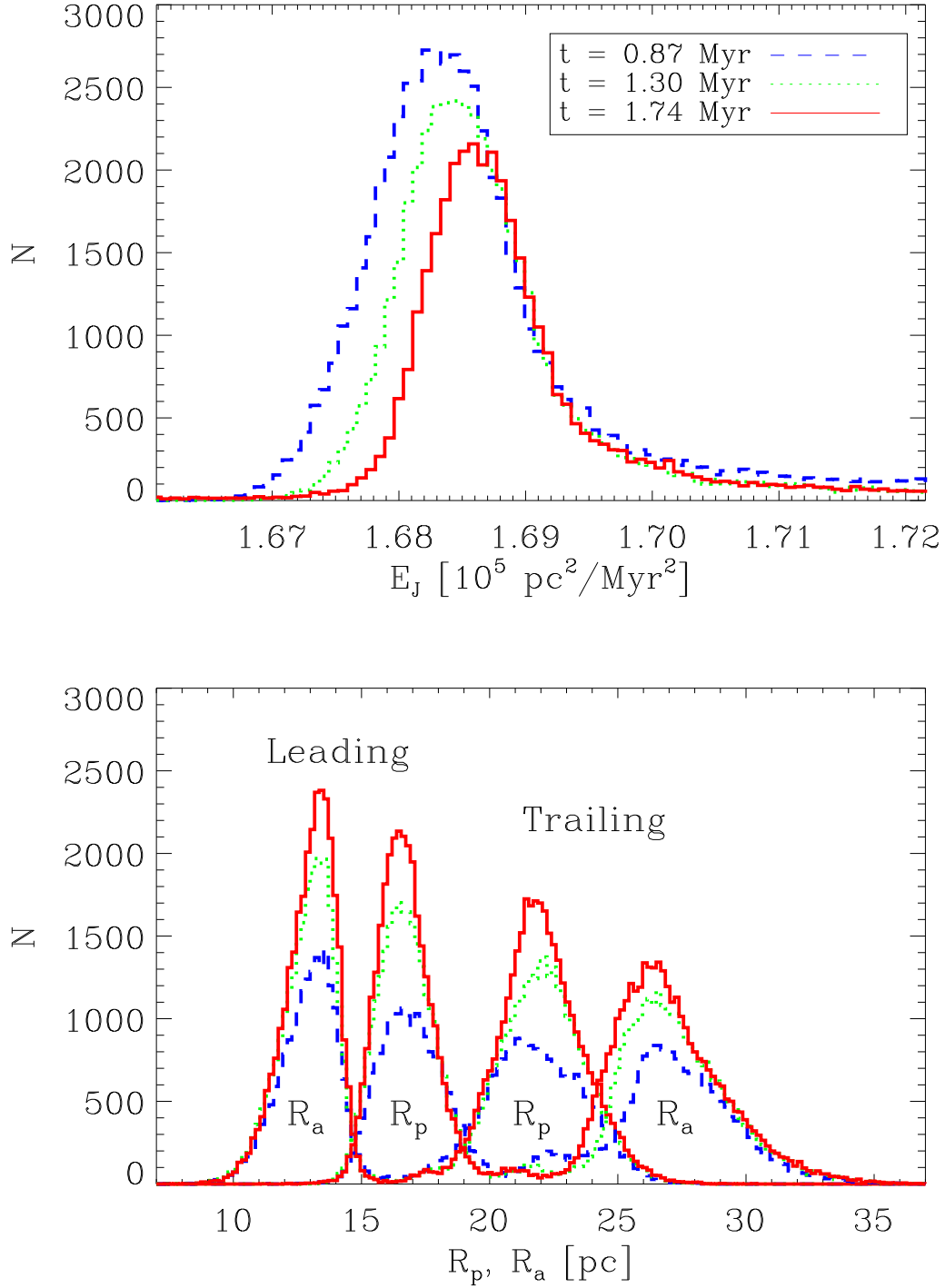


Figure 9.14: Histograms for model C9 (II). Top panel: Distribution of Jacobi energies. Bottom panel: Histogram of peri- and apocenter radii of the cycloid orbits in the tidal arms.

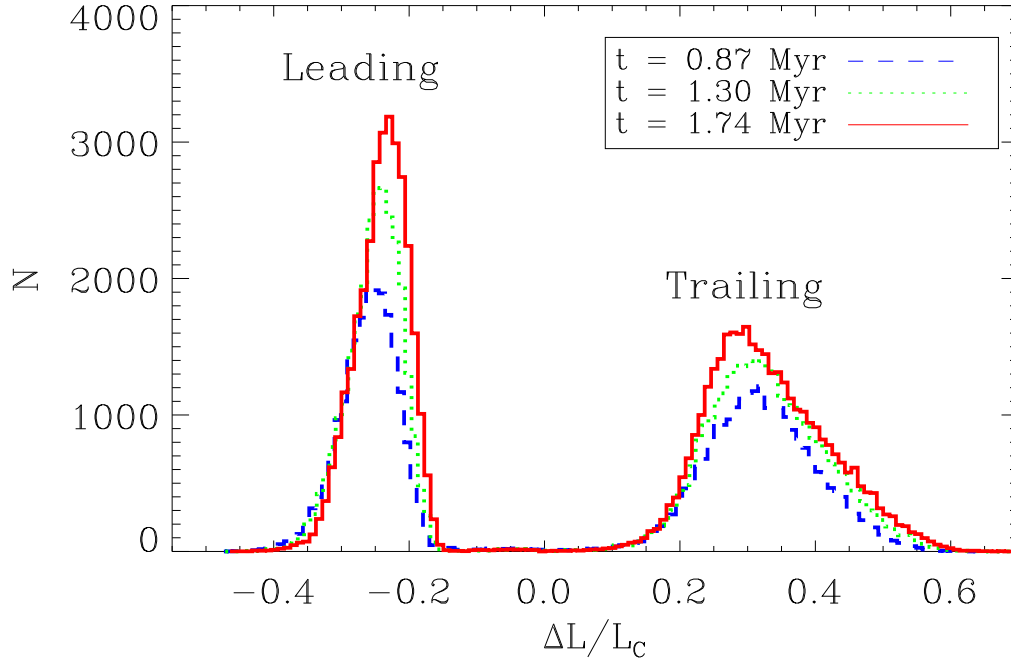


Figure 9.15: Histograms for model C9 (III). Distribution of $\Delta L/L_C$ for the first clump in the leading and trailing arm, respectively. All particles outside of 25 degrees around the density maximum have been excluded from the statistics. The same has been done for the second clump in the leading arm (not shown). For more explanations see the text.

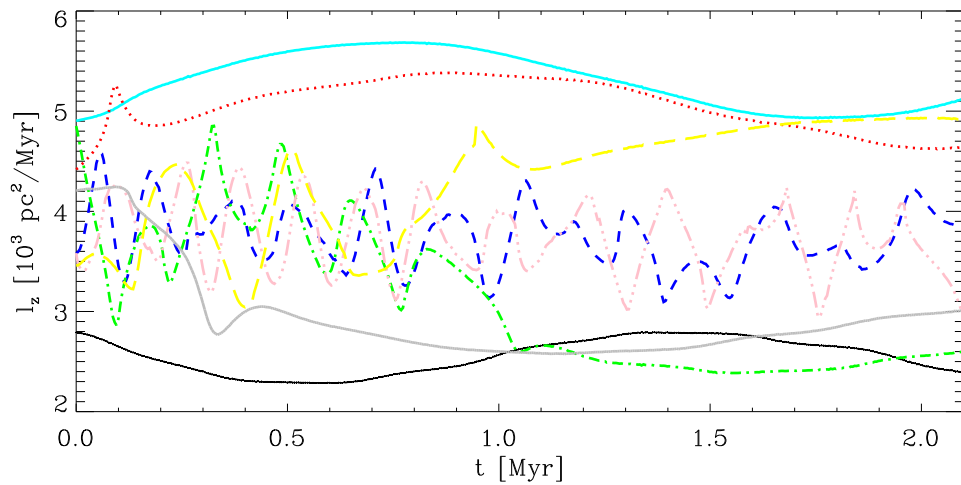


Figure 9.16: The z -component of angular momentum with respect to the Galactic center for a few orbits. In the cluster the angular momentum is not conserved since the cluster potential breaks the axisymmetry of the effective tidal potential. In the tidal arms the angular momentum is only approximately conserved.

investigated further by di Matteo, Capuzzo Dolcetta & Miocchi (2005) [9]. They noted already the wave-like nature of this phenomenon.

The top panel of Figure 9.10 shows a spherical cloud of tracer particles (coloured brown). Figure 9.11 shows how the tracer particles have travelled further into the tidal arm while the position of the density maximum in the clump stayed (approximately) constant. Thus the clumps can be interpreted as wave knots of a density wave similar to density waves in spiral galaxies although the formation mechanism is completely different.

A theoretical explanation for such clumps was published in Küpper, Macleod & Heggie (2008) [12]. The top panel of Figure 9.12 shows for a few particles that they move on cycloids. The clumps appear at the position where many of the loops or turning points of the cycloids overlap. For a more detailed theory, see Just et al. (2009) [13] or Chapter 4. The bottom panel of Figure 9.12 shows the radius as a function of time. We find approximate harmonic motion in the tidal arms.

The dotted lines from the Galactic center in Figures 9.9, 9.10 and 9.11 show the angles φ_0 between density maxima in the leading and trailing arm. In order to plot these angles the author determined the w coordinate of the maxima in the mean density (cf. the top panel of Figure 9.18 below) and obtained the corresponding Cartesian coordinates from the data files.

Figure 9.13 shows the histogram of the epicenter radii R_{E0} and the the epicyclic periods $T_{\kappa 0}$ of the cycloid orbits for different times. For the epicenter radii (and the epicyclic periods), stars within twice (and once) the membership radius were not included in the statistics. The epicenter radii are given by the arithmetic mean of the last maximum and minimum in the epicyclic amplitude. The epicyclic period is given by the time between the last two minima in the epicyclic amplitude. Note that at $t = 0.87$ Myr not all particles have completed one epicyclic period.

Figure 9.14 shows the distribution of Jacobi energies E_J and the histogram of apo- and peri-center radii of the cycloid orbits in the tidal arms.

Figure 9.15 shows the distribution of the dimensionless angular momentum differences $\Delta L/L_C = (L - L_C)/L_C$ for the first clump in the leading and trailing arm, respectively, where L_C is the angular momentum of the circular orbit. For the dimensionless angular momentum differences only stars within 25 degrees around the density maximum in the clump were included in the statistics. This has been done in order to select particles which have left the star cluster in a certain time window. Due to the dynamical evolution of the star cluster, a difference between the first and second clump should be detectable. In Figure 9.15 one can see two side lobes corresponding to the leading and trailing arms.

For the scale free model, the angle φ_0 can be expressed exactly as

$$\varphi_L = T_\kappa \Delta\omega = \frac{2\pi}{\beta_S} \left[1 - \frac{\omega_C}{\omega} \right] = \frac{2\pi}{\sqrt{\alpha+1}} \left[1 - \left(1 + \frac{\Delta L}{L_C} \right)^{\frac{3-\alpha}{\alpha+1}} \right] \quad (9.2)$$

where T_κ is the epicyclic period, $\Delta\omega = \omega - \omega_C$, ω_C and ω are the circular frequencies at the radius R_C of the circular orbit and in the vicinity of R_C , β_S is given by Equation (2.23) and $\Delta L/L_C$ is the most frequent dimensionless angular momentum difference. Note that the subscript ‘‘L’’ refers in the following discussion to quantities which are expressed as a function of $\Delta L/L_C$.⁴

The epicenter radius of the cycloids is given by

$$R_{EL} = R_C \left(1 + \frac{\Delta L}{L_C} \right)^{\frac{2}{\alpha+1}}. \quad (9.3)$$

For the Galactic center case, the epicyclic amplitude in a scale free model can be expressed as

$$\Delta x_L \approx \frac{1}{\omega_E} \sqrt{\frac{2}{\alpha+1} \left[\frac{3-\alpha}{2\alpha+2} R_C^2 \omega_C^2 \frac{\Delta L^2}{L_C^2} + \Delta E_J \right]} \quad (9.4)$$

⁴except for the case of the tidal radius r_L , where the subscript ‘‘L’’ refers to the Lagrangian points L_1 and L_2

where $1/\omega_E$ is the reciprocal of the angular frequency of the circular orbit at the epicyclic radius which can be expressed exactly with

$$\frac{1}{\omega} = \frac{1}{\omega_C} \left(1 + \frac{\Delta L}{L_C} \right)^{-\frac{\alpha-3}{\alpha+1}} \quad (9.5)$$

for the scale free model or approximated by the Taylor expansion (4.55) to the desired accuracy. Furthermore, $\Delta E_J = E_J - \Phi_{\text{eff,tid}}(R_C)$ is the Jacobi energy difference with respect to the effective tidal potential at R_C (Just et al. 2009 [13] and Chapter 4).

Table 9.2 shows a comparison of the measured angles, epicyclic radii, epicyclic amplitudes, peri- and apocenters and the theoretical estimates from the dimensionless angular momentum difference. Values are given for the first and second clump in the leading arm and for the first clump in the trailing arm. The second clump in the trailing arm is not well defined. Given is the measured angle φ_0 , the estimate φ_L according to Equation (9.2), the error $\Delta\varphi/\varphi_0 = (\varphi_0 - \varphi_L)/\varphi_0$ in percent, the most frequent epicyclic radius R_{E0} in Figure 9.13, the epicyclic radius R_{EL} according to Equation (9.3), the most frequent epicyclic period $T_{\kappa 0}$ in Figure 9.13 and the theoretical epicyclic period $T_{\kappa}(R_{EL})$ using Equation (2.22) with the epicyclic radius R_{EL} . Furthermore, the tidal radius $r_L = \{GM_{cl}/[(4 - \beta^2)\omega_C^2]\}^{1/3}$ (King 1962), the arc length $y_0 = R_C\varphi_0$, the A factors (Just et al. 2009 [13]),

$$A_{y0} = \frac{1}{\pi} \frac{\sqrt{\alpha+1}}{3-\alpha} \frac{y_0}{r_L}, \quad A_L = \frac{|R_{E,L} - R_C|}{r_L} \quad (9.6)$$

where A_{y0} is a first-order approximation and the error $\Delta A/A_{y0} = (A_{y0} - A_L)/A_{y0}$ in percent are given. Stated are also the most frequent peri- and apocenter radii R_{P0} and R_{A0} from Figure 9.14, the most frequent scaled Jacobi energy difference $\Delta E_J/\omega_E^2$ from Figure 9.14, the epicyclic amplitude Δx_L from Equation (9.4) and the obtained peri- and apocenter radii R_{PL} and R_{AL} , where $|R_{PL} - R_{EL}| = |R_{AL} - R_{EL}| = \Delta x_L$.

There are systematic errors in both φ_L and A_L and also in R_{PL} and R_{AL} . The reason is shown in Figure 9.16. In the tidal arms the angular momentum is only approximately conserved. The reason is the influence of the cluster potential which breaks the axisymmetry of the effective potential. However, in the cluster the angular momentum changes on a much shorter time scale. An estimate for the cumulative perturbation ΔL of L is given by

$$\Delta L = \left| \int (\mathbf{R} \times \mathbf{a}) dt \right| \approx \frac{R \Phi_{cl}}{V_{\text{drift}}} \quad (9.7)$$

where \mathbf{a} , $R = |\mathbf{R}|$, Φ_{cl} and V_{drift} are the acceleration, galactocentric radius, potential energy of the cluster and the drift velocity, respectively. Thus a slow drift velocity increases the change in L . Here a more detailed theory is desirable.

For Figures 9.17 - 9.19, the author averaged over spheres with a radius which was approximately equal to the width of the tidal arms in the xy plane (see Section 8.6 for the details). Since the Figures were still noisy, the author has used a median smoothing in addition. The width of the smoothing kernel has been taken to be twice the membership radius r_m defined in Equation (8.3).

For four different times, the top panel of Figure 9.17 shows the z -component of the dimensionless mean specific angular momentum difference $[l_z(w) - l_z(0)]/l_z(0)$ along the tidal arms. The specific angular momentum was calculated with respect to the Galactic center. In order to show the asymmetry between the leading and trailing arms, the lines for the leading arm have been rotated by 180 degrees about the origin and replotted in grey. This kind of asymmetries arise from the geometry of the effective potential.

The bottom panel of Figure 9.17 shows the same for the mean specific energy (i.e., energy per unit mass) difference $[e(w) - e(0)]/e(0)$. The specific energy was calculated with respect to the Galactic center. For the definition of the energy, see Section 8.3.2. A positive energy difference corresponds to the trailing arm while a negative energy difference corresponds to the leading arm.

#	t [Myr]	Arm	Clump	$\Delta L/L_C$	$ \varphi_0 $ [deg.]	$ \varphi_L $ [deg.]
1	0.87	lead.	1	-0.232	57.5	47.1
2	"	lead.	2	-0.273	67.6	55.7
3	"	trail.	1	0.320	68.6	61.9
4	1.30	lead.	1	-0.215	57.5	43.6
5	"	lead.	2	-0.227	53.3	46.1
6	"	trail.	1	0.276	68.4	53.6
7	1.74	lead.	1	-0.209	52.6	42.4
8	"	lead.	2	-0.205	51.5	41.5
9	"	trail.	1	0.273	64.2	53.0
#	$\Delta\varphi/\varphi_0$ [%]	$R_C(t)$ [pc]	R_{E0} [pc]	R_{EL} [pc]	$T_{\kappa 0}$ [Myr]	$T_\kappa(R_{EL})$ [Myr]
1	18.1	19.0	14.9	14.9	0.32	0.35
2	17.6	"	"	14.2	"	0.34
3	24.2	18.8	24.2	24.5	0.55	0.55
4	24.2	18.8	14.7	15.1	0.33	0.36
5	13.5	"	"	14.9	"	0.35
6	21.6	"	24.7	23.5	0.51	0.53
7	19.4	18.6	14.7	15.0	0.32	0.36
8	19.4	"	"	15.1	"	0.36
9	17.4	"	24.0	23.2	0.51	0.53
#	$r_L(t - T_{\kappa 0})$ [pc]	y_0 [pc]	A_{y_0}	A_L	$A_{R_{E0}}$	$\Delta A/A_{y_0}$ [%]
1	2.67	19.1	1.88	1.54	1.54	18.1
2	"	22.4	2.20	1.80	"	18.1
3	2.87	22.7	2.07	1.92	1.81	7.2
4	2.40	18.9	2.07	1.54	1.71	25.6
5	"	17.5	1.91	1.63	"	14.7
6	2.63	22.4	2.23	1.79	2.24	19.7
7	2.21	17.1	2.03	1.63	1.76	19.7
8	"	16.7	1.98	1.58	"	20.2
9	2.29	20.8	2.38	2.01	2.36	15.5
#	R_{P0} [pc]	R_{A0} [pc]	$\Delta E_J/\omega^2(R_{EL})$ [pc ²]	Δx_L [pc]	R_{PL} [pc]	R_{AL} [pc]
1	16.6	13.6	3.80	2.8	17.7	12.1
2	"	"	3.46	2.9	17.1	11.3
3	21.3	26.2	9.25	5.3	19.2	29.8
4	16.5	13.3	6.50	3.1	18.2	12.0
5	"	"	6.39	3.1	18.0	11.8
6	22.1	26.2	14.4	5.1	18.4	28.6
7	16.5	13.3	11.5	3.7	18.7	11.3
8	"	"	11.6	3.7	18.8	11.4
9	21.4	26.0	25.2	6.0	17.2	29.2

Table 9.2: Comparison of measurements and theory for the angles of the density maxima, the A factors and the epicyclic amplitudes. For explanations see the text.

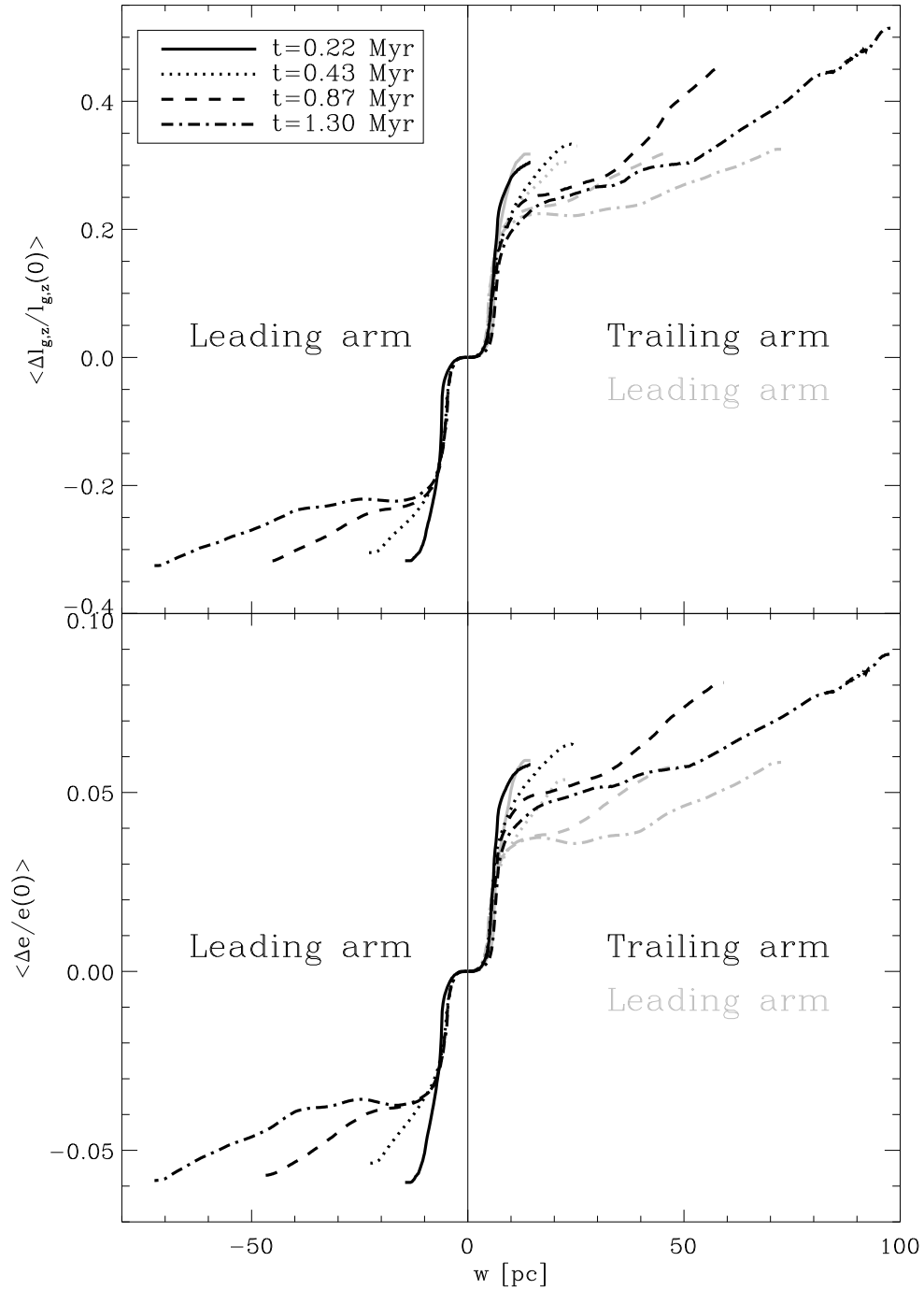


Figure 9.17: Top panel: Time evolution of the angular momentum difference between the cluster center and the position in the tidal arm for the model C9. The angular momentum difference is normalized by the angular momentum of the cluster center. In order to show the asymmetry between the leading and trailing arms, the lines for the leading arm have been rotated by 180 degrees about the origin and replotted in grey. Bottom panel: As in the top panel, but for the energy (internal and external) difference between the cluster center and the position in the tidal arm for the model C9. The energy difference is normalized by the energy of the cluster center.

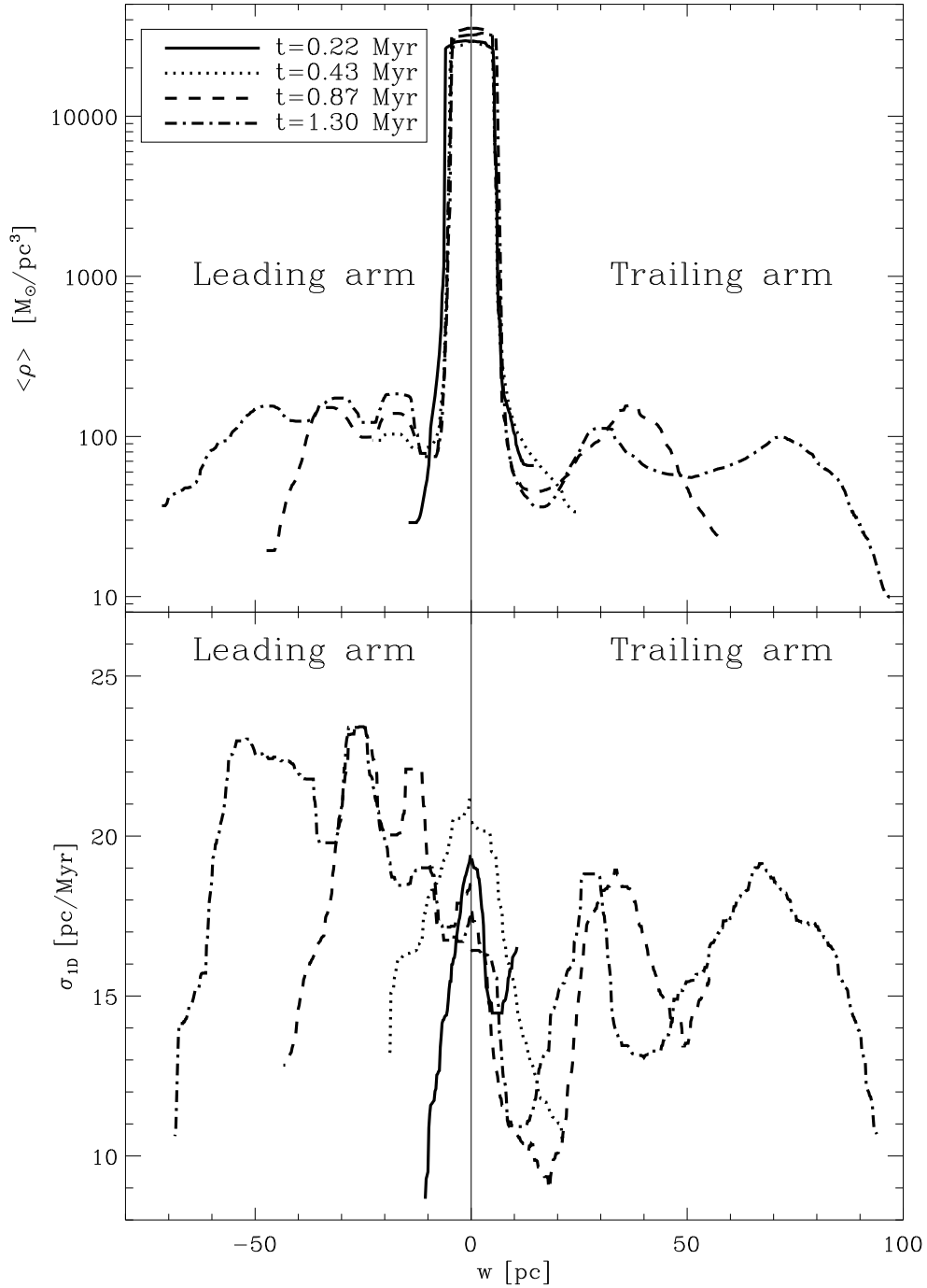


Figure 9.18: Top panel: Time evolution of the mean density of stars along the tidal arms for the model C9. One can see that several density wave maxima develop with time. Bottom panel: Time evolution of the 1D velocity dispersion along the tidal arms for the model C9. The characteristic features in the mean density (top panel) can also be seen in the velocity dispersion.

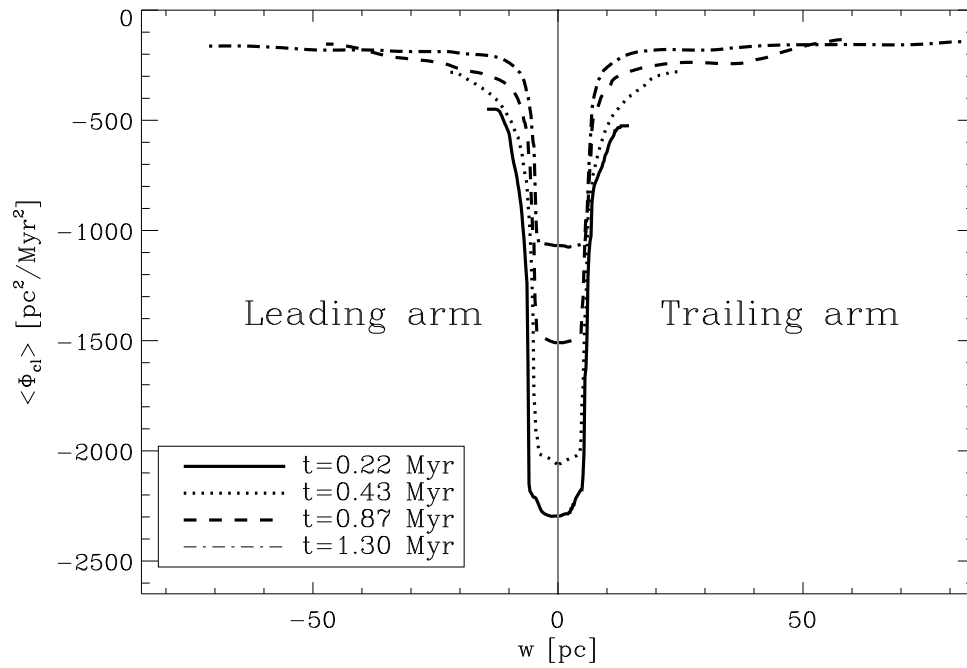


Figure 9.19: Time evolution of the mean star cluster potential along the tidal arms for the model C9. One can see that the potential well is deeper in the beginning but gets shallower as the cluster loses mass.

This is in accordance with the positive normalization in Equation (2.21) for the scale free potential in Equation (2.18). This Figure also shows an asymmetry between leading and trailing arm. What can be seen in this plot is that with the time more and more particles with a low energy difference with respect to the cluster center stream into the tidal arms. Thus the modulus of the mean energy difference falls off with time. In this connection it is worthwhile to mention that the particles with a low Jacobi energy stream into the tips of the tidal arms. This can be seen in Figure 9.11 (and in the top panel of Figure 9.23 below): The stars in the tips of the tidal arms are far away from the potential wall of the effective tidal potential which lies below the solid line of the orbit of the star cluster center.

The top panel of Figure 9.18 shows the density profile along the tidal arm coordinate w . At $t = 0.43$ Myr, one clump can be seen in the leading arm. At $t = 0.87$ Myr, two clumps can be seen in the leading arm and one in the trailing arm. At $t = 1.30$ Myr, three clumps can be seen in the leading arm and two in the trailing arm.

The bottom panel of Figure 9.18 shows the profile of the 1D velocity dispersion along the tidal arm coordinate w . The velocity dispersion profile also exhibits local maxima at the positions of the density maxima. This is in accordance with the notion that the clumps in the tidal arms occur at the positions where many of the loops or turning points of the cycloid orbits overlap. At these positions, the random velocities should exhibit maxima as well. Note that the first maximum in the leading arm at $t = 0.43$ Myr cannot yet be seen clearly in the bottom panel of Figure 9.18. Figure 9.9 shows that this density maximum is still in the process of building up.

Figure 9.19 shows the profile of the cluster gravitational potential along the tidal arm coordinate w at four different times. One can see that the potential well of the star cluster is deeper in the beginning but gets shallower as the cluster loses mass.

Figure 9.20 shows the evolution of the cluster mass contained within the tidal radius for the model C9. In addition, the mass in the tidal arms is shown as a function of time. It can be seen that more particles escape into the trailing arm than into the leading arm. In the relaxation-driven dissolution scenario this would be paradoxical since the inner Lagrange point L_1 is at a lower energy than the outer Lagrange point L_2 according to Figure 6.3. However, most stars are in the high-energy regions of the star cluster (see next Section). For these particles the phase space for escape into the trailing arm is larger than that for escape into the leading arm. The calculation of the basins of escape would give a hint for the understanding. A 3D calculation is necessary in order to calculate the fraction of orbits which escape into the leading and trailing arms, respectively.

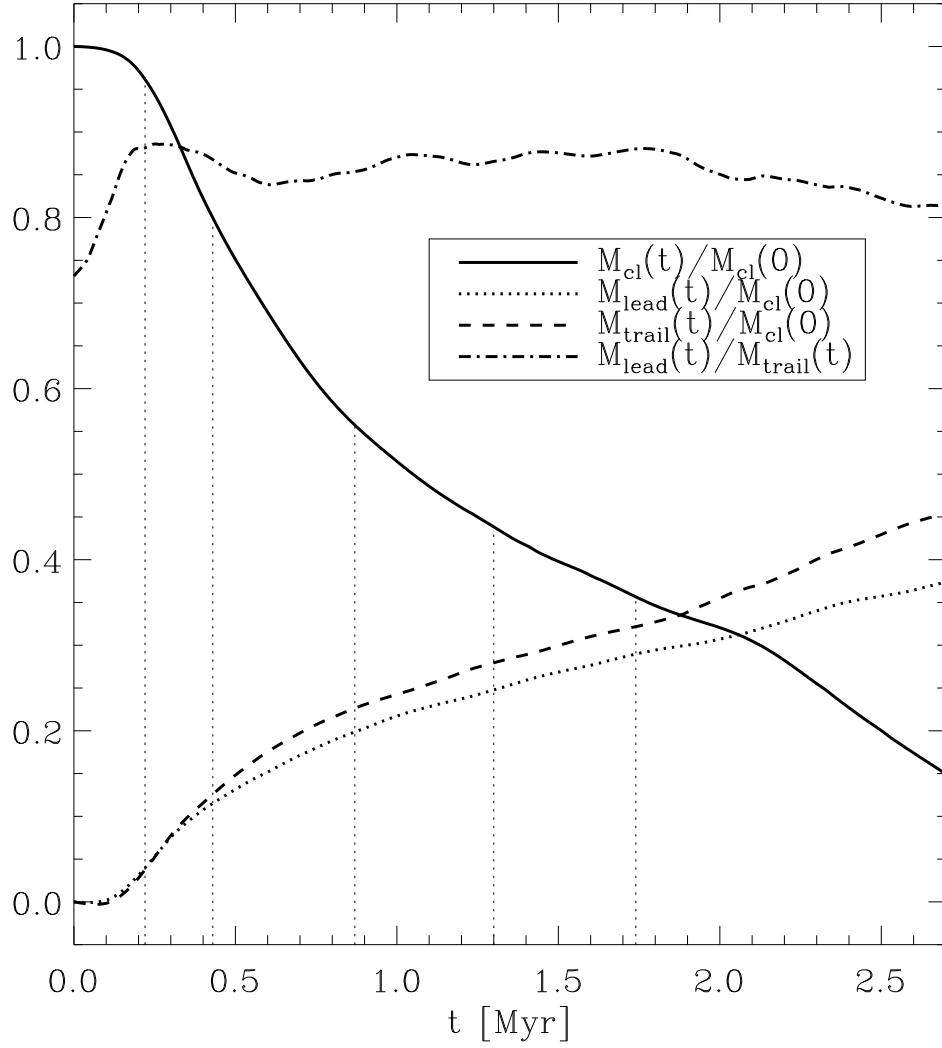


Figure 9.20: Evolution of the cluster mass within the tidal radius and the mass in the tidal arms for the model C9. It can be seen that more particles escape into the trailing arm than into the leading arm. The ratio of leading arm mass to trailing arm mass is always roughly 85%. The thin vertical dotted lines correspond to $t = 0.22, 0.43, 0.87, 1.30$ and 1.74 Myr.

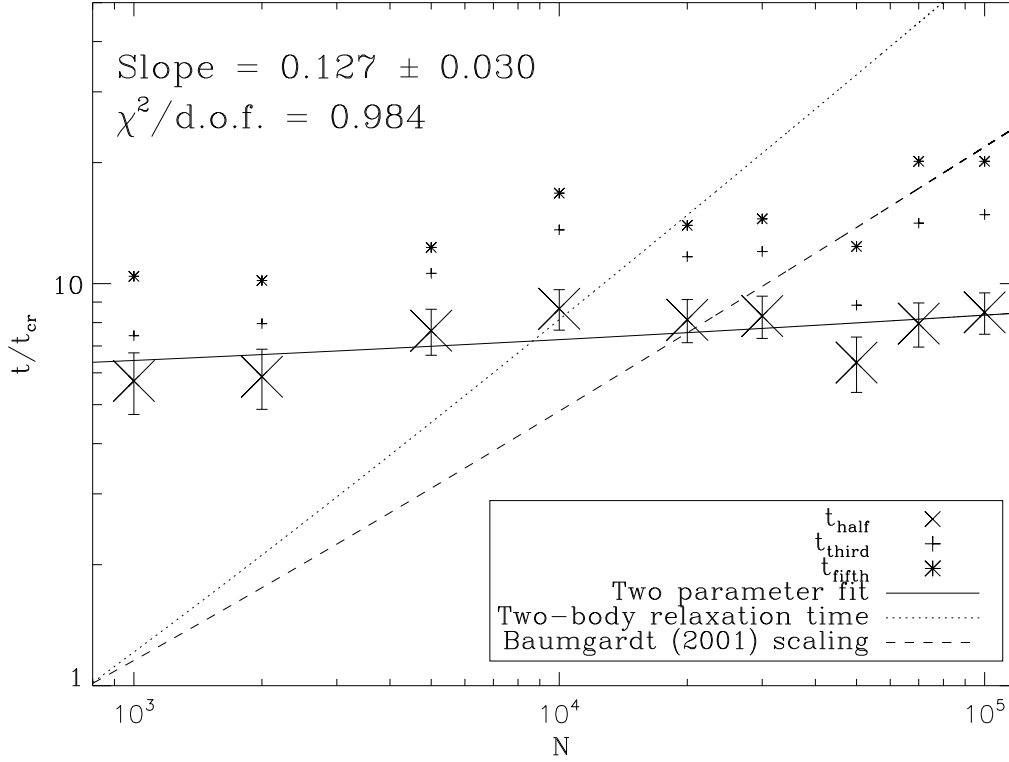


Figure 9.21: Scaling of the ratio of half-mass time t_{half} to crossing time t_{cr} as a function of the particle number N for the models C1 - C9. The errors correspond to 1 crossing time t_{cr} . We have $t_{cr} = 0.123$ Myr in all models. The “third-” and “fifth-mass” times are also shown.

9.3 Lifetime scaling and RE classification

Figure 9.21 shows the scaling of the half-mass time as a function of the particle number. The half-mass time is the time after which the star cluster has lost half of its initial mass due to escaping stars. It also shows as dots the times, when the cluster has one third or one fifth, respectively, of its initial mass. The particle number in Figure 9.21 ranges from $N = 10^3$ up to $N = 10^5$. The χ^2 fit of a power law shows that the half-mass time depends only slightly on the particle number N . This is in contrast to the relaxation-driven dissolution of star clusters. If the dissolution is relaxation-driven, the stars are scattered above the escape energy (or a critical Jacobi energy) by two-body relaxation before they can escape through exits in the equipotential surfaces around the Lagrangian points L_1 and L_2 . In this case the half-mass or dissolution time should depend more strongly on the particle number than in Figure 9.21. Baumgardt 2001 [47] developed a detailed theory for the relaxation-driven dissolution of star clusters on circular orbits in a steady tidal field with back-scattering of potential escapers in which the half-mass time scales as $t_{half} \propto t_{rh}^{3/4}$.

Fukushige & Heggie (2000) [5] give a hint for the understanding of the scaling of the half-mass time in our models. In Figure 9.22 one can see that the cluster fills the energetic region above the total effective potential of Figure 6.3 in Chapter 6. Many stars are initially outside of the tidal radius $\bar{r}_L = [x(L_1) + x(L_2)]/2$ and most particles have Jacobi energies E_J per unit mass which are higher than the mean effective potential $\bar{E}_{J,L} = [E_J(L_1) + E_J(L_2)]/2$ of both Lagrange points L_1 and L_2 . We initially have for the model C9 the following ratio of particle numbers:

$$\frac{N_{r > \bar{r}_L}}{N_{r < \bar{r}_L}} \approx 0.37 \quad \text{and} \quad \frac{N_{E_J > \bar{E}_{J,L}}}{N_{E_J < \bar{E}_{J,L}}} \approx 1.80. \quad (9.8)$$

The stars which are outside of \bar{r}_L and the high-energy particles with respect to the critical Jacobi energy $\bar{E}_{J,L}$ can leave the cluster relatively fast as compared with the relaxation time, provided they are not bound by a non-classical integral of motion which would hinder their escape. Figure 6.5 shows that above a certain Jacobi energy threshold in the high-energy regions all orbits are chaotic and not subject to a non-classical integral of motion.

It is possible to classify the particles initially according to their membership to one of four regions:

1. Large Radius High Energy (LRHE) region
2. Small Radius High Energy (SRHE) region
3. Large Radius Low Energy (LRLE) region
4. Small Radius Low Energy (SRLE) region

The distinction between these regions is shown with dashed lines in Figure 9.22. We call this the Radius-Energy (RE) classification. The classification arises due to the existence of the Lagrange points L_1 and L_2 at proximate (or equal) Jacobi energies. For the model C9 with $N = 10^5$, we initially have the following occupation numbers of the four regions,

$$N_{\text{LRHE}} = 24370, \quad N_{\text{SRHE}} = 39854, \quad N_{\text{LRLE}} = 2831, \quad N_{\text{SRLE}} = 32945. \quad (9.9)$$

The top panel of Figure 9.23 shows that the particles in the LRLE region move into the tips of the tidal arms. The bottom panel shows that most particles in the LRHE region have also moved towards the tips of the tidal arms, but it is interesting to note that many particles of this region are still bound to the cluster after $t = 1.74$ Myr even though their initial location is outside the tidal radius. These particles belong to retrograde orbits which are bound to the star cluster by a non-classical integral of motion. The calculation of Poincaré surfaces of section shows indeed that there exist regular retrograde orbits for particles in the LRHE region.

Furthermore, the division of the stellar mass into the four regions seems to play a crucial role in the dissolution process. Particularly the ratio

$$\alpha_M = \frac{M_{\text{LRLE}} + M_{\text{LRHE}} + M_{\text{SRHE}}}{M_{\text{SRLE}}} \quad (9.10)$$

determines the physics of the dissolution process, where M_{LRLE} , M_{LRHE} , M_{SRHE} and M_{SRLE} are the occupation masses of the four regions. If α_M is close to zero the main process which leads to the dissolution of the cluster is two-body relaxation, which scatters stars from the SRLE region into the two high-energy regions. The larger the particle number N is, the slower is this process. The author speculates that α_M was very small for the old globular clusters in the halo of the Milky Way and that their dissolution is relaxation-driven, but that many young star clusters (open clusters) with larger values of α_M may form at all times in the Milky Way and dissolve fast as compared with the Hubble time. If α_M is sufficiently large, mass loss from the SRLE region seems to be dominated by a self-regulating process of increasing Jacobi energy due to the weakening of the potential well of the star cluster, which is induced by the mass loss itself (Just et al. 2009 [13]). A simple estimation shows that the critical Jacobi energy $\bar{E}_{J,L}$ increases more slowly with time as compared with the Jacobi energy E_J of a star in the non-stationary gravitational potential of the star cluster. While the LRLE, LRHE and SRHE regions of the star cluster dissolve, particles are continually shifted from the SRLE region into the two high-energy regions as the potential well of the star cluster gets shallower (cf. Figure 9.19). In addition, a fraction of particles is scattered from

the SRLE region into the high-energy regions by two-body relaxation. The two-body relaxation leads to the small slope 0.127 ± 0.030 in Figure 9.21. It is small since α_M is very large for the models C1 - C9. From the values in (9.9) we obtain $\alpha_M \approx 2$ for the model C9 with the valid assumption that the particles of different mass are initially uniformly mixed in radius and Jacobi energy per unit mass.

If the physical tidal radius is equal to the radius where the density of the star cluster (King) model vanishes, we have $N_{\text{LRLE}} = N_{\text{LRHE}} = 0$ and only two of the four regions are occupied with particles. This is the standard case used in N -body simulations of star clusters in a tidal field so far (e.g. Baumgardt & Makino 2003 [209], Trenti, Heggie & Hut 2007 [210], Ernst et al. 2005 [3]). On the other hand, Tanikawa & Fukushige (2005) [211] adopted initial models where the King cutoff radius was not equal to the physical tidal radius.

The author argues that the situation that the cluster is divided into the four regions of the RE classification (with certain occupation numbers and masses) is the typical situation for newly formed star clusters. A first crucial question is whether stars can form in all regions. The answer is yes, if the condition for star formation is fulfilled. According to the modern picture of gravo-turbulent star formation (e.g. Mac Low & Klessen 2004 [212], Ballesteros-Paredes et al. 2007 [213]), supersonic turbulence and shocks create initial density enhancements in a molecular cloud. The formed molecular cloud core contracts gravitationally and fragments eventually. Finally, protostellar seeds form, accrete in-falling material and become main sequence stars. The condition for star formation is independent of the distinction between high- and low-energy regions of the effective potential. Thus one would expect that stars form initially in the high-energy regions and the SRLE region slowly builds up as more material moves towards the center of the new star cluster. Due to the turbulent structure within the molecular cloud it is also possible that a small fraction of stars forms in the LRLE region. Predictions about the fractions of stars which belong to the four different regions (i.e., the occupation numbers and masses) may be an important result of the emerging theory of star cluster formation. What are typical ratios of occupation numbers and masses in regions with efficient star formation? How do the occupation numbers and masses differ between open and globular clusters? From the side of stellar dynamics the scaling problem of the dissolution times (see Section 7.2) needs to be solved for the new dissolution mechanism due to a non-stationary gravitational potential combined with the effect of two-body relaxation.

In the Galactic center, the supersonic shock and turbulent velocities must be high enough to form mean densities which withstand the tidal shear forces. According to Morris (1993) [29], the critical mean number density for gravitationally bound clouds in the Galactic center region is given by

$$n_{\text{crit}} = 10^7 \text{ cm}^{-3} \left(\frac{1.6 \text{ pc}}{R_g} \right)^{1.8}, \quad (9.11)$$

where R_g is the galactocentric radius.

The picture sketched above would be similar if the star cluster formation in the Galactic center is triggered by the collision of two clouds. For typical parameters (e.g. for the formation of clusters like Arches and Quintuplet) the rate of such cloud collisions in the Galactic center is low as compared with the reciprocal of the lifetime of OB stars and can be crudely estimated to be

$$R_{\text{col}} = 5 \times 10^{-8} \text{ yr}^{-1} \left(\frac{M_{\text{cloud}}}{10^6 M_{\odot}} \right)^{-1} \left(\frac{N_{H_2}}{10^{23} \text{ cm}^{-2}} \right)^{-1} \left(\frac{\sigma_v}{20 \text{ km s}^{-1}} \right) \quad (9.12)$$

where M_{cloud} , N_{H_2} and σ_v are the mass, the column density and the velocity dispersion of a cloud (Hasegawa et al. 1994 [214], Stolte et al. 2008 [154]).

Finally, we note that the Jeans time scale is of the same order as the dissolution times of the author's models in the Galactic center. According to Hartmann (2002) [215], who explored an earlier idea by Larson (1985) [216], the Jeans (or fragmentation) time scale of a gaseous filament can be written as

$$\tau \approx 3.7 \left(\frac{T}{10 \text{ K}} \right)^{1/2} A_V^{-1} \text{ Myr} \quad (9.13)$$

where T is the temperature and $A_V \approx 5$ is the visual extinction through the center of the filament (see also Klessen et al. 2004 [217]).

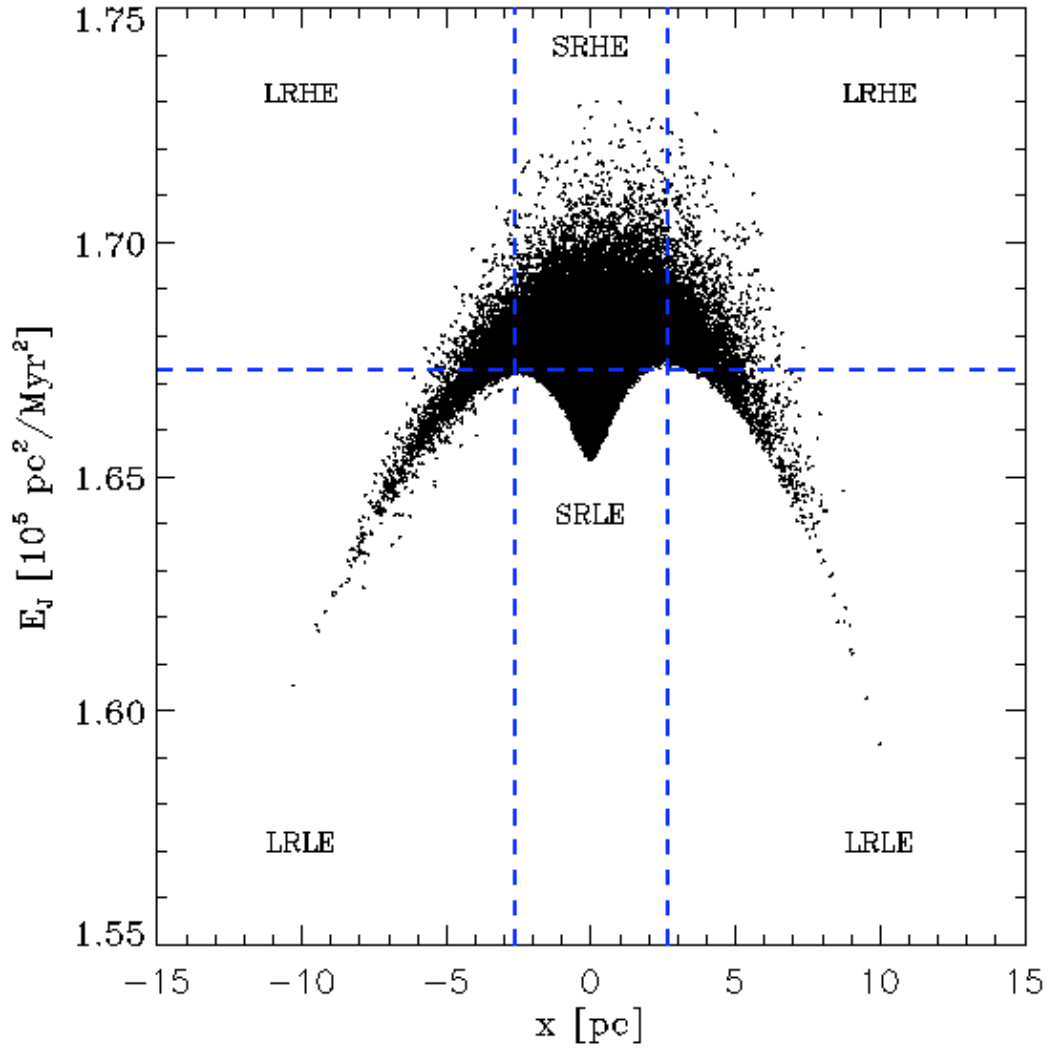


Figure 9.22: Projection of initial Jacobi energies of stars onto the $x - \Phi_{\text{eff}}$ plane of Figure 6.3 for the model C9. The dashed lines mark the different regions of the Radius-Energy (RE) classification.

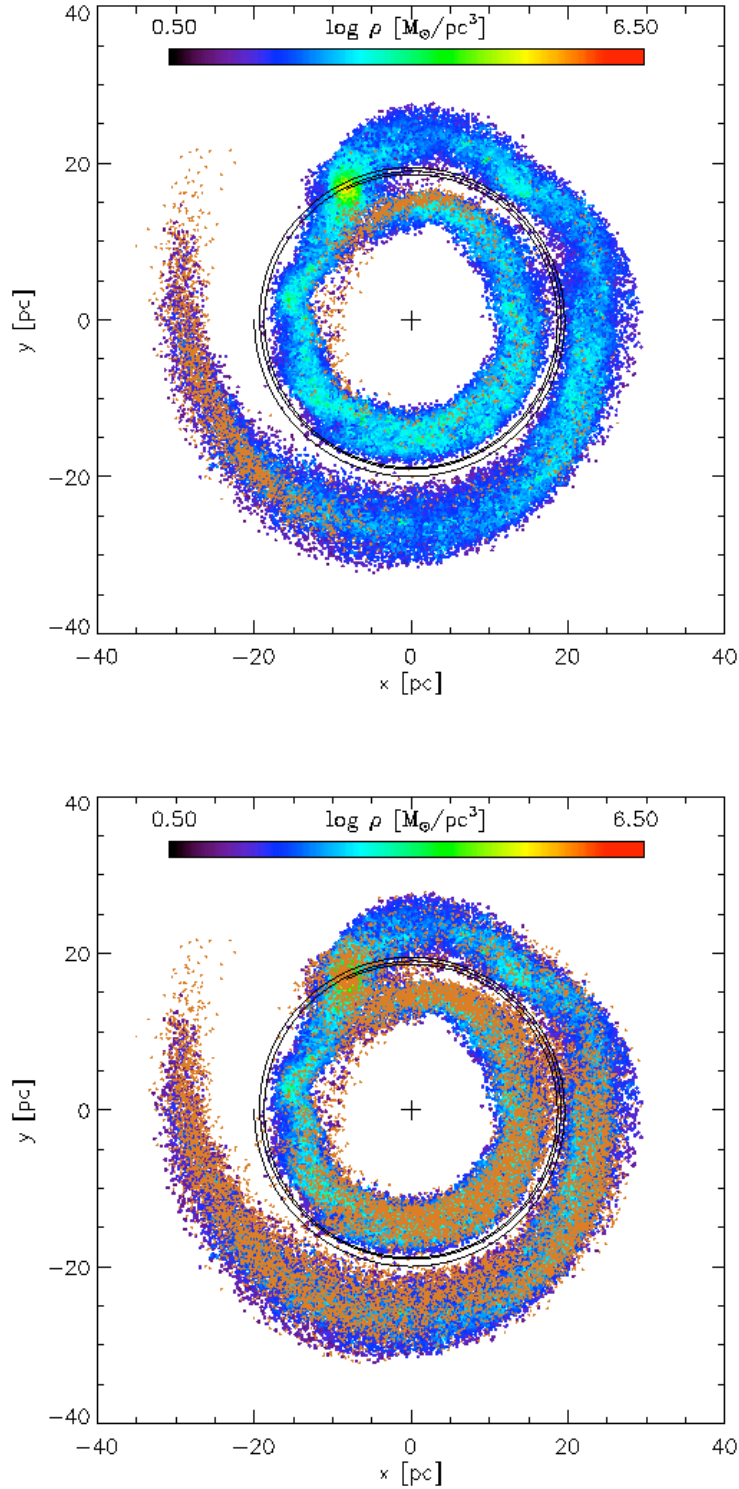


Figure 9.23: The model C9 at $t = 1.74$ Myr. The tracer particles (brown colored) have moved into the tidal arms. Top panel: The tracer particles are the particles which were initially in the LRLE region. Bottom panel: The tracer particles are those which were initially in the LRHE region.

9.4 Eccentric star cluster orbit scenario

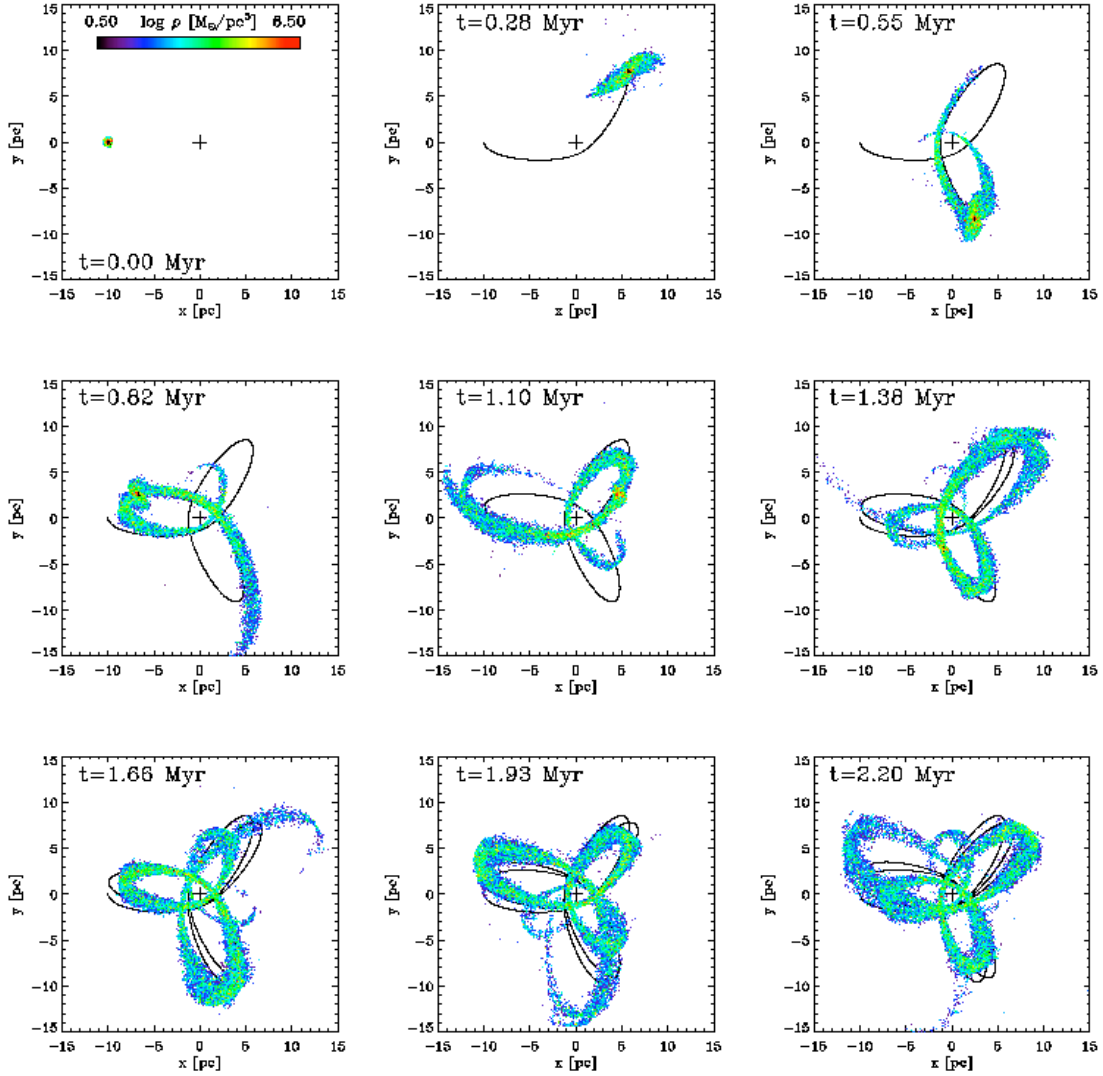


Figure 9.24: Evolution for the eccentric orbit of model E2 as snapshots from $t = 0$ Myr to $t = 2.2$ Myr. The orbit of the star cluster center is shown as a solid line.

In Section 9.2 we have seen in the case of the model C9 with the large cluster mass of $M_{cl} = 10^6 M_{\odot}$ that the inspiral time scale due to dynamical friction with the modified Coulomb logarithm according to Just & Peñarrubia (2005) [200] was very slow as compared with the dissolution time. The modified Coulomb logarithm was more than a factor of five smaller than than the value $\ln \Lambda = 10$ which had been adopted in Gerhard (2001) [31]. This fact makes the star cluster inspiral scenario improbable for circular orbits with realistic star cluster masses and realistic initial galactocentric radii.

In this section, a case of a different scenario is investigated: The eccentric star cluster orbit scenario. In this scenario, the eccentricity of the star cluster orbit is crucial for the transport of young stars into the central parsec and not the orbital decay due to dynamical friction as in

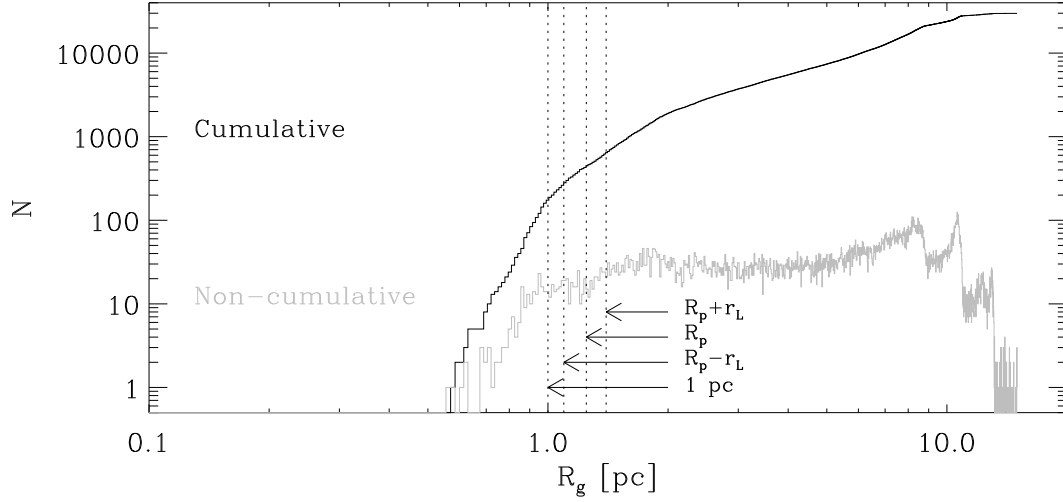


Figure 9.25: Cumulative and non-cumulative logarithmic histograms of galactocentric distances of all cluster stars at $t = 2.20$ Myr for the model E2. The pericenter radius R_p of the star cluster orbit, the tidal radius r_L of the star cluster and the central parsec are marked with dotted lines.

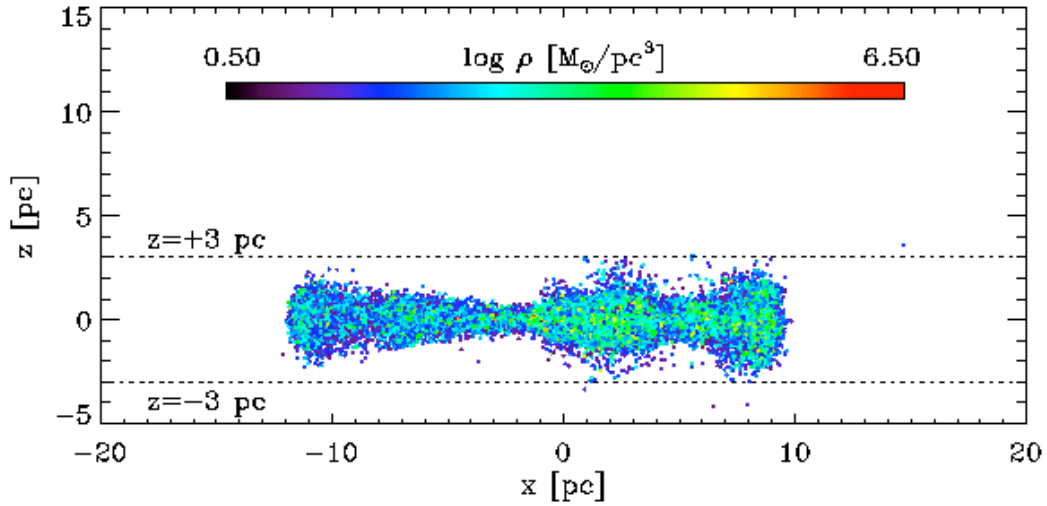


Figure 9.26: Snapshot of model E2 at $t = 2.20$ Myr in the $x - z$ plane. The dotted lines mark ± 3 pc in z -direction.

the star cluster inspiral scenario (Gerhard 2001 [31]). For the model E2, an extremely eccentric star cluster orbit with an initial galactocentric radius of $R_g(0) = 10$ pc has been chosen. The initial velocity for the model E2 is $V_g(0) = 0.25 V_c(R_g(0))$, where V_c is the circular velocity. The parameters of the scale free model of the central region of the Galactic bulge are the same as in Table 6.1 in Chapter 6. For the star cluster, a King model with $W_0 = 6$ and a half-mass radius of $r_h \approx 0.1$ pc has been adopted. For this model the physical tidal radius is initially equal to the 100% Lagrangian radius, beyond which the density of the N -body realization of the King model vanishes. The particle number is $N = 3 \times 10^4$. If we assume a mean stellar mass of $\langle m \rangle = 0.4 M_\odot$, the total mass would be $M_{cl} = 1.2 \times 10^4 M_\odot$. For such a small mass dynamical friction is not effective. It has been switched off. Therefore it was possible to switch off the density center correction as well in order to follow the evolution beyond the dissolution of the cluster.

Figure 9.24 shows snapshots of the evolution of model E2 from $t = 0$ to $t = 2.2$ Myr. The orbit of the star cluster is shown as a solid line. It can be seen that the leading tidal arm wraps around the Galactic center. The angular momentum of the stars with respect to the Galactic center is not conserved due to the symmetry breaking effect which has been mentioned in Chapter 6.⁵ While the leading arm wraps around the Galactic center, the trailing arm extends well beyond the initial apocenter radius of the orbit of the star cluster center after some time.

Figure 9.25 shows a logarithmic histogram of the galactocentric distances of the stars at $t = 2.20$ Myr. It can be seen that a fraction of stars (≈ 200) resides within the central parsec around the Galactic center. However, no star has reached a galactocentric distance smaller than 0.5 pc.

Figure 9.26 shows a snapshot of model E2 at $t = 2.20$ Myr in the $x - z$ plane. The spatial extent is less than 3 pc in both positive and negative z -direction as marked by the dotted lines. One is tempted to conclude that the stars in the central parsec resemble a disk-like configuration. A further inspection of Figure 9.24 shows that there are local maxima in the density of stars corresponding to both the galactocentric peri- and apocenter radii of the stellar orbits in the tidal arms. If the stars of the CWS (and CCWS?) have been members of a star cluster on a very eccentric orbit, it should be possible to detect additional spots of enhanced density of young stars which correspond to the galactocentric apocenter radii of the stellar orbits in the tidal arms. Since the stellar density of the background stars decreases as $\rho_g \propto R_g^{-1.8}$ outwards (Mezger, Duschl & Zylka 1996 [104]) the detection should be theoretically possible according to Figure 9.24. Thus it is conceivable to test the eccentric star cluster orbit scenario observationally.

⁵However, the theoretical framework from Chapter 6 has not yet been extended to eccentric star cluster orbits.

Chapter 10

Conclusions

The author has studied the chaotic dynamics within a star cluster on a circular orbit which is embedded in the tidal field of the Milky Way. He calculated within the framework of the tidal approximation Poincaré surfaces of section, the basins of escape and the chaotic saddle as the intersection of its stable and unstable invariant manifolds. The system is non-hyperbolic which has important consequences for the dynamics, i.e. there are orbits which do not escape if relaxation and the change of the star cluster potential with time are neglected. These are mainly the retrograde orbits as has been shown earlier by Fukushige & Heggie (2000) [5]. Since the corresponding asymmetry in the Poincaré surfaces of section is due to the Coriolis forces, it may be termed a Coriolis asymmetry (cf. Innanen 1980 [90]). The escape times are longest for initial conditions near the fractal basin boundaries. The decay law is a power law for those stars which escape from the regions without sensitive dependence on the initial conditions in Figure 3.5 (i.e. with short escape times, as can be seen in Figure 3.6). On the other hand, the decay law is exponential for orbits which escape from the regions with sensitive dependence on the initial conditions (i.e. with long escape times). The effect of relaxation (i.e. a diffusion in the Jacobi energy and the non-classical integral among different stellar orbits) and a changing star cluster potential on the chaotic dynamics which has been investigated in this work may be a very interesting topic for future research.

Also, the dissolution of star clusters in an analytic background potential of the Galactic center has been studied by means of direct N -body simulations. The author described in detail the algorithm of the new parallel N -body program NBODY6GC which is based on Sverre Aarseth's series of N -body codes (Aarseth 1999 [177], 2003 [175], Spurzem 1999 [184]). It includes a realistic dynamical friction force with a variable Coulomb logarithm based on the work by Just & Peñarrubia (2005) [200]. The initial value for the circular orbit of the model C9 is $\ln \Lambda \approx 1.7$. It turns out that, even for a $10^6 M_\odot$ cluster, the dynamical friction force is too weak to let a cluster on a circular orbit at $R_C = 20$ pc spiral into the Galactic center within the lifetime of its most massive stars.

The author has studied in detail the dynamics of dissolving star clusters on circular orbits in the Galactic center. The key to the understanding of this dynamical problem is the gravitational potential which is the superposition of the effective tidal potential and the star cluster potential. Along the orbit of the star cluster, the effective tidal potential resembles a parabolic wall. However, in the close vicinity of the Galactic center there are deviations from the parabolic shape due to higher-order terms in the Taylor expansion of the effective tidal potential around the ring of local maxima corresponding to the circular orbit. Due to this asymmetry, the Lagrange points L_1 and L_2 lie at different energies.

The properties of the tidal arms of a dissolving star cluster in the Galactic center have been studied in detail. The density wave phenomenon found by Capuzzo Dolzetta, di Matteo & Mocchi (2005) [11] and di Matteo, Capuzzo Dolzetta & Mocchi (2005) [9] appears in our model C9. The

angles of the clumps can be calculated with the analytical theory in Just et al. (2009) [13] and Chapter 4.

The author has presented a method to study the structure of tidal arms by using an eigensolver. The eigensolver computes numerically a 1D coordinate system along the tidal arms and evaluates characteristic dynamical quantities along this coordinate system.

The half-mass times of the author's models C1 - C9 depend only weakly on the particle number which indicates that two-body relaxation is not the dominant mechanism leading to the dissolution. The reason is that the initial models are divided into four different regions in radius and specific Jacobi energy space. This division has been termed the Radius-Energy (RE) classification. The division of a newly formed star cluster into the four regions of the RE classification is probably a typical situation according to the modern picture of gravoturbulent star formation (e.g. Mac Low & Klessen 2004 [212], Ballesteros-Paredes et al. 2007 [213]). If the ratio α_M (which has been defined in Section 9.3) is large enough, the dissolution is no longer relaxation-driven but the mass loss is governed by a self-regulating process of increasing Jacobi energy due to the weakening of the potential well of the star cluster, which is induced by the mass loss itself (Just et al. 2009 [13]).

It may be of interest to note that more particles escape into the trailing tidal arm than into the leading tidal arm. For the high-energy particles the phase space for escape into the trailing arm is larger than that for escape into the leading arm. The reason is probably non-trivial. A 3D computation of the basins of escape can shed light on this issue.

Finally, the author briefly investigated a case of the eccentric star cluster orbit scenario. In this scenario, the eccentricity of the star cluster orbit is crucial for the transport of young stars into the central parsec of our Galaxy and not the orbital decay due to dynamical friction. The eccentric star cluster orbit scenario can be tested observationally by the detection of spots of enhanced density of young stars corresponding to the galactocentric apocenters of the stellar orbits in the tidal arms.

Appendix A

Useful expressions

A.1 Constants and units

$$\begin{aligned} 1 \text{ pc} &= 3.08567802 \times 10^{18} \text{ cm} \\ 1 \text{ Myr} &= 3.1558149984 \times 10^{13} \text{ sec} \\ 1 M_{\odot} &= 1.989 \times 10^{33} \text{ g} \\ G &= 6.672 \times 10^{-8} \text{ cm}^3 \text{g}^{-1} \text{ sec}^{-2}, \\ &= (222.3)^{-1} \text{ pc}^3 M_{\odot}^{-1} \text{ Myr}^{-2} \\ 1 \text{ pc Myr}^{-1} &= 0.977775320 \text{ km sec}^{-1} \\ 1 \text{ km sec}^{-1} &= 1.02272984 \text{ pc Myr}^{-1} \end{aligned}$$

A.2 Formulas

$$\cos(\arctan \phi) = \frac{1}{\sqrt{1 + \phi^2}} \quad (\text{A.1})$$

$$\sin(\arctan \phi) = \frac{\phi}{\sqrt{1 + \phi^2}} \quad (\text{A.2})$$

$$\cos\left(\frac{\phi}{2}\right) = \sqrt{\frac{1 + \cos \phi}{2}} \quad (\text{A.3})$$

$$\sin \phi = 2 \sin\left(\frac{\phi}{2}\right) \cos\left(\frac{\phi}{2}\right) \quad (\text{A.4})$$

$$\arcsin(1) = \arccos(0) = 2 \arctan(1) = \frac{\pi}{2} \quad (\text{A.5})$$

$$\int_0^{2\pi} \cos \theta \, d\theta = \int_0^{2\pi} \sin \theta \, d\theta = 0 \quad (\text{A.6})$$

$$\int_0^{b_1} \frac{b \, db}{b_0^2 + b^2} = \frac{1}{2} \ln \left(1 + \frac{b_1^2}{b_0^2} \right) \quad (\text{A.7})$$

$$\ln(1 + \Lambda^2) \approx 2 \ln \Lambda \quad \text{for } \Lambda \gg 1 \quad (\text{A.8})$$

Appendix B

Basins of attraction

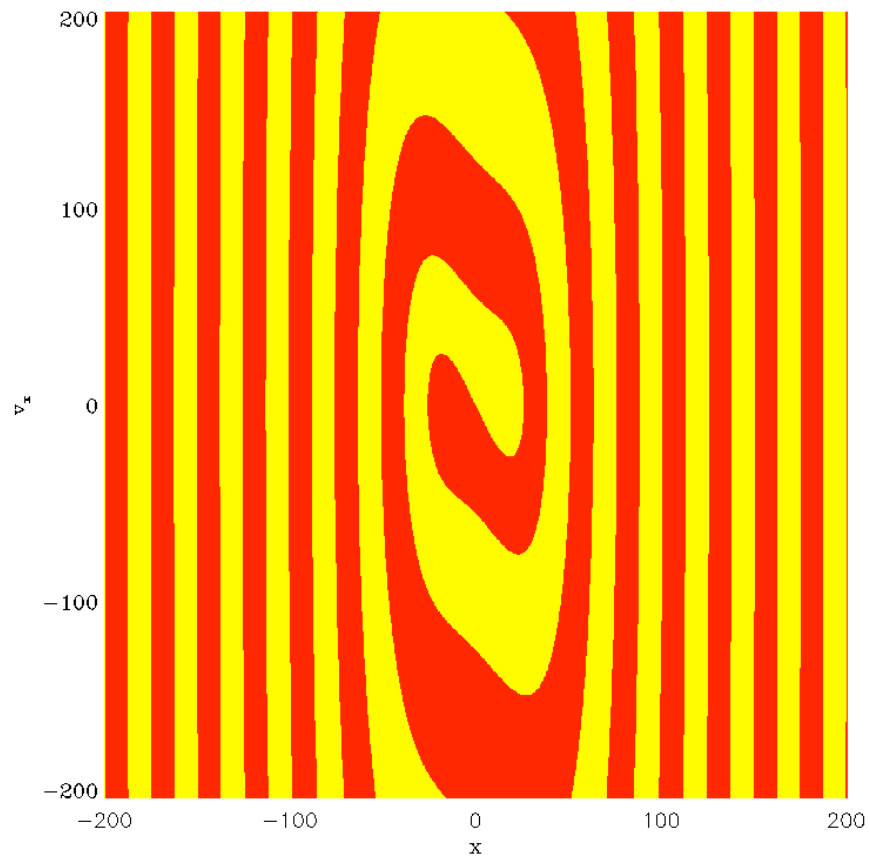


Figure B.1: Example of basins of attraction for the motion of a particle in a double well potential $\Phi(x) = -\alpha x^2 + \beta x^4$ ($\alpha = 1, \beta = 1/400$) with a simple friction force $f(v_x) = -v_x/\tau_{\text{fric}}$, where v_x is the velocity and $\tau_{\text{fric}} = 1$ is a time scale. The two colors denote the two potential wells in which the particle can be captured.

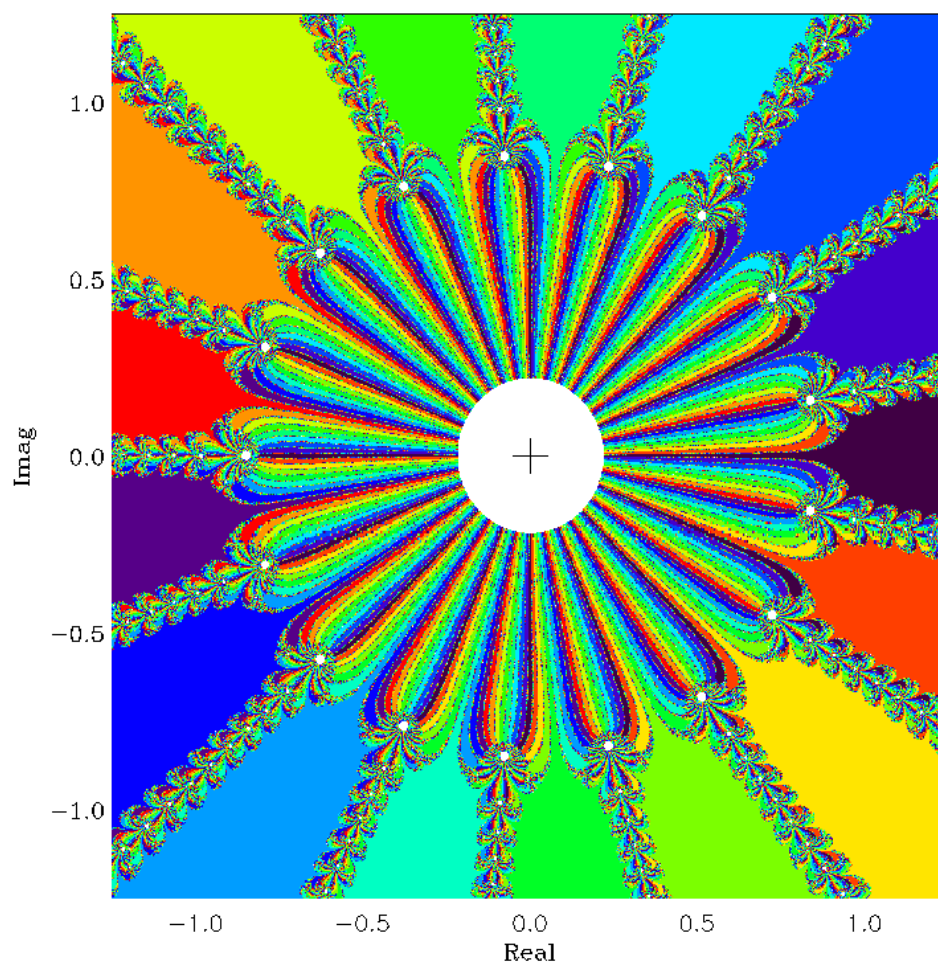


Figure B.2: Newton-Raphson fractal for the algebraic equation $x^{17} = 1$. The 17 colors denote the basins of attraction of the roots in the complex plane. In 1796, Gauß showed how to construct the corresponding polygon with 17 corners with compass and straightedge.

Appendix C

GRID computing

Today, in the 21th century, large-scale scientific research relies heavily on High-Performance Computing (HPC). Massively parallel supercomputer architectures exist in most European countries, providing an infrastructure for scientific computing in many fields of science, including astrophysics. The idea that all these supercomputers could be connected to one huge European GRID led to the DEISA initiative (“Distributed European Infrastructure for Supercomputing Applications”). A similar GRID initiative called TeraGrid exists in the US. In addition, there are smaller GRID initiatives on a national level in many countries including the D-GRID initiative in Germany, which is subdivided into smaller community projects corresponding to different branches of science, e.g. the AstroGrid-D for astrophysical applications.

The N -body simulations which are presented in this thesis have been carried out on supercomputers within the DEISA GRID. For the historian, the author lists some of the properties of the systems which were used.

Properties of the “Jump” system (see Figure C.1):

- Location: Research Center Jülich, Germany
- IBM p690 system
- 1312 Power4+ processors with 1.7 GHz
- 32 processors and 128 GB memory per node
- Gigabit-Ethernet network with 10 Gbit/s bandwidth
- Peak performance: 8.9 Tflops/s

Properties of the “Louhi” system (see Figure C.2):

- Location: CSC Espoo, Finland
- Cray XT4 system
- 1012 dual-core AMD Opteron 2.6 GHz compute nodes
- 1 GB memory per core
- Cray SeaStar2™ interconnect with 6.4 GB/s bandwidth
- Peak performance: 10.5 Tflops/s



Figure C.1: The IBM p690 cluster “Jump” at the John von Neumann Institute for Computing at the Research Center Jülich, Germany.



Figure C.2: The Cray XT4 system “Louhi” at CSC, Finland.

Properties of the “Huygens” system (see Figure C.3):

- Location: SARA Computing and Networking Services, Amsterdam, the Netherlands
- IBM clustered SMP system
- 1920 Power5+ processors with 1.9 GHz
- 8 processors and 64 GB memory per node
- Infiniband network with $4.5 \mu\text{s}$ latency and 1.2 GB/s bandwidth
- Peak performance: 14.6 Tflops/s



Figure C.3: The IBM cluster “Huygens” at SARA, the Netherlands.

Appendix D

Dynamical friction

Historically, dynamical friction has been derived in Chandrasekhar (1943) [218]. Dynamical friction is the result of a polarization effect as is illustrated in the sketch on the left-hand side of Figure D.1. If a massive particle moves with a certain velocity through a medium of light particles, the orbits of the light particles will be deflected, and a polarization cloud of light particles forms behind the massive perturber. This “wake” decelerates the perturber by exerting a gravitational force on it.

In the derivation of dynamical friction in the classical particle picture the author follows the excellent lecture notes by Hénon (1973) [219] and the treatment in Binney & Tremaine 1987 [32]. The test particle which suffers the dissipative drag force will be labelled with subscript “1” and the field particles with subscript “2”. Suppose the test particle with mass m_1 is moving with relative velocity \mathbf{v}_{21} (with respect to the field particles) along the x axis (see Figure D.2) encountering field particles with mass m_2 which deflect it.

At first we consider one single encounter and use the classical theory of the two-body problem. The sketch on the right-hand side of Figure D.1 depicts a hyperbolic encounter between two particles and shows the quantities which are involved. After one encounter the velocity of the test star will be deflected by an angle β which is given by

$$\tan\left(\frac{\beta}{2}\right) = \frac{G(m_1 + m_2)}{bv_{21}^2} = \frac{b_0}{b} \quad (\text{D.1})$$

where G is the gravitational constant, b the impact parameter and $b_0 = G(m_1 + m_2)/v_{21}^2$ a fundamental length scale of the problem. It is the impact parameter where the deflection equals 90 degrees. We switch now into the center of mass system between the test particle and one field particle it encounters. In this system, the velocities of the test particle and the field particle, respectively, are given by

$$\mathbf{v}_1 = \frac{m_2 \mathbf{v}_{21}}{m_1 + m_2} \quad \mathbf{v}_2 = -\frac{m_1 \mathbf{v}_{21}}{m_1 + m_2} \quad (\text{D.2})$$

Assuming that all field stars have velocity \mathbf{v}_2 , the situation can be depicted as in the sketch in Figure D.2. It is convenient to introduce a system of cylindrical coordinates x, b, θ . After one encounter, the velocity of the test particle will be deflected by an angle β given by (D.1) in the plane xOP . The velocity of the test star after one encounter will be \mathbf{v}'_1 :

$$\mathbf{v}_1 = \begin{pmatrix} v_1 \\ 0 \\ 0 \end{pmatrix}, \quad \mathbf{v}'_1 = \begin{pmatrix} v_1 \cos \beta \\ v_1 \sin \beta \cos \theta \\ v_1 \sin \beta \sin \theta \end{pmatrix} \quad (\text{D.3})$$

Thus the velocity change is given by

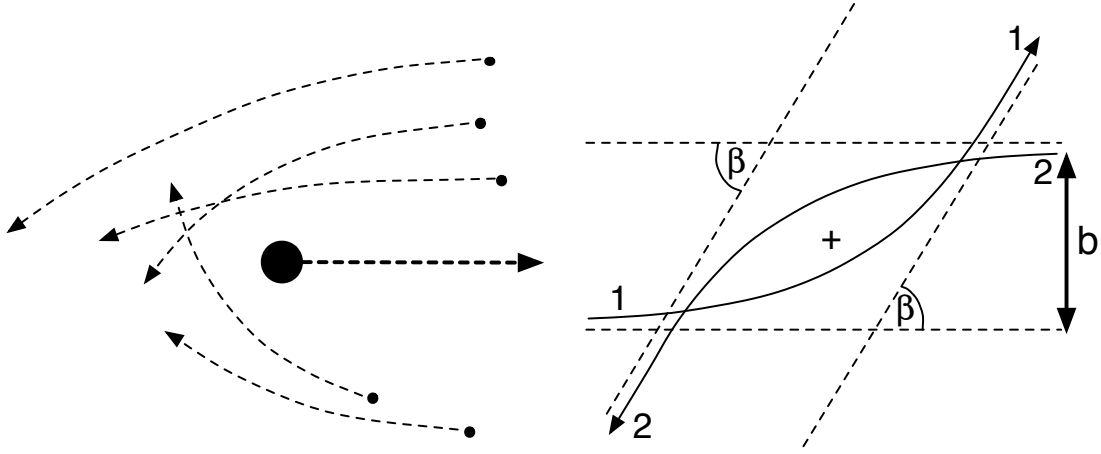


Figure D.1: Left sketch: A polarization cloud forms. Right sketch: Hyperbolic encounter between two stars.

$$\Delta \mathbf{v}_1 = \mathbf{v}'_1 - \mathbf{v}_1 = v_1 \begin{pmatrix} \cos \beta - 1 \\ \sin \beta \cos \theta \\ \sin \beta \sin \theta \end{pmatrix} = \frac{2v_1}{b_0^2 + b^2} \begin{pmatrix} -b_0^2 \\ b_0 b \cos \theta \\ b_0 b \sin \theta \end{pmatrix} \quad (\text{D.4})$$

where we have used the trigonometric identities (A.1), (A.3) and (A.4) given in Appendix A in the last step.

So far we have considered only one encounter. We apply now the statistics over many encounters. The differential probability for the test star to encounter a field star with impact parameter b and angle θ within a time interval dt is simply

$$dp = n\sigma v_{21} dt \quad (\text{D.5})$$

where the number density n of field stars and the cross section σ are given by

$$n = \int f(v_2) d^3 v_2, \quad \sigma = b db d\theta, \quad (\text{D.6})$$

and $f(v_2)$ is the phase space distribution function of field stars.

The mean velocity change is then given by

$$\begin{aligned} \langle \Delta \mathbf{v}_1 \rangle &= \int \Delta \mathbf{v}_1 dp \\ &= \int_0^{2\pi} \int_0^{b_1} \frac{2v_1}{b_0^2 + b^2} \begin{pmatrix} -b_0^2 \\ b_0 b \cos \theta \\ b_0 b \sin \theta \end{pmatrix} n b db d\theta v_{21} dt \\ &= -\frac{2\pi G^2 (m_1 + m_2) m_2}{v_{12}^2} \frac{\mathbf{v}_{21}}{v_{21}} \ln \left(1 + \frac{b_1^2}{b_0^2} \right) \begin{pmatrix} 1 \\ 0 \\ 0 \end{pmatrix} dt \int_0^{v_{21}} f(v_2) d^3 v_2 \quad (\text{D.7}) \end{aligned}$$

where b_1 is the maximum impact parameter and we have used the integrals (A.6) and (A.7) given in Appendix A in the last step. The non-vanishing mean change of velocity in the direction opposite to the velocity itself is called dynamical friction. We define the ratio of maximum and

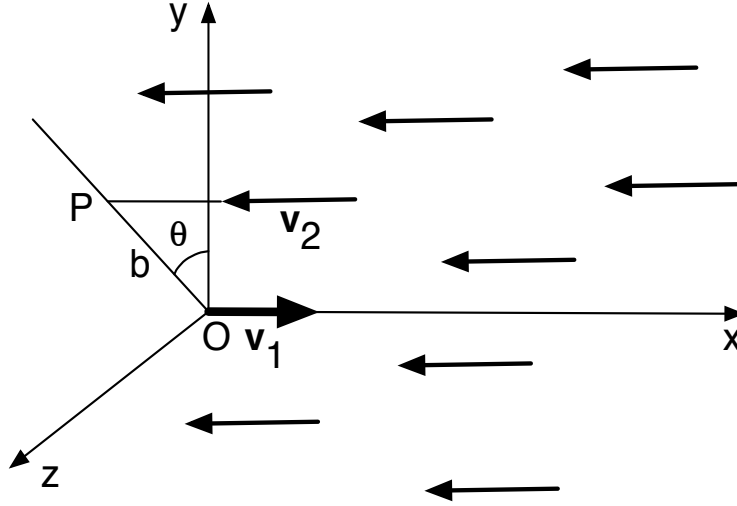


Figure D.2: Sketch of the coordinate systems. It is convenient to introduce a system of cylindrical coordinates x, b, θ . After one encounter, the velocity of the test particle will be deflected by an angle β given by Equation (D.1) in the plane xOP .

minimum impact parameters as $\Lambda = b_1/b_0$ and use the approximation (A.8) given in the Appendix to simplify the argument of the logarithm. For a Maxwellian distribution of field stars, the integral over velocity space is readily carried out. The dynamical friction is then given by

$$\frac{d\mathbf{v}_1}{dt} = -\frac{4\pi G^2(m_1 + m_2)m_2 \ln \Lambda n_0}{v_1^2} \left[\operatorname{erf}(X) - \frac{2X}{\sqrt{\pi}} \exp(-X^2) \right] \frac{\mathbf{v}_1}{v_1} \quad (\text{D.8})$$

where $X = v_1/(\sqrt{2}\sigma)$ and we have dropped the subscript “2”.

D.1 Variable Coulomb logarithm

The Coulomb logarithm is the result of an integration over impact parameters. A variable Coulomb logarithm has been introduced by Just & Peñarrubia (2005) [200]. A crucial assumption in the derivation of dynamical friction is the local approximation of the distribution function of field stars. It is the notion that there exists an infinite homogeneous medium of field stars whose distribution function is everywhere equal to the local distribution function (Binney & Tremaine 1987 [32], p. 510). The expression in (D.6) for the number density n of field stars is essentially based on the local approximation of the distribution function which breaks down if the maximum impact parameter b_1 is larger than the local scale length L of the density profile, i.e. one should postulate that

$$b_1 < L = \frac{n}{|\nabla n|} = \frac{\rho}{|\nabla \rho|}. \quad (\text{D.9})$$

where n and ρ are number and mass densities, respectively. Thus, the local scale length of the density profile serves as a physically significant upper cutoff of the integral over impact parameters.

D.2 Realistic χ function

The χ function is the result of an integration over velocity space. It is given by

$$\chi = \int_0^{v_1} f(v_2) d^3 v_2. \quad (\text{D.10})$$

It depends on the velocity v_1 of the test particle through the upper limit in the integral and is not constant for eccentric orbits of the test particle. The χ function is shown for different models in Figure D.3. For the Plummer model with a flat core, the χ function is given by the analytical expression (2.41). In the derivation of dynamical friction we used a Maxwellian velocity distribution. For the Dehnen and Hernquist models, which are suitable for cuspy galactic bulges (see Hernquist 1990 [220], Dehnen 1993 [221], Tremaine et al. 1994 [222]) the integral has to be calculated numerically.

The spherically symmetric Dehnen models (Dehnen 1999 [221], Tremaine et al. 1994 [222]) are characterized by a dimensionless parameter γ and a length scale a . We define the following quantities,

$$\Phi_0 = \frac{GM}{a}, \quad v_e(r) = \sqrt{2|\Phi(r)|}, \quad x = \frac{v}{v_e}, \quad p = \frac{\Phi}{\Phi_0}, \quad y = p(1 - x^2) \quad (\text{D.11})$$

where Φ_0 is the energy unit, G is the gravitational constant, M is the total mass, v_e is the escape speed, $\Phi(r)$ is the potential and x , p and y are the dimensionless velocity, potential and energy, respectively. The distribution function of the Hernquist model which is a special case of the Dehnen model with $\gamma = 1$ is (Hernquist 1990 [220])

$$f(y) = \frac{M}{4(2\pi^2 GMa)^{3/2}} \frac{1}{(1-y)^{5/2}} \left[3 \arcsin(\sqrt{y}) - \sqrt{y(1-y)} (3 + 2y - 24y^2 + 16y^3) \right] \quad (\text{D.12})$$

and we have

$$p_{\max} = -\Phi(0)/\Phi_0 = 1, \quad x_{\max} = 1, \quad (\text{D.13})$$

since the potential for Dehnen models with $\gamma < 2$ is finite at $r = 0$. The distribution function for the Dehnen model with $\gamma = 3/2$ is (Dehnen 1993 [221])

$$f(y) = \frac{3M}{2(2\pi^2 GMa)^{3/2}} \frac{\sqrt{y}}{(2-y)^4} \left[-\frac{9}{16} - \frac{99}{16}y + \frac{405}{8}y^2 - \frac{3705}{56}y^3 + \frac{561}{14}y^4 - \frac{181}{14}y^5 \right. \\ \left. + \frac{15}{7}y^6 - \frac{1}{7}y^7 + \frac{3(3+32y-8y^2)}{8\sqrt{y(2-y)}} \arcsin\left(\sqrt{\frac{y}{2}}\right) \right] \quad (\text{D.14})$$

and we have

$$p_{\max} = -\Phi(0)/\Phi_0 = 2, \quad x_{\max} = 1. \quad (\text{D.15})$$

Using the trapezoidal rule, we can numerically integrate over velocity space by calculating

$$y(p, x) = p(1 - x^2) \\ \chi(p, x) = \int_0^x f(y(p, x')) x'^2 dx' \quad (\text{D.16})$$

This gives the χ functions for dynamical friction which are shown in Figure (D.3).

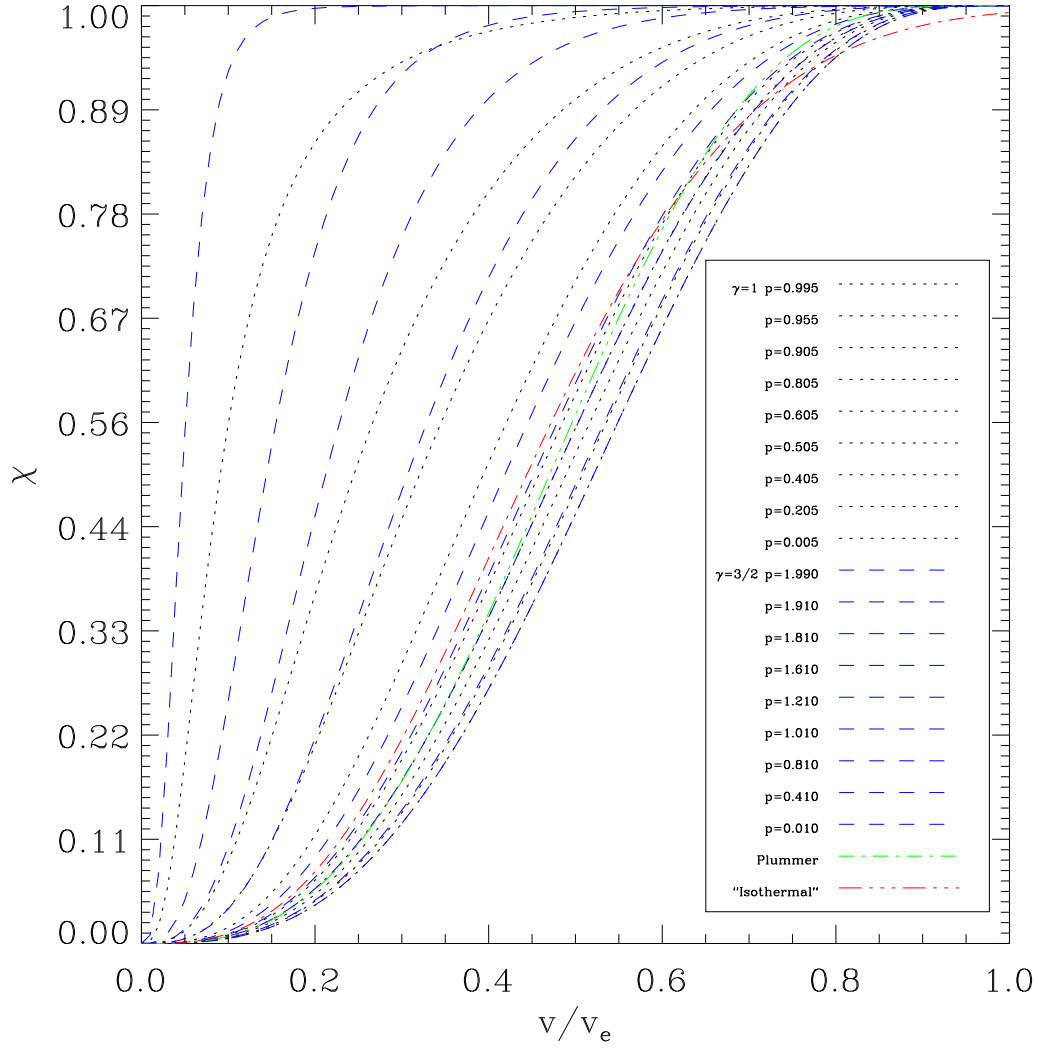


Figure D.3: The χ function for dynamical friction for different models of stellar systems. The quantities v , v_e and p are the velocity, the escape velocity and the potential in units of the central potential, respectively. For the Hernquist and Dehnen models, the normalized potential decreases from left to right. For the singular isothermal sphere we made the ad hoc assumption that the isothermal sphere were of finite mass and in virial equilibrium (i.e., $\langle v_e^2 \rangle = 12\sigma_2^2$) which makes it possible to define an escape velocity from the velocity dispersion. The data for the Hernquist and Dehnen models are by A. Just (priv. comm.).

Appendix E

New Subroutines

Subroutine	Function	Called by subroutine
GALCEN	GC external force on star cluster	REGINT, KSPERT
GCBULGE	Calculates all bulge quantities	OUTPUT, GCINIT, GCINT, GCCHECK, GCLMASS, GCCHI, GCXCOUL
GCCHECK	GC energy check	ADJUST, OUTPUT
GCCHI	Calculates current value of χ	GCINT, OUTPUT
GCENERGY	Calculate GC energy	GCCHECK, GCINIT, GCINT, GCLMASS
GCFORCE	Calculate GC force	GCINIT, GCINT, GALCEN
GCFPR	Time transformation (optional)	GCINIT, GCINT
GCINIT	GC initializations	START
GCINT	GC integrator	INTGRT
GCIPOLE	Interpolation of GC jerk	GCINT
GCLMASS	Update star cluster mass and memberships	GCINIT, GCINT
GCXCOUL	Calculates current value of $\ln \Lambda$	GCINIT, OUTPUT

Table E.1: New subroutines of NBODY6GC.

Appendix F

Input file: galcen.dat

```
1.0 0.0 0.25 25.0 2.0 2
0 7 1 2 10.0 1.0
0.589048 100. 0. 1.2 0.1 10.0 10.0
```

```
ETAG,GAMMA,VCIRC,RGAL,XTIDAL,ICLUST
NBULGE,NCB,NCHI,VARI,XCOUL,QFIT
CB(K)
```

ETAG: Accuracy parameter for GC integration
GAMMA: Optional potential energy exponent for time transformation
(=0.0 constant time steps)
VCIRC: Tangential cluster velocity in units of circular velocity at
cluster position (=1.0 circular orbit)
RGAL: Distance of cluster from GC in units of the virial cluster radius
XTIDAL times RTIDAL is assumed as spherical cluster boundary
ICLUST select how to treat cluster mass:
=0 constant mass
=1 tidal radius approximation using XTIDAL
=2 with tidal radius and dyn. fr. only for cluster members
NBULGE: Bulge model (see model-par.txt)
NCB: Number of CB(K) parameters
NCHI: Type of Chi function for dynamical friction (see model-par.txt)
VARI: Type of variable Coulomb logarithm (see model-par.txt)
XCOUL: Coulomb Logarithm
QFIT: Fitting factor for Coulomb Logarithm [see Just & Penarrubia,
A&A 431, 861 (2005)]
CB(K): Bulge parameters (see model-par.txt)

Appendix G

Documentation file: model-par.txt

NBULGE: Type of bulge

- 0 Scale free with black hole
- 1 Kepler
- 2 Homogeneous sphere
- 3 Isothermal with core and cutoff
- 4 Dehnen model
- 5 Plummer model
- 6 Scale free without black hole

NCHI: Type of chi function

- 0 from file $\chi(v,\phi)$ (e.g. Dehnen models)
- 1 Maxwell with $2\sigma^2 = v_{\text{c}} r_{\text{h}}^2$
- 2 King model (not yet implemented)
- 3 Plummer model

VARI: Type of Coulomb logarithm

- 0 fixed Coulomb logarithm
- 1 linearly increasing during first orbit?
- 2 variable Coulomb logarithm [Just & Penarrubia, A&A 431, 861 (2005)]

CB(K): Bulge parameter in N-body units

- 1 r_{core} (isothermal), a (Dehnen, Plummer)
- 2 r_{cut} (isothermal, Dehnen)
- 3 σ_0 (isothermal)
- 4 Power index for galactic bulge mass profile (Scale free)
 γ (Dehnen)
- 5 ρ (homogeneous sphere)
- 6 Galactic bulge mass at 1 pc (Scale free)
Total mass in units of star cluster mass (Dehnen, Plummer, isothermal)
- 7 Black hole mass (Scale free, Kepler)

Appendix H

Setting up a run

Choose star cluster parameters:

1. Particle number N
2. Type of model (King, Plummer) $\rightarrow r_h/r_V$ [see Table 1 in Gürkan (2004) [164]]
3. Half-mass radius r_h [pc] $\rightarrow r_V$ [pc], RBAR
4. Star cluster mass M_{cl} [M_\odot] \rightarrow ZMBAR

Choose bulge parameters:

1. Type of model (Scale free, Dehnen, Kepler, Plummer)
2. CB constants (see model-par.txt, note that some constants depend on M_{cl} !)

Choose dynamical friction treatment

1. Fixed / Variable Coulomb logarithm
2. Type of χ function

Choose initial conditions of star cluster orbit:

1. Initial galactocentric radius $R_g(0)$ [r_V]
2. Initial velocity $V_g(0)$ [V_c]

Determine time scales:

1. N -body time unit $t_V \approx \sqrt{222.3 \text{ RBAR}^3 / \text{ZMBAR}} \text{ Myr}$
2. Orbital time scale of star cluster t_{orb} (use INTGC)
3. Half-mass relaxation time $t_{\text{rh}} \approx 0.192N / \ln(\gamma N) t_V$
4. Crossing time inside the star cluster $t_{\text{cr}} = 2\sqrt{2} t_V$

Appendix I

Abbreviations

Abbreviation	Meaning
ARI	Astronomisches Rechen-Institut, Heidelberg, Germany
BCH	Baker-Campbell-Hausdorff (identity)
CMZ	Central molecular zone
CWS	Clockwise system
CCWS	Counter clockwise system
DEISA	Distributed European Infrastructure for Supercomputing Applications
GC	Galactic center
HPC	High performance computing
IMBH	Intermediate-mass black hole
IRS	Infrared source
KS	Kustaanheimo-Stiefel (regularization)
LBV	Luminous Blue Variable
LRHE	Large Radius High Energy (region)
LRLE	Large Radius Low Energy (region)
NR	Numerical Recipes in Fortran 77, Press et al. (2001) [199]
RE	Radius-Energy (classification)
SMBH	Supermassive black hole
SRHE	Small Radius High Energy (region)
SRLE	Small Radius Low Energy (region)
SNR	Supernova remnant
ULX	Ultra-luminous X-ray source

Table I.1: Abbreviations used in this thesis.

Bibliography

- [1] V. A. Ambartsumian, *Ann. Leningrad State Univ.* **22**, 19 (1938).
- [2] L. Spitzer, *MNRAS* **100**, 396 (1940).
- [3] A. Ernst, Diplomarbeit, University of Heidelberg, 2005.
- [4] A. Ernst *et al.*, *MNRAS* **377**, 465 (2007).
- [5] T. Fukushige and D. C. Heggie, *MNRAS* **318**, 753 (2000).
- [6] G. Cantor, *Acta Mathematica* **4**, 381 (1884).
- [7] G. Contopoulos, *Order and Chaos in Dynamical Astronomy* (Springer, Berlin, 2002).
- [8] M. Odenkirchen *et al.*, *Astron. J.* **126**, 2385 (2003).
- [9] P. di Matteo, R. Capuzzo Dolcetta, and P. Miocchi, *Celestial Mechanics and Dynamical Astronomy* **91**, 59 (2005).
- [10] M. Odenkirchen *et al.*, *Ap. J. Lett.* **548**, L165 (2001).
- [11] R. Capuzzo Dolcetta, P. Di Matteo, and P. Miocchi, *Astron. J.* **129**, 1906 (2005).
- [12] A. H. W. Küpper, A. MacLeod, and D. C. Heggie, *MNRAS* **387**, 1248 (2008).
- [13] A. Just, P. Berczik, M. Petrov, and A. Ernst, *MNRAS* **392**, 969 (2009).
- [14] M. Morris and E. Serabyn, *Ann. Rev. Astron. Astrophys.* **34**, 645 (1996).
- [15] T. Nagata *et al.*, *Ap. J.* **351**, 83 (1990).
- [16] H. Okuda *et al.*, *Ap. J.* **351**, 89 (1990).
- [17] T. Nagata, C. E. Woodward, M. Shure, and N. Kobayashi, *Astron. J.* **109**, 1696 (1995).
- [18] F. Yusef-Zadeh, M. Morris, and D. Chance, *Nature* **310**, 557 (1984).
- [19] R. Timmermann *et al.*, *Ap. J.* **466**, 242 (1996).
- [20] C. C. Lang, K. E. Johnson, W. M. Goss, and L. F. Rodríguez, *Astron. J.* **130**, 2185 (2005).
- [21] R. F. Coker, J. M. Pittard, and J. H. Kastner, *Astron. Astrophys.* **383**, 568 (2002).
- [22] J. P. Maillard, T. Paumard, S. R. Stolovy, and F. Rigaut, *Astron. Astrophys.* **423**, 155 (2004).
- [23] P. Tamblyn and G. H. Rieke, *Ap. J.* **414**, 573 (1993).
- [24] A. Krabbe *et al.*, *Ap. J.* **447**, L95 (1995).

- [25] J. R. Lu *et al.*, *Ap. J.* **625**, L51 (2005).
- [26] K. Mužić *et al.*, **482**, 173 (2008).
- [27] A. M. Ghez *et al.*, *Ap. J.* **620**, 744 (2005).
- [28] F. Eisenhauer *et al.*, *Ap. J.* **628**, 246 (2005).
- [29] M. Morris, *Ap. J.* **408**, 496 (1993).
- [30] A. M. Ghez *et al.*, *Ap. J. Lett.* **586**, L127 (2003).
- [31] O. Gerhard, *Ap. J.* **546**, L39 (2001).
- [32] J. Binney and S. Tremaine, *Galactic Dynamics* (Princeton University Press, Princeton, New Jersey, USA, 1987).
- [33] L. Spitzer and J. M. Shull, *Ap. J.* **200**, 339 (1975).
- [34] H. C. Plummer, *MNRAS* **71**, 460 (1911).
- [35] M. Miyamoto and R. Nagai, *PASJ* **27**, 533 (1975).
- [36] H. Dejonghe, *MNRAS* **224**, 13 (1987).
- [37] I. R. King, *Astron. J.* **71**, 64 (1966).
- [38] A. Ernst, A. Just, R. Spurzem, and O. Porth, *MNRAS* **383**, 897 (2008).
- [39] S. Chandrasekhar, *Principles of Stellar Dynamics* (University of Chicago Press, Chicago, USA, 1942).
- [40] I. R. King, *Astron. J.* **64**, 351 (1959).
- [41] M. Hénon, *Ann. Astrophys.* **23**, 668 (1960).
- [42] M. Hénon, *Astron. Astrophys.* **2**, 151 (1969).
- [43] W. M. Tscharnuter, *Ap&SS* **14**, 11 (1971).
- [44] L. J. Spitzer and S. L. Shapiro, *Ap. J.* **173**, 529 (1972).
- [45] R. Wielen, in *Gravitational N-body problem, Proceedings of IAU Colloquium 10* (Reidel Publishing Company, Dordrecht, 1972).
- [46] R. Wielen, in *Stars and the Milky Way System. Proceedings of the First European Astronomical Meeting, Athens, Sept. 4-9, 1972*, edited by L. N. Mavridis (Springer, Berlin, 1974), Vol. 2, p. 326.
- [47] H. Baumgardt, *MNRAS* **325**, 1323 (2001).
- [48] R. Spurzem, M. Giersz, K. Takahashi, and A. Ernst, *MNRAS* **364**, 948 (2005).
- [49] D. L. Rod, *J. Diff. Eq.* **14**, 129 (1973).
- [50] R. C. Churchill, G. Pecelli, and D. L. Rod, *J. Diff. Eq.* **17**, 329 (1975).
- [51] G. Contopoulos, *Astron. Astrophys.* **231**, 41 (1990).
- [52] G. Contopoulos and D. Kaufmann, *Astron. Astrophys.* **253**, 379 (1992).
- [53] C. Siopis, H. E. Kandrup, and G. Contopoulos, *Cel. Mech. Dyn. Astron.* **65**, 57 (1997).

- [54] J. F. Navarro and J. Henrard, *Astron. Astrophys.* **369**, 1112 (2001).
- [55] J. Schneider, T. Tél, and Z. Neufeld, *Phys. Rev. E* **66**, 066218 (2002).
- [56] B. Eckhardt and C. Jung, *J. Phys. A: Math. Gen.* **19**, L829 (1986).
- [57] C. Jung, *J. Phys. A: Math. Gen.* **20**, 1719 (1987).
- [58] C. Jung and H. J. Scholz, *J. Phys. A: Math. Gen.* **20**, 3607 (1987).
- [59] B. Eckhardt, *J. Phys. A: Math. Gen.* **20**, 5971 (1987).
- [60] C. Jung and S. Pott, *J. Phys. A: Math. Gen.* **22**, 2925 (1989).
- [61] S. Bleher, E. Ott, and C. Grebogi, *Phys. Rev. Lett.* **63**, 919 (1989).
- [62] C. Jung and E. Ziemniak, *J. Phys. A: Math. Gen.* **25**, 3929 (1992).
- [63] E. Ott *et al.*, *Phys. Rev. Lett.* **71**, 4134 (1993).
- [64] J. C. Sommerer and E. Ott, *Nature* **365**, 138 (1993).
- [65] J. C. Sommerer and E. Ott, *Phys. Lett. A* **214**, 243 (1996).
- [66] S. Bleher, C. Grebogi, E. Ott, and R. Brown, *Phys. Rev. A* **38**, 930 (1988).
- [67] A. P. S. D. Moura and P. S. Letelier, *Phys. Lett. A* **256**, 362 (1999).
- [68] J. Aguirre, J. C. Vallejo, and M. A. F. Sanjuán, *Phys. Rev. E* **64**, 066208 (2001).
- [69] J. Aguirre and M. A. F. Sanjuán, *Phys. Rev. E* **67**, 056201 (2003).
- [70] J. Aguirre, J. C. Vallejo, and M. A. F. Sanjuán, *Int. J. Mod. Phys. B* **17**, 4171 (2003).
- [71] J. Aguirre, Ph.D. thesis, Universidad Rey Juan Carlos, Spain, 2003.
- [72] J. M. S. Sepúlveda, Ph.D. thesis, Universidad Rey Juan Carlos, 2007.
- [73] Y. C. Lai, *Phys. Rev. E* **56**, 6531 (1997).
- [74] B. R. Hunt, E. Ott, and J. A. Yorke, *Phys. Rev. E* **54**, 4819 (1996).
- [75] Y. C. Lai, C. Grebogi, J. A. Yorke, and I. Kan, *Nonlinearity* **6**, 779 (1993).
- [76] A. E. Motter and Y. C. Lai, *Phys. Rev. E* **65**, 015205 (2001).
- [77] K. Stumpff, *Himmelsmechanik, Vol. 2* (VEB Deutscher Verlag der Wissenschaften, Berlin, 1965).
- [78] V. Szebehely, *Theory of orbits. The restricted problem of three bodies* (Academic Press, New York, 1967).
- [79] C. L. Siegel and J. K. Moser, *Lectures on Celestial Mechanics* (Springer, Berlin, 1971).
- [80] P. Glaschke, Ph.D. thesis, University of Heidelberg, 2006, online available: <http://www.ub.uni-heidelberg.de/archiv/6553>.
- [81] M. Hénon and C. Heiles, *Astron. J.* **69**, 73 (1964).
- [82] F. Gustavson, *Astron. J.* **71**, 670 (1966).
- [83] P. Finkler, C. E. Jones, and G. A. Sowell, *Phys. Rev. A* **42**, 1931 (1990).

- [84] J. K. Moser, Mem. AMS **81**, 1 (1968).
- [85] C. Clementi and M. Pettini, Cel. Mech. Dyn. Astron. **84**, 263 (2002).
- [86] I. R. King, Astron. J. **67**, 471 (1962).
- [87] J. H. Oort, in *Galactic Structure*, edited by A. Blaauw and M. Schmidt (University of Chicago Press, Chicago, USA, 1965).
- [88] M. Feast and P. Whitelock, MNRAS **291**, 683 (1997).
- [89] J. Holmberg and C. Flynn, MNRAS **313**, 209 (2000).
- [90] K. A. Innanen, Ap. J. **85**, 81 (1980).
- [91] P. Laplace, in *Oeuvres Complètes de Laplace, Volume VII.* (Gauthier-Villars, Paris, 1820).
- [92] E. Dekker, Phys. Rep. **24**, 315 (1976).
- [93] F. Eisenhauer *et al.*, Ap. J. **597**, L121 (2003).
- [94] N. Mouawad *et al.*, Astron. Nachr. **326**, 83 (2005).
- [95] R. Schödel *et al.*, Astron. Astrophys. **469**, 125 (2007).
- [96] http://www.ph1.uni-koeln.de/workgroups/obs_astronomy/galactic_center/new/.
- [97] S. F. Portegies Zwart, J. Makino, S. L. W. McMillan, and P. Hut, Ap. J. **565**, 265 (2002).
- [98] R. Genzel *et al.*, MNRAS **317**, 348 (2000).
- [99] A. M. Ghez *et al.*, Nature **407**, 349 (2000).
- [100] R. Schödel *et al.*, Nature **419**, 694 (2002).
- [101] A. Eckart *et al.*, in *The Evolution of Starbursts*, Vol. 783 of *American Institute of Physics Conference Series*, edited by S. Hüttemeister, E. Manthey, D. Bomans, and K. Weis (Springer, Berlin, 2005), p. 17.
- [102] A. M. Beloborodov *et al.*, Ap. J. **648**, 405 (2006).
- [103] M. Lindqvist, H. J. Habing, and A. Winnberg, Astron. Astrophys. **259**, 118 (1992).
- [104] P. G. Mezger, W. J. Duschl, and R. Zylka, Astron. Astrophys. Rev. **7**, 289 (1996).
- [105] R. Genzel *et al.*, Ap. J. **594**, 812 (2003).
- [106] J. Frank and M. J. Rees, MNRAS **176**, 633 (1976).
- [107] T. Paumard *et al.*, Ap. J. **643**, 1011 (2006).
- [108] Y. Levin and A. M. Beloborodov, Ap. J. **590**, L33 (2003).
- [109] J. Goodman, MNRAS **339**, 937 (2003).
- [110] M. Milosavljević and A. Loeb, Ap. J. **604**, L45 (2004).
- [111] S. Nayakshin, J. J. Cuadra, and R. Sunyaev, Astron. Astrophys. **413**, 173 (2004).
- [112] S. Nayakshin and J. J. Cuadra, Astron. Astrophys. **437**, 437 (2005).
- [113] S. Nayakshin and R. Sunyaev, MNRAS **364**, L23 (2005).

- [114] S. Nayakshin, MNRAS **372**, 143 (2006).
- [115] A. Krabbe, R. Genzel, S. Drapatz, and V. Rotaciuc, Ap. J. **382**, L19 (1991).
- [116] J. P. Maillard, T. Paumard, M. Morris, and F. Rigaut, in *Dynamics of Star Clusters and the Milky Way*, Vol. 228 of *ASP Conference Series*, edited by S. Deiters *et al.* (Astronomical Society of the Pacific, San Francisco, 2001), p. 509.
- [117] T. Paumard, J. P. Maillard, M. Morris, and F. Rigaut, Astron. Astrophys. **366**, 466 (2001).
- [118] R. F. Coker and J. M. Pittard, Astron. Astrophys. **361**, L13 (2000).
- [119] B. M. S. Hansen and M. Milosavljević, Ap. J. **593**, L77 (2003), arXiv:astro-ph/0306074.
- [120] S. L. W. McMillan and S. F. Portegies Zwart, Ap. J. **596**, 314 (2003).
- [121] R. Schödel *et al.*, Ap. J. **625**, L111 (2005).
- [122] S. F. Portegies Zwart and S. L. W. McMillan, Ap. J. **576**, 899 (2002).
- [123] M. J. Reid and A. Brunthaler, Ap. J. **616**, 872 (2004).
- [124] G. Meynet, Astron. Astrophys. **298**, 767 (1995).
- [125] P. S. Conti, in *Observational Tests of the Stellar Evolution Theory*, Vol. 105 of *IAU Symposium*, edited by A. Maeder and A. Renzini (Reidel, Dordrecht, 1984), p. 233.
- [126] D. F. Figer, I. S. McLean, and M. Morris, Ap. J. **514**, 202 (1999).
- [127] R. Genzel *et al.*, Ap. J. **472**, 153 (1996).
- [128] S. Gillessen *et al.*, ArXiv e-prints (2008).
- [129] F. Martins *et al.*, Ap. J. Lett. **672**, L119 (2008).
- [130] U. Löckmann, H. Baumgardt, and P. Kroupa, Ap. J. Lett. **683**, L151 (2008).
- [131] P. Chang, ArXiv e-prints (2008).
- [132] D. Merritt, A. Gualandris, and S. Mikkola, ArXiv e-prints (2008).
- [133] K. L. J. Rygi *et al.*, , arXiv:0812.0905.
- [134] E. Vanhollebeke *et al.*, Astron. Astrophys. **455**, 645 (2006).
- [135] M. Lindqvist, A. Winnberg, H. J. Habing, and H. E. Matthews, Astron. Astrophys. Suppl. Ser. **92**, 43 (1992).
- [136] L. O. Sjouwerman *et al.*, in *The Central Parsecs of the Galaxy*, Vol. 186 of *ASP Conference Series*, edited by H. Falcke *et al.* (Astronomical Society of the Pacific, San Francisco, 1999), p. 379.
- [137] H. J. Habing *et al.*, Astron. Astrophys. **128**, 230 (1983).
- [138] L. O. Sjouwerman, H. J. van Langevelde, A. Winnberg, and H. J. Habing, A&A Suppl. **128**, 35 (1998).
- [139] M. J. Reid, Ann. Rev. Astron. Astrophys. **31**, 345 (1993).
- [140] Y. M. Pihlström and L. O. Sjouwerman, Journal of Physics Conference Series **54**, 77 (2006).

- [141] F. Yusef-Zadeh *et al.*, in *Astrophysical Masers and Their Environments. Proceedings IAU Symposium No. 242, 2007, IAU*, edited by J. Chapman and W. Baan (PUBLISHER, ADDRESS, 2007).
- [142] G. B. Taylor, M. Morris, and E. Schulman, *Astron. J.* **106**, 1978 (1993).
- [143] D. A. Levine, D. F. Figer, M. Morris, and I. S. McLean, *Ap. J. Lett.* **447**, L101+ (1995).
- [144] J. L. Caswell, in *The Galactic Center*, Vol. 102 of *ASP Conference Series*, edited by R. Gredel (Astronomical Society of the Pacific, San Francisco, 1996), p. 247.
- [145] D. C. Lis, E. Serabyn, R. Zylka, and Y. Li, *Ap. J.* **550**, 761 (2001).
- [146] F. Yusef-Zadeh, C. Law, and M. Wardle, *Ap. J.* **568**, L121 (2002).
- [147] D. F. Figer *et al.*, *Ap. J.* **525**, 750 (1999).
- [148] D. F. Figer *et al.*, *Ap. J.* **506**, 384 (1998).
- [149] T. R. Geballe, F. Najjarro, and D. F. Figer, *Ap. J. Lett.* **530**, L97 (2000).
- [150] A. Stolte *et al.*, *Ap. J. Lett.* **628**, L113 (2005).
- [151] D. F. Figer *et al.*, *Ap. J.* **581**, 258 (2002).
- [152] R. D. Blum *et al.*, *Astron. J.* **122**, 1875 (2001).
- [153] E. Serabyn, D. Shupe, and D. F. Figer, *Nature* **394**, 448 (1998).
- [154] A. Stolte *et al.*, *Ap. J.* **675**, 1278 (2008).
- [155] E. Serabyn, D. Shupe, and D. F. Figer, in *The Central Parsecs of the Galaxy*, Vol. 186 of *ASP Conference Series*, edited by H. Falcke *et al.* (Astronomical Society of the Pacific, San Francisco, 1999), p. 320.
- [156] G. Mandushev, A. Staneva, and N. Spasova, *Astron. Astrophys.* **252**, 94 (1991).
- [157] A. Stolte, E. K. Grebel, W. Brandner, and D. F. Figer, *Astron. Astrophys.* **394**, 459 (2002).
- [158] A. Stolte, Ph.D. thesis, University of Heidelberg, 2003, online available: <http://www.ub.uni-heidelberg.de/archiv/3611>.
- [159] G. Contopoulos and T. Papayannopoulos, *Astron. Astrophys.* **92**, 33 (1980).
- [160] S. F. Portegies Zwart, J. Makino, S. L. W. McMillan, and P. Hut, *Ap. J.* **546**, L101 (2001).
- [161] S. F. Portegies Zwart, S. L. W. McMillan, and O. Gerhard, *Ap. J.* **593**, 352 (2003).
- [162] S. F. Portegies Zwart, S. L. W. McMillan, and H. Baumgardt, in *The Formation and Evolution of Massive Young Star Clusters*, Vol. 322 of *ASP Conference Series*, edited by H. J. G. L. M. Lamers, L. J. Smith, and A. Nota (Astronomical Society of the Pacific, San Francisco, 2004), p. 439.
- [163] S. S. Kim, D. F. Figer, and M. Morris, *Ap. J.* **607**, L123 (2004).
- [164] M. A. Gürkan, M. Freitag, and F. A. Rasio, *Ap. J.* **604**, 632 (2004).
- [165] M. A. Gürkan and F. A. Rasio, *Ap. J.* **628**, 236 (2005).
- [166] S. F. Portegies Zwart *et al.*, *Ap. J.* **641**, 319 (2006).

- [167] E. K rding, E. Colbert, and H. Faleke, *Astron. Astrophys.* **436**, 427 (2005).
- [168] M. Fujii, M. Iwasawa, Y. Funato, and J. Makino, *Ap. J.* **686**, 1082 (2008).
- [169] Y. Hashimoto, Y. Funato, and J. Makino, *Ap. J.* **582**, 196 (2003).
- [170] S. von Hoerner, *Zeitschrift fur Astrophysik* **50**, 184 (1960).
- [171] S. von Hoerner, *Zeitschrift fur Astrophysik* **57**, 47 (1963).
- [172] S. von Hoerner, Ph.D. thesis, University of G ttingen, 1951.
- [173] S. von Hoerner, *Die zeitliche Rate der Sternentstehung*. (Habilitation, University of Heidelberg, Heidelberg, 1959).
- [174] S. von Hoerner, in *Dynamics of Star Clusters and the Milky Way*, Vol. 228 of *ASP Conference Series*, edited by S. Deiters *et al.* (Astronomical Society of the Pacific, San Francisco, 2001), p. 11.
- [175] S. J. Aarseth, *Gravitational N-body Simulations: Tools and Algorithms* (Cambridge University Press, Cambridge, 2003).
- [176] S. J. Aarseth, *MNRAS* **126**, 223 (1963).
- [177] S. J. Aarseth, *PASP* **111**, 1333 (1999).
- [178] A. Ahmad and L. Cohen, *Journal of Computational Physics* **12**, 389 (1973).
- [179] P. Kustaanheimo and E. L. Stiefel, *J. f r reine angewandte Mathematik* **218**, 204 (1965).
- [180] S. Mikkola and S. J. Aarseth, *Cel. Mech. Dyn. Astron.* **47**, 375 (1990).
- [181] S. Mikkola and S. J. Aarseth, *Cel. Mech. Dyn. Astron.* **57**, 439 (1993).
- [182] S. Mikkola and S. J. Aarseth, *Cel. Mech. Dyn. Astron.* **64**, 197 (1996).
- [183] S. Mikkola and S. J. Aarseth, *New Astronomy* **3**, 309 (1998).
- [184] R. Spurzem, *J. Comp. Applied Maths.* **109**, 407 (1999).
- [185] O. Porth, Diplomarbeit, University of Heidelberg, 2007.
- [186] D. Prialnik, *An Introduction to the Theory of Stellar Structure and Evolution* (Cambridge University Press, Cambridge, UK, 2000).
- [187] D. C. Heggie and R. D. Mathieu, in *The Use of Supercomputers in Stellar Dynamics*, Vol. 267 of *Lecture Notes in Physics*, edited by P. Hut and S. L. W. McMillan (Springer, Berlin, 1986), p. 233.
- [188] M. Giersz and D. C. Heggie, *MNRAS* **268**, 257 (1994).
- [189] L. Spitzer and M. H. Hart, *Ap. J.* **164**, 399 (1971).
- [190] S. J. Aarseth, *Ap&SS* **14**, 118 (1971).
- [191] J. Makino and S. J. Aarseth, *PASJ* **44**, 141 (1992).
- [192] R. I. McLachlan, *SIAM J. Sci. Comp.* **16**, 151 (1995).
- [193] H. Yoshida, *Phys. Lett. A* **150**, 262 (1990).
- [194] S. Mikkola and S. Aarseth, *Cel. Mech. Dyn. Astron.* **84**, 343 (2002).

- [195] M. Suzuki, Phys. Lett. A **146**, 319 (1990).
- [196] W. Kahan and R.-C. Li, Math. Comput. **66**, 1089 (1997).
- [197] G. Sutmann, in *Computational Nanoscience: Do It Yourself! Lecture Notes. NIC Series, Vol. 31*, edited by J. Grotendorst, S. Blügel, and D. Marx (John von Neumann Institute for Computing, Jülich, Germany, 2006), p. 159.
- [198] S. Casertano and P. Hut, Ap. J. **298**, 80 (1985).
- [199] W. H. Press, S. A. Teukolsky, W. T. Vetterling, and B. P. Flannery, *Numerical Recipes in Fortran 77* (Cambridge University Press, Cambridge, 2001).
- [200] A. Just and J. Peñarrubia, Astron. Astrophys. **431**, 861 (2005).
- [201] P. Kroupa, C. A. Tout, and G. Gilmore, MNRAS **262**, 545 (1993).
- [202] V. A. Antonov, Scient. Trans. Leningrad Univ. **20**, 19 (1962).
- [203] D. Lynden-Bell and R. Wood, MNRAS **138**, 495 (1968).
- [204] I. Hachisu and D. Sugimoto, Progr. Theor. Phys. **60**, 123 (1978).
- [205] I. Hachisu, Y. Nakada, K. Nomoto, and D. Sugimoto, Progr. Theor. Phys. **60**, 393 (1978).
- [206] D. C. Heggie and P. Hut, *The Gravitational Million-Body Problem* (Cambridge University Press, Cambridge, UK, 2003).
- [207] M. Giersz and D. C. Heggie, MNRAS **270**, 298 (1994).
- [208] M. Giersz and D. C. Heggie, MNRAS **279**, 1037 (1996).
- [209] H. Baumgardt and J. Makino, MNRAS **340**, 227 (2003).
- [210] M. Trenti, D. C. Heggie, and P. Hut, MNRAS **374**, 344 (2007).
- [211] A. Tanikawa and T. Fukushige, PASJ **57**, 155 (2005).
- [212] M.-M. Mac Low and R. S. Klessen, Rev. Mod. Phys. **76**, 125 (2004).
- [213] J. Ballesteros-Paredes, R. S. Klessen, M.-M. Mac Low, and E. Vazquez-Semadeni, in *Protostars and Planets V*, edited by B. Reipurth, D. Jewitt, and K. Keil (University of Arizona Press, Tucson, 2007), pp. 63–80.
- [214] T. Hasegawa, F. Sato, J. B. Whiteoak, and R. Miyawaki, Ap. J. **429**, L77 (1994).
- [215] L. Hartmann, Ap. J. **578**, 914 (2002).
- [216] R. B. Larson, MNRAS **214**, 379 (1985).
- [217] R. S. Klessen, J. Ballesteros-Paredes, Y. Li, and M.-M. Mac Low, in *The Formation and Evolution of Massive Young Star Clusters*, Vol. 322 of *ASP Conference Series*, edited by H. J. G. L. M. Lamers, L. J. Smith, and A. Nota (Astronomical Society of the Pacific, San Francisco, 2004), pp. 299–+.
- [218] S. Chandrasekhar, Ap. J. **97**, 255 (1943).
- [219] M. Hénon, in *Dynamical structure and evolution of stellar systems, Lectures of the 3rd Advanced Course of the Swiss Society for Astronomy and Astrophysics (SSAA)*, edited by L. Martinet and M. Mayor (Geneva Observatory, Sauverny, 1973), p. 183.

- [220] L. Hernquist, *Ap. J.* **356**, 359 (1990).
- [221] W. Dehnen, *MNRAS* **265**, 250 (1993).
- [222] S. Tremaine *et al.*, *Astron. J.* **107**, 634 (1994).

Danksagung

“There should be no mysteries in stellar dynamics.”

Sverre J. Aarseth

Der Verfasser dieser Arbeit verdankt vieles den Gesprächen und Diskussionen mit den Mitgliedern der Stelldynamik-Arbeitsgruppe am Astronomischen Rechen-Institut und anderen Menschen.

Ich möchte zunächst meinem Doktorvater, PD Dr. Andreas Just, herzlich für die Betreuung dieser Arbeit danken. Vor allem in den schwierigen Phasen der Doktorarbeit bemühte sich Andreas seinerseits, durch Gespräche zu ihrem Gelingen beizutragen, ganz abgesehen davon, daß ich zu jedem Zeitpunkt durch die offene Tür seines Büros treten durfte, wenn wissenschaftlicher Diskussionsbedarf bestand. Ich erinnere mich noch gut an einen Nachmittag im Jahr 2007, an dem ich Andreas' Büro betrat und ihn auf Knoten in den Gezeitenarmen aufmerksam machte, die ich in meinen Simulationen entdeckt hatte. Ich bemerkte, daß es doch wohl interessant wäre, dieses Phänomen näher zu untersuchen. Die Literatur war mir damals noch gar nicht bekannt. Kurze Zeit später fand Peter Berczik, nur ein Büro entfernt, die Knoten auch in seinen Simulationen. Mit gewecktem Interesse entwickelte Andreas die analytische Theorie der Dynamik in den Gezeitenarmen weiter, die ausführlich in Kapitel 4 behandelt wurde und die ich dann - in analytischen Rechnungen nicht so bewandert - erfolgreich auf die Auflösung eines Sternhaufens im Galaktischen Zentrum anwenden konnte. Ohne Andreas würde diese Arbeit in der vorliegenden Form nicht existieren.

Mein besonderer Dank gilt auch Prof. Dr. Rainer Spurzem, der das Zweitgutachten dieser Arbeit übernommen hat, nachdem er bereits meine Diplomarbeit betreut hatte. Beim Gedanken an Rainer kommt mir manchmal das altgriechische Wort $\varphi\rho\nu\nu\epsilon\sigma\zeta$ in den Sinn, welches bei Aristoteles eine der dianoetischen Tugenden bezeichnet, die auch den großen Staatsmännern und -frauen, wie Perikles oder Angela Merkel, zu eigen sein soll.¹ Rainer ist stets reich an Rat. Bemerkenswert ist auch sein unermüdlicher Einsatz für seine Arbeitsgruppe. Ohne die von Rainer beantragte Rechenzeit im DEISA-Grid wären wohl viele Ergebnisse dieser Arbeit ausgeblieben. Und was wäre die Stelldynamik-Arbeitsgruppe am Astronomischen Rechen-Institut ohne Rainers Tatkraft und seine Leitung des wöchentlichen Teeminars (=Tee-Seminars)? Ohne Rainer würde diese Arbeit in der vorliegenden Form auch nicht existieren.

Auch den übrigen ehemaligen und gegenwärtigen Mitgliedern der Arbeitsgruppe danke ich herzlich: Kristina Wäcken, Oliver Porth, Jonathan Downing, Fazeel Khan, Ovidiu Furdui, Dr. Miguel Preto, Dr. Patrick Glaschke, Dr. José Fiestas, Dr. Andrea Borch, Dr. Ingo Berentzen and Dr. Peter Berczik. Mit Kristina zoffte ich mich einmal, als es darum ging, vor dem Teeminar noch Teelichter aus dem “Lidl” zu holen. Mit Oliver führte ich meistens wichtige wissenschaftliche Diskussionen. Jonathan glaubte mir nicht, wenn ich manche Vertreter des Dunkle-Materie-Paradigmas des quasi-religiösen Fundamentalismus verdächtigte. When I walked once with Fazeel back from the Mensa on the main campus, I noticed an astronomical sundial at one house. Mit Ovidiu führte ich im Winter Diskussionen darüber, ob die Heizung im “Wintergarten” unseres Büros in der Weberstraße 13 auf dem Maximum oder dem Minimum stehen solle. Without Miguel's microwave oven a delicate experiment to study the structure of polymer molecules together with Oliver would not have been possible. Von Patrick lernte ich die Dimensionsanalyse und im Prinzip auch, was theoretische Physik ist. Was wäre die Arbeitsgruppe ohne José und Wendy? Nichts. Andrea hat hoffentlich in Indien den Faust I gelesen. Ingo erklärte mir einmal

¹Achtung: Ich studierte einst Philosophie im Nebenfach.

interessant die Resonanzphänomene in Balkengalaxien und empfahl mir das wirklich beste Buch über Chaostheorie. Peter is always tireless in his help.

Dr. Peter Schwekendiek und Thomas Brüesemeister danke ich herzlich für die Unterstützung in Computerdingen. Herzlich danke ich auch Marc-André Hermanns am Forschungszentrum Jülich für seine tatkräftige Unterstützung im Rahmen unseres DEISA-Projektes. Ich danke Dr. Godehard Sutmann am Forschungszentrum Jülich dafür, daß er mich auf die Existenz von Kompositionsverfahren zur Integration der Hamiltonschen Bewegungsgleichungen aufmerksam machte, and I am grateful to Dr. Seppo Mikkola for his help with the implicit midpoint method at the Cambridge summer school in Cambridge in 2006 which was organized by Sverre Aarseth. I thank Dr. Marc Freitag for his reference values for Table 2.1 and Prof. Douglas Heggie and an anonymous referee for comments which finally led to the RE classification.

I am grateful for financial support by the International Max Planck Research School (IMPRS) for Astronomy and Cosmic Physics at the University of Heidelberg. I would like to specially thank the student representatives, Ros Skelton and Marcello Cacciato and the coordinator Dr. Christian Fendt. Furthermore, I thank the DEISA Consortium (www.deisa.eu), co-funded through EU FP6 projects RI-508830 and RI-031513, for support within the DEISA Extreme Computing Initiative.

Es ist mir nun noch überlassen, leise zu erwähnen, daß diese Arbeit ohne das Lebenswerk von Dr. Sverre Aarseth, Cambridge, UK, nicht existieren würde. Takk, Sverre!